University of Arkansas, Fayetteville
ScholarWorks@UARK

Graduate Theses and Dissertations

12-2015

The Aerodynamic and Dynamic Loading of a Slender Structure by an Impacting Tornado-Like Vortex: The Influence of Relative Vortex-to-Structure Size on Structural Loading

Matthew Nicholas Strasser
University of Arkansas, Fayetteville

Follow this and additional works at: https://scholarworks.uark.edu/etd

 Part of the Acoustics, Dynamics, and Controls Commons, Aerodynamics and Fluid Mechanics Commons, and the Civil Engineering Commons

Citation

Strasser, M. N. (2015). The Aerodynamic and Dynamic Loading of a Slender Structure by an Impacting Tornado-Like Vortex: The Influence of Relative Vortex-to-Structure Size on Structural Loading. *Graduate Theses and Dissertations* Retrieved from https://scholarworks.uark.edu/etd/1371

This Dissertation is brought to you for free and open access by ScholarWorks@UARK. It has been accepted for inclusion in Graduate Theses and Dissertations by an authorized administrator of ScholarWorks@UARK. For more information, please contact scholar@uark.edu.

The Aerodynamic and Dynamic Loading of a Slender Structure by an Impacting Tornado-Like Vortex: The Influence of Relative Vortex-to-Structure Size on Structural Loading

A dissertation submitted in partial fulfillment
of the requirements for the degree of
Doctor of Philosophy in Civil Engineering

by

Matthew N. Strasser
Harding University
Bachelor of Science in Mechanical Engineering, 2011
University of Arkansas
Master of Science in Civil Engineering, 2012

December 2015
University of Arkansas

This dissertation is approved for recommendation to the Graduate Council.

_____
Dr. R. Panneer Selvam
Dissertation Director

_____
Dr. Ernest Heymsfield
Committee Member

_____
Dr. Rick Couvillion
Committee Member

_____
Dr. Micah Hale
Committee Member

ABSTRACT

Structural loading produced by an impacting vortex is a hazardous phenomenon that is encountered in numerous applications ranging from the destruction of residences by tornados to the chopping of tip vortices by rotors. Adequate design of structures to resist vortex-induced structural loading necessitates study of the phenomenon that control the structural loading produced by an impacting vortex. This body of work extends the current knowledge base of vortex-structure interaction by evaluating the influence of the relative vortex-to-structure size on the structural loading that the vortex produces. A computer model is utilized to directly simulate the two-dimensional impact of an impinging vortex with a slender, cylindrical structure. The vortex's tangential velocity profile (TVP) is defined by a normalization of the Vatistas analytical (TVP) which realistically replicates the documented spectrum of measured vortex TVPs. The impinging vortex's maximum tangential velocity is fixed, and the vortex's critical radius is incremented from one to one-hundred times the structure's diameter. When the impinging vortex is small, it interacts with vortices produced on the structure by the free stream, and maximum force coefficient amplitudes vary by more than 400% when the impinging vortex impacts the structure at different times. Maximum drag and lift force coefficient amplitudes reach asymptotic values as the impinging vortex's size increases that are respectively 94.77% and 10.66% less than maximum force coefficients produced by an equivalent maximum velocity free stream. The vortex produces maximum structural loading when its path is shifted above the structure's centerline, and maximum drag and lift force coefficients are respectively up to 4.80% and 34.07% greater than maximum force coefficients produced by an equivalent-velocity free stream. Finally, the dynamic load factor (DLF) concept is used to develop a generalized methodology to assess the dynamic amplification of a structure's response to vortex loading and to assess the

dynamic loading threat that tornados pose. Typical civil and residential structures will not experience significant response amplification, but responses of very flexible structures may be amplified by up to 2.88 times.

ACKNOWLEDGMENTS

I first and foremost thank God for bestowing upon me the capability, desire, and fortitude to pursue this work to its completion. Without him, nothing is possible (Proverbs 25:2, Philippians 4:13).

I must express my deepest gratitude to Dr. Panneer Selvam for his mentorship over the last four and one-half years. Under his guidance, my capability to conduct independent research and to self-educate in new fields has greatly improved. I will certainly miss our talks about issues in global politics, religion, and investing which have broadened my perspective.

I would like to thank Dr. Ernest Heymsfield, Dr. Micah Hale, and Dr. Rick Couvillion for serving on my dissertation committee and providing invaluable criticism and suggestions that greatly enhanced the overall quality of the work.

I would like to thank my friends and colleagues Philip Varney, Cyrus Garner, and Dr. Eric Fernstrom for their continual support and aid with troubleshooting numerous research-related problems and proof reading of my technical papers.

Lastly, I would like to acknowledge the members of my research group: Nawfal Ahmed, Majdi Yousef, Blandine Kemayou, Alhussin Aliwan, and Damoso Domingo. Thank you for contributing to a pleasant work environment, and I wish you all the best as you complete your work and move forward in life.

TABLE OF CONTENTS

CHAPTER 1: INTRODUCTION AND OBJECTIVES 1

1.1 Introduction 1

1.2 Thesis Objectives 9

1.2.1 Objective 1 9

1.2.2 Objective 2 10

1.2.3 Objective 3 10

1.2.4 Objective 4 11

1.2.5 Objective 5 12

CHAPTER 2: LITERATURE REVIEW 14

2.1 Introduction 14

2.2 Physical Experiments 14

2.2.1 Blade-Vortex Interaction 14

2.2.2 Tornado Simulator Experiments 15

2.3 Computer Simulation 16

2.3.1 Two-Dimensional Simulations 16

2.3.2 Three-Dimensional Simulations 18

2.4 Post-Storm Damage Rating Investigation 18

2.4.1 Damage Rating Scales 19

2.4.2 Applicability of Damage Rating Scales 20

2.4.3 Why are Different Damage Ratings Used for Tornados and Hurricanes? 22

2.4.4 Tornado and Hurricane Occurrence Statistics 23

2.5 Dynamic Structure Loading by Tornados 26

2.6 Comparison of Real-World and Simulated Tornado and Hurricane Vortices 28

2.7 The Tangential Velocity Profile of a Vortex 30

2.8 Summary and Thesis Motivation 34
2.8.1 Summary of Literature Review 34
2.8.2 Thesis Motivation 36
2.8.3 Progression of Thesis 39
CHAPTER 3: SELECTION OF REALISTIC TANGENTIAL VELOCITY PROFILES 41
3.1 Analytical Tangential Velocity Profiles 42
3.1.1 Bi-Regional Profiles 42
3.1.2 Continuous Profiles 43
3.1.3 Algebraic Profiles 45
3.1.4 Normalization and Comparison of Analytical Profiles 46
3.2 Measured Tangential Velocity Profiles 48
3.2.1 Vortex Chamber Experiments 48
3.2.2 Tornado Simulator Experiments 50
3.2.3 Fixed-Wing Experiments 51
3.2.4 Rotor Experiments 53
3.2.5 Measured Tornados 54
3.2.6 Measured Hurricanes 56
3.3 Comparison and Analysis of Analytical and Measured Profiles 57
3.4 Conclusions 59
CHAPTER 4: COMPUTER MODEL 61
4.1 Problem Description 61
4.1.1 System Parameters 62
4.1.2 Low Reynolds Number Limitation 62
4.2 Governing Equations 64
4.2.1 Vortex Tangential Velocity Profile 65

4.3 Numerical Method 66
4.4 Domain, Grid, and Boundary Conditions 67
4.4.1 Domain and Grid 67
4.2.2 Boundary Conditions 70
4.5 Numerical Validation 72
4.5.1 Validation Using Free Stream Simulations 72
4.5.2 Validation by Assessment of Vortex Transport 75
CHAPTER 5: THE INFLUENCE OF THE IMPINGING VORTEX'S SIZE AND PATH ON STRUCTURAL LOADING 79
5.1 Chapter Overview and Progression 79
5.2 Variation in Maximum Cylinder Loading Due to Vortex Impact Time 80
5.2.1 Methodology and Approach 80
5.2.2 Maximum Force Coefficient Amplitudes 83
5.2.3 Visualization of the Interaction between Impinging and Attached Vortices 88
5.2.4 Summary of Interaction between Impinging and Attached Vortices 92
5.3 Influence of Relative Vortex-to-Cylinder Size on Cylinder Loading 93
5.3.2 Trend in Maximum Cylinder Loading with Impinging Vortex Size 96
5.3.3 Visualization of Cylinder Loading Trend with Increasing Vortex Size 101
5.3.4 Summary of Cylinder Loading Trend with Increasing Vortex Size 104
5.4 Influence of Vortex Path on Structural Loading 105
5.4.1 Methodology and Approach 105
5.4.2 Trend in Structural Loading with Vortex Path Shift 105
5.4.3 Why the Vortex Produces Greater Loading than the Free Stream 108
5.4.4 Visualization of Vortex-Cylinder Interaction Influenced by Vortex Path Shift 114
5.5 Summary and Conclusions 116
CHAPTER 6: DYNAMIC AMPLIFICATION OF TORNADO WIND LOADS 120

6.1 Overview 120
6.2 The Vortex's Tangential Velocity 121
6.3 Single Degree of Freedom Response Model 123
6.3.1 Reduction of System Order 124
6.3.2 RK4 Formulation and Validation 127
6.4 The Dynamic Load Factor 129
6.4.1 Construction of DLF Curves 131
6.5 Definition of the Vortex Loading Period 136
6.5.1 Methodology 137
6.5.2 Influence of Vortex Size on Vortex Loading Period 139
6.5.3 Influence of Vortex Translational Velocity on Vortex Loading Period 141
6.5.4 Influence of Vortex Profile on Vortex Loading Period 142
6.5.5 Why Use the DLF Instead of the Fourier transform to Identify T_v? 144
6.6 Use of Empirical Equations to Define Vortex Loading 146
6.6.1 Overview 146
6.6.2 Validation of Empirical Equation-Defined Forcing 147
6.6.3 Influence of Vortex Velocity Ration on Vortex Loading Period 150
6.7 Definition of DLF Curves for Vortex Loading 152
6.8 Definition of the Generalized DLF Curve for Tornado Wind Loads 154
6.8.1 Tornado Vortex Parameters and Fundamental Structure Periods 154
6.8.2 Generalized DLF Curve for Tornado Wind Loads 157
6.8.3 Practical Assessment of Tornado Dynamic Loading Threat 159
6.9 Summary and Conclusions 161
CHAPTER 7: SUMMARY AND CONCLUSIONS 163
7.1 Summary 163

7.2 Conclusions 164
7.2.1 Objective 1 165
7.2.2 Objective 2 166
7.2.3 Objective 3 167
7.2.4 Objective 4 169
7.2.5 Objective 5 170
7.3 Primary Contributions to the Scientific Community 172
7.4 Limitations of the Present Study 173
7.5 Suggested Future Work 174
CITED WORK 177
APPENDIX A: USE OF CFD CODE "FCIR24.EXE" 191
A.1 Introduction and Overview 191
A.2 Preparation of Input Data File f2dinp.txt 194
A.2.1 Sample Input Data File 195
A.2.2 Use of GW.f to Produce f2dinp.txt 196
A.2.3 Source Code for GW.f 197
APPENDIX B: DATA EXTRACTION PROGRAM "GET_DAT.M" 200
B.1 Overview and Description 200
B.2 Demonstration of Use 201
B.3 Source Code 203
APPENDIX C: DLF ANALYSIS PROGRAM "DLF.M" 206
C.1 Overview and Description 206
C.2 Demonstration of Use 207
C.3 Source Code (Dimensional) 208
C.4 Source Code (Dimensionless) 211

APPENDIX D: EMPERICAL CYLINDER LOADING BY VORTEX “EFC.F” 214

D.1 Overview and Description 214

D.2 Demonstration of Use 215

D.3 Source Code 217

CURRICULUM VITAE 219

FIGURE CAPTIONS

Figure 1.1: (a) The May 2011 Joplin, MO tornado and (b) damage track through a subdivision in Joplin, MO (Magill, 2012). [1]

Figure 1.2: Rotor tip vortices produced by (a) de Havilland Canada DHC-5 Buffalo turbo-prop plane and (b) Cobra attack helicopter (Diaz, 2010). [2]

Figure 1.3: Wing tip vortices behind (a) CF 18 Hornet (Chandler, 2005) and (b) Boeing 727 (uiowa, 1999). [2]

Figure 1.4: Vortex shedding from mountains on islands near Chile (NASA, 2013) and (b) cluster of tall buildings in Dubai (Cheong, 2015). [3]

Figure 1.5: (a) 3D and (b) 2D schematics of parallel interaction of a vortex with a cylinder. [7]

Figure 2.1: (a) Documented tornados in the United States in 2014 (Taken from NOAA, 2014a) and (b) tornado occurrences per 10,000 mi^2 land area in each state (Taken from NOAA, 2015a). [25]

Figure 2.2: Average annual tornado occurrence as function of (a) month and (b) time of day (NOAA, 2015a). [25]

Figure 2.3: Examples of real-world atmospheric and mechanically-produced vortices. [32]

Figure 3.1: Comparison of normalized S-K, L-O, and RCVM vortex TVPs with their replications by the normalized (a) Vatistas and (b) W-W profiles. [47]

Figure 3.2: (a) Schematic of the vortex chamber experiment configuration and (b) vortex TVPs from vortex chamber experiments. [49]

Figure 3.3: (a) Schematic of the translating tornado simulator at Iowa State University (Modified from Haan et al. (2010)) and (b) vortex TVPs from tornado simulator experiments. [50]

Figure 3.4: (a) Prandtl's fixed-wing experiment (Modified from Barba (2013)) and (b) vortex TVPs from fixed-wing experiments. [52]

Figure 3.5: (a) Schematic of the rotor tip vortex experiment, (b) shadowgraph of a rotor tip vortex (Modified from Bagai and Leishman (1993)), and (c) measured vortex TVPs from rotor tip experiments. [53]

Figure 3.6: (a) Measurement of tornado vortex TVP via mobile Doppler radar (Modified from NSF (2005)) and (b) measured tornado vortex TVPs. [55]

Figure 3.7: (a) Deployed dropsonde (Modified from UCAR (2012)) and unmanned Global Hawk (Gutro and Braun, 2012) and (b) measured hurricane TVPs. [57]

Figure 3.8: Comparison of analytical TVPs with measured TVPs from (a) vortex chamber, fixed-wing, and rotor tip experiments and (b) tornado simulators, tornados, and hurricanes. [59]

Figure 4.1: Schematic of the parallel interaction of an impinging vortex with a long, rigid, circular cylinder. [61]

Figure 4.2: Schematic of the computational domain and boundary conditions. [67]

Figure 4.3: Illustrations of (a) Grid 1 and (b) Grid 2 along with close-up views of grid refinement around the cylinder for (c) Grid 1 and (d) Grid 2. [68]

Figure 4.4: Schematic illustrating terms used to compute transient velocity boundary condition. [71]

Figure 4.5: Comparison of free stream cylinder loading data computed using the present model and grids with data from literature (a) Cd, (b) St, (c) Cd', and (d) Cl'. [74]

Figure 4.6: Comparison of L-O vortex transport accuracy using Grid 1 and Grid 2: (a) G1, r_c = 1·D, (b) G1, r_c = 2·D, (c) G2, r_c = 1·D, and (d) G2, r_c = 2·D. [76]

Figure 4.7: Comparison of analytical (a-b) and simulated (c-d) vortex tangential velocity profiles. [77]

Figure 5.1: (a) Vorticity contour and velocity vectors of free stream vortex shedding at Re = 150 and (b) corresponding drag and lift force coefficients. [81]

Figure 5.2: (a) Shedding of a CW vortex from the top of the cylinder and (b) illustration of the lag between maximum values of the lift and drag force coefficients. [81]

Figure 5.3: (a) Selected period of the VSC and (b) discretization of the VSC with 25 TOI (Strasser and Selvam, 2015). [83]

Figure 5.4: Force coefficient time histories for impinging vortex of radius r_c = 1·D impacting the cylinder at (a) TOI 1, (b) TOI 2, (c) TOI 3, and (d) TOI 4 (Strasser and Selvam, 2015). [84]

Figure 5.5: (a) Extraction of signed amplitudes from a typical force coefficient time history and (b) summary of signed amplitudes for impinging vortex impact at 25 TOI (Strasser and Selvam, 2015). [85]

Figure 5.6: Maximum force coefficient amplitudes for impinging vortex impact at 25 TOI for impinging vortex radii of (a) 2·D and (b) 3·D (Strasser and Selvam, 2015). [86]

Figure 5.7: Vorticity contours and velocity vectors at TOI 1-4 (by row) for free stream flow over the cylinder (column a) and for the three relative positions of the vortex to the cylinder illustrated in row 5 (columns b-d) (Strasser and Selvam, 2015). [89]

Figure 5.8: (a) Maximum force coefficient amplitudes for impinging vortex ($r_c = 1 \cdot D$) impact at 25 TOI and (b) Separation of 25 TOI into 5 sets of 5. [95]

Figure 5.9: Typical time histories for impinging vortex radii (a) $1 \cdot D$, (b) $10 \cdot D$, and (c) $100 \cdot D$. [97]

Figure 5.10: Mean maximum force coefficient amplitudes from five simulations (envelopes mark the variation with vortex impact time) (a) for $1 \leq r_c/D \leq 20$ and (b) for $1 \leq r_c/D \leq 50$. [97]

Figure 5.11: Mean maximum force coefficients and envelopes as function of impinging vortex size for (a-b) RCVM and (c-d) S-K vortex tangential velocity profiles. [99]

Figure 5.12: Schematic of the cylinder (a) within the leading edge of the vortex, (b) alligning with the vortex center, and (c) within the trailing edge of the vortex. [101]

Figure 5.13: Vorticity contour plots of the vortex-cylinder interaction for impinging vortex of radius $1 \cdot D$ (Row 1), $10 \cdot D$ (Row 2), and $100 \cdot D$ (Row 3). [103]

Figure 5.14: Schematic of vertical shift of vortex's path by (a) $\delta = r_c$, (b) $\delta = 0$, and (c) $\delta = -r_c$. [106]

Figure 5.15: Force coefficient time histories for impinging vortex having r_c of $50 \cdot D$ and (a) $\delta = r_c$, (b) $\delta = 0$, and (c) $\delta = -r_c$. [106]

Figure 5.16: Maximum force coefficients for impinging vortex of $r_c = 50 \cdot D$ and vertical path shift of $-4 \leq \delta/r_c \leq 4$. Horizontal lines indicate maximum force coefficients for free stream flow at equivalent maximum velocity ($U = U_\infty + V_{\theta,max}$). [107]

Figure 5.17: Forces produced on a cylinder (a) a free stream and (b) a stream incident from any direction. [108]

Figure 5.18: (a) Typical free stream force coefficient time histories and (b) free stream force coefficient amplitudes as functions of V_R. [109]

Figure 5.19: Maximum (a) drag and (b) lift force coefficient amplitude as a function of resultant velocity incidence angle. [111]

Figure 5.20: Comparison of force coefficient time histories from computer simulation and defined using Eqs. (5.2-6) for impinging vortices travelling at (a) $\delta = r_c$ and (b) $0.75 \cdot r_c$. [112]

Figure 5.21: Time histories of resultant V_R magnitude and incidence angle for (a) $\delta = r_c$ and (b) $0.75 \cdot r_c$. [113]

Figure 5.22: Vorticity contour plots of the vortex-cylinder interaction for impinging vortex of radius 50·D and vertical offset of $\delta = r_c$ (Row 1), $\delta = 0$ (Row 2), and $\delta = -r_c$ (Row 3). [116]

Figure 6.1: Time histories of (a) cross-stream velocity component, (b) lift force coefficient, and (c) decomposed lift force coefficient. [122]

Figure 6.2: (a) Physical representation of the SDOF response model and (b) free body diagram of the SDOF system. [123]

Figure 6.3: Comparison of the response spectra defined analytically by Eq. (6.25) and that defined numerically by the RK4 numerical solution. [128]

Figure 6.4: DLF curves for some common forcing profiles ($\zeta = 0$). [130]

Figure 6.5: Sinusoid impulse applied as forcing. [131]

Figure 6.6: Responses of the four SDOF structures defined in Table 6.1 to the sinusoidal forcing shown in Figure 6.5. [132]

Figure 6.7: Dimensionless response of the four SDOF structures to the sinusoid forcing. [133]

Figure 6.8: DLF curve for a single period of sinusoidal loading. [135]

Figure 6.9: (a) Sinusoid forcing profile having application period T_d and (b) vortex forcing profile having unknown application period T_v. [136]

Figure 6.10: Free stream lift force coefficient (a) time history and (b) DLF curve. [138]

Figure 6.11: Vortex loading lift force coefficient (a) time history and (b) DLF curve. [139]

Figure 6.12: (a) Lift force coefficient DLF curves and (b) zoomed view of f_v illustrating the progressive decrease in f_v with increasing r_c. [140]

Figure 6.13: (a) Vortex loading period as function of vortex critical radius for $r_c = 2 \cdot D$ to $10 \cdot D$ and (b) dimensionless region of the L-O vortex's tangential velocity profile corresponding to T_v. [141]

Figure 6.14: (a) Vortex loading period as function of vortex translational velocity and (b) consolidation of vortex loading period curves using Eq. (6.29). [142]

Figure 6.15: (a) Definition of $T_v(r_c)$ for the three vortex profiles and (b) dimensionless regions of the three vortex tangential velocity profiles corresponding to T_v^*. [143]

Figure 6.16: (a) Lift force coefficient time history, (b) corresponding Fourier Transform, and (c) corresponding dynamic load factor curve for (1) simulated free stream flow over a cylinder and (2) simulated vortex impact with a cylinder. [145]

Figure 6.17: Comparison of force coefficient time histories from computer simulation and defined by the empirical equations: (a) $V_{\theta,max}/U_{\infty} = 1.0$ and (b) $V_{\theta,max}/U_{\infty} = 4.3$. [148]

Figure 6.18: (1) Mean lift force coefficient time histories for (a-c) RCVM, L-O, and S-K vortex profiles and (2) comparison of T_v from DLF of equation-defined forcing (black dots) with Eq. (6.18) (dashed line). [149]

Figure 6.19: Variation in (a) tangential velocity time history and (b) the mean lift force coefficient time history with variation in vortex velocity ratio. [150]

Figure 6.20: (a) Vortex loading period curves for considered vortex velocity ratios and (b) comparison of vortex loading periods with the definition given by Eq. (6.29). [151]

Figure 6.21: DLF curves for vortex loading by vortices having (a) RCVM, (b) L-O, and (c) S-K tangential velocity profiles. [152]

Figure 6.22: DLF curves for (a) triangle wave and (b) sine wave forcing profiles. [153]

Figure 6.23: DLF curves produced by application of only the portion of the vortex forcing profile defined by T_v for (a) RCVM, (b) L-O, and (c) S-K vortex profiles. [154]

Figure 6.24: Illustration of the four structure period groups G1-G4 and examples of structures within these ranges. [156]

Figure 6.25: (a) DLF curves for three vortex tangential velocity profiles and (b) 3-region, piecewise curve fit defining the maximum DLF value for each fundamental structure period. [158]

Figure 6.26: (a) Generalized maximum DLF curve for tornado wind loads as function of T_n and (b) illustration of maximum DLF values for structure groups G1-G4. [158]

Figure A.1: Flow chart illustrating the simulation process using fcir24. [191]

Figure A.2: Illustration of process for compressing individual movie files into a running movie using Tecplot®. [193]

Figure A.3: Grid produced using the sample f2dinp.txt data file. [196]

Figure B.1: (a) Original data plot and (b) .jpg impage of the original data plot. [201]

Figure B.2: Illustration of "Capture.jpg" in the Matlab® environment and the three axis that the user must click-select and assign values of. [202]

Figure B.3: Comparison of original data points with extracted data points. [203]

Figure C.1: (a) Force coefficient time histories and (b) corresponding DLF curves. [207]

Figure D.1: (a) Mean force coefficient time histories from “FC(Mean).plt” and (b) force coefficient envelop time histories from “FC(Envelopes).plt”. [216]

TABLE CAPTIONS

Table 1.1: Summary of studies on the influence of relative vortex-to-structure size on structure loading amplitude. [5]

Table 2.1: Saffir-Simpson damage scale (NOAA, 2012). [19]

Table 2.2: Enhanced Fujita damage Scale (McDonald et al., 2009). [19]

Table 2.3: Summary of hurricane occurrence from 1851-2004 (Blake et al., 2005). [24]

Table 2.4: Summary of tornado occurrence from 1995-2009 (Edwards and Brooks, 2010). [24]

Table 2.5: Summary of documented tornado and hurricane wind speeds. [28]

Table 2.6: Summary of vortex parameters for computer experiments. [29]

Table 2.7: Summary of vortex parameters from three-dimensional tornado simulator at Iowa State University. [30]

Table 3.1: Values of exponent "x" used in the literature for tornado and hurricane TVPs. [42]

Table 3.2: Exponents used to replicate derived TVPs using Eq. (3.13). [46]

Table 3.3: Vortex Reynolds number ranges for tornado simulator TVPs. [51]

Table 3.4: Chord Reynolds number range for fixed wing vortex experiments. [52]

Table 3.5: Chord Reynolds number range for rotor vortex experiments. [54]

Table 3.6: Details for mobile Doppler radar measurement of tornado TVPs. [55]

Table 4.1: Summary of domain dimensions for Grid 1 and Grid 2. [68]

Table 4.2: Summary of computer simulations and associated CPU time for the simulations reported in this thesis. [69]

Table 4.3: Free stream computer simulations used to validate the present model. [73]

Table 4.4: Percentage of $V_{\theta,max}$ transported for each vortex size and profile. [78]

Table 5.1: Greatest and least maximum force coefficient amplitudes for impinging vortex of radius $r_c = 1 \cdot D$ impacting the cylinder at 25 TOI (Illustrated in Figure 5.5a). [85]

Table 5.2: Mean and mean-normalized standard deviation of maximum force coefficient amplitude curves for impinging vortex critical radii of $1 \cdot D$ to $3 \cdot D$. [87]

Table 5.3: Summary of greatest and least maximum force coefficient amplitudes for impinging vortex radii of 1·D to 3·D. [88]

Table 5.4: Comparison of mean maximum force coefficient amplitudes computed with 5 sets of 5 TOI with mean maximum force coefficient amplitudes computed using all 25 TOI as a set. [95]

Table 5.5: Summary of asymptotic maximum force coefficient amplitudes for RCVM, L-O, and S-K vortex tangential velocity profiles. [100]

Table 5.6: Comparison of maximum force coefficients produced by the vortex within the free stream with those produced by an equivalent maximum velocity free stream. [108]

Table 5.7: Comparison of maximum force coefficients computed using Eqs. (5.2-6) and maximum force coefficients from computer simulation. [114]

Table 6.1: Parameters for the four considered SDOF structures. [132]

Table 6.2: Range of documented tornado vortex parameters for defining T_v using Eq. (6.18). [155]

Table 6.3: Fundamental periods for real-world structures. [155]

Table 6.4: Minimum vortex loading period for each vortex profile. [157]

NOMENCLATURE

English

A	Projected cylinder area per unit length, $D \cdot L$ (m^2)
A_F	Forcing function amplitude (N)
A_s	Structure response amplitude (m)
C	Damping constant (kg/s)
Cd	Drag force coefficient, $2 \cdot Fd / A \cdot \rho \cdot U_\infty^2$ (dim)
$Cd'(+)$	Maximum positive drag coefficient amplitude (dim)
$Cd'(-)$	Maximum negative drag coefficient amplitude (dim)
C_F	Any force coefficient (dim)
Cl	Lift force coefficient, $2 \cdot Fl / A \cdot \rho \cdot U_\infty^2$ (dim)
$Cl'(+)$	Maximum positive lift coefficient amplitude (dim)
$Cl'(-)$	Maximum negative lift coefficient amplitude (dim)
C_N	Normal force coefficient, analogous to Cl for free stream (dim)
C_S	Stream-wise force coefficient, analogous to Cd for free stream (dim)
C_S'	Amplitude of stream-wise force coefficient (dim)
c	Airfoil chord length (m)
D	Diameter of the cylinder (m)
F_d	Drag force (N)
F_l	Lift force (N)
F_o	Maximum forcing amplitude (N or dim)
f_{Cl}	Frequency of vortex shedding (Hz)
f_n	Natural frequency of structure, $\omega_n/2 \cdot \pi$ (Hz)

f_v	Vortex loading frequency (Hz)
K	Structural stiffness (N/m)
$k_{1\text{-}4}$	Kutta coefficients for Runge-Kutta solution (dim)
L	Reference structure length (m)
M	Structure mass (kg)
N	Exponent for Vatistas' vortex model (dim)
P_∞	Ambient/Reference Pressure (N/m^2)
P^*	Dimensionless pressure, $P/\rho \cdot U_\infty^2$ (dim)
Q	Axial volumetric flow rate through vortex (m^3/s)
q_1	State variables for position in the response model (m)
q_2	State variables for velocity in the response model (m/s)
R	Radial coordinate of the vortex (m)
Re	Reynolds number, $D \cdot U_\infty/\nu$ (dim)
Re_c	Chord Reynolds number, $c \cdot U_\infty/\nu$ (dim)
Re_v	Vortex Reynolds number, Γ_∞/ν (dim)
R_m	Dimensionless mass term for response model, $\rho \cdot D \cdot A/M$ (dim)
r_c	Critical radius for the vortex (m)
r_p'	Radial distance between the vortex center and the boundary node (dim)
S	Vortex swirl ratio, $0.5 \cdot \Gamma_\infty \cdot r_c/Q$ (dim)
St	Strouhal number, dimensionless vortex shedding frequency, $f_{Cl} \cdot D/U_\infty$ (dim)
T_d	Dynamic load application period (s)
T_{lag}	Time required for the vortex and cylinder centers to align, X_o/U_∞ (dim)
T_n	Fundamental structure period (s)

T_v	Loading period of impacting vortex (s)
T_v^*	Dimensionless vortex shedding period (dim)
T^*	Period of vortex shedding for Re = 150, 1/St (dim)
t	Time (s)
t*	Dimensionless time ($t \cdot U_\infty / D$)
U	Horizontal velocity (m/s)
U_∞	Bulk velocity of the fluid stream (m/s)
U_∞^*	Dimensionless bulk velocity for response model, $U_\infty/\omega_n \cdot D$ (dim)
U^*	Dimensionless horizontal velocity, U/U_∞ (dim)
V	Vertical velocity (m/s)
V_θ	Tangential velocity of the vortex (m/s)
V^*	Dimensionless vertical velocity, V/U_∞ (dim)
V_R	Dimensionless Magnitude of velocity incident on the structure (dim)
X	Horizontal coordinate (m)
X_o	Starting location of the vortex (dim)
X^*	Dimensionless horizontal coordinate, X/D (dim)
X’	Horizontal coordinate of translating reference frame attached to vortex (dim)
x	Structure position or displacement (m)
$\dot{x}$	Structure velocity (m/s)
$\ddot{x}$	Structure acceleration (m/s^2)
x^*	Dimensionless structure position or displacement, x/D (dim)
$\dot{x}^*$	Dimensionless structure velocity, $U_\infty \cdot \dot{x}^*$ (dim)
$\ddot{x}^*$	Dimensionless structure acceleration, $U_\infty^2/D \cdot \ddot{x}^*$ (dim)

$x_{o,st}$	Maximum displacement from static application of forcing, F_o / K (m or dim)
x_p	Horizontal coordinate of boundary node with respect to cylinder center (dim)
x_p'	Horizontal coordinate of boundary node with respect to vortex center (dim)
Y	Vertical coordinate (m)
Y^*	Dimensionless vertical coordinate, Y/D (dim)
Y'	Vertical ordinate of translating reference frame attached to vortex (dim)
y_p	Vertical coordinate of boundary node with respect to cylinder center (dim)
y_p'	Vertical coordinate of boundary node with respect to vortex center (dim)

Greek

α	Dimensionless angular velocity of the vortex (dim)
α_o	Oseen vortex constant, 1.25643 (dim)
β	Sullivan vortex constant, 6.238 (dim)
δt^*	Solution time step (dim)
ζ	Damping ratio (dim)
Δr	Radial node spacing (dim)
ρ	Density of the fluid (kg/m^3)
ν	Kinematic viscosity of the fluid (m^2/s)
κ, η, λ	Coefficients for W-W vortex model (dim)
θ	Incidence angle of stream's velocity (deg)
Γ_∞	Infinite or total circulation, $2 \cdot \pi \cdot r_c \cdot V_{\theta,max}$ (m^2/s)
ω_d	Damped natural frequency (rad/s)
ω_f	Forcing frequency (rad/s)
ω_n	Natural frequency (rad/s)

Acronyms

BVI	Body Vortex Interaction
CW	Clockwise
CCW	Counter Clockwise
EF	Enhanced Fujita Scale
L-O	Lamb-Oseen
NSD	Mean Normalized Standard Deviation
ODE	Ordinary Differential Equation
RCVM	Rankine Combined Vortex Model
RK4	Fourth Order Runge-Kutta
SDOF	Single Degree of Freedom
S-K	Scully-Kaufmann
SS	Saffir-Simpson Scale
TOI	Time of Impact
TVP	Tangential Velocity Profile
UP	Under Prediction
VSC	Vortex Shedding Cycle
W-W	Wood and White

CHAPTER 1: INTRODUCTION AND OBJECTIVES

1.1 Introduction

On May 22, 2011, the devastating tornado depicted in Figure 1.1 struck the city of Joplin, MO. Despite the adequate advanced warning provided by the National Weather Service (NWS), 158 people lost their lives and an additional 1,000 residents sustained injuries (NWS, 2011). It is unlikely that loss of life due to severe tornados can be eliminated. However, the numbers of fatalities and injuries can certainly be reduced by adequately designing structures to resist tornado wind loads.



(a) (b)

Figure 1.1: (a) The May 2011 Joplin, MO tornado and (b) damage track through a subdivision in Joplin, MO (Magill, 2012).

Structural loading by impacting vortices is a hazardous phenomenon encountered in numerous applications of engineering significance. Severe atmospheric vortices, specifically tornados and hurricanes, cause 122 deaths (NWS, 2014) and $5.5 billion in financial losses (NWS, 2012) in the United States and its territories each year. Rotor-tip vortices produced by rotorcraft propellers (See Figure 1.2) are chopped by propeller blades, producing impulsive noise, aircraft vibration, and accelerated fatigue of the propeller blades (Bagai and Leishman, (1993), Ramasamy and Leishman, (2006), and Vatistas, (2006)). Wing-tip vortices produced by fixed-wing aircraft (See Figure 1.3) form hazardous, turbulent wakes that limit the capacity of

large airports (Bhagwat and Leishman, 2002). Vortices shed within clusters of tall structures (See Figure 1.4) impact downstream structures producing uncomfortable noise and vibration in the downstream structures (Rockwell, 1998). These few examples demonstrate that structural loading by vortices is a hazardous phenomenon that is relevant to much of society.



(a)



(b)

Figure 1.2: Rotor tip vortices produced by (a) de Havilland Canada DHC-5 Buffalo turbo-prop plane and (b) Cobra attack helicopter (Diaz, 2010).



(a) (b)

Figure 1.3: Wing tip vortices behind (a) CF 18 Hornet (Chandler, 2005) and (b) Boeing 727 (uiowa, 1999).



(a) (b)

Figure 1.4: Vortex shedding from mountains on islands near Chile (NASA, 2013) and (b) cluster of tall buildings in Dubai (Cheong, 2015).

It is imperative that the amplitude and character of structural loading produced by vortices be understood so that adequate design methodology may be adopted to resist the loading.

The aforementioned scenarios of structural loading by vortices collectively illustrate that the relative size of the impinging vortex to the impacted structure vary greatly depending upon the impact scenario. Tornado and hurricane vortices may have critical radii greater than 2 km (NOAA, 2013b) and 45 km (NOAA, 1980) respectively, meaning that they are many times larger than the structures that they load. Wing tip vortices and vortices produced within clusters of tall structures are similar-sized to the structures that they impact. Finally, critical radii of rotor tip vortices are several times smaller than the chord length of the rotors that chop them. This summary highlights the fact that structure loading by vortices occurs at practically all relative vortex-to-structure size scales. The question that immediately arises is "How does the relative vortex-to-structure size influence the character and amplitude of the resulting structure loading?"

Three methodologies are used to study structure loading by vortices: post-storm damage investigation, physical experiment, and computer simulation.

Post-storm damage investigation is premised on the fact that vortex induced loading is no different than loading produced by equivalent-velocity straight-line wind. Pre-determined

structural damage levels are used to estimate maximum wind speeds occurring in tornados via the Enhanced Fujita or "EF" scale (McDonald et al., 2009) and in hurricanes via the Saffir-Simpson or "SS" scale (Simpson and Saffir, 1974). Post-storm damage investigation affords an effective method to qualitatively document severe storm occurrence but is subject to bias (Such as: similar damage levels appearing differently, failure to document the most severe local damage, etc) and is based on the fallacious premise that vortex- and straight-line wind loading are equivalent. Post-storm damage investigation provides no direct information regarding the forces produced by atmospheric vortices, hence alternative methodology is needed to assess the loading that an impacting vortex produces on a structure.

Physical experiments have replicated impact of convecting vortices with air foils (Thom and Duraisamy, 2010) as well as the impact of sustained, tornado-like vortices with prismatic structures (Haan et al., 2008, 2010, and 2014). However physical experiments are costly and difficult to control. Convecting vortices are distorted by turbulence and high wind speeds within wind tunnels (Horner et al., 1996) in addition to being attenuated by interaction with side walls (Seath et al., 1989). Haan et al.'s (2008, 2010, and 2014) sustained vortices have unrealistic properties, raising question as to whether or not realistic tornado-like vortices can be reproduced in laboratory settings. In short, it is difficult to physically simulate impact of structures by vortices and therefore physical experimentation is not currently a viable approach to develop correlations between vortex parameters and the loading that vortices produce.

The inherent uncertainty, physical complexity, and high cost of alternative assessment methodologies encourages that vortex-structure interaction be studied via computer simulation. Upon developing an accurate computer model, practically all vortex parameters are accessible variables, and meaningful correlations can be developed between vortex parameters and the

resulting structural loading. The primary drawback to investigation via computer simulation is that model validation is difficult due to the lack of data from physical experiments, so combinations of common benchmark problems are required for validation.

Several studies utilize computer simulation to study the influence of relative vortex-to-structure size on structure loading amplitude as summarized in Table 1.1. The collective conclusion of the three studies is that structure loading amplitude progressively increases as the relative vortex-to-structure size increases. Due to the variation in simulation and body type, there is apprehension to generally accept this conclusion. Although a relatively wide range of relative vortex-to-structure size ratios is covered, three different body geometries are utilized, and two different vortex wind field models are used. Furthermore, the grid refinement utilized in most of Alrasheedi's (2012) work is far too coarse to adequately resolve flow around the structure. Consequently, the only reliable force coefficients available in the literature are likely for impinging vortices having radii of $0.15 \cdot D$ to $4.0 \cdot D$, which is far below the range possible for tornado and hurricane vortices.

Table 1.1: Summary of studies on the influence of relative vortex-to-structure size on structure loading amplitude.

Property	Study		
	Ilie (2009)	Alrasheedi (2012)	Gorecki and Selvam (2013)
Simulation Type	2D	3D	2D
Impacted Body	Airfoil	Prism	Circular Cylinder
Vortex Critical Radius	$0.15 \cdot D$ to $0.50 \cdot D$	$0.375 \cdot D$ to $30.0 \cdot D$	$1.0 \cdot D$ to $4.0 \cdot D$

The impact of a vortex with a structure is a transient loading event. Substantial research effort has been spent evaluating the capability of tornado vortices to produce dynamically-amplified structure response. Mehta and McDonald (1986) and Womble et al. (2009) believe that tornados are too large to dynamically load structures. However, a collection of studies apply assumed tornado forcing time histories and collectively conclude that dynamically amplified

structure response to tornado wind loads is in fact a real threat (Wen (1975), Tan (1975), Seniwongse (1977), Dutta et al. (2002)). The collective shortcoming of these studies is that they fail to develop an applicable and generalized methodology to assess the dynamic loading threat that tornados pose to real world structures but rather assess the dynamic amplification of specific structures' responses to specific forcing histories. Furthermore, their forcing time histories are computed from empirical equations that correlate straight-line wind speed to forces. Consequently, aerodynamic effects such as the shape of the structure and the rotational nature of the vortex wind field are not accounted for.

Adequate design of aerospace vehicles and residential and civil structures necessitates accurate computation of vortex-induced loading. Therefore, the overarching goal of this thesis is to establish the influence of relative vortex-to-structure size on both the structure loading amplitude and the possible dynamic amplification thereof.

A thorough literature review is conducted on the factors that influence the amplitude of vortex loading by structures along with the dynamic amplification thereof. Subsequently, an exhaustive review of vortex tangential velocity profiles (TVPs) is conducted. The present study utilizes computer modelling to simulate vortex impact with structures. Physically-realistic computer simulation necessitates the use of a realistic vortex model. Therefore, analytical and measured vortex TVPs are compiled and compared. Analytical profiles that best represent the measured TVPs are identified and integrated into the computer model for use in subsequent computer simulation.

The physical system modeled in the present work is the parallel impact of a vortex with a rigid circular cylinder, which is illustrated by the schematic Figure 1.5a. The term "parallel" defines the orientation of the impacting vortex's axis of rotation to the major axis of the cylinder

(The Z – axis). Filipone and Afgan (2008) extensively survey and illustrate impact orientations, and parallel impact is most commonly encountered (Weland and Vlachos, 2009), thereby prompting its selection. Generally stated, the vortex having maximum tangential velocity $V_{\theta,max}$ at critical radius r_c travels within a free stream having velocity U_∞ to impact the cylinder having diameter D. The vortex and cylinder are both long in the z-direction, meaning the effects of flow around the cylinder ends is negligible and the interaction is two-dimensional as illustrated in Figure 1.5b.

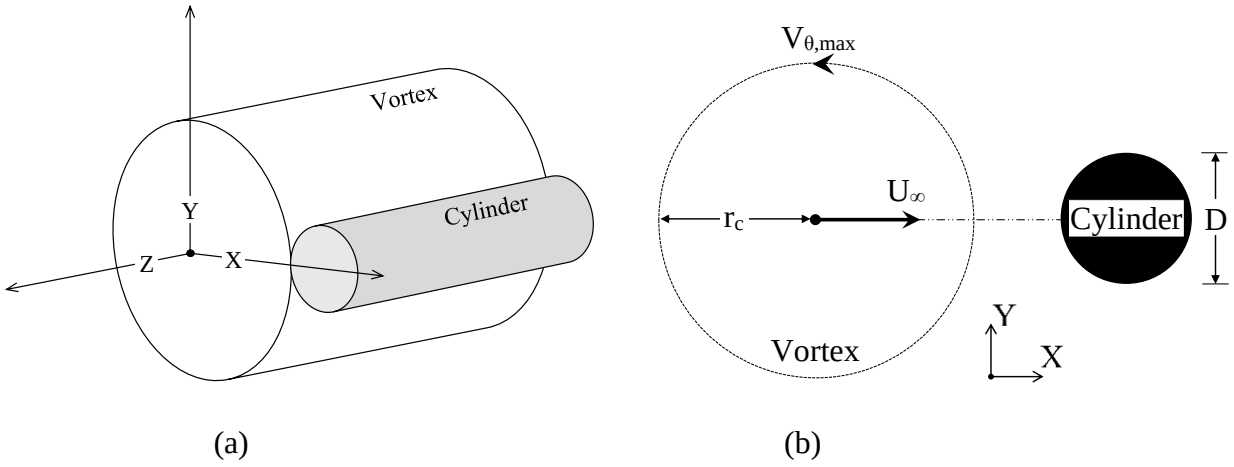


Figure 1.5: (a) 3D and (b) 2D schematics of parallel interaction of a vortex with a cylinder.

The selected, physically-realistic vortex models are integrated in an adaption of Selvam's (1997b) incompressible finite element model, and parallel vortex impact with a circular cylinder is directly simulated. The computer model is validated using the common benchmark problem of free stream flow over an immersed cylinder and then by evaluating the accuracy with which the impinging vortex is transported across the computational domain. Necessary grid refinement for accurate vortex transport increases rapidly as the impinging vortex size decreases, therefore, the minimum impinging vortex critical radius is $1 \cdot D$. The vortex critical radius is progressively increased at fixed $V_{\theta,max}$ until the structure loading amplitude becomes asymptotic, and the

corresponding trend in structure loading amplitude is documented. Unique phenomenon controlling the trend in structure loading amplitude with respect to impinging vortex critical radius are illustrated and explained.

Yang et al. (2009 and 2011) conduct physical experiments and report that shifting the path travelled by the vortex center in the Y-direction (See Figure 1.5b) increases structure loading amplitude up to a maximum path shift of one critical radii. However, Ilie (2009) conducts a similar study via computer simulation and reports that structure loading amplitude decreases for a Y-direction vortex path shift. Yang et al. (2009 and 2011) use a counter-clockwise (CCW) vortex and positive Y-direction path shift, while Ilie (2009) uses a clockwise (CW) vortex and negative Y-direction path shift, meaning they effectively conduct the same study and attain different results. This study utilizes the impinging vortex size which produces asymptotic cylinder loading amplitude to define the influence of Y-direction vortex path shift on structure loading amplitude. The vortex path is shifted so that it travels both above and below the structure, and maximum loading amplitude is extracted and used to define the structure loading amplitude trend with respect to path shift. The maximum structure loading amplitude that a vortex can produce is assessed, and the question as to whether or not a rotational flow field can produce greater loading than a free stream of equivalent velocity is answered.

The final section of this thesis evaluates the capability of impacting vortices to produce dynamically-amplified structure response. Previous studies define tornado forcing using empirical equations developed for straight-line wind. The forcing is then applied to a response model, and the dynamic amplification of the assumed structure's response to the assumed tornado forcing is reported. The present study simulates vortex impact with a cylindrical structure, and utilizes force coefficient time history from the computer simulation as forcing. The

dynamic load factor concept is then utilized develop and generalize a procedure to assess possible dynamic amplification of a structure's response. Documented tornado vortex parameter ranges are then used to develop a generalized definition of the possible dynamic response of a structure as function of its fundamental period. Documented fundamental periods of real-world structures are compiled, and conclusions are drawn regarding the dynamic loading threat that tornados pose to real-world structures.

1.2 Thesis Objectives

Following the introductory chapter of this thesis, a comprehensive literature review on vortex loading of structures is provided. The literature review focuses on the current body of knowledge of structure loading by vortices and is grouped according to study methodology: physical experiment, computer simulation, or post-storm damage investigation. Additional discussion of atmospheric vortex occurrence and damage statistics as well as theories about the physics controlling the structure of vortices' tangential velocity profiles are discussed as well. The subsequent chapters address the primary thesis objectives outlined below.

1.2.1 Objective 1

- *To select physically-realistic analytical vortex tangential velocity profiles (TVPs) for use in computer simulation of structural loading by vortices.*

Physically-realistic computer simulation of structural loading by vortices necessitates the use of physically-realistic vortex TVPs. Analytical vortex TVPs that adequately replicate at least one measured vortex TVPs are documented in the literature. However, no single analytical TVP adequately represents the entire spectrum of measured TVPs. The present study will assemble, compile, and normalize common analytical TVPs found in the literature. Measured vortex TVPs will also be assembled from all experimental and atmospheric vortices documented in the

literature. Analytical vortex TVPs which best represent the typical measured TVPs and bound the range of measured TVPs will be identified and used in computer simulation.

1.2.2 Objective 2

- *To identify the phenomenon that cause variation in structural loading when an impinging vortex impacts a structure, which is shedding vortices, at different times and to quantify the possible variation in the maximum force coefficient amplitude.*

During preliminary stages of this study, it was observed that computer-simulated vortex impact produced different structural loading when an impinging vortex impacted the structure at different times with respect to the beginning of the simulation. This finding is counterintuitive, as one would assume that an impacting vortex having fixed parameters would produce the same structural loading. If structural loading amplitude produced by an impacting vortex is time dependent, using maximum force coefficient amplitudes from a single simulation could lead to dramatic under-prediction of the maximum forces that the impacting vortex can produce. The present study will systematically simulate direct vortex impact by a single-sized vortex at different times to assess the variation in maximum force coefficient amplitude with vortex impact time. Contour plots of the velocity and vorticity fields will be utilized to identify the phenomenon that produce the variation in maximum structure loading amplitude. Subsequently the impinging vortex size will be increased, and the influence of the impinging vortex size on the variation in structure loading with vortex impact time will be assessed as part of Objective 3.

1.2.3 Objective 3

- *To define the trend in maximum force coefficient amplitude produced by a directly-impacting vortex when the vortex size is increased at fixed maximum tangential velocity and to explain the phenomenon controlling the maximum force coefficient amplitude trend.*

Structural loading by vortices is a hazardous phenomenon at practically all relative vortex-to-structure size scales, yet the literature is devoid of a systematic evaluation of how the size of an impacting vortex influences the amplitude the structural loading that it produces. The present study will evaluate the influence of the impacting vortex's size on the amplitude of structural loading that it produces by simulating the direct vortex impact with a slender structure. The maximum tangential velocity of the vortex will be fixed, and the vortex's size will be incrementally increased. Maximum force coefficient amplitudes will be reported for each impinging vortex size, and phenomenon controlling the trend in structural loading amplitude with respect to impinging vortex size will be illustrated and explained using contour plots of velocity and vorticity. As identified in Objective 2, maximum force coefficient amplitudes may vary when the impinging vortex impacts the structure at different times. A sufficient number of simulations will be conducted for each impacting vortex size to quantify the influence of the vortex size on the variation in structural loading when the vortex impacts at different times.

1.2.4 Objective 4

- *To evaluate the influence of shifting an impacting vortex's path from the structure's centerline on the maximum structural loading produced by the vortex and to determine if the vortex produces greater structural loading than an equivalent-velocity free stream.*

An impinging vortex may not impact a structure directly, rather the vortex's path may be offset from the centerline of the structure that it loads. Adequate structural design for loading from impacting vortices necessitates that the impinging vortex path which produces maximum force coefficient amplitudes be identified and considered. The present study will evaluate the influence of shifting the impinging vortex's path from the impacted structure's centerline on the structural loading that the impacting vortex produces. The impinging vortex size that produces

the asymptotic, maximum force coefficient amplitudes for direct vortex impact is identified in Objective 3. This vortex size will be exclusively used, and its path will be shifted so that it travels both above and below the impacted structure's centerline. Maximum force coefficient amplitudes will be reported, and the vortex path shifts that produce maximum structural loading amplitude will be identified. Maximum force coefficients produced by the impacting vortex will be compared with those produced by an equivalent-velocity free stream to evaluate if the vortex travelling within a free stream produces greater structural loading than a free stream having equivalent maximum velocity to the vortex within the free stream.

1.2.5 Objective 5

- *To develop a generalized methodology to assess dynamic amplification of structures' response to loading produced by an impacting vortex and to apply the methodology to assess the dynamic loading threat that tornados pose to residential and civil structures.*

Vortex impact with a structure produces a transient loading event, hence there is propensity for the vortex to produce dynamically-amplified response of the impacted structure. Numerous studies evaluate the capability of atmospheric vortices to dynamically excite structures. Hurricane vortices are massive and slow-moving, hence it is evident that they are incapable of dynamically exciting any realistic structure. However, tornados may be small and translate rapidly, hence their capability to dynamically load structures cannot be simply dismissed. Previous studies have concluded that the tornado-like wind loadings can excite some structures. However, these studies assume that tornado wind loads are no different that straight-line wind loads, and more significantly, they fail to produce a generalized, applicable methodology to assess the possible dynamic amplification of vortex-induced loading.

The present study will use the dynamic load factor (DLF) concept to develop the first generalized methodology to assess dynamic amplification of structures' response to loading produced by an impacting vortex. The load-application period T_v of an impacting vortex will be defined as a function of its TVP and parameters. Subsequently, documented tornado-vortex parameters will be surveyed and utilized to establish the possible range of tornado-vortex T_v values. Finally, the possible dynamic amplification of a structure's response to tornado-vortex loading will be defined as a function of the structure's fundamental period. Documented fundamental periods of real-world structures will be surveyed and used to evaluate the dynamic loading threat that tornados pose to typical residential and civil structures.

CHAPTER 2: LITERATURE REVIEW

2.1 Introduction

This review summarizes the documented studies of structure loading by vortices from the literature. Subsequent subsections are organized to discuss studies conducted via the three primary approaches: physical experiment, computer simulation, and post-storm damage investigation. Post-storm damage investigation produces valuable statistics that allow assessment of the risk of severe storm occurrence based upon region of the country; this is valuable information for the designer of a structure, hence the statistics are included and discussed as well. Following the review of structure loading by vortices, the review proceeds to discuss the vortex tangential velocity profile. Vortices that produce loading in engineering applications are intense, meaning the tangential velocity component is much greater than the axial or radial velocity components; therefore, the vortex tangential velocity profile is of great importance in the present study. Theories regarding the underlying physics controlling vortex structure are presented and discussed. The reader is then referred to Chapter 3 for a thorough review and comparison of measured and analytical vortex tangential velocity profiles. Finally, the review structure loading by vortices is summarized, and the thesis motivation and progression are outlined.

2.2 Physical Experiments

2.2.1 Blade-Vortex Interaction

There are no concise studies of structure loading from blade-vortex interaction experiments reported in the literature. The typical experiment configuration is a pair of in-line airfoils; the leading air foil produces a vortex that is tripped by some mechanism (wire, plunge, etc.) and shed to impact the trailing air foil (Ilie, 2009). Vortices can be consistently generated,

and the locations of the foils can be adjusted to ensure that the impinging vortex impacts the downstream air foil. However, the major problem with these physical experiments is that the shed vortex is rapidly attenuated as it is convected to impact the downstream air foil. Horner et al. (1996) report that it is difficult to transport a vortex through a distance that is more than a few times its diameter when the free stream velocity is greater than 50 m/s. Seath et al. (1989) report that interaction with the side-walls of the wind tunnel also rapidly attenuates the vortex during transport. Ilie (2009) reports that most blade-vortex interaction experiments use free stream velocity exceeding 100 m/s, thereby explaining why it is difficult to find reliable measurements of blade loads produced by impacting vortices. Briefly summarized, the impinging vortex is attenuated while being convected within the wind tunnel to impact the blade. Therefore, the parameters of the vortex that actually impacts the blade are not known. Consequently, it is not possible to develop meaningful correlations between impacting vortex parameters and the blade loading that is produced.

2.2.2 Tornado Simulator Experiments

The research group at Iowa State University uses the first large-scale, translating tornado simulator; their research is the current state of art in physical simulation of structure loading by tornado-like vortices. Sengupta et al. (2006 and 2008) report that tornado-like vortices produce greater loading when they travel at slow speeds than when they travel rapidly. They illustrate that interaction with the ground's boundary layer causes the vortex to tilt with the portion on the ground lagging behind the top of the vortex and conclude that this distortion is responsible for the decreased structure loading. Yang et al. (2009 and 2011) study the influence of y-direction (See Figure 1.5) path shift on the structure loading amplitude. They conclude that the greatest structure loading is produced when the vortex center travels above the structure at a shift of r_c.

Haan et al. (2010) simulate loading of a typical gabled residence. They report that lateral wall loading and uplift produced on the roof are respectively 1.5 and 1.8 to 3.2 times greater for tornado-like vortex loading than for equivalent-velocity straight-line wind.

2.3 Computer Simulation

The complexity and high cost of physically simulating vortex-structure interaction encourages the use of computer simulation. Numerical diffusion is a plaguing issue that attenuates the impinging vortex as is the case in physical experiments. However, the substantial benefit afforded by computer simulation is that the exact properties of the vortex that impacts the loaded structure are known. Furthermore, at the expense of computational time, increased grid resolution and superior numerical solution methodologies can be utilized to reduce numerical vortex diffusion. Consequently, meaningful correlations may be developed between parameters of impacting vortices and the resulting structure loading that they produce.

2.3.1 Two-Dimensional Simulations

2.3.1.1 Blade-Vortex Interaction

Blade-vortex interaction is primarily studied for application in rotorcraft design. Computer simulations typically consider a fixed- rather than rotating rotor. This is primarily because meshing a rotating system is very difficult and computationally expensive (Ilie, 2009). Furthermore, Ilie (2009) explains that the relative speed between the impinging vortex and the rotating rotor is the most important interaction parameter. This implies that impact of a stationary rotor by an impinging vortex is realistic representation of the chopping of a vortex by a rotating rotor.

Ilie (2009) simulates impact of an air foil by a clockwise-rotating, Scully-Kaufmann vortex at chord Reynolds number $Re_c = 1.3 \cdot 10^6$. The air foil chord length is c = 0.2 m, and the

critical radius of the impinging vortex is increased from $0.2 \cdot c$ and $0.5 \cdot c$. The kinematic viscosity of air at 300 K ($\nu = 1.56 \cdot 10^{-5}$ m^2/s) is used in the present study to approximate the unreported free stream velocity $U_\infty \approx 100$ m/s, and contour plots are used to approximate the unreported maximum vortex tangential velocity $V_{\theta,max} \approx 25$ m/s. Maximum drag and lift force coefficient amplitudes progressively increase as the impinging vortex size is increased. The path of the impinging vortex is shifted in the y-direction (See Figure 1.5) so that the impinging vortex travels below the air foil centerline by up to $\delta = -1.25 \cdot r_c$. Maximum drag and lift force coefficient amplitudes progressively decrease as the magnitude of δ is increased. Later work performed in the same group reports that increasing the air foil angle of attack from 0^o to 9^o progressively increases drag and lift force coefficient amplitudes produced by vortex impact.

2.3.1.2 Circular Cylinder-Vortex Interaction

The circular cylinder is one of the most commonly-used body shapes in computational fluid dynamics simulations. Selvam et al. (2002) report preliminary work where they simulate loading of slender cylinder by a Rankine vortex at free stream Reynolds number $Re = 10^3$. The vortex critical radius is $r_c = 3 \cdot D$ (The cylinder diameter D = 1) and the maximum vortex tangential and vortex translational velocity are respectively $V_{\theta,max} = 4.5$ and $U_\infty = 1$. Selvam and Gorecki (2012) also simulate loading of a slender cylinder by a Rankine vortex at free stream Reynolds number $Re = 10^3$. The maximum vortex tangential velocity and free stream velocity are respectively fixed at $V_{\theta,max} = 3$ and $U_\infty = 1$. The critical radius of the impinging vortex is increased from $r_c = 1 \cdot D$ to $4 \cdot D$; the maximum lift force coefficient progressively increases with increasing size while the maximum drag force coefficient amplitude remains constant.

2.3.2 Three-Dimensional Simulations

Selvam and Millet (2003a, 2003b, and 2005) and Millet and Selvam (2005) simulate three-dimensional impact of a Rankine vortex with cube-shaped structures. The free stream velocity, maximum vortex tangential velocity, and vortex critical radius are fixed at $U_\infty = 1$, $V_{\theta,max} = 4.5$, and $r_c = 3 \cdot D$ for all simulations. These studies collectively concluded that the vortex loading produces maximum lateral and uplift forces that are respectively 1.5 and 2 times greater than forces produced by an equivalent-velocity free stream. Also, the vortex loading produces a net torque about the vertical axis that is not produced by an incident free stream.

Alrasheedi and Selvam (2011) and Alrasheedi (2012) simulate three-dimensional impact of a Rankine vortex with square cross-sectioned, prismatic structures. The ratio of the vortex critical radius to the structure side length r_c/L is increased from 0.375 (vortex smaller than structure) to 30 (vortex much larger than structure), and the trend in force coefficients produced on the structure is documented with respect to r_c/L. Force coefficient amplitudes progressively increase as the ratio r_c/L increases. However, the grid refinement is too coarse to accurately resolve the boundary layer around the slender structures, as less than 20 span-wise control volumes are used to discretize structure faces when $r_c/L > 4$ (Compare with 120 – 180 tangential nodes in the present study).

2.4 Post-Storm Damage Rating Investigation

Post-storm damage investigation is not a usable approach to study the loading produced on individual structures by impacting vortices. It does however afford a viable means to qualitatively document severe damage from atmospheric vortices and document the regional threat thereof. This information can then be used to assess the probability of severe storm

occurrence at the location where a structure is to be constructed so that adequate design loads for the potential wind loading may be utilized.

2.4.1 Damage Rating Scales

Tornados and hurricanes are categorized based upon the maximum wind speeds that they produce. Generally stated, local structure damage levels are correlated to equivalent, straight-line wind speeds required to produce similar damage based upon pre-defined damage markers (removed shingles, collapsed walls, uprooted trees, etc.). Saffir and Simpson (1974) develop the SS damage rating scale used to rate hurricane damage, and Fujita (1971) develops the F scale

Table 2.1: Saffir-Simpson damage scale (NOAA, 2012).

Category	Sustained Wind	Damage Description
1	33 – 43 m/s (74 – 95 mph)	**Some Damage:** roof, shingles, vinyl siding, gutters. Large tree branches snapped, shallow-rooted trees uprooted. Extensive Power Line damage.
2	43 – 49 m/s (96 – 110 mph)	**Extreme Damage:** major roof and siding damage. Shallowly-rooted trees are snapped and uprooted. Most power knocked out.
3	49 – 58 m/s (111 – 129 mph)	**Devastating Damage:** major roof damage and removal of roof decking/ gables. Many trees snapped. Power outages for days-weeks.
4	58 – 70 m/s (130 – 156 mph)	**Catastrophic Damage:** loss of roof structure and exterior walls. Most trees snapped, and power will be out for weeks-months.
5	> 70 m/s (> 157 mph)	**Catastrophic Damage:** many framed homes will be destroyed, with total roof failure and wall collapse.

Table 2.2: Enhanced Fujita damage Scale (McDonald et al., 2009).

Rating	Wind Speed	Damage Description
EF0	29 – 38 m/s (65 – 85 mph)	**Light Damage:** Damage to chimneys and antennas; twigs broken off trees shallow-rooted trees pushed over.
EF1	39 – 49 m/s (86 – 110 mph)	**Moderate Damage:** Shingles removed, windows broken, trailers overturned, cars pushed off road, trees uprooted.
EF2	50 – 60 m/s (111 – 135 mph)	**Considerable Damage:** Roofs removed, light buildings demolished, light missiles generated, boxcars overturned, large trees snapped/uprooted.
EF3	61 – 74 m/s (136 – 165 mph)	**Severe Damage:** Roofs and walls removed, steel-framed hangers and warehouses torn, cars picked up, most trees flattened.
EF4	75 – 89 m/s (166 – 200 mph)	**Devastating Damage:** Houses leveled (debris left); steel structures damaged; trees debarked; cars/trains thrown; large missiles generated.
EF5	> 89 m/s (> 200 mph)	**Incredible Damage:** Houses tossed from foundations; reinforced concrete structures damaged badly; car-sized missiles generated.

used to rate tornado damage. McDonald et al. (2009) explain that the F scale over-predicts wind speeds and scale down the original wind speeds attributed to the categories of damage markers thereby producing the Enhanced Fujita or EF scale. Table 2.1 and Table 2.2 respectively summarize the associated straight-line wind speeds and damage markers used to define the SS and EF ratings of hurricanes and tornados.

2.4.2 Applicability of Damage Rating Scales

The SS and EF scales are good tools to document the occurrence of severe atmospheric vortices on the basis of the damage that they cause. This documented information yields valuable statistics regarding the risk of local severe storm occurrence. However, this is the extent of the applicability of post-storm damage investigation data to study structure loading by vortices.

It must be understood that the premise of both rating systems is correlating observed structural damage to straight line wind speeds required to cause the same damage. Both computer simulation (Selvam and Millet (2003a, 2003b, and 2005) and Millet and Selvam (2005)) and physical simulation (Haan et al., 2010) show that force coefficients produced by vortex loading of structures may be 1.5 to 3.2 times greater than force coefficients produced by a free stream having the same maximum velocity. This implies that the character of tornado wind loads increases the forces that they produce on structure compared with the forces produced by equivalent-velocity, straight-line wind. Consequently, the true maximum wind velocity within a tornado vortex may be much less than the correlated wind speed from damage investigation.

An additional problem with post-storm damage investigation is that numerous factors may influence the rating of observed local damage along the storm track. Investigation teams often consist of multiple investigators whom may assign different damage ratings to the same damaged structure. Furthermore, there is no guarantee that the most severely damaged structures

are located at each damage sight. Inconsistent construction techniques may cause structures that outwardly appear similar to suffer very different damage levels. Progressive damage due to longer time of exposure to high wind speeds may result in more severe damage from large tornados than from small tornados having similar maximum wind speeds. Womble et al. (2009) add the fact that damage from storm surge, flying debris, etc. may result in higher damage ratings being assigned than should be attributed to the local wind speed.

The preceding discussion introduces numerous flaws in post-storm damage investigation; however, ever-improving technology will continue to increase the viability of post-storm damage investigation in the future. Recent studies reported in Selvam et al. (2015a and 2015b) demonstrate the viability and extreme benefits of utilizing aerial photography to document and study tornado damage tracts. High-resolution photographs provided by sources such Google Earth and Civil Air Patrol are used to accurately document not only the tornado damage track but to assess the influence of topography on tornado damage levels. Damage documentation via aerial photography not only allows a single investigator to document the entire damage track but also readily provides access to areas that may not be reachable by road. As the quality and availability of aerial photography improves in the future, the process and ease of conducting post-storm damage investigation will be substantially improved.

Briefly summarized, the damage rating scales provide a good method to document the occurrence of severe atmospheric vortices and to identify regions of the country where extra design precautions against severe wind loadings should be made. Observed damage can be used to estimate maximum wind speeds, but the wind speed is likely overestimated.

2.4.3 Why are Different Damage Ratings Used for Tornados and Hurricanes?

The EF and SS scales discussed in the previous section correlate observed structure damage produced by tornados and hurricanes, respectively, to straight line wind speeds required to produce the same damage levels. One may question why two separate rating scales are needed and note that different wind speeds are required to produce similar damage levels in the SS and EF scales. Are hurricane wind loadings different than tornado wind loadings?

This discussion is prefaced by noting that abnormal vortex structure (multi-vortex, etc.) is not considered. Furthermore, the relative size of tornados to hurricanes is the primary difference between the two types of vortices. Womble et al. (2009) compare damage produced by hurricanes and tornadoes of similar maximum wind speeds. They conclude that neither tornados nor hurricanes are likely a concern for dynamic loading and that both are effectively turbulent straight line wind. Mehta and McDonald (1986) and McDonald et al. (2009) reach the same conclusion, specifically that tornados and hurricanes are effectively straight line turbulent wind. The literature concludes that both tornados and hurricanes can be considered straight line wind, hence the necessity for separate damage rating systems is still not understood.

Mehta and McDonald (1986) conclude that the difference in structure damage levels caused by tornados and hurricanes is due to the difference in time of exposure to high wind speeds, because of the difference in vortex size, and the different "character" of the winds. Womble et al. (2009) use similar language, attributing the difference in damage levels cause by tornados and hurricanes to the differences in "temporal and spatial variation in wind speeds".

Attributing different damage levels to the difference in time of exposure to high wind speeds is reasonable, as progressive failure with time of exposure to high wind speeds could increase the structure damage levels. However, if both tornados and hurricanes act as straight

line turbulent wind (ie. Mehta and Mcdonald (1986) and McDonald et al. (2009)), what is the difference in wind "character" that influences structure loading?

Womble et al. (2009) identify a much more realistic reason for the use of separate damage scales: typical structures constructed in hurricane-prone areas (U.S. Atlantic and Gulf coasts) are designed to be more wind-resistant than structures in tornado-prone areas (U.S. Midwest). The EF and SS scales have been developed using observed structural damage from atmospheric vortices observed in different regions of the country where building codes may differ greatly. In short, a structure constructed for less wind resistance will exhibit greater damage for lower wind speeds than a structure constructed for higher wind resistance. Therefore, damage investigation scales calibrated for a region where structures typically have greater wind resistance is not directly applicable in a region where structures have decreased wind resistance. As long as hurricanes and tornados are to be considered as separate storms rather than collectively as atmospheric vortices, it is necessary that separate damage rating scales be used.

2.4.4 Tornado and Hurricane Occurrence Statistics

Post-storm damage investigation is used to document the severity of both the hurricanes that make landfall on the Atlantic coast and the tornados occurring within the United States each year. Tables 2.3 and 2.4 summarize recorded hurricane and tornado data respectively. Note that hurricanes occurring prior to the creation of the SS scale in 1974 were likely post-documented based upon recorded damage.

Far fewer hurricanes make landfall each year (< 2) than documented tornados that occur (> 1200). However, due to the large size, duration, and storm surge that accompany hurricanes, they cause about 10 times greater financial loss (Brooks and Doswell, 2001) than do tornados

annually. However, hurricanes are slow-moving and easily tracked long before making landfall, meaning warnings can be delivered for evacuation of areas that will take severe damage.

Table 2.3: Summary of hurricane occurrence from 1851-2004 (Blake et al., 2005).

1851-2004	Saffir-Simpson Category					Total
	1	2	3	4	5	
Rating at Landfall	109	72	71	18	3	273
Percentage	39.93%	26.37%	26.01%	6.59%	1.10%	
Cumulative	39.93%	66.30%	92.31%	98.90%	100.00%	
Avg. Per Decade	7.1	4.7	4.6	1.2	0.2	17.8

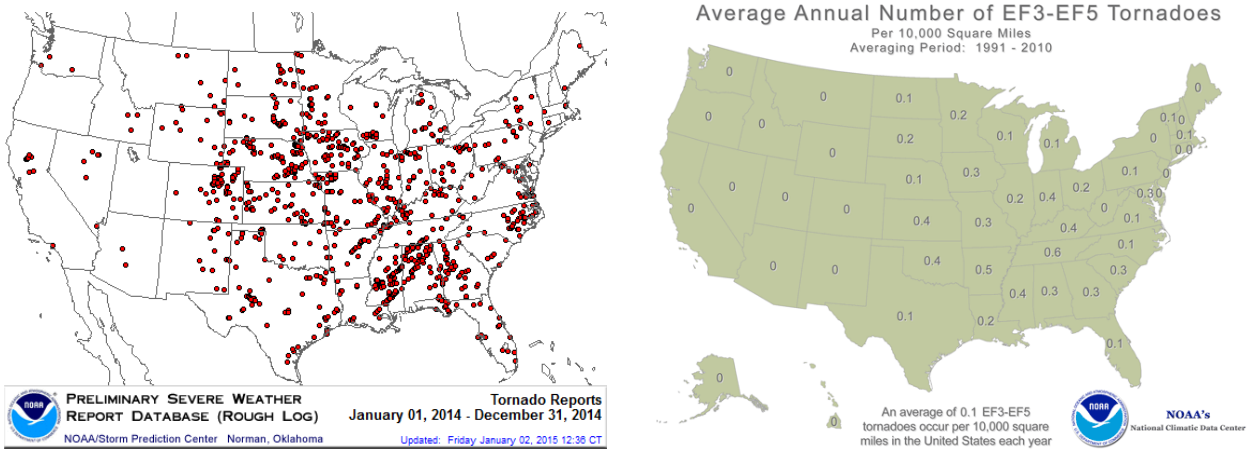
Table 2.4: Summary of tornado occurrence from 1995-2009 (Edwards and Brooks, 2010).

1995-2009	Enhanced Fujita Rating					Total
	0 - 1	2	3	4	5	
Damage Rating	17,095	1,440	419	85	7	19,046
Percentage	89.76%	7.56%	2.20%	0.45%	0.04%	
Cumulative	89.76%	97.32%	99.52%	99.96%	100.00%	
Avg. Per Decade	11,396.7	960.0	279.3	56.7	4.7	12,697.3

Tornados occur much more sporadically, and are likely on the ground for only a few minutes. Therefore, assessment of the risk of tornado activity in various regions of the country is a valuable statistic. Figure 2.1a illustrates the documented tornados in the United States for the year 2014, which is typical of the annual distribution of documented tornados. Figure 2.1b illustrates the density or average number of severe (EF3-EF5) tornados occurring in each state per 10,000 mi^2 of land area. Much of the western half of the United States has minimal risk of severe tornado occurrence. However, "Tornado Ally" in the central region of the United States along with many Eastern states have significant risk of severe tornado activity.

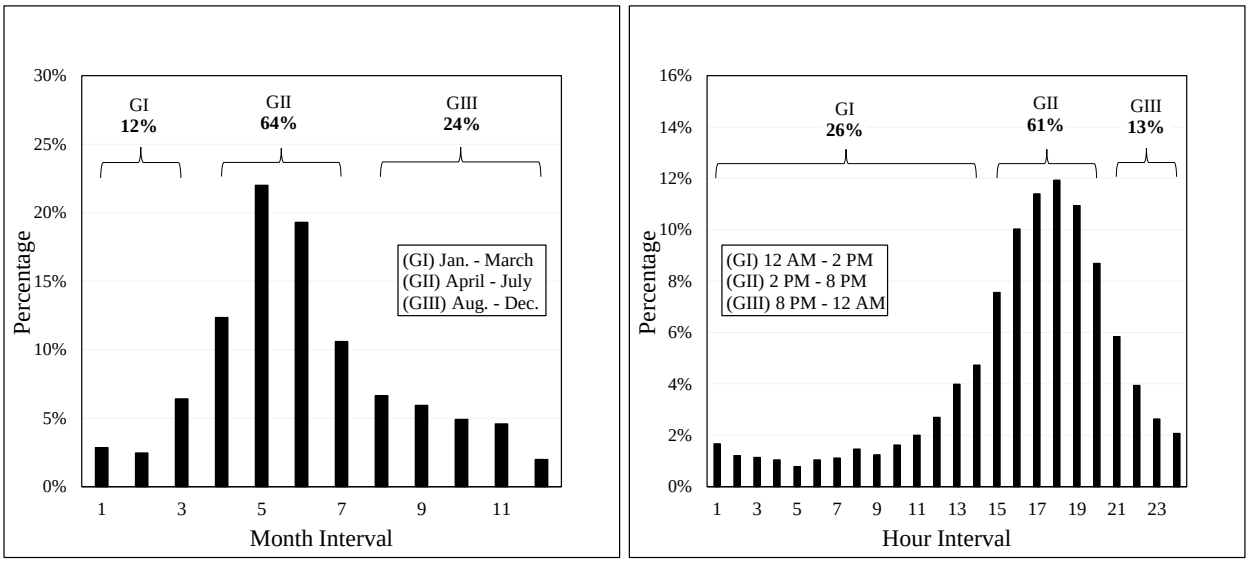
For staffing of emergency personnel, better prediction of tornado occurrence, and field study of tornados, it is helpful to know the time of year (Figure 2.2a) and time of day (Figure 2.2b) when tornados are likely to occur. Figures 2.2a and 2.2b show that most tornados occur in

the four-month interval from April to July, and most tornados occur within the six-hour interval 2:00-8:00 PM. It should be noted that tornados may be under-documented in the late evening and early morning hours due to the absence of sunlight to see them.



(a) (b)

Figure 2.1: (a) Documented tornados in the United States in 2014 (Taken from NOAA, 2014a) and (b) tornado occurrences per 10,000 mi^2 land area in each state (Taken from NOAA, 2015a).



(a) (b)

Figure 2.2: Average annual tornado occurrence as function of (a) month and (b) time of day (NOAA, 2015a).

2.5 Dynamic Structure Loading by Tornados

Tornados and hurricanes produce transient structure loading events, and there is question as to whether or not they can produce dynamically-amplified structure loading. Researchers from the post-storm damage investigation community reason that both tornados and hurricanes are too large to dynamically load a structure (Mehta and McDonald (1986) and Womble et al. (2009)). Hurricanes are many kilometers in diameter and move slowly, hence it is intuitive that they cannot dynamically load any practical structure. Tornados, however, range greatly in size and translational speed, hence their capability to dynamically load structures cannot be so simply dismissed.

The literature contains no physical experiments measuring dynamically-amplified structure response to vortex loading. However, several studies evaluate dynamic structure response amplification to assumed tornado wind loads. All studies define the time history of the wind velocity incident on the building and then use empirical equations defined as functions of the incident wind velocity to define the forcing time history. Wen (1975) studies the response of a multi-story building to a simplified Kuo (1971) vortex and reports that the maximum structure response is amplified by a dynamic load factor (DLF) of 4.0. Two similar studies evaluate multi-story structures' responses to a modified RCVM vortex (The potential vortex region decays linearly) and report maximum response amplification of DLF = 2.0 (Tan (1975) and Seniwongse (1977)). Dutta et al. (2002) analyze the responses of single- and multi-story structures to a tornado wind field assigned using Fujita's (1976) wind speed record and Mehta et al.'s (1976) vortex model and report maximum structure response amplification of DLF = 1.735.

The preceding collection of studies jointly conclude that transient tornado wind loads are capable of dynamically amplifying structures' responses. Significant findings from the studies are outlined below.

- Structure response amplitude may be amplified by DLF of 1.735 (Dutta et al., 2002) to 4.0 (Wen, 1975).
- The threat of dynamic amplification of tornado wind loads is greatest when the structure is directly on the tornado's path ($\delta = 0$) due to the rapid change in direction and amplitude of the flow incident on the cylinder which is augmented by the vortex's tangential velocity ((Wen, 1975), (Tan, 1975) and (Seniwongse, 1977)).
- The y-direction forcing has (See Figure 1.5) greatest propensity to produce amplified structure response, hence it is the forcing component that need be considered for dynamic analysis ((Tan, 1975) and (Seniwongse, 1977)).

The collective shortcoming of these studies is that they fail to yield generalized results, but rather discuss the dynamic amplification of a particular structure's response to loading by a particular wind field. Furthermore, all of the studies define the forcing time histories using empirical equations developed for straight-line wind loading, hence they premise that the rotational nature of the vortex's wind field does not influence the structural loading.

Measured tornado parameters and wind field profiles, as well as real-world structure parameters, vary widely. Adequate structure design for dynamically-amplified structure response to tornado wind loads necessitates the definition of a generalized methodology to assess the possible dynamic amplification of a structures response to loading by all possible tornado vortices.

2.6 Comparison of Real-World and Simulated Tornado and Hurricane Vortices

Numerous physical and computer simulations of vortex-structure interaction have been discussed. However, to better understand real-world vortex loading of structures, simulation parameters need be realistic, or realistically scaled systems. Parameters for some significant tornados as well as a single hurricane are provided in Table 2.5. The Tri-state and Bridge Creek-Moore tornados are specifically selected because they are the fastest-translating and having the highest recorded wind speeds respectively. Translational velocities (U_∞) are known based upon progressive damage documentation. The tangential velocities are back-computed based upon measured total velocity or approximated using the EF damage rating. Hurricane Allen is included here because it produced the fastest recorded hurricane wind speeds.

Table 2.5: Summary of documented tornado and hurricane wind speeds.

Title	V_{max} m/s	$V_{\theta,max}$ m/s	U_∞ m/s	$V_{\theta,max}/U_\infty$ dim	r_c m	Source
Tri-State	134.1	101.5	32.6	3.11	800	Fujita, 1973
GG Nuclear Plant	68.9	53.6	15.2	3.53	46	Fujita, 1981
Bridge Creek-Moore	134.6	123.2	11.4	10.85	1,609	NOAA, 1999
El Reno	132.3	116.7	15.7	7.45	2,008	NOAA, 2013a
Moore	93.9	82.3	11.6	7.08	1,004	NOAA, 2013b
Mayflower	89.4	71.1	18.3	3.88	600	NOAA, 2014b
Hurricane Allen	84.9	76.0	8.9	8.50	46 (km)	NOAA, 1980

The vortex velocity ratio for tornados is $3.11 \leq V_{\theta,max}/U_\infty \leq 10.85$ for the cases presented in Table 2.5, which seem to be the representative range of fast-moving to slow and rapidly-rotating. Hurricane wind speeds shortly prior to, and just after landfall, are not precisely documented in the literature. NOAA (2012) averages the forward speed of 39,877 North Atlantic hurricanes and reports the average forward speed to 5.59 m/s. Using the wind speed for a SS1 hurricane (33 m/s) as a lower velocity bound and Hurricane Allen's wind speed as the upper

velocity bound, the velocity ratio range for hurricanes is $4.90 \leq V_{\theta,max}/U_\infty \leq 14.19$. Therefore, for atmospheric vortices, a reasonable velocity ratio range is $3.11 \leq V_{\theta,max}/U_\infty \leq 14.19$.

The maximum tangential and translational velocities for vortices in computer and physical blade-vortex interaction simulations is not often documented precisely in the literature. However, since the vortices are produced by flow over rotating and fixed wings, it is reasonable to conclude the maximum velocity ratio for blade-vortex interaction experiments is less than one (deduced from contours in (Ilie, 2009) and (Porter et al., 2010)). These vortices are not maintained, hence they decay as they convect away from the rotor or blade that produces them. Therefore, the velocity ratio range relevant for blade vortex interaction can be defined as $V_{\theta,max}/U_\infty \leq 1$.

Table 2.6 summarizes the parameters of vortices used in computer simulations used in previously-discussed computer simulations. Parameters for the non-CFD studies of Wen (1975) and Dutta et al. (2002) are included as well. No blade-vortex interaction simulations are reported here, because complete sets of parameters are not provided in any of the cited studies. However,

Table 2.6: Summary of vortex parameters for computer experiments.

Source	Type	V_{max} m/s	$V_{\theta,max}$ m/s	U_∞ m/s	$V_{\theta,max}/U_\infty$ dim	r_c/D dim
Wen, 1975	Eqs.	92.0	74.0	18.0	4.11	2.50
Duttah et al., 2002	Measured	100	82	18.0	4.56	$r_c \approx 25$ m
Selvam et al., 2002	2D CFD	111.7	91.4	20.3	4.50	3.00
Selvam and Millet, 2003a	3D CFD	111.7	91.4	20.3	4.50	3.00
Selvam and Millet, 2003b	…	…	…	…	…	…
Selvam and Millet, 2005	…	…	…	…	…	…
Millet and Selvam, 2005	…	…	…	…	…	…
Selvam and Gorecki, 2012	2D CFD	80.0	60.0	20.0	3.00	1.00 to 4.00

It is again noted that both V_θ/U_∞ and r_c/D are typically less than or equal to unity in the blade-vortex studies in Ilie (2009) and Porter et al. (2010). The velocity ratio range used in these

simulations, $3.0 \leq V_\theta/U_\infty \leq 4.56$, is very close to, or within the atmospheric vortex velocity ratio range defined previously.

Parameters from the three-dimensional tornado simulations conducted by the group at Iowa State University are summarized in Table 2.7. It is immediately observed that the velocity ratio range $11 \leq V_{\theta,max}/U_\infty \leq 65$ is much greater than that typically observed in tornados. However, it must also be pointed out that tornados change wind speed and direction frequently and may even stop, at which point $V_{\theta,max}/U_\infty \rightarrow \infty$. Therefore, the velocity ratio used in the Iowa State three-dimensional experiments is not physically impossible, although it is not typical of the tornado vortices that they are supposedly studying.

Table 2.7: Summary of vortex parameters from three-dimensional tornado simulator at Iowa State University.

Source	$V_{\theta,max}$ m/s	V_θ m/s	U_∞ m/s	$V_{\theta,max}/U_\infty$ dim	r_c/D dim
Sengupta et al., 2006	≤ 11.6	11.0	0.30 - 0.61	18 - 37	2.62 - 5.32
Sengupta et al., 2008	≤ 10.3	9.7	0.30 - 0.61	16 - 32	2.62 - 9.82
Haan et al., 2010	≤ 10.4	6.8-9.8	0.15 - 0.61	11 - 65	5.06 - 11.64
Haan et al., 2014	10.0	9.8	0.15	65	2.00 - 5.60

2.7 The Tangential Velocity Profile of a Vortex

Vortices are very complex flow features that are produced and sustained by different sources. Atmospheric vortices may be narrow and laminar as illustrated in Figures 2.3a, 2.3c, and 2.3e or wide and turbulent as illustrated in Figures 2.3b and 2.3d. Atmospheric vortices are large, exhibit three-dimensional flow, and are created and sustained by convection currents. Conversely, rotor- and wing-tip vortices are small, mechanically-produced and non-maintained flow structures that decay rapidly after detaching from the wing or rotor from which they originate. Despite the noted differences in scale and production of atmospheric and rotor/wing-

tip vortices, they still exhibit very similar structure as can be seen by comparing the hurricane vortex illustrated in Figure 2.3g and the rotor-tip vortex illustrated in Figure 2.3h.

Vortices are primarily investigated by the meteorological, structural, and aerospace communities. Meteorological researchers have placed substantial research effort on forecasting the trajectory and growth of hurricanes so that ample warning can be given to coastal areas before the hurricanes make landfall (Goerss and Jeffries (1994), Vickery et al. (2009), and Cao et al. (2011)). Research effort has been spent studying the three-dimensional structure of tornados (Lewellen (1993), Nolan and Farrell (1999), and Davies-Jones et al. (2001)) as well as the influence of topography on the near-ground behavior of tornados (Gorecki and Selvam (2014) and Gorecki and Selvam (2015)). The remaining research effort within the structural design and aerospace communities focuses on predicting structure loading by vortices.

The radial profile of a vortex can be thought of as three regions: a laminar core, a transition region, and a turbulent exterior region, as labeled in Figure 2.3h. The literature contains numerous analytical expressions for the radial tangential velocity profile $V_\theta(r)$ or TVP of a vortex. The aerospace community describes shed vortices using the vortex Reynolds number ($Re_v = \Gamma_\infty/\nu$), where the maximum circulation Γ_∞ is the path integral of the maximum tangential velocity ($\Gamma_\infty = 2 \cdot \pi \cdot r_c \cdot V_{\theta,max}$). Vatistas (2006) concludes that the TVP increasingly flattens for $r > r_c$ as Re_v increases, implying a slower decay in tangential velocity. He attributes the increased profile flattening to increasingly-turbulent diffusion of the vortex. The most commonly-used TVPs by the aerospace community are the Scully-Kaufmann (Vatistas, 2006) and Lamb-Oseen (Leishman and Martin, 2006) models. These are both laminar, solutions of the Navier-Stokes equations. Vatistas (2006) shows that both profiles accurately approximate high-Re_v rotor tip vortices when they are normalized so that $V_\theta(r_c)/V_{\theta,max} = 1$. Tornados and hurricanes are most

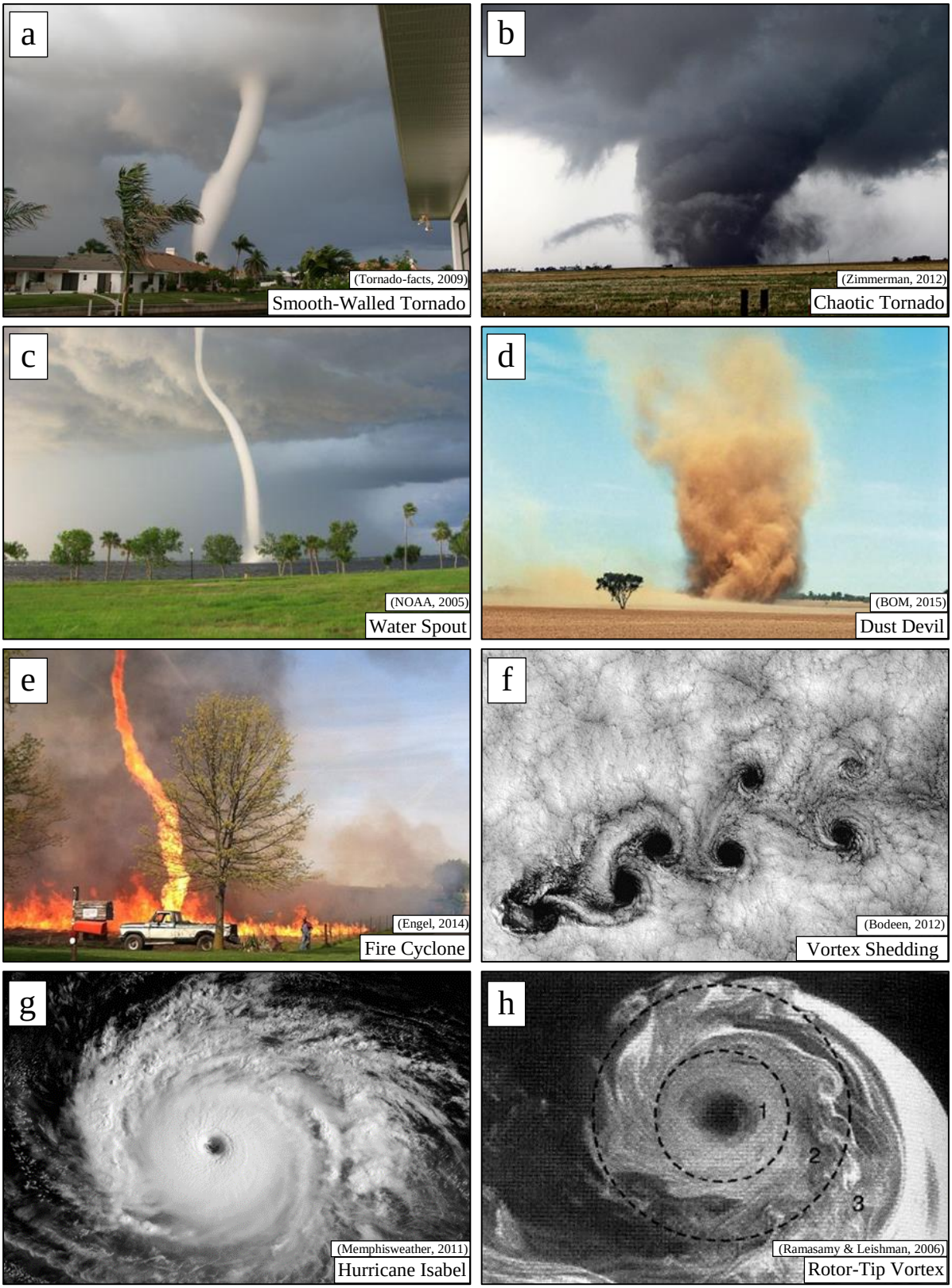


Figure 2.3: Examples of real-world atmospheric and mechanically-produced vortices.

commonly modeled using the Modified Rankine Combined or Burgers-Rott TVPs (Wood and White, 2011).

Much research effort has been put into defining the correct TVP in the various vortices of engineering interest. However, understanding of, and analytical approximation of vortices is still at best an educated guess. Laboratory investigation of vortices produced by rotor tips typically measure vortices characterized by $Re_v < 3 \cdot 10^5$ (Bagai and Leishman (1993), Bhagwat and Leishman (2000), and Martin et al. (2003)), while real-world rotorcraft produce vortices at $Re_v > 10^7$ (Bhagwat and Leishman, 2002). Field measurements of TVPs within tornados accurately fit several different analytical profiles (Tanamachi et al. (2007), Wurman et al. (2007), and Wood and White (2011)). However, as noted by Kessler (1970) the tornado structure varies widely between tornados, ranging from laminar (Figures 2.3a) to turbulent (Figures 2.3b), hence no single TVP fits all measured profiles.

Mobile Doppler radar has substantially improved the research community's knowledge of tornado wind field structure in recent years. However, radar measurements are limited to about 30 m from the ground, hence the near-ground wind structure of tornado wind fields remains an educated guess (Wurman et al. (2007)). Measured TVPs within hurricanes have also been accurately fit with analytical models (Mallen et al. (2005) and Wood and White (2011)). However, the vortex structure varies significantly between storms, with the inner core ranging from v- to u-shaped (Kepert, 2010). Furthermore, hurricane structure is influenced by numerous parameters: season, basin environmental pressure, time of day, etc. as discussed in Cao et al. (2011). The fact that all of these parameters influence the hurricane TVP leads to the conclusion that no single TVP profile can analytically represent all hurricanes.

Briefly summarizing the preceding discussion, numerous vortex structures are possible for both mechanically produced (rotor, blade, etc.) and convection driven (tornado, hurricanes, etc.) vortices. The vortex structures change continuously due to viscous diffusion, ground interaction, etc., hence it is not possible to analytically define a single analytical TVP that fits all vortices, even within a specific classification (Rotor tip, tornado, hurricane, etc.).

2.8 Summary and Thesis Motivation

2.8.1 Summary of Literature Review

Vortex impact with structures is a complex phenomenon that produces hazardous structure loading and in numerous engineering applications. The aerospace community desires to better predict air loads placed on rotors of rotorcraft as they chop vortices produced by other rotors or shed from leading wings and stabilizers. The structural design community seeks to better understand structure loading produced on residences and civil structures by atmospheric vortices such as tornados and hurricanes so that adequate design provisions may be adopted. Despite the far-reaching necessity for better understanding of structure loading by vortices, the current knowledge base is limited, and that information which is supposedly "known" is typically debated as summarized below.

Both three-dimensional computer simulations (Selvam and Millet, 2003a and 2003b) and three-dimensional physical experiments (Haan et al., 2010) demonstrate that structure loading by tornado-like vortices respectively produces 1.5 and 3.2 times the lateral and uplift forces that are produced by equivalent-velocity, straight-line wind. However, some still reason that both tornado and hurricane wind loads can be assumed to behave as straight-line wind (McDonald et al. (2009) and Womble et al. (2009)). This demonstrates that the academic community still in

unsure whether or not the rotational flow structure of vortices produces greater structure loading than straight-line wind having the same velocity.

Two-dimensional computer simulations are used to show that structure loading amplitude progressively increases as the size of the impinging vortex is increased. Ilie (2009) simulates impact of a Scully-Kaufmann vortex with an airfoil and shows that the air foil loading amplitude progressively increases as the vortex critical radius is increased from $0.2 \cdot c$ to $0.5 \cdot c$ (c is the airfoil chord length). Gorecki and Selvam (2013) simulate impact of a Rankine vortex with a slender, circular cylinder and show that the cylinder loading amplitude progressively increases as the vortex crucial radius is increased from $1 \cdot D$ to $4 \cdot D$. Gorecki and Selvam (2013) fix the vortex's maximum tangential velocity, and Ilie (2009) does not report his treatment thereof.

Both two-dimensional computer simulation (Ilie, 2009) and three-dimensional physical experiments (Yang et al., 2009 and 2011) demonstrate that shifting the impinging vortex path relative to the impacted structure greatly influence the structure loading amplitude. Ilie (2009) simulates impact of an airfoil by a clockwise-rotating vortex and finds that structure loading amplitude progressively decreases as the impinging vortex path is shifted below the structure by up to $\delta = 1.25 \cdot r_c$. Yang et al. (2009 and 2011) effectively perform the same study by shifting the path of a counter-clockwise vortex by up to $\delta = 7 \cdot r_c$ above the structure. However, Yang et al. (2009 and 2011) report that structure loading amplitude increases up to $\delta = r_c$. Therefore, it is concluded that the physical influence of vortex path shift on the produced structure loading amplitude is not clearly defined in the literature.

Several studies evaluate the capability of tornado wind loads to produce dynamically-amplified structure response (Wen (1975), Tan (1975), Seniwongse (1977), and Dutta et al. (2002). In all cases, a time history of the assumed tornado wind field is defined and then

converted to a forcing time history using empirical equations; the forcing is then applied to a response model. All studies conclude that tornado wind loads are capable of dynamically amplifying structure response, with maximum reported dynamic load factor values ranging from 1.735 (Dutta et al., 2002) to 4.0 (Wen, 1975). However, others conclude that neither tornados nor hurricanes pose a dynamic loading threat simply upon the basis of post-storm damage investigation and intuition (Mehta and McDonald (1986) and Womble et al. (2009)).

Numerous analytical expressions have been developed for the radial tangential velocity profile (TVP) within a viscous vortex. The aerospace community typically uses the Lamb-Oseen (Leishmann and Martin, 2006) or Scully-Kaufmann (Vatistas, 2006) TVPs to approximate rotor and wing-tip vortices. Atmospheric vortices are typically approximated with the Modified Rankine Combined or Burgers-Rott (Wood and White, 2011) TVPs. Theoretical discussions of the factors influencing the TVP of a vortex are present in the literature, but the noted variation in structure between similar types of vortices underscores the fact that the physics governing vortex structure is not well-understood. At the present time that there is no single analytical vortex model that can be used to represent all vortices.

2.8.2 Thesis Motivation

Structure loading by vortices is a complex phenomenon, and the resulting structure loading introduces hazards in numerous fields. The complexity of vortex structure interaction necessitates study by physical experiment and computer simulation. Physical experiments are inherently expensive and difficult to utilize. Computational power of computers is rapidly increasing, and it is becoming possible to utilize increasingly-realistic computer models to simulate realistic vortex-loading of structures. The goal of this thesis is to analyze and define some of the key aspects of vortex loading of structures, the shortcomings of which have been

summarized in the previous subsections. The attained understanding can then be applied in numerous fields to increase structure resistance to vortex loading.

Vortex impact with structures is a relevant, load-producing phenomenon at practically all relative vortex-structure size scales. Rotor- and wing tip vortices may be much smaller than the chord length of the rotors that chop them ($r_c/c \leq 0.15$). Tornado and hurricanes respectively have critical radii exceeding 2 km and 45 km, so the relative vortex-structure size ratio $r_c/D \rightarrow \infty$. Practical engineering applications necessitate understanding of structure loading amplitude produced by vortices across the relative size ratio range of $0.15 \leq r_c/D \leq \infty$. However, the current range covered in the literature, neglecting the coarse-grid simulations of Alrasheedi (2012), is $0.15 \leq r_c/D \leq 4.0$. Furthermore, the computer simulations spanning this range utilize different physical systems (airfoil vs. slender cylinder) and different vortex models (Scully-Kaufmann vs. Rankine Combined). In short, the upper bound of the relative size ratio range at 4.0 is far below the upper bound for practical situations. A consistent data set attained using a fixed physical system and vortex model is needed to establish the influence of the relative vortex-structure size on the trend in maximum structure loading amplitude.

In aerospace applications, vortices are produced by- and chopped by rotors, so designers may know the vortex path with respect to the rotor. However, in scenarios such as tornado loading of structures, the vortex may travel along any path relative to the loaded structure. The literature contains computer simulations and physical experiments that simulate vortex travel above and below the loaded structures; however, the studies use different physical models (air foil vs. prismatic structure) and vortex rotation directions (clockwise vs. counter-clockwise). A consistent data set is needed to establish the influence of vortex path shift on structure loading amplitude. This knowledge can potentially be applied in the design of aerospace vehicles to

minimize vortex-applied air loads or to assess the maximum loading that tornado or hurricane vortices can produce on structures.

The capability of tornados to produce dynamically amplified structure response is reported in the literature. Investigators relying on intuition and post-storm damage investigation conclude that tornados are too large to dynamically load structures. However, researchers who apply assumed tornado wind fields to response models arrive at the contradictory conclusion that tornado wind loads may be amplified by as much as four times. Current design codes make no provision for tornado wind loads, which have already been demonstrated by computer simulation and physical experiment to produce 1.5 to 3.2 times greater aerodynamic loading than straight line wind of the same maximum velocity. Dynamic amplification of the already under predicted aerodynamic forces could result in structure loading that is much greater than that predicted by assuming that tornado wind loads are the same as straight line wind loads. The collective shortcomings of the previous study are that they simply dismiss the dynamic loading threat and those that consider it fail to develop a generalized, applicable assessment or methodology to assess the possible dynamic load amplification of a given structure. Integration of provisions for dynamic amplification of structure response to tornado wind loads necessitates the definition of a generalized methodology to assess the possible dynamic amplification of any structure's response to any tornado wind loading.

Realistic simulation of vortex loading of structures requires the use a realistic vortex model. Vortices that pose structure loading threats are "intense", meaning that the tangential velocity is much greater than the radial or axial velocity components. Tangential velocity profiles of real-world vortices are qualitatively similar, but differ quantitatively, hence no single analytical vortex tangential velocity profile realistically represents all vortex tangential velocity

profiles. Therefore, it is necessary to identify a group of analytical vortex tangential velocity profiles that represent the possible range of measured profiles for use in computer simulation.

2.8.3 Progression of Thesis

Chapter 3 documents the selection of realistic vortex tangential velocity profiles (TVPs) for use in computer simulation. Analytical TVPs are assembled and normalized so that $V_\theta(r_c) = 1$ for comparison. Measured TVPs from various types of experimentally-produced vortices as well as from field-measured tornado and hurricane vortices are then assembled and normalized for comparison as well. Analytical TVPs that best represent the upper and lower bounds of the measured TVPs are identified along with the analytical TVP that best represents the typical measured TVP.

Chapter 4 introduces and outlines the physical model and numerical method used to simulate two-dimensional impact of a slender cylinder by a vortex. Boundary conditions and specific details of the utilized grids are illustrated and discussed. The model and grids are then validated using simulated free stream flow over an immersed cylinder. The capability of the model and grid to transport the impinging vortices is subsequently assessed.

Chapter 5 defines the trend in maximum cylinder loading amplitude with respect to the relative vortex-structure size. The impinging vortex critical radius is incremented from one to one-hundred times the cylinder diameter while the free stream velocity and maximum vortex tangential velocity are fixed. Phenomenon influencing the cylinder loading amplitude trend are illustrated and explained. The vortex size beyond which cylinder loading amplitude becomes asymptotic is identified. The vortex size producing asymptotic loading is then used to evaluate the influence of vortex path shift on structure loading amplitude. The vortex path is shifted so that the vortex center travels both above and below the cylinder. The trend in cylinder loading

with respect to path shift is documented, and illustrations are presented and discussed to explain the loading trend.

Chapter 6 is the final portion of this thesis and evaluates the capability of tornados to produce dynamically amplified structure response. The dynamic load factor concept is utilized to define the load application period of an impinging vortex as function of its critical radius, translational velocity, and tangential velocity profile. Fundamental periods of real-world structures are surveyed and categorized. The range of documented tornado vortex parameters is compiled and applied to define a universal dynamic load factor curve for tornado wind loads as function of the fundamental period of the loaded structure.

CHAPTER 3: SELECTION OF REALISTIC TANGENTIAL VELOCITY PROFILES

Realistic computer simulation of structure loading by vortices necessitates the use of a physically-realistic vortex velocity field model. Vortices of interest in engineering applications are "intense", meaning the tangential velocity V_θ is much greater than the radial or axial velocity components (Vatistas, 1998). Therefore, it is imperative that vortex model used in the present study have a physically-realistic tangential velocity profile (TVP).

The literature contains many analytical vortex TVP models, which are reviewed extensively by Bhagwat and Leishman (2002) and Wood and White (2011). Most of the analytical TVPs are derived by using simplifying assumptions to solve the Navier Stokes equations. Each analytical TVP realistically represents a measured experimental or atmospheric vortex TVP. However, measured vortex TVPs vary greatly ((Wurman et al., 2007) and (Kepert, 2010)) and no single analytical TVP represents all of the measured TVPs. The goal of the forthcoming study is to establish a group of analytical TVPs that represent the range of measured vortex TVPs.

The following sections begin with a review of the commonly-used analytical TVPs. Derivations and simplifying assumptions are not discussed herein, but the interested reader may find them in the referenced studies. The analytical TVPs are then normalized as necessary so that $V_\theta(r_c) = \alpha \cdot r_c$. Subsequently, measured TVPs are extracted from the literature, normalized for comparison, and categorized according to experiment and vortex type. Finally, the analytical and measured TVPs are compared, and the analytical TPVs which best represent the measured TVPs are identified for subsequent use in computer-simulated vortex loading of structures.

3.1 Analytical Tangential Velocity Profiles

3.1.1 Bi-Regional Profiles

The Rankine Combined Vortex Model (RCVM) developed by Rankine (1882) is the oldest and simplest TVP that is still in use. The TVP is bi-regional, consisting of a solid-body inner core ($r/r_c \leq 1$) and an potential vortex beyond the critical radii ($r/r_c > 1$). The RCVM TVP exhibits a sharp peak at the critical radius ($r = r_c$) where the TVP transitions from a solid-body vortex to a potential vortex. This sharp peak is not realistic of real-world vortices because the fluid's viscosity causes dissipation of the vortex, producing a smooth, rounded peak at the critical radius (Vatistas et al., 1991). The solid-body inner core and exterior potential vortex are defined by Eqs. (3.1) and (3.2) respectively.

$$V_{\theta,RCVM}(r) = \left(\frac{r}{r_c}\right) \qquad (0 \leq r/r_c \leq 1.0) \tag{3.1}$$

$$V_{\theta,RCVM}(r) = \left(\frac{r_c}{r}\right) \qquad (r/r_c > 1.0) \tag{3.2}$$

Hughes (1952) modifies Rankine's (1882) profile by adding an exponent (x) to the definition of the potential vortex, defining the Modified Rankine Combined Vortex Model (MRCVM). The MRCVM is used extensively to model tornado and hurricane TVPs in the literature, with values of x ranging from 0.04 to 0.9 as summarized in Table 3.1.

Table 3.1: Values of exponent "x" used in the literature for tornado and hurricane TVPs.

Source	Vortex Type	x
Hughes (1952)	Hurricane	0.62
Goerss and Jefferies (1994)	Hurricane	< 0.9
Leslie and Holland (1995)	Hurricane	0.5 to 0.6
Mallen et al. (2005)	Hurricane	0.04 to 0.67
Wurman et al. (2007)	Tornado	0.6
Kosiba and Wurman (2010)	Tornado	0.4 to 1.0
Holland et al. (2010)	Hurricane	0.5

High values of x theoretically correlate to a laminar vortex because the TVP decays rapidly for $r/r_c > 1$; conversely, low values of x correlate to a slowly-decaying vortex for $r/r_c > 1$ whose profile is flattened due to turbulent diffusion. The solid-body inner core and modified exterior potential vortex regions are defined by Eqs. (3.3) and (3.4) respectively.

$$V_{\theta,\mathrm{MRCVM}}(r) = \left(\frac{r}{r_c}\right) \qquad (0 \le r/r_c \le 1.0) \tag{3.3}$$

$$V_{\theta,\mathrm{MRCVM}}(r) = \left(\frac{r_c}{r}\right)^x \qquad (r/r_c > 1.0) \tag{3.4}$$

3.1.2 Continuous Profiles

The Lamb (1932) – Oseen (1912) (L-O) TVP is commonly used to model rotor-tip vortices (Ramasamy and Leishmann, 2006). The TVP is defined in Eq. (3.5). Rotor tip vortices are not maintained after being shed and progressively grow larger due to the fluid viscosity. The growth of the vortex is incorporated into the TVP using the time-dependent critical radius definition Eq. (3.6), where $\alpha_o = 1.25643$ is the Oseen constant. The L-O TVP is singular at the center of the vortex (r = 0), hence special provision must be made when defining the TVP at this ordinate.

$$V_{\theta,\mathrm{L-O}}(r) = \frac{r_c}{r} \cdot \left[1 - \exp\left(-\alpha_o \cdot \frac{r^2}{r_c^2}\right)\right] \tag{3.5}$$

$$r_c(t) = \sqrt{4\alpha_o \nu t} \tag{3.6}$$

Burgers (1948) and Rott (1958) propose a steady solution of the L-O TVP by fixing the vortex critical radius. Their steady solution is used extensively to represent the TVP of maintained atmospheric vortices such as tornados (Tanamachi et al., 2007).

Sullivan (1958) derives the "two-cell" vortex TVP defined using Eqs. (3.7) and (3.8). Sullivan's TVP is used extensively to represent tornado vortex TVPs (Wood and White, 2011).

$$V_{\theta,S}(r) = \frac{r_c}{r} \cdot \left[\frac{H\left(\frac{ar^2}{2\nu}\right)}{H(\infty)} \right] \tag{3.7}$$

$$H(x) = \int_0^x \exp\{-\tau + 3\int_0^\tau [(1 - e^{-\tau})/\tau]\}d\tau \tag{3.8}$$

Wood and White (2011) simplify and normalize Eq. (3.7) so that $V_\theta(r_c) = 1$, yielding Eq. (3.9). Further simplification is provided by Leslie and Snow (1980) who report that the denominator of Eq. (3.9) is 37.9043 and by Vatistas (1998) who reports that $\beta = 6.238$. Incorporating these two constants, the simplified and normalized adaption of Sullivan's TVP is provided in Eq. (3.10).

$$V^*_{\theta,S}(r) = \frac{r_c}{r} \cdot \left[\frac{H(\beta \cdot (r/r_c)^2)}{\lim_{r/r_c \to \infty} H(\beta \cdot (r/r_c)^2)} \right] \tag{3.9}$$

$$V^*_{\theta,S}(r) = \frac{r_c}{r} \cdot \left[\frac{H(6.238 \cdot (r/r_c)^2)}{37.9043} \right] \tag{3.10}$$

Leslie and Snow (1980) show that $H(x)/H(\infty) \geq 0.99$ for $r/r_c \geq 1.3$. This means that the Sullivan TVP (Defined in Eq. (3.7)) is effectively the potential vortex defined in Eq. (3.2) for $r/r_c \geq 1.3$. However, numerical integration of Eq. (3.10) is required to define the TVP for each radial ordinate where $r/r_c < 1.3$. Consequently, use of the Sullivan TVP is cumbersome and time consuming if the vortex tangential velocity need be known at many radial ordinates.

The Scully (1975) – Kaufmann (1962) (S-K) TVP defined in Eq. (3.11) is used extensively to define rotor tip vortices ((Vatistas, 2006), (Thom and Duraisamy, 2010), and (Liu et al., 2012)). Bhagwat and Leishman (2002) demonstrate that the S-K profile realistically represents measured vortex TVPs; Vatistas (2006) reports that it is especially realistic for radial ordinates $r/r_c > 3$. Aboelkassem et al. (2005) note that the S-K TVP typically under-predicts the maximum vortex tangential velocity near the critical radius. One noted advantage that the S-K profile holds over the L-O profile is that it is defined at the vortex center.

$$V_{\theta,S-K}(r) = \left(\frac{r \cdot r_c}{r^2 + r_c^2}\right) \tag{3.11}$$

For the sake of completeness, the H-family of profiles developed by G.J. Holland between 1980 and 2010 shall be briefly discussed. The first and latest versions, referred to as H80 and H10 respectively, are the most commonly-used TVPs for modeling hurricane vortex wind fields (Kepert, 2010). However, the H-family TVPs require an excessive number of parameters (Fluid density, fluid temperature, assumed wind speeds at specified heights, etc.) along with calibration of various constants based upon "peripheral observations" (Holland et al., 2010). Forecasting applications may require such an extensively detailed profile, as the trajectory of a hurricane may be greatly influenced by its TVP (Cao et al., 2011). Hurricanes are often tracked for weeks before they make landfall, hence it is feasible to collect the large number of parameters and update models. However, other vortices (tornado, rotor-tip, etc.) are short-lived and volatile, so readily collecting and updating the many parameters is not feasible. Consequently, application of the H-family of profiles is limited to the study of hurricanes.

3.1.3 Algebraic Profiles

The term "algebraic profiles" refers to TVPs that are developed to replicate the commonly-used, derived profiles that have been discussed up to this point. The algebraic profiles are advantageous for use in computer modeling because they can be used to study vortices having numerous TVPs without recursive modification of the program. Furthermore, the algebraic profiles afford a much more time-efficient manner to compute profiles such as the Sullivan profile (Defined in Eqs. (3.7) to (3.10)).

Vatistas et al. (1991) introduce the n-family of TVPs defined in Eq. (3.12). The exponent (n) is varied to accurately reproduce the most commonly-used, derived TVPs from ***Section 3.1.1***: S-K (n = 1), steady L-O (n = 2), and RCVM (n = 100). Vatistas (1998) modifies Eq. (3.12) to

replicate the two-celled Sullivan vortex. However, the definition of this new TVP cannot be evaluated directly, hence it difficult and cumbersome to use.

$$V_{\theta,V}(r) = \frac{(r \cdot r_c)}{(r^{2n} + r_c^{2n})^{1/n}} \tag{3.12}$$

Wood and White (2011) begin with Vatistas' (1991) profile, and develop possibly the most robust algebraic profile. Eq. (3.13) approximates both single- and two-celled vortex TVPs with great accuracy. Three exponents are used to modify the profile: κ controls the slop of the profile in the inner core ($r \leq r_c$), η controls the decay rate of the free vortex ($r > r_c$), and λ controls the profile shape. Values of the three exponents that reproduce the common, derived TVPs are summarized in Table 3.2. Wood and White (2011) report that these exponents replicate the L-O and Sullivan TVPs with RMS error of only 0.008 and 0.005 respectively, demonstrating the accuracy of these approximation.

$$V_{\theta,W-W}(r) = \frac{(r/r_c)^{\kappa}}{\left[1 + \frac{\kappa}{\eta} \cdot ((r/r_c)^{\kappa/\lambda} - 1)\right]} \tag{3.13}$$

Table 3.2: Exponents used to replicate derived TVPs using Eq. (3.13).

Model	κ	η	λ
Scully	0.850	1.700	0.700
L-O	1.000	2.265	0.830
Sullivan	2.401	3.433	0.435
RCVM	1.000	2.000	0.010

3.1.4 Normalization and Comparison of Analytical Profiles

For comparison, all vortex parameters are normalized with respect to the maximum vortex tangential velocity and the vortex critical radius so that $V_\theta(r_c) = V_{\theta,max} = 1$. The Rankine TVPs Eqs. (3.1-4) and the W-W TVP Eq. (3.13) are already normalized; however, the L-O, S-K, and Vatistas profiles need be normalized. Eqs. (3.5), (3.11), and (3.12) are evaluated at r = rc, yielding Eqs. (3.14-16) respectively; the steady version of Eq. (3.5), where r_c is fixed, is used.

$$V_{\theta,L-O}(r_c) = (1 - \exp(-\alpha_o)) \tag{3.14}$$

$$V_{\theta,S-K}(r_c) = 0.5 \tag{3.15}$$

$$V_{\theta,V}(r_c) = 2^{-1/n} \tag{3.16}$$

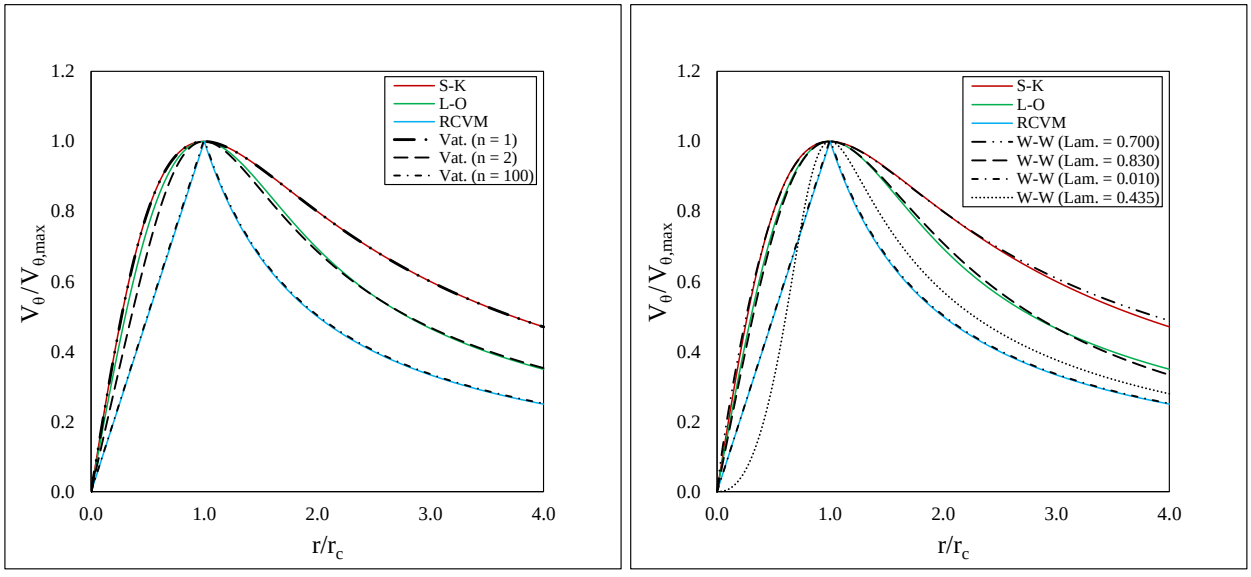
Now the TVPs defined in Eqs. (3.5), (3.11), and (3.12) are divided by their respective limits given in Eqs. (3.14-3.16). The normalized TVPs are listed in Eqs. (3.17-3.19) respectively.

$$V^*_{\theta,L-O}(r) = \frac{1}{(1 - \exp(-\alpha_o))} \cdot \frac{r_c}{r} \cdot \left[1 - \exp\left(-\alpha_o \cdot \frac{r^2}{r_c^2}\right)\right] \tag{3.17}$$

$$V^*_{\theta,S-K}(r) = 2 \cdot \left(\frac{r \cdot r_c}{r^2 + r_c^2}\right) \tag{3.18}$$

$$V^*_{\theta,V}(r) = r \cdot r_c \cdot \left[\frac{2}{r_c^{2n} + r^{2n}}\right]^{1/n} \tag{3.19}$$

Figure 3.1a and Figure 3.1b respectively illustrate qualitative comparison of normalized adaptions of the S-K, L-O, and RCVM TVPs with their replications by the normalized Vatistas profile and W-W profile. Vatistas' TVP is more accurate for $r/r_c > 1$, while the W-W TVP is



(a) (b)

Figure 3.1: Comparison of normalized S-K, L-O, and RCVM vortex TVPs with their replications by the normalized (a) Vatistas and (b) W-W profiles.

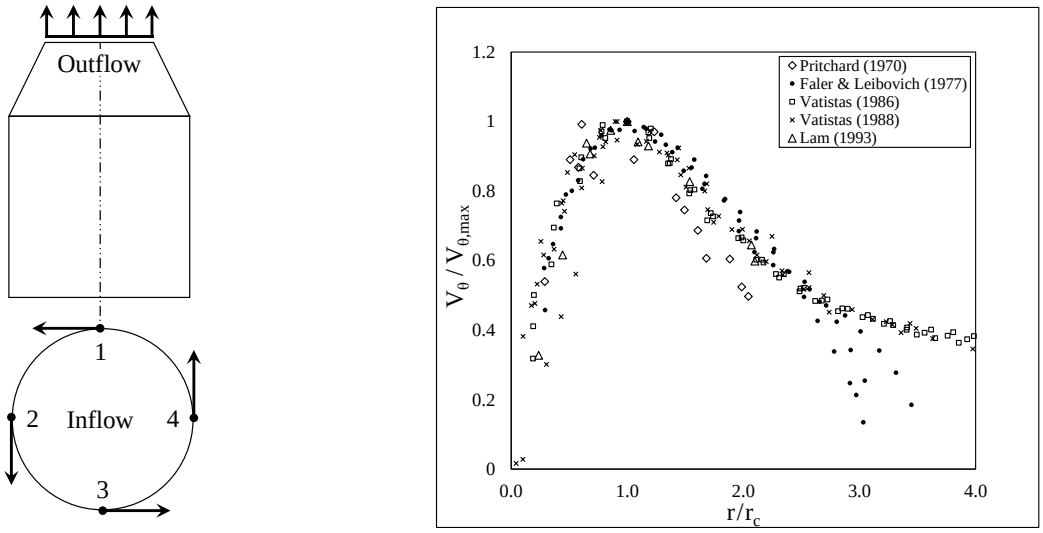
3.2 Measured Tangential Velocity Profiles

The literature contains numerous measured vortex TVPs. These range from small, mechanically-produced and maintained experimental vortices to large, convection-driven, atmospheric vortices such as tornados and hurricanes. The measured TVPs are assembled and grouped into six categories based upon vortex type: vortex chamber experiments, tornado simulation experiments, fixed-wing experiments, rotor-experiments, measured tornado, and measured hurricane. Details of the vortices in each of the six groups as well as the measurement methodology used to record the TVP are discussed. All measured TVPs are reported in the same normalized format $V_\theta(r_c) = V_{\theta,max} = 1$ as the analytical TVPs for ease of comparison.

3.2.1 Vortex Chamber Experiments

Vortex chambers are common experiment configurations for studying flows in vortex combustors and separators ((Vatistas et al., 1986), (Vatistas and Lin, 1988), and (Lam, 1993)). Figure 3.2a is a general schematic of a vortex chamber. Specifically, fluid is input at one end of the cylindrical chamber as four tangential jets spaced at $\pi/2$ around the circumference of the chamber and extracted as a single axial stream at the opposite end of the chamber. Vatistas et al. (1986) provide a thorough description of the flow within vortex chambers.

Faler and Leibovich (1977) report that their experiments are characterized by the Reynolds number range of $3000 \leq Re \leq 6{,}000$; however, they do not discuss how they calculate Re. The remaining four sources do not discuss Re for their experiments. Pritchard (1970) stirs a vat of water, and uses "streak photographs" to deduce the TVP. Faler and Leibovich (1977) use a vortex chamber with water as fluid, and measure TVPs via laser Doppler velocimetry. Vatistas et al. (1986) and Vatistas and Lin (1988) use a vortex chamber with air as fluid, measure pressure



(a) (b)

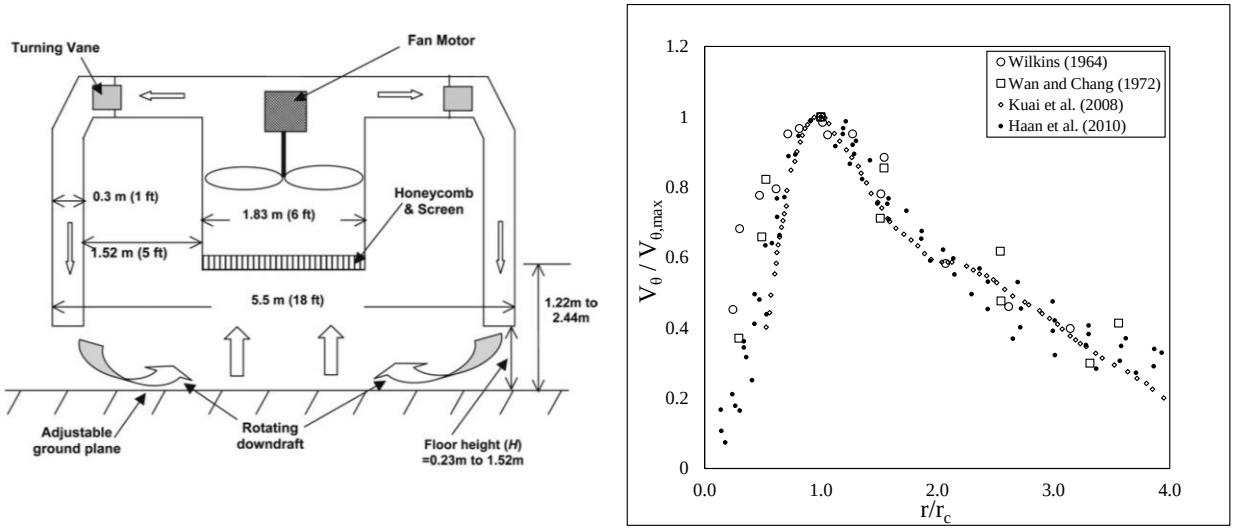
Figure 3.2: (a) Schematic of the vortex chamber experiment configuration and (b) vortex TVPs from vortex chamber experiments.

using a three-dimensional probe, and compute the TVP based upon the pressure profile. Lam (1993) also uses air in a vortex chamber, measures pressure using a 5-hole pitot tube, and back-computes the TVP.

The measured TVPs are summarized in Figure 3.2b; all profiles are qualitatively similar. In the range $r/r_c < 2$, Pritchard's (1970) data exhibits greatest deviation from the other data. This is likely because his experiment is less controlled than the vortex chambers used by all of the other authors. Also, his method of measuring the TVP via streak photographs is less accurate than directly measuring velocity or measuring pressure and back-computing velocity. Faler and Leibovich's (1977) data separates from the three remaining data sets and exhibits unrealistically-rapid decay for $r/r_c > 2.5$. It is therefore postulated that the measurements were taken too close to the walls of the vortex chamber, hence the TVP was artificially damped by the presence of the wall.

3.2.2 Tornado Simulator Experiments

Tornado simulators are used to study both the general structure of tornados (Church et al., 1979) and the loading they produce on structures (Haan et al., 2010). Figure 3.3a is a schematic of the state of the art, translating tornado simulator currently in use at Iowa State University. Haan et al. (2008) discuss the technical parameters and specifications of the tornado simulator. Church and Snow (1993) provide a thorough review of early tornado simulators and studies. Generally speaking, a powerful blower or fan is mounted at the top of a cylindrical or dome-shaped hood, and fluid is pulled into the hood through numerous angled vanes spaced around the hood's circumference. The hood may be stationary ((Wilkins, 1964) and (Wan and Chang, 1972)) or may translate ((Kuai et al., 2008) and (Haan et al., 2010)).



(a) (b)

Figure 3.3: (a) Schematic of the translating tornado simulator at Iowa State University (Modified from Haan et al. (2010)) and (b) vortex TVPs from tornado simulator experiments.

The simulated tornado vortices are characterized using the vortex Reynolds number $Re_v = \Gamma_\infty/\nu$, where total circulation $\Gamma_\infty = V_{\theta,max} \cdot r_c \cdot 2\pi$ is the path integral of the maximum tangential velocity. Some studies choose to report the swirl ratio (S), which is the ratio of tangential to axial vortex velocity, instead of Γ_∞. Given the volumetric flow rate through the fan (Q), the total

circulation is defined $\Gamma_\infty = 2 \cdot S \cdot Q \cdot r_c^{-1}$. The ranges of Re_v for the considered studies are summarized in Table 3.3.

Table 3.3: Vortex Reynolds number ranges for tornado simulator TVPs.

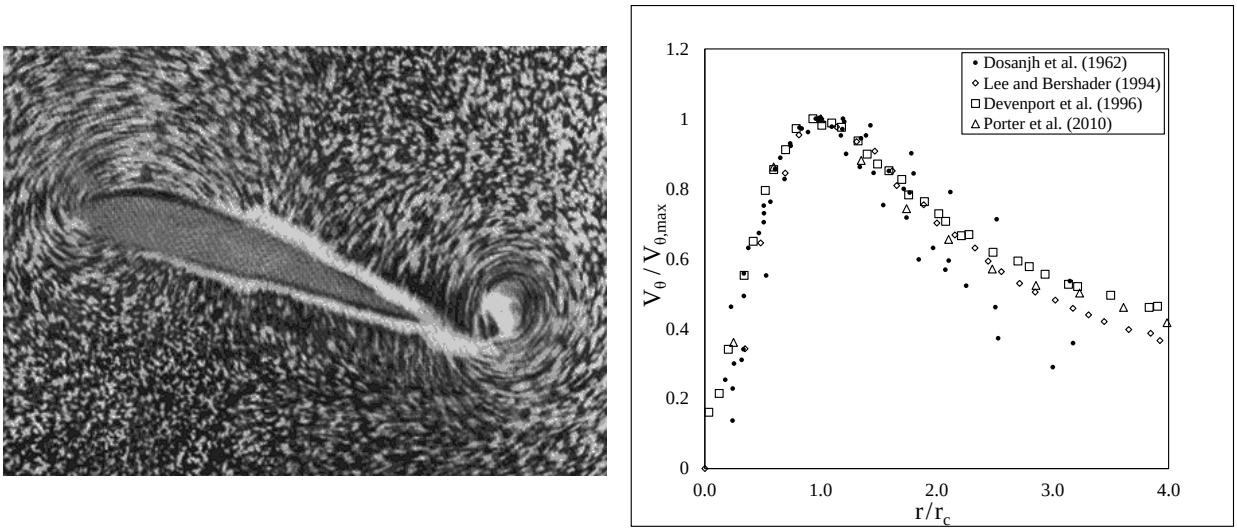
Source	Re_v
Wilkins (1964)	205,000
Wan and Chang (1972)	710,000 to 1,300,000
Kuai et al. (2008)	1,798,000 to 2,062,000
Haan et al. (2010)	1,800,000 to 4,165,000

Wilkins (1964) uses a small cup anemometer to directly measure velocity; he also attains the same TVP by computing the velocity profile from a pressure profile measured using a pitot tube. Wan and Chang (1972) measure the TVP directly using a constant temperature anemometer with hot film probes as sensors. Kuai et al. (2008) and Haan et al. (2010) use the same 18-point pressure probe to measure the vortex pressure profile, from which, the vortex TVP is back-computed.

Measured TVPs from the tornado simulator experiments are summarized in Figure 3.3b; all profiles are qualitatively similar. The tornado simulator TVPs are visibly sharper than the vortex chamber TVPs (Figure 3.2b). This is counter-intuitive, as the literature currently theorizes that the TVP should flatten as Re_v increases due to increased turbulence in the potential vortex (Vatistas, 2006).

3.2.3 Fixed-Wing Experiments

Vorticies produced by fixed wings are typically studied in the aerospace community where the objective is to evaluate air-loads produced on trailing aerospace vehicles when they encounter vortices shed from leading aerospace vehicles (Dosanjh et al., 1962). Figure 3.4 illustrates the shedding of a vortex from the downstream edge of a fixed wing. Generally speaking, a wing is rigidly fixed in a tank and fluid is circulated over it.



(a) (b)

Figure 3.4: (a) Prandtl's fixed-wing experiment (Modified from Barba (2013)) and (b) vortex TVPs from fixed-wing experiments.

Fixed-wing experiments are classified using the chord Reynolds number $Re_c = c \cdot U_\infty / \nu$. The range of Re_c for the considered studies, all of which use air as fluid, is summarized in ***Table 3.4***. Dosanjh et al. (1962) fix the wing in a wind tunnel, measure the vortex pressure profile, and compute the TVP. Lee and Bershader (1994) fix the wing in a shock tube and also measure the vortex pressure profile then back-compute the TVP. Devenport et al. (1996) fix the wing in a wind tunnel and use a four-sensor, hot-wire probe to directly measure the vortex TVP. Porter et al. (2010) also fix the wing in a wind tunnel and use hot wire anemometry to directly measure the vortex TVP.

Table 3.4: Chord Reynolds number range for fixed wing vortex experiments.

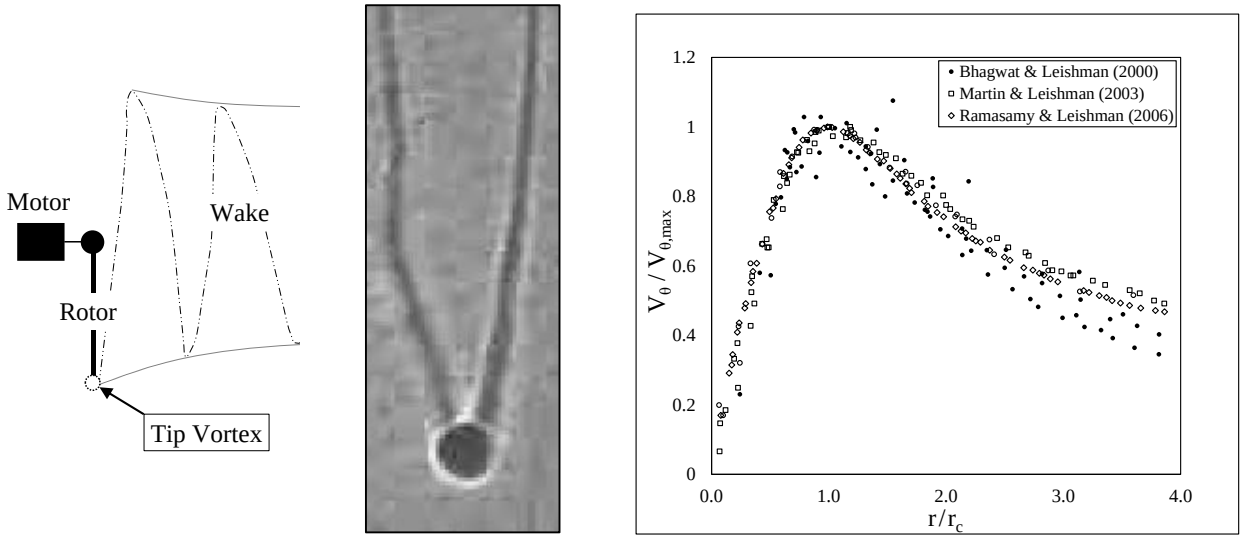
Source	Re_c
Dosanjh et al. (1962)	10,000
Lee and Bershader (1994)	900,000 to 1,300,000
Devenport et al. (1996)	318,000 to 742,000
Porter et al. (2010)	830,000

The fixed-wing vortex TVPs are summarized in Figure 3.4b; all profiles are qualitatively similar and generally well grouped. The data of Dosanjh et al. (1962) deviates from the other

three tightly-grouped data sets for $r/r_c > 1.5$. This deviation is attributed to the fact that Dosanjh et al. (1962) use a much lower Re_c than is used in the other three studies. It is also noted that the fixed-wing vortex TVPs resemble the vortex chamber TVPs (Figure 3.2b) rather than the tornado simulator TVPs (Figure 3.3b).

3.2.4 Rotor Experiments

Rotor votices are primarily studied in the aerospace community for mitigation of the impulsive noise and vibration of helicopters (Ramasamy and Leishman, 2004). The schematic Figure 3.5a illustrates the layout of the common single-rotor experiment. Figure 3.5b is a shadowgraph (density gradient measurement) illustrating the scale of a rotor-tip vortex to the propeller that produces it. Generally stated, the rotor is driven to rotate by the motor and different techniques are used to measure the vortices developed on the rotor and shed in its wake.



(a) (b) (c)

Figure 3.5: (a) Schematic of the rotor tip vortex experiment, (b) shadowgraph of a rotor tip vortex (Modified from Bagai and Leishman (1993)), and (c) measured vortex TVPs from rotor tip experiments.

Table 3.5: Chord Reynolds number range for rotor vortex experiments.

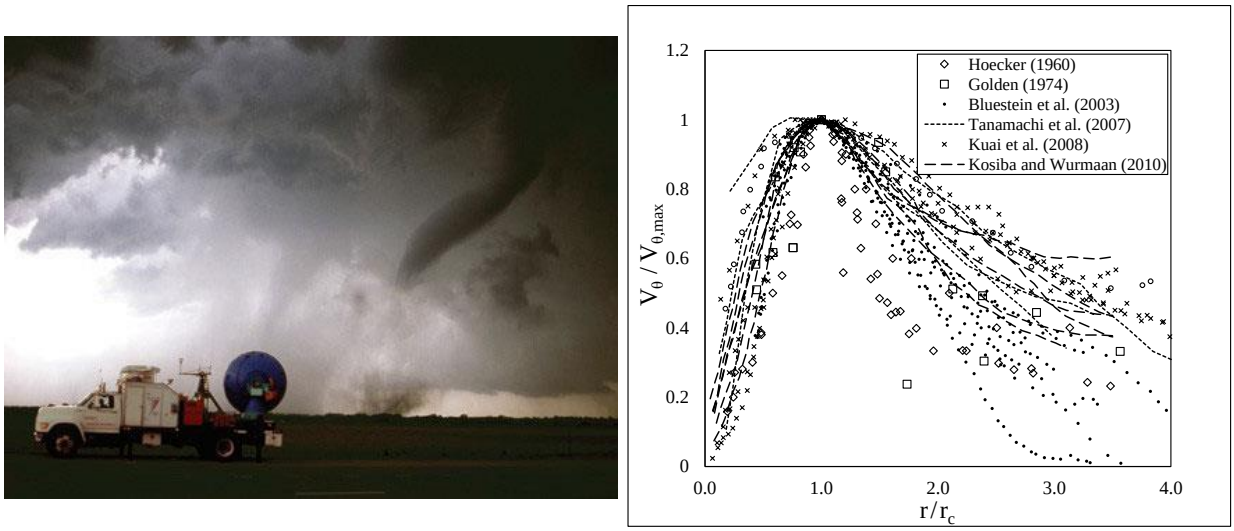
Source	Re_c
Bhagwat and Leishman (2000)	270,000
Martin and Leishman (2003)	272,000
Ramasamy and Leishman (2006)	272,000

Bhagwat and Leishman (2000) seed the air with olive oil having particle diameter $d_p = 6 \pm 2$ μm and use laser Doppler velocimetry to directly measure the vortex TVP. Martin and Leishman (2003) also use laser Doppler velocimetry to directly measure the TVP, but they use a "mineral oil fog" with particle diameter $d_p < 0.5$ μm to seed the air, which improves the resolution of their measurements. Ramasamy and Leishman (2006) also measure the TVP directly using laser Doppler velocimetry with mineral oil fog as seed particles.

Measured TVPs from the rotor tip vortex experiments are summarized in Figure 3.5c; the TVPs are qualitatively similar and well-grouped. Bhagwat and Leishman's (2000) data exhibits more scatter than the other two data sets. This is likely due to tracking error (discussed in Martin and Leishman (2003)) because the olive oil seeding particles are much larger than the mineral oil seeding particles. It is noted that the measured rotor-tip TVPs are similar to the vortex chamber and fixed-wing TVPs rather than exhibiting the sharp profile observed in the tornado simulator TVPs.

3.2.5 Measured Tornados

Tornado vortices are studied primarily so that the wind loadings that they place on structures may be better understood. The current state of the art in measurement of tornado TVPs is via mobile Doppler radar as illustrated in Figure 3.6a. Generally stated, those working in the field attempt to forecast the tornado path and position themselves so that they can record the tornado from the closest safe distance.



(a) (b)

Figure 3.6: (a) Measurement of tornado vortex TVP via mobile Doppler radar (Modified from NSF (2005)) and (b) measured tornado vortex TVPs.

Hoecker (1960) takes successive, timed photographs of debris and using the change in debris location to approximate the tornado-vortex TVP. Golden (1974) uses similar methodology to approximate the TVP within waterspouts.

The four remaining studies use mobile, W-band Doppler radar (λ = 3 mm, f = 95 Hz) to measure tornado TVPs. Bluestein et al. (2003) and Tanamachi et al. (2007) use measurements made by their group in 1999. Kuai et al. (2008) analyze measurements recorded in 1998 and reported in Alexander and Wurman (2005). Kosiba and Wurman (2010) also analyze measurements recorded in 1998. Summary of measurement details is provided in Table 3.6. All measurements were made using similar radar technology and at similar measurement distances.

Table 3.6: Details for mobile Doppler radar measurement of tornado TVPs.

Source	Measurement Year	Measurement Height	Measurement Distance
Bluestein et al. (2003)	1999	N/A	2.3 to 7.0 km
Tanamachi et al. (2007)	1999	70 to 155 m	4.5 to 6.8 km
Kuai et al. (2008)	1998	20 to 660 m	1.7 to 12.9 km
Kosiba and Wurman (2010)	1998	≈ 40 m	1.7 to 6.5 km

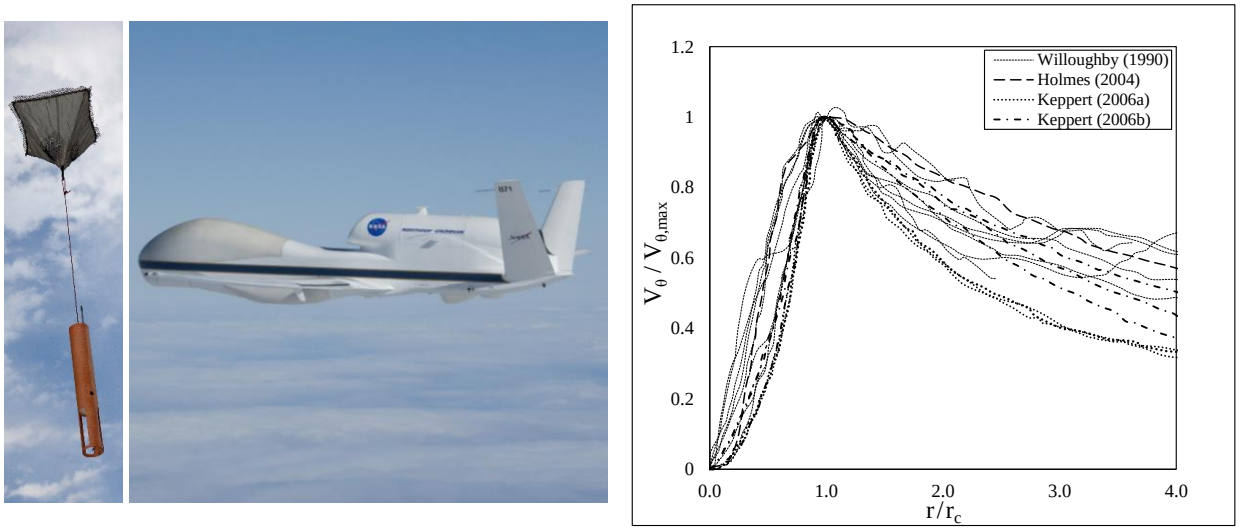
Figure 3.6b summarizes the measured tornado-vortex TVPs. The data are qualitatively similar for $r/r_c \leq 1$; however, there is substantial scatter in the data for $r/r_c > 1$. The data acquisition methodology of Hoecker (1960) and Golden (1974) is imprecise and at best yields an estimate of the TVP. Now considering the radar data, several of the series reported in Bluestein et al. (2003) exhibit abnormally-rapid decay for $r/r_c > 1.5$. The accuracy of radar measurements depend upon the strength of the reflected signal, which can be attenuated and distorted by numerous sources (moisture in the atmosphere, level of precipitation, debris in the vortex, etc.), hence it is believed that Bluestein et al.'s results do not accurately represent the TVP for $r/r_c > 1.5$.

3.2.6 Measured Hurricanes

Hurricane vortices are primarily studied to allow better forecasting of their trajectory and strength at landfall. Early studies report measurements collected via manned flight through the hurricane eyewall, which is obviously hazardous to human life. Modern studies are conducted by flying above the tropical cyclone (NOAA uses the manned WP-3D Orion (NOAA, 2015b) and NASA uses the unmanned Global Hawk (Newman, 2013)) and seeding the hurricane with dropsondes (Discussed in Hock and Franklin, (1999)). Dropsondes transmit their location (via GPS), horizontal and vertical velocity, temperature, pressure, and relative humidity with high accuracy (EOL, 2015). Illustration of a deployed dropsonde and the Global Hawk delivery plane of NASA are provided in Figure 3.7a.

Willoughby (1990) and Holmes (2004) report hurricane TVP measurements made via manned aircraft flight through the hurricanes. Keppert (2006a and 2006b) report the measured TVP within hurricanes at 500, 1000, and 2000 meters elevation measured using dropsondes. The hurricane considered in Keppert (2006a) shows minimal variation in the TVP with elevation

while the TVP of the hurricane considered in Keppert (2006b) progressively flattens with increased elevation.



(a) (b)

Figure 3.7: (a) Deployed dropsonde (Modified from UCAR (2012)) and unmanned Global Hawk (Gutro and Braun, 2012) and (b) measured hurricane TVPs.

The measured hurricane TVPs are summarized in Figure 3.7b. Generally, the data are well-grouped and follow a consistent trend. Simply due to the scale of the hurricane vortex, there is question regarding the resolution of the measurements. To put this in perspective, Kepert (2006a) uses 4 to 5 dropsondes to define the 25 km critical radius, a cluster of dropsondes are dropped at the critical radius, and another cluster are dropped at approximately 75 km from the center of the hurricane; the TVP is defined from this data. Kepert (2006b) uses more than twice as many dropsondes to define the TVP, hence he has much better resolution.

3.3 Comparison and Analysis of Analytical and Measured Profiles

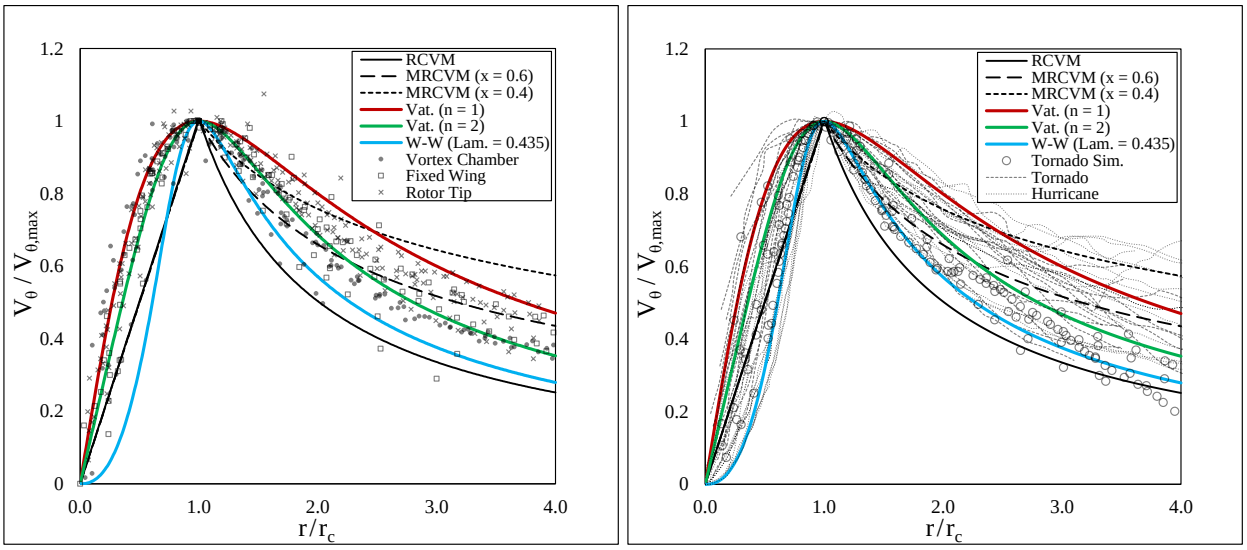
Six sources of measured vortex TVPs have been discussed, and measured TVPs from each source have been compiled and normalized. Now the measured TVPs shall be compared with the normalized analytical profiles defined in Section 3.1, so that the most realistic analytical TVPs can be identified. Section 3.2 identifies several measured TVPs that deviating substantially

from the other TVPs within their classification. These data sets are summarized below and omitted from comparison with the analytical TVPs for the noted reasons.

- From the vortex chamber experiments (Section 3.2.1):
    - Faler and Leibovich (1977)
        - The vortex TVP exhibits unrealistically-rapid decay for $r/r_c > 2.5$.
- From the measured tornados (Section 3.2.5):
    - Hoecker (1960) and Golden (1974)
        - The vortex TVPs are computed by tracking debris movements in successive, timed photographs. These measurements are qualitative and deviate substantially from the direct radar-measured TVPs for $r/r_c > 1$.
    - Bluestein et al. (2003)
        - Many of the vortex TVPs exhibit unrealistically-rapid decay for $r/r_c > 1.5$.

Six commonly-used, analytical TVPs are selected for comparison with the measured vortex TVPs. The selected analytical TVPs are: RCVM, MRCVM (x = 0.6), MRCVM (x = 0.4), Vatistas (n = 2) which approximates the steady L-O profile, Vatistas (n = 1) which approximates the S-K profile, and W-W ($\lambda = 0.435$) which approximates the Sullivan profile. The six groups of measured TVPs are split into two groups of three to avoid excessive data overlap and compared with the analytical TVPs in Figures 3.8a and 3.8b.

Figure 3.8a shows that Vatistas n = 1 and n = 2 profiles are excellent representation of the inner core ($r/r_c \leq 1$) of the measured vortex chamber, fixed-wing and rotor tip TVPs. The n = 1 profile is an upper boundary to the measured TVPs beyond the critical radius ($r/r_c > 1$). The n = 2 profile falls from the middle of the measured TVPs at $r/r_c = 1$ to be the lower boundary of the measured TVPs at $r/r_c > 4$.



(a) (b)

Figure 3.8: Comparison of analytical TVPs with measured TVPs from (a) vortex chamber, fixed-wing, and rotor tip experiments and (b) tornado simulators, tornados, and hurricanes.

The Rankine and W-W profiles under-predict the tangential velocity within the critical radius. Beyond the critical radius, the MRCVM (x = 0.6) profile is a good representation of the measured TVPs. However, the RCVM and W-W profiles decay much more rapidly than the measured TVPs while the MRCVM (x = 0.4) profile decays much more slowly than the measured TVPs.

Figure 3.8b shows that the W-W profile is an effective lower boundary for the measured tornado simulator, tornado, and hurricane TVPs. Vatistas n = 2 profile consistently falls in the middle of the measured TVPs. Vatistas n = 1 profile is near the top of the measured TVPs, but some of the measured hurricane TVPs fall above it. The MRCVM (x = 0.4) is a better upper boundary for $r/r_c > 2.5$, but it is a poor fit of the measured TVPs for $r/r_c < 1.25$.

3.4 Conclusions

Physically-realistic analytical vortex tangential velocity profiles (TVPs) are required to simulate physically-realistic vortex-structure interaction. All measured vortex TVPs are qualitatively similar but differ quantitatively, hence no single analytical vortex TVP can

represent all measured vortex TVPs. Measured vortex TVPs are exhaustively surveyed in the literature and compiled. Analytical vortex TVPs are also compiled and normalized so that the maximum tangential velocity is unity at the critical vortex radius $V_\theta(r_c) = 1$ for comparison with the measured vortex TVPs. A group of analytical vortex TVPs which adequately represent the spectrum of measured vortex TVPs are identified for use in computer simulation of vortex-structure interaction. Based upon the content presented in Chapter 3, the subsequent conclusions have been reached.

1. The Vatistas n = 1 TVP (Marked by red line in Figure 3.8) which replicates the normalized S-K profile is the best upper boundary to most of the measured TVPs.
    a. This implies the n = 1 profile represents a "flat" and supposedly turbulent vortex.
2. The Vatistas n = 2 TVP (Marked by green line in Figure 3.8) which replicates the normalized, steady L-O profile bisects most of the measured TVPs.
    a. This implies the n = 2 profile represents a "typical" vortex.
3. The W-W $\lambda = 0.435$ TVP (Marked by blue line in Figure 3.8) which replicates the normalized Sullivan profile is the best lower boundary to the measured TVPs.
    a. This implies the W-W profile represents a "sharp" and supposedly laminar vortex.
    b. The W-W profile is an excellent lower boundary for the measured tornado simulator, tornado, and hurricane TVPs. However, when the measured vortex chamber, fixed-wing, and rotor tip TVPs are considered, the Rankine profiles are a better lower boundary for $r/r_c < 1$, and the W-W profile is a better lower boundary for $r/r_c > 1$.
4. The Vatistas n = 2 TVP best represents a typical vortex, hence it should be used as the default vortex TVP for computer simulations of vortex-structure interaction.

CHAPTER 4: COMPUTER MODEL

4.1 Problem Description

The physical system modeled in the present study is the parallel interaction of a vortex with a long, rigid, circular cylinder that is immersed in a free stream. As illustrated in Figure 4.1, the vortex is initialized at some horizontal ordinate (X_o) to the left of the cylinder and travels within the free stream at bulk velocity (U_∞) to impact the cylinder. The cylinder is "long", implying that flow around the ends of the cylinder is negligible, and hence the problem is two-dimensional. The vortex's impact with the cylinder is defined as "parallel" because the vortex's axis of rotation and the major cylinder axis are always parallel. The vortex and cylinder centers may be on the same horizontal line, or the vortex's path may be shifted vertically by some distance (δ).

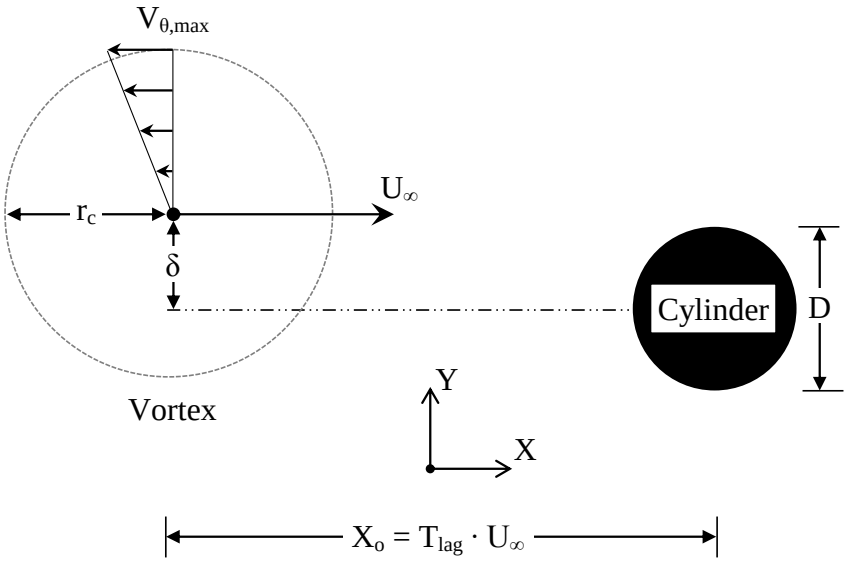


Figure 4.1: Schematic of the parallel interaction of an impinging vortex with a long, rigid, circular cylinder.

The vortex's tangential velocity (V_θ) increases with radius (r) from the center of vortex and reaches a maximum value ($V_{\theta,max}$) at the critical radius (r_c). The maximum tangential velocity $V_{\theta,max}$ is the product of r_c and the dimensionless vortex angular velocity (α). The time

lag (T_{lag}) is specified so that the vortex and cylinder centers fall on the same vertical line when dimensionless time (t^*) is zero. The time lag T_{lag} is illustrated in Figure 4.1 by fixing the starting position X_o of the vortex.

4.1.1 System Parameters

The fluid density ($\rho = 1$), fluid kinematic viscosity ($\nu = 1/150$), and cylinder diameter ($D = 1$) are fixed throughout the study. The stream-wise (X-direction) drag force (Fd) and cross-stream (Y-direction) lift force (Fl) are computed by integrating the pressure and shear force acting on the cylinder surface. The drag and lift forces are then converted to the commonly-discussed drag ($Cd = 2 \cdot Fd / \rho \cdot A \cdot U_{ref}^2$) and lift ($Cl = 2 \cdot Fl / \rho \cdot A \cdot U_{ref}^2$) force coefficients, where $A = D \cdot L$ is the reference area per unit cylinder length ($L = 1$).

All simulations in the present study use maximum vortex tangential velocity and free stream velocity of unity ($V_{\theta,max} = U_\infty = 1$). Consequently, the free stream Reynolds number $Re = U_\infty \cdot D / \nu$ is 150 for all simulations. The vortex critical radius r_c ranges from $1 \leq r_c/D \leq 100$. Noting that $V_{\theta,max} = \alpha \cdot r_c = 1$, it follows that the vortex's dimensionless angular velocity is the inverse of the vortex critical radius ($\alpha = r_c^{-1}$). The vortex impacts the cylinder directly ($\delta = 0$) unless otherwise stated, but its path is also shifted so that it travels above or below the cylinder by path shift of $-4 \leq \delta/r_c \leq 4$.

4.1.2 Low Reynolds Number Limitation

The simulations performed herein utilize a free stream Reynolds number of 150, which is quite low considering the fact that vortex interaction with rotors and impact of atmospheric vortices with structures are both characterized by high Reynolds numbers ($Re > 10^7$). A low Reynolds number is utilized for two primary reasons which are identified below and expounded subsequently. Firstly, the numerical model directly simulates the vortex-structure interaction, and

grid resolution requirements increase rapidly with increasing simulation Reynolds number. Secondly, the physical system modeled herein is the two-dimensional impact of a vortex with a slender, circular cylinder, and simulation at Reynolds numbers above 300 necessitates use of a three-dimensional model.

The presently-used computer model resolves the velocity field by solving conservation of mass and momentum at each tie step. This approach is known as "Direct Simulation" because no terms are added to the momentum conservation equations to model turbulence. Direct simulation is more physically realistic than using turbulence models, but requires excessive grid refinement to resolve the boundary layer around a structure as well as the turbulence in its wake. When directly simulating flow over a cylindrical structure, the first radial node spacing is generally $\Delta r_o < 0.1 \cdot Re^{-0.5}$ ((Selvam and Paterson, 1993) and (Cao et al., 2010)). The boundary layer around the structure progressively becomes thinner as Re increases, hence the necessary grid refinement to resolve the boundary layer rapidly increases with Reynolds number. Illie (2009) reports that grid resolution requirements increase with Reynolds number according to $Re^{9/4}$ and reasons that $Re \approx 5{,}000$ is a practical limit for direct simulations.

Grid resolution requirements aside, the other major factor constraining the free stream Reynolds number to a low value is that the physical system modeled herein is two-dimensional. Free stream flow over a cylindrical structure produces opposite-signed vortices on the cylinder which are alternately shed. Williamson's (1996) physical experiments show that the structure of these vortices is two-dimensional up to approximately Re of 190 but begins to transition to three dimensional at higher Reynolds numbers. The transition is not abrupt, and Williamson's (1996) experimental data shows that vortex shedding can adequately be resolved using a two-dimensional model up to Re of 300 (See Figure 4.5b). The sum of the maximum vortex

tangential velocity and the free stream velocity used throughout this study is 2.0, hence all computer simulations are characterized by Re ≤ 300 based upon the maximum velocity in the domain.

4.2 Governing Equations

The simulation is governed by incompressible conservation of mass Eq. (4.1) and conservation of x- and y-direction momentum which are expressed in Eqs. (4.2a) and (4.2b) respectively.

$$\frac{\partial U}{\partial x} + \frac{\partial V}{\partial y} = 0 \tag{4.1}$$

$$\frac{\partial U}{\partial t} + U\frac{\partial U}{\partial x} + V\frac{\partial U}{\partial x} + \frac{1}{\rho}\frac{\partial P}{\partial V} - \frac{\mu}{\rho}\left[\frac{\partial^2 U}{\partial x^2} + \frac{\partial^2 U}{\partial y^2}\right] = 0 \tag{4.2a}$$

$$\frac{\partial V}{\partial t} + U\frac{\partial V}{\partial x} + V\frac{\partial V}{\partial y} + \frac{1}{\rho}\frac{\partial P}{\partial y} - \frac{\mu}{\rho}\left[\frac{\partial^2 V}{\partial x^2} + \frac{\partial^2 V}{\partial y^2}\right] = 0 \tag{4.2b}$$

Eqs. (4.1) and (4.2) are non-dimensionalized using the dimensionless groups summarized in Eq. (4.3), where the asterisk implies that a value is dimensionless.

$$U^* = \frac{U}{U_\infty} \qquad V^* = \frac{V}{U_\infty} \qquad x^* = \frac{x}{D} \qquad y^* = \frac{y}{D} \qquad t^* = \frac{t \cdot U_\infty}{D} \qquad P^* = \frac{P}{\rho \cdot U_\infty^2} \qquad Re = \frac{D \cdot U_\infty}{\nu} \tag{4.3}$$

Mass and momentum conservation are written in dimensionless format in Eqs. (4.4) and (4.5) respectively using the compact tensor notation. Subscript "i" is the index, and subscripts "i and j" are 1 for "x" or 2 for "y". Subscript "t" corresponds to time, and a comma implies differentiation with respect to the following subscript.

$$U^*_{i,i} = 0 \tag{4.4}$$

$$U^*_{i,t} + U^*_j U^*_{i,j} + P^*_{,i} + Re^{-1}\left[U^*_{i,j} + U^*_{j,i}\right]_{,j} = 0 \tag{4.5}$$

The convection term $U_j^* U_{i,j}^*$ in Eq. (4.5) is nonlinear, hence it is difficult to numerically approximate accurately. Selvam (1998) reviews techniques for numerical approximation of the

convection term and concludes that the balance tensor diffusion scheme (Dukowicz and Ramshaw, 1979) is the most accurate approach. Specifically, $-\delta t^{*}/2\cdot(U_j^{*}U_k^{*}U_{i,j}^{*})_{,k}$ is added to $U_j^{*}U_{i,j}^{*}$, where δt^{*} is the solution time step. Selvam (1997a) provides further details regarding the implementation of the balance tensor diffusion scheme.

4.2.1 Vortex Tangential Velocity Profile

The three most commonly-used, analytical vortex tangential velocity profiles (TVPs) are the Scully-Kaufmann (S-K), steady Lamb-Oseen (L-O), and the Rankine Combined (RCVM). Chapter 3 contains a thorough review and comparison of measured and analytical vortex TVPs. The S-K profile forms the upper boundary to most of the measured TVPs, hence it is a "flat", theoretically turbulent vortex. The L-O profile falls within the middle of the measured TVPs making it a "typical" vortex. The Sullivan profile is named the best representative of the lower boundary of the measured TVPs, hence it is a "sharp" theoretically laminar vortex. The RCVM profile also realistically represents a "sharp" vortex profile and is utilized much more commonly in the literature. The present study utilizes the S-K, L-O, and RCVM TVPs in computer simulations.

As shall be discussed subsequently, the impinging vortex is introduced into the computational domain using a transient boundary condition that combines the free stream and vortex tangential velocity. It is therefore convenient to use the previously defined and normalized version of Vatistas (1991) TVP given by Eq. (4.6), because the exponent (n) can be specified as 1, 2, or 100 to replicate the S-K, L-O, and RCVM profiles respectively. This eliminates the need to modify the computer program when simulating different vortex profiles.

$$V_\theta(r) = r \cdot r_c \cdot \left[\frac{2}{r_c^{2n} + r^{2n}}\right]^{1/n} \tag{4.6}$$

Eq. (4.6) is currently formatted so that $V_{\theta,max}$ is unity. Although all simulations in the present study, use vortices having maximum tangential velocity of unity, it is desired that the maximum tangential vortex velocity be specifiable. Therefore, Eq. (4.6) is scaled by the dimensionless vortex angular velocity α and critical radius r_c so that $V_{\theta,max}$ of $\alpha \cdot r_c$ can be specified. The resulting expression has r_c^2 in the numerator; this term is distributed to reduce the number of necessary computations when computing V_θ, resulting in Eq. (4.7) which is the TVP definition used in the present model. The exponent n = 2, corresponding to the steady L-O profile, is used for all simulations unless otherwise noted.

$$V_\theta(r) = \alpha \cdot r \cdot \left[\frac{2}{(r/r_c)^{2n} + 1}\right]^{1/n} \tag{4.7}$$

4.3 Numerical Method

The present numerical model is a finite element adaption of the node-centered, non-staggered, control volume procedure introduced in Selvam (1997a). Time advancement is performed using the Backward Euler scheme. The velocity and pressure fields are resolved at each time step using the four-step advancement procedure outlined below. Steps 1 and 3 use pre-conditioned conjugate gradient solvers where Jacobi and Incomplete Choleski preconditioners are used respectively. Steps 1-4 are iterated until the average residual at each node falls below 10^{-7} at each time step.

- Step 1 - Solve U_i^* from Eq. (4.5)
- Step 2 - Update velocity field: $U_i^{**} = U_i^* + \delta t^* \cdot P_{,i}^*$
- Step 3 - Solve for pressure field: $(P_{,i}^*)_{,i} = U_{i,i}^{**} / \delta t^*$
- Step 4 - Correct velocity for incompressibility: $U_i^* = U_i^{**} - \delta t^* \cdot P_{,i}^*$

Equal-order interpolation of the velocity and pressure terms, along with Step 2, eliminates the checkerboard pressure field discussed in Patankar (1980). The higher order portion of the convection term and the diffusion term are solved implicitly, removing the restriction on maximum time step for numerical stability. A constant time step of $\delta t^* = 0.01$ is used for all simulations so that the Courant–Friedrichs–Lewy (CFL) number is always less than one. Selvam (1997b) provides further discussion of the finite element methodology and solution algorithm.

4.4 Domain, Grid, and Boundary Conditions

4.4.1 Domain and Grid

The computational domain is illustrated by the schematic in Figure 4.2 where X_i, X_o, and X_s are the inflow, outflow and span-wise boundary dimensions respectively. Two grids are used in the present study. Grid 1 (G1) is smaller, more refined, and used exclusively in Chapter 5. Grid 2 (G2) is larger, less refined, and used for the remaining studies reported in Chapters 6 and 7. Summary of the domain boundary dimensions for Grids 1 and 2 is provided in Table 4.1.

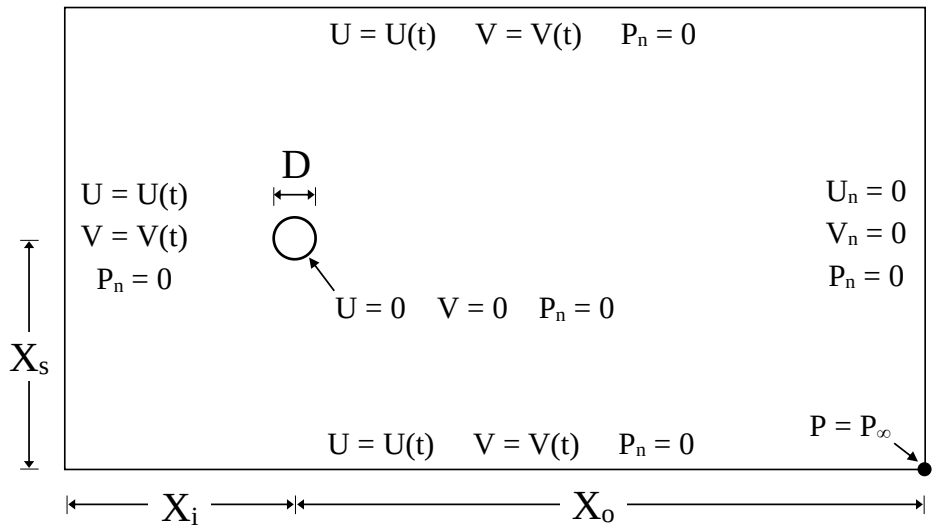


Figure 4.2: Schematic of the computational domain and boundary conditions.

Table 4.1: Summary of domain dimensions for Grid 1 and Grid 2.

Grid	X_i	X_o	X_s
1	12.5·D	42.5·D	25.0·D
2	15.0·D	50.0·D	30.0·D

Figures 4.3a and 4.3b respectively illustrate Grid 1 and Grid 2, and Figures 4.3c and 4.3d respectively illustrate close-up views of the grid refinement around the cylinder. The first radial node spacing from the cylinder surface is $\Delta r_o = 0.0075 \cdot D$. Subsequent node spacing is stretched according to $\Delta r_i = 1.10 \cdot \Delta r_{i-1}$ until the specified maximum radial node spacing Δr_m is

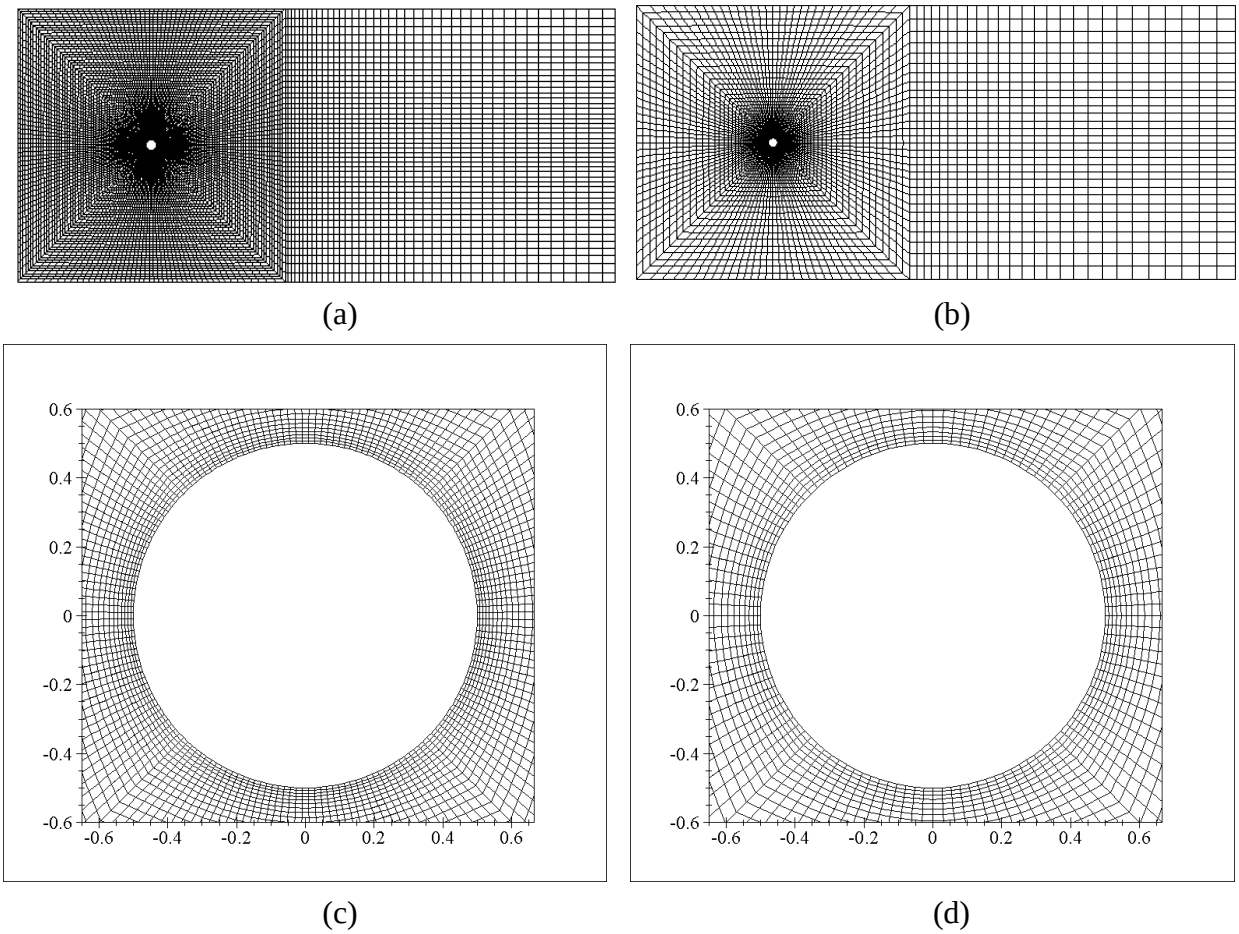


Figure 4.3: Illustrations of (a) Grid 1 and (b) Grid 2 along with close-up views of grid refinement around the cylinder for (c) Grid 1 and (d) Grid 2.

reached ($\Delta r_i \leq \Delta r_m$). After reaching the maximum radial node spacing, constant radial node spacing of Δr_m is used for the remainder of the computational domain. The maximum radial node

spacing Δr_m is 0.25·D for Grid 1 and 0.5·D for Grid 2. The surface of the cylinder is defined using 181 nodes for Grid 1 and 121 nodes for Grid 2; the tangential node spacing is 2º and 3º for the respective grids. Grids 1 and 2 are respectively composed of 15,700 and 7,526 nodes.

The primary reason for utilizing the less-refined Grid 2 is that it requires much less CPU time to execute a simulation than is required by Grid 1. Grid 1 is composed of approximately twice as many grid points as Grid 2; however a simulation of length $t^* = 250$ requires 11.5 hours to execute on a personal computer when Grid 1 is used as opposed to 3 hours when Grid 2 is used. This correlates to an increase in computational time of 3.83 for an increase in nodes of only 2.09 times. ***Table 4.2*** summarizes the grid, number of simulations, and simulation time required

Table 4.2: Summary of computer simulations and associated CPU time for the simulations reported in this thesis.

Grid	Simulations	Duration (Δt^*)	CPU Time	
			Hours	Days
Free Stream Validation Studies (Chapter 4.5)				
1	18	300	248.4	10.4
2	18	300	64.8	2.7
Load Variation with Vortex Impact Time (Chapter 5.2)				
1	76	250	874.0	36.4
Influence of Vortex Size (Chapter 5.3)				
2	15	200	36.0	1.5
···	30	300	108.0	4.5
···	5	450	27.0	1.1
···	10	600	72.0	3.0
···	20	3000	720.0	30.0
···	10	4000	480.0	20.0
···	5	6000	360.0	15.0
Influence of Vortex Path Shift (Chapter 5.4)				
2	23	3000	828.0	34.5
Defining the Vortex Loading Period (Chapter 6)				
2	1	200	12	0.5
···	2	400		
···	15	2100	378.0	15.8
Totals	248		4208.2	175.3

for the simulations reported in this thesis. Utilizing Grids 1 and 2, the required simulation time is 175.3. If the same simulations were conducted only using Grid 1, the required simulation time would be increased to 503.3 days, or by a factor of 2.87. This demonstrates the time savings benefit of designing grids tailored to specific studies.

4.2.2 Boundary Conditions

Boundary conditions are indicated along each surface of the computational domain schematic Figure 4.2, where the subscript (n) implies differentiation with respect to the normal direction. The no-slip or zero velocity condition is applied at the cylinder surface. The downstream boundary is assumed to be sufficiently far from the cylinder for flow to re-develop, hence the normal derivative of velocity is zero. The normal derivative of pressure at the cylinder surface and domain boundaries is zero. The pressure value at the lower-downstream corner of the domain is specified to be the ambient pressure (P_∞) as is needed in the adopted solution procedure. Finally, velocity is specified as a transient boundary condition along the upstream and span-wise domain boundaries. This boundary condition is the vehicle for introducing the impinging vortex into the domain and is first implemented by Selvam (1985).

The schematic Figure 4.4 aids in understanding the computation of the transient velocity boundary condition. The fixed XY coordinate system originates from the cylinder center. The moving X'Y' coordinate system is attached to the vortex center and translates with it. The XY and X'Y' coordinate systems are linked by the fact the vortex and cylinder centers are aligned on the Y-axis when $t^* = 0$.

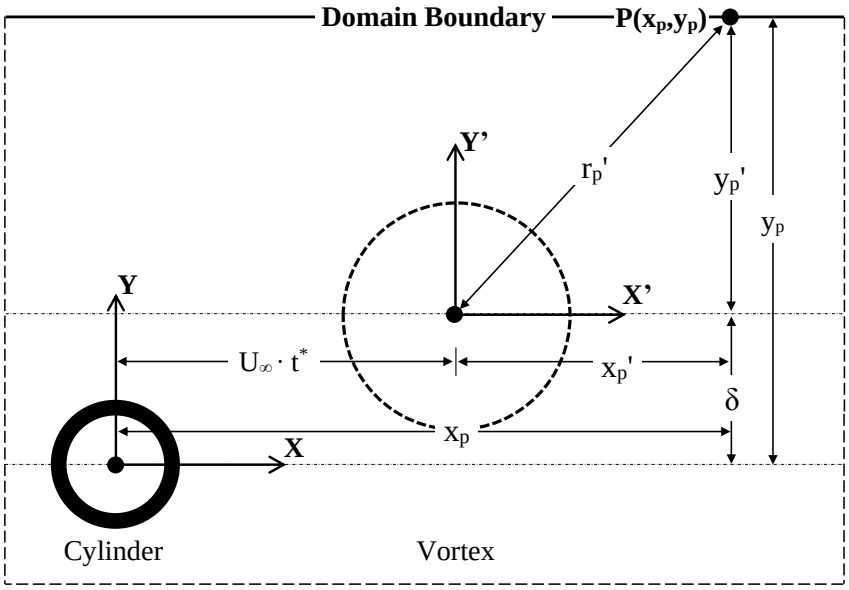


Figure 4.4: Schematic illustrating terms used to compute transient velocity boundary condition.

The coordinates (x_p, y_p) of each boundary point (P) are constant. The relative position (x_p', y_p') of each boundary point with respect to the vortex center is computed at each time step using Eqs. (4.8a) and (4.8b). The radial distance (r_p') between the vortex center and the boundary point is then computed using Eq. (4.9).

$$x_p' = x_p - U_\infty \cdot t^* \tag{4.8a}$$

$$y_p' = y_p - \delta \tag{4.8b}$$

$$r_p' = \left(x_p'^2 + y_p'^2\right)^{1/2} \tag{4.9}$$

Now $V_\theta(r_p')$ is computed using Eq. (4.6), and Eqs. (4.10a) and (4.10b) are used to transform the tangential velocity into horizontal and vertical components and add them to the free stream velocity. This process is repeated for each boundary node at each time step. Eqs. (4.10a) and (4.10b) are also valid for any node within the computational domain and are used to initialize the velocity field based upon the initial position of the vortex.

$$U(t) = U_\infty - V_\theta(r_p') \cdot y_p'/r_p' \tag{4.10a}$$

$$V(t) = V_\theta(r_p') \cdot x_p'/r_p' \tag{4.10b}$$

4.5 Numerical Validation

The literature contains very few studies of vortex loading of structures, hence model validation is challenging. In the present study, a two-stage model validation procedure is adopted. First, free stream flow over the cylinder is simulated using both grids. This is a common benchmark problem for many studies within the realm of fluid mechanics, and data from previous studies are available for comparison. This phase of the model validation allows assessment of the model and grids' capability to resolve the boundary layer around the cylinder. Subsequently, the model's capability to transport the impinging vortex across the domain to impact the cylinder is assessed by extracting the vortex TVP at discrete intervals and comparing it with the TVP defined by Eq. (4.6). This validation study is used to demonstrate that (1) the numerical model accurately resolves the flow and (2) that the specified vortex impacts the cylinder. It is therefore argued that the resulting cylinder loading is realistic representation of the loading that an impacting vortex would produce.

4.5.1 Validation Using Free Stream Simulations

All simulations in the present study are characterized by $Re \leq 300$; the present validation study is performed for the Reynolds number range of 50 to 300. Few physical experiments that measure loading on a cylinder immersed in a free stream are reported in the literature. This is likely because such low-Re flows produce minimal loading that is difficult to measure. Therefore, all data used to validate the present model is from other computer simulations except for the data of Williamson (1996).

Table 4.3 summarizes the details of the free stream computer simulations from which data is taken to validate the present model. These studies are selected because the report sufficient data points for characterizing the cylinder loading across the specified Reynolds

number range. Also, they utilize domains that are large enough to avoid blockage effects which are produced by imposition of boundary conditions and artificially inflate Cd (Posdziech and Grundmann, 2007).

Table 4.3: Free stream computer simulations used to validate the present model.

Source	Model	Re	Domain			
			Type	X_i	X_o	X_s
Franke et al. (1990)	DS·CV	50-5000	O	···	20·D	···
Henderson (1995)	DS·SE	10-1000	R	16·D	25·D	28·D
Park et al. (1998)	DS·CV	2-160	C	50·D	20·D	50·D
Posdz. and Grund. (2001)	SE	40-240	C/R	70·D	50·D	70·D
Mittal (2005)	DS·FE	50-350	R	···	50·D	···
Baranyi and Lewis (2006)	DS·FD	10-220	O	···	40·D	···
Stålberg et al. (2006)	DS·FD	7-180	O	···	40·D	···
Labbe and Wilson (2007)	LES·CV	40-1000	O	···	15·D	···
Posdz. and Grund. (2007)	SE	5-250	C/R	···	4000·D	···
Li et al. (2009)	LB	50-300	R	···	50·D	···
Qu et al. (2013)	DS·CV	50-200	R	···	60·D	···
Current (G1)	DS·FE	50-300	R	12.5·D	45·D	12.5·D
Current (G2)	···	···	···	15·D	50·D	15·D

*CV (Control Volume), DS (Direct Simulation), FD (Finite Difference), FE (Finite Element)

*LB (Lattice Boltzman), LES (Large Eddy Simulation), SE (Spectral Element)

Figures 4.5a – 4.5d compares cylinder loading data from the present model (Grid 1 and Grid 2) with data reported by the studies listed in Table 4.3. Cd is the mean drag force coefficient, Cd' and Cl' are the amplitudes of the drag and lift force coefficients respectively, and $St = f_{Cl} \cdot D/U_\infty$ is the Strouhal number, which is the dimensionless vortex shedding frequency. Mean drag force coefficient (Figure 4.5a) and Strouhal number (Figure 4.5b) are the typical metrics used in model validation. Values computed by the present model are in excellent agreement with values reported in the literature. The Cd curve for Grid 2 falls below the curve for Grid 1 because Grid 2 is larger, hence the blockage effect is reduced. It is interesting to note that a portion of Williamson's (1996) experimental Strouhal number data falls away from the

data from computer simulations for Reynolds numbers above 190. This is because the vortex shedding becomes three-dimensional in some of the experiments. Figures 4.5c and 4.5d respectively compare drag and lift force coefficient amplitudes computed by the current model with data from the literature. Computed values of Cd' and Cl' generally agree well with the literature although Cd' begins to fall below data from the literature for Re > 190.

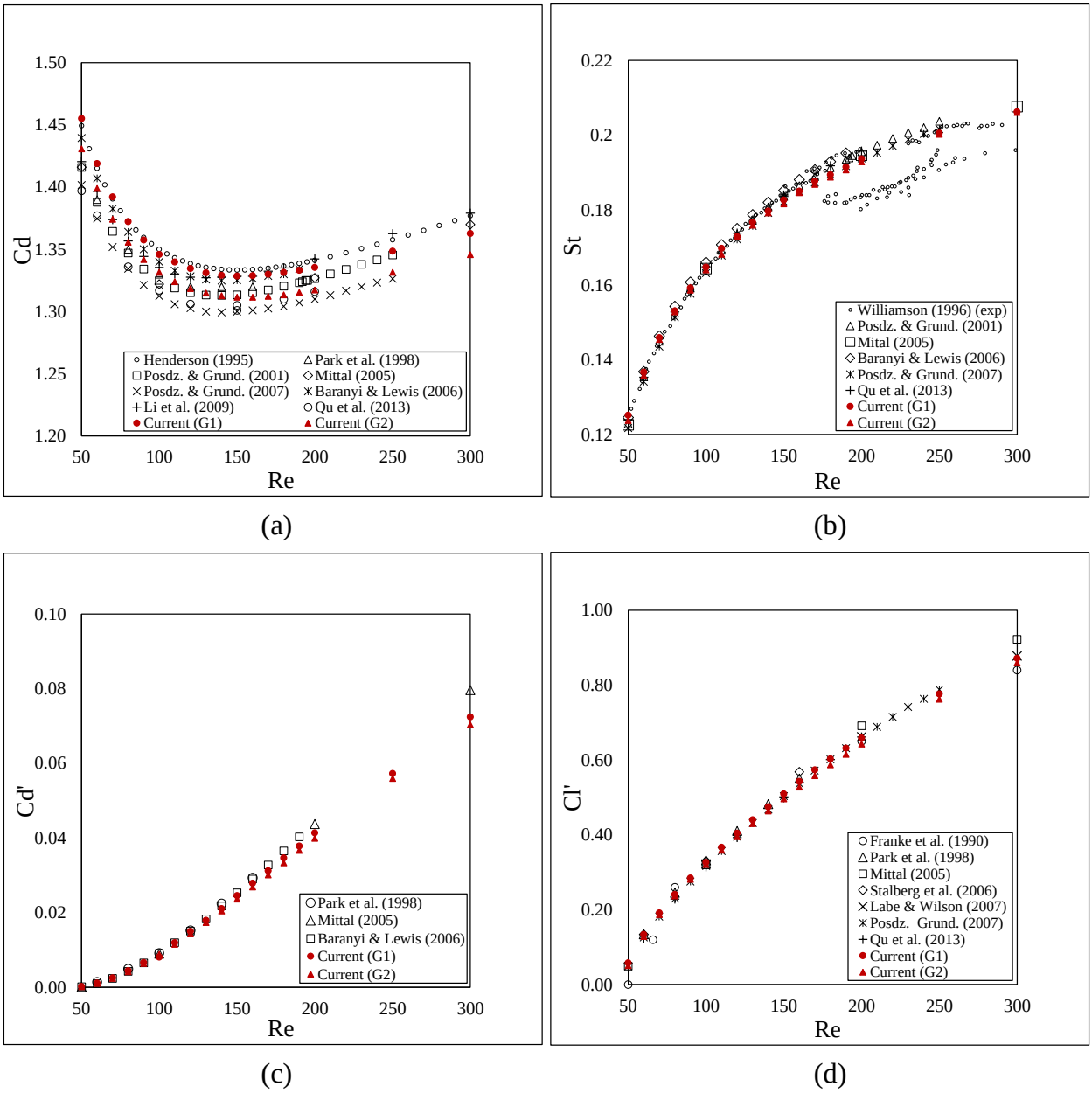


Figure 4.5: Comparison of free stream cylinder loading data computed using the present model and grids with data from literature (a) Cd, (b) St, (c) Cd', and (d) Cl'.

The free stream cylinder loading from the present model and grids adequately corresponds to that from the literature. Therefore, it is concluded that the present model and grids can accurately resolve the boundary layer around the cylinder in the considered regime that is characterized by Reynolds numbers less than 300.

4.5.2 Validation by Assessment of Vortex Transport

Both Selvam (1998) and Tamura et al. (2008) cite the difficulty in convectively transporting a vortex. The vortex is transported through the nonlinear convection term of Eq. (4.5), and numerical dissipation alters the vortex profile as it is transported across the domain. It is therefore necessary to quantify the dissipation of the vortex so that the structure of the vortex that actually traverses the domain and impacts the cylinder is known. The L-O vortex profile is used primarily in the present study, hence the first stage in assessing the accuracy of vortex transport is to compare the accuracy with which Grid 1 and Grid 2 transport a L-O vortex. The vortex TVP is extracted at discrete intervals as the vortex crosses the domain and compared with the analytical profile defined by Eq. (4.6) where n = 2. The study is performed for impinging vortex sizes of $r_c = 1 \cdot D$, which is the smallest impinging vortex size considered in this study, and $2 \cdot D$. Figures 4.6a – 4.6d summarize the extracted TVPs from simulation and compare them with the analytical TVPs.

Numerical diffusion progressively flattens the TVP and reduces the maximum tangential velocity as the vortex crosses the domain. For G1, $V_{\theta,max}$ is reduced to 83% ($r_c = 1 \cdot D$) and 97% ($r_c = 2 \cdot D$) of the analytical value by the time the impinging vortex impacts the cylinder. The dissipation of the vortex is greater for G2, where $V_{\theta,max}$ is reduced to 77% ($r_c = 1 \cdot D$) and 94% ($r_c = 2 \cdot D$) of the analytical value prior to impacting the cylinder. The vortex transport accuracy

progressively increases with impinging vortex size because more grid points are used to approximate the TVP.

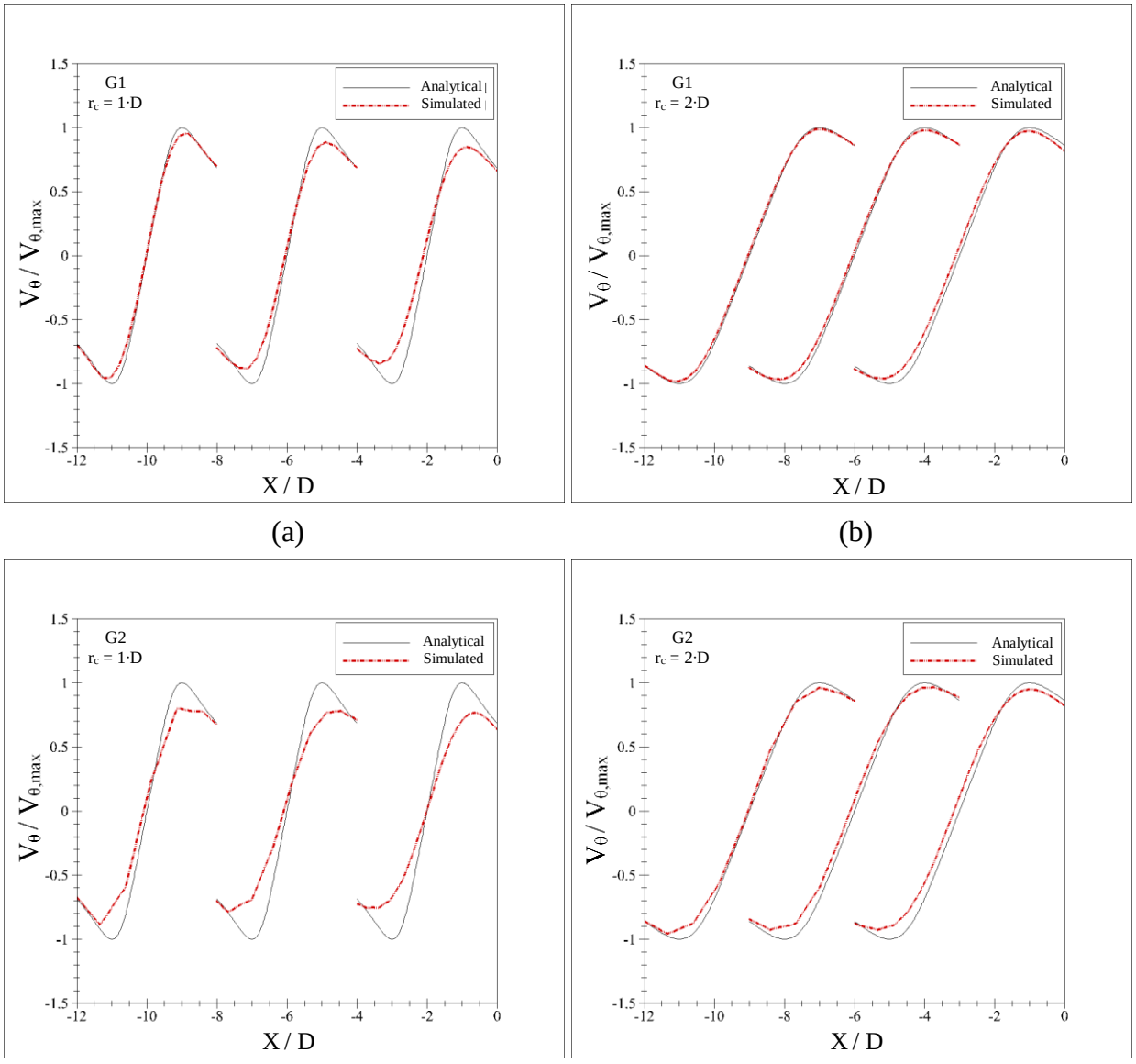


Figure 4.6: Comparison of L-O vortex transport accuracy using Grid 1 and Grid 2: (a) G1, r_c = 1·D, (b) G1, r_c = 2·D, (c) G2, r_c = 1·D, and (d) G2, r_c = 2·D.

The sharpness of the vortex TVP greatly influences the vortex transport accuracy because a sharper profile changes more between grid points hence the approximation accuracy decreases. This is illustrated by simulating the transport of S-K, L-O, and RCVM vortices having critical

radii of 2·D and 3·D using Grid 2. Analytical TVPs are summarized in Figures 4.7.1a – 4.7.1c, and simulated profiles are summarized in Figures 5.7.2a – 4.7.2c.

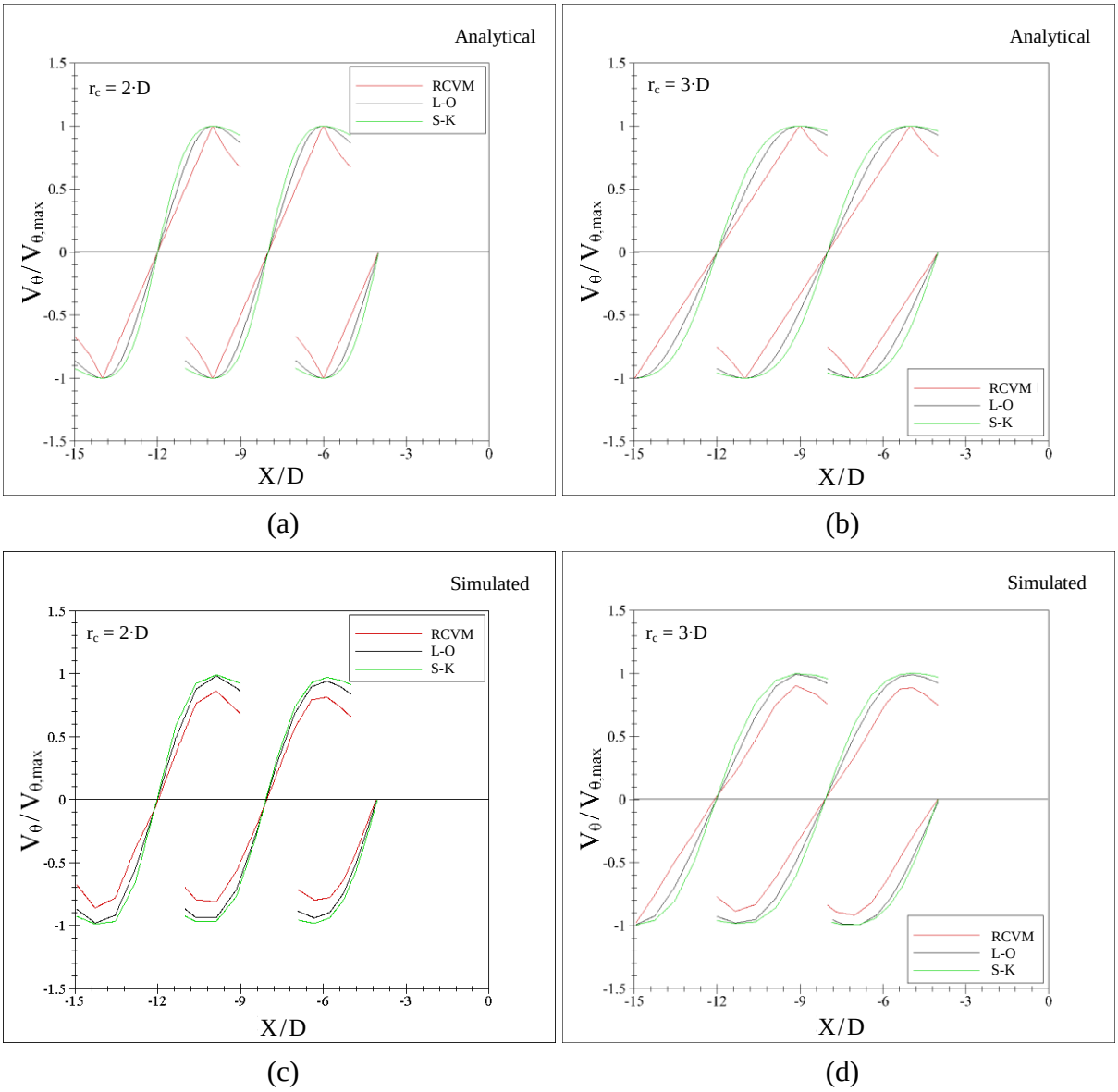


Figure 4.7: Comparison of analytical (a-b) and simulated (c-d) vortex tangential velocity profiles.

From ***Figures*** 4.7a – 4.7d, it is evident that the RCVM profile is transported with much less accuracy than the L-O or S-K profiles. This is because the sharp discontinuity in the RCVM profile near $r = r_c$ cannot be accurately approximated without excessive grid refinement. Table 4.4 summarizes the percentage of $V_{\theta,max}$ that is actually transported across the domain to the

cylinder. The smooth and continuous L-O and S-K profiles are transported with excellent accuracy for $r_c \geq 3 \cdot D$, while the RCVM profile must be larger ($r_c \geq 5 \cdot D$) to be transported with excellent accuracy.

Table 4.4: Percentage of $V_{\theta,max}$ transported for each vortex size and profile.

r_c	Profile		
	RCVM	L-O	S-K
2·D	80%	94%	98%
3·D	91%	> 99%	> 99%

From this study, it is concluded that S-K and L-O vortices having $r_c \geq 3 \cdot D$ and RCVM vortices having $r_c \geq 5 \cdot D$ can be transported with excellent accuracy by the coarser Grid 2. Numerical diffusion decreases the transport accuracy when smaller vortices are simulated. Simulations are conducted and reported in the present study using vortices as small as $r_c = 1 \cdot D$ because the simulation results are physically meaningful. However, care must be taken when the cylinder loading from these simulations is being analyzed, as the smaller vortices are weakened by numerical diffusion prior to impacting the cylinder.

CHAPTER 5: THE INFLUENCE OF THE IMPINGING VORTEX'S SIZE AND PATH ON STRUCTURAL LOADING

5.1 Chapter Overview and Progression

Structures are loaded by vortices at practically all relative vortex-to-structure size scales. Rotor- and wing-tip vortices encountered in aerospace applications are similar in size to the structures that they load. Atmospheric vortices such as tornados and hurricanes range from similar-sized to many times larger than the structures that they load. The forthcoming study simulates vortex impact with a slender, cylindrical to study and document the influence of the impinging vortex's size on the resulting structural loading.

The first portion of the forthcoming study simulates direct vortex impact (See Figure 5.14b) with the structure to identify and explain a unique phenomenon that produces variation in the structural loading when the impinging vortex impacts the structure at different times. The phenomenon is illustrated and explained, and the range of variation in the structural loading amplitude for vortex impact at different times is quantified. Subsequently, the impinging vortex size is incrementally increased while holding the vortex's maximum tangential velocity constant. Direct vortex impact is simulated for each impinging vortex size, and maximum force coefficient amplitudes are utilized to define the structural loading amplitude trend with respect to impinging vortex size. Also, the influence of the impinging vortex size on the aforementioned variation in structural loading amplitude with vortex time is assessed. Phenomenon controlling the trend in structural loading with respect to the impinging vortex size are illustrated and discussed. Finally, the influence of laterally shifting the impinging vortex's path (See Figures 5.14a and 5.14c) on the structural loading amplitude is evaluated. A single vortex size is selected, and its path is incrementally shifted so that it travels above and below the structure. Maximum force coefficients are utilized to assess the trend in structural loading amplitude with respect to the

vortex's path shift. Maximum force coefficients produced by the vortex are compared with maximum force coefficients produced by an equivalent-velocity free stream to assess whether the rotational nature of the vortex produces greater structural loading than a free stream.

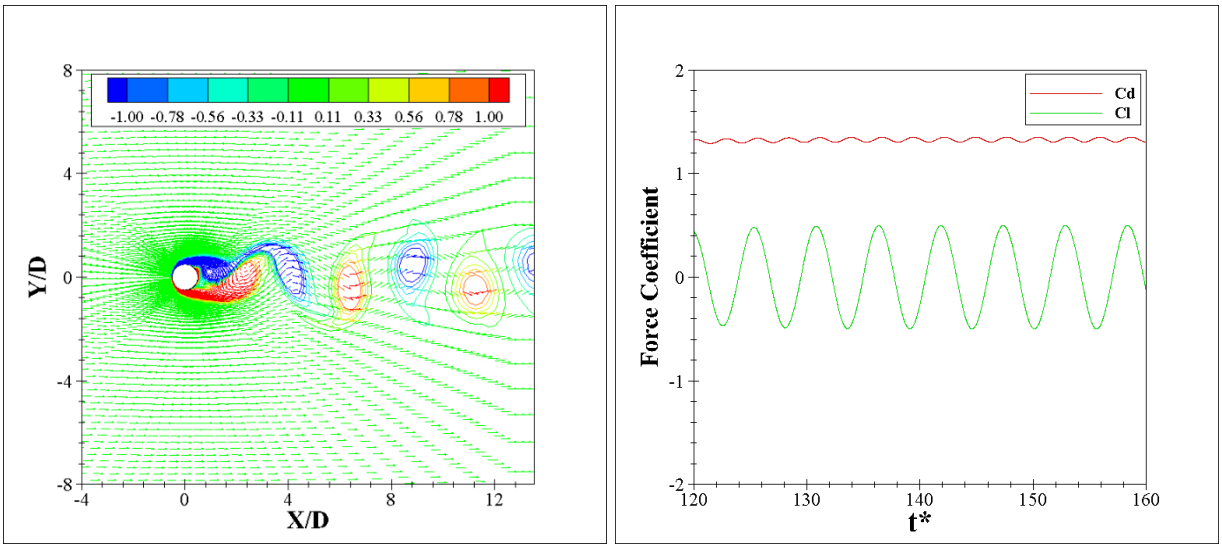
5.2 Variation in Maximum Cylinder Loading Due to Vortex Impact Time

Direct vortex impact of $r_c \leq 3 \cdot D$ vortices with a cylindrical structure is simulated to illustrate, explain, and quantify variation in structural loading amplitude when the impinging vortex directly impacts (Direct impact is illustrated in Figure 5.14b) the structure at different times. During the early stages of this study, it was observed that an $r_c = 1 \cdot D$ vortex produces different structural loading when directly impacts the structure at different times with respect to the start of the simulation. This implies that the vortex's starting position X_o (See Figure 4.1) physically influences the structural loading that the vortex produces upon impacting the structure and is a fallacious. The starting position of the vortex X_o is set sufficiently far to the left of the cylinder so that vortex shedding from the cylinder develops well before vortex impact. The relative size and strength of the vortices attached to the cylinder change continuously during vortex shedding, hence changing X_o effectively causes the impinging vortex to impact the structure at different times with respect to the vortex shedding cycle (The vortex shedding cycle is discussed in the subsequent subsection). It is postulated that interaction between the impinging vortex and different attached vortices produces the variation in structural loading when X_o is changed. The subsequent subsections develop and implement methodology to assess this postulation.

5.2.1 Methodology and Approach

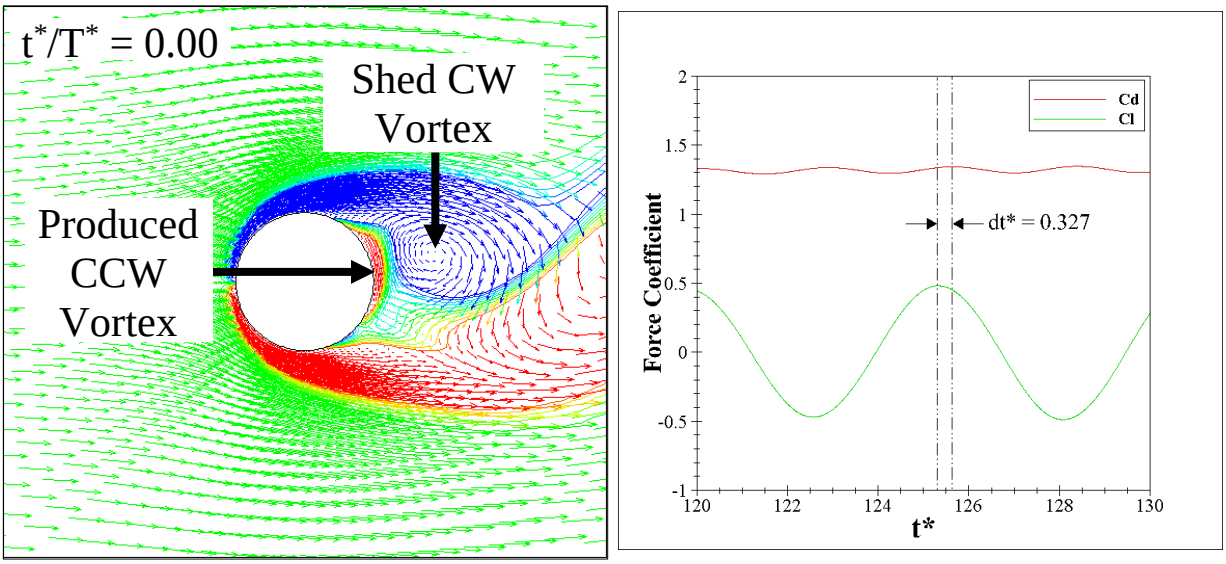
A cylinder immersed in a free stream characterized by the approximate range $47 \leq Re \leq 2 \cdot 10^{-5}$ alternately sheds clockwise (CW) and counter-clockwise (CCW) vortices from its top and

base respectively. The alternate shedding of these vortices produces harmonic cylinder loading both in the stream direction and normal to the stream direction. Figure 5.1a illustrates vortex shedding from a cylinder at Re = 150, and Figure 5.1b illustrates the resulting cylinder loading.



(a) (b)

Figure 5.1: (a) Vorticity contour and velocity vectors of free stream vortex shedding at Re = 150 and (b) corresponding drag and lift force coefficients.



(a) (b)

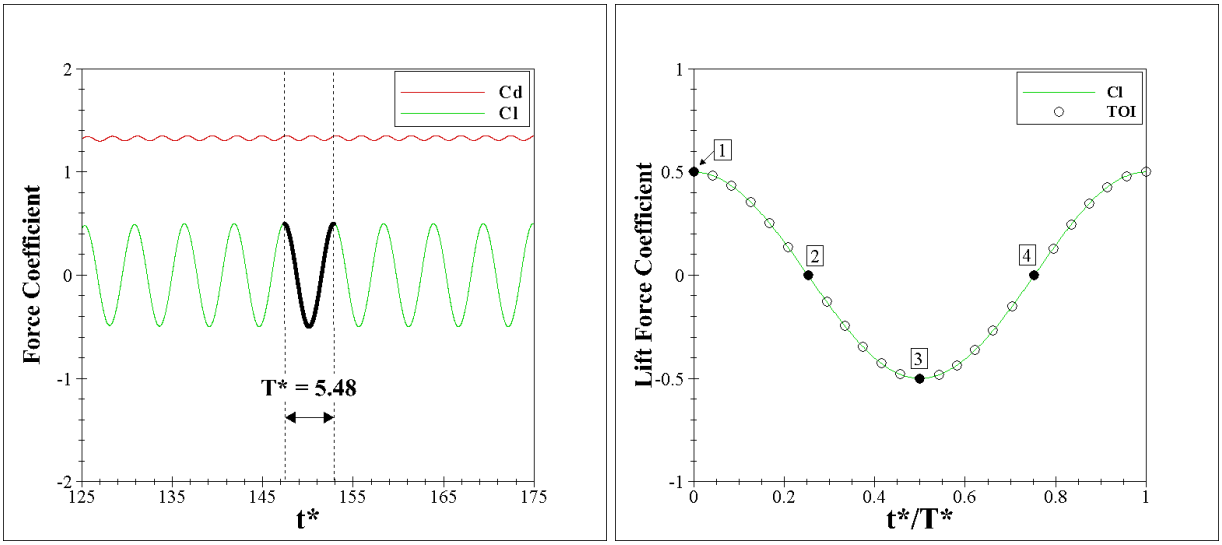
Figure 5.2: (a) Shedding of a CW vortex from the top of the cylinder and (b) illustration of the lag between maximum values of the lift and drag force coefficients.

The lift force coefficient frequency (f_{Cl}) is the frequency at which same-signed vortices are shed, and the drag force coefficient frequency is $f_{Cd} = 2 \cdot f_{Cl}$. The lift force coefficient reaches maximum positive amplitude when a CW vortex is shed from the top of the cylinder and maximum negative amplitude when a CCW vortex is shed from the base of the cylinder. The drag force coefficient reaches its maximum positive amplitude shortly after the shedding of a vortex of either sign as indicated by dt^* in Figure 5.2b. The positive amplitude peak in Cd is caused by the opposite-signed vortex produced on the downstream edge of the cylinder when a vortex of either sign is shed; this is illustrated in Figure 5.2a for the shedding of a CW vortex from the top of the cylinder.

The present study defines the vortex shedding cycle (VSC) as one period (T^*) of the lift force coefficient. The VSC begins and ends with the shedding of a CW vortex from the cylinder, and its duration is $T^* = 5.48$ for a free stream characterized by Re = 150 on Grid 1. The relative size and strength of the attached CW and CCW vortices change continuously during the VSC, and it is postulated that interaction between the impinging vortex and different attached vortices produces the variation in structure loading amplitude. It is therefore necessary to simulate vortex impact at discrete intervals throughout T^* to evaluate the variation in cylinder loading amplitude when the impinging vortex impacts at different times.

Free stream flow around an immersed cylinder is simulated, and the temporal location of a single period of the VSC is identified (See Figure 5.3a). The VSC period $T^* = 5.48$ is then discretized by assigning 25 times of vortex impact (TOI) spaced at $\Delta t^* \approx 0.23$ interval as shown in Figure 5.3b. Note that there is no scientific basis for using 25 TOI to discretize T^*, rather this number of TOI is sufficient to capture the variation in cylinder loading amplitude for the given system and parameters. The vortex starting position X_o is adjusted for each simulation so that the

vortex impacts the cylinder at each TOI. The present study defines "impact" as the instant that the leading edge of the vortex touches the leading edge of the cylinder assuming no slowing or deformation of the impinging vortex due to interaction with the cylinder's boundary layer. The greatest and least values of the drag and lift force coefficient are extracted following each simulation. These are reported as signed amplitudes (Cl'(+), Cl'(-), Cd'(+), and Cd'(-)), which are computed by subtracting the mean values of the drag and lift force coefficient for Re = 150 flow over an immersed circular cylinder (Cd,mean = 1.329 and Cl,mean = 0.0).



(a) (b)

Figure 5.3: (a) Selected period of the VSC and (b) discretization of the VSC with 25 TOI (Strasser and Selvam, 2015).

5.2.2 Maximum Force Coefficient Amplitudes

Four vortex impact times are marked by boxed numbers 1-4 in Figure 5.3b. These TOI are specifically selected to illustrate the variation in structure loading when the impinging vortex impacts the cylinder at different times in the VSC because the structure of the vortices attached to the cylinder is well understood at these times, as shall be expounded in Section 5.2.2.2. Vortex impact at TOI 1-4 is simulated, where the critical radius of the impinging vortex is $r_c = 1 \cdot D$, and the four resulting force coefficient time histories are illustrated in Figures 5.4a – 5.4d. Both the

character and maximum amplitudes of both force coefficients exhibit great variation when the impinging vortex impacts the cylinder at different times.

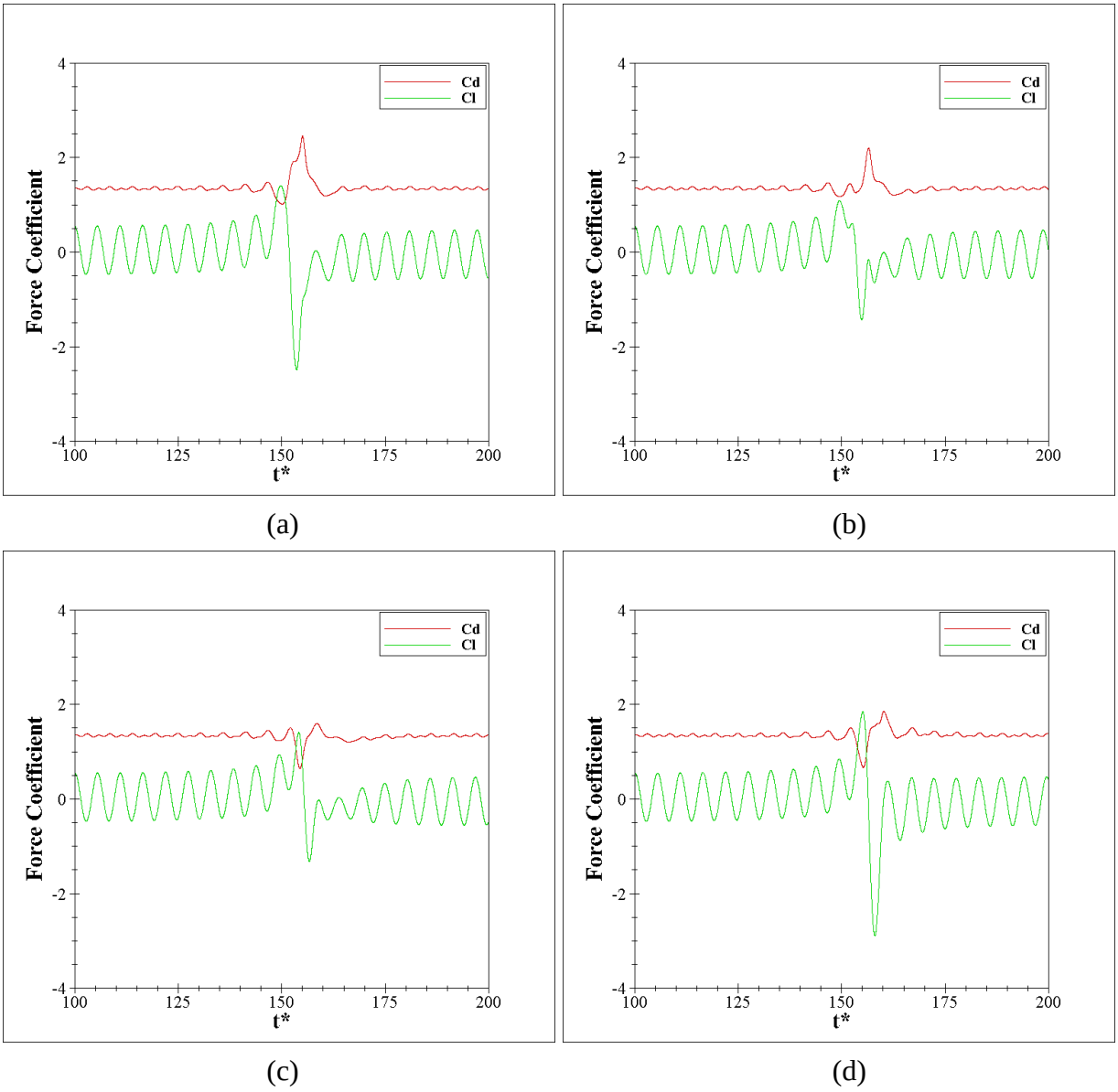
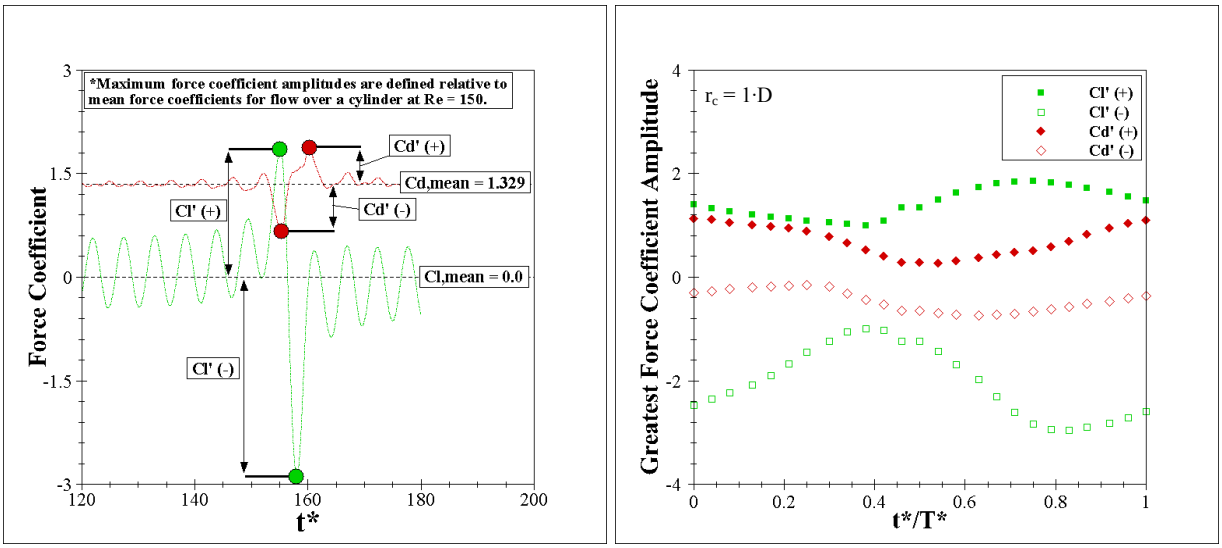


Figure 5.4: Force coefficient time histories for impinging vortex of radius r_c = 1·D impacting the cylinder at (a) TOI 1, (b) TOI 2, (c) TOI 3, and (d) TOI 4 (Strasser and Selvam, 2015).

Now, the starting position of the impinging vortex is adjusted for each simulation so that the vortex impacts the cylinder at the 25 TOI defined in Figure 5.3b. Maximum force coefficient amplitudes are extracted from each force coefficient time history as illustrated in Figure 5.5a following each simulation and summarized in Figure 5.5b. The curves of maximum force

coefficient amplitudes in Figure 5.5b are smooth and continuous. The curves are smooth because the attached vortex structure changes continuously rather than abruptly throughout the VSC. The continuous nature of the curves confirms that the 25 TOI used to discretize the VSC provide sufficient resolution to capture the variation in cylinder loading with vortex impact time.



(a) (b)

Figure 5.5: (a) Extraction of signed amplitudes from a typical force coefficient time history and (b) summary of signed amplitudes for impinging vortex impact at 25 TOI (Strasser and Selvam, 2015).

The greatest and least values of each of the four signed force coefficient amplitudes from Figure 5.5b are tabulated and compared in Table 5.1. The maximum underprediction (UP) of the greatest amplitude by the least amplitude is computed and also reported in Table 5.1.

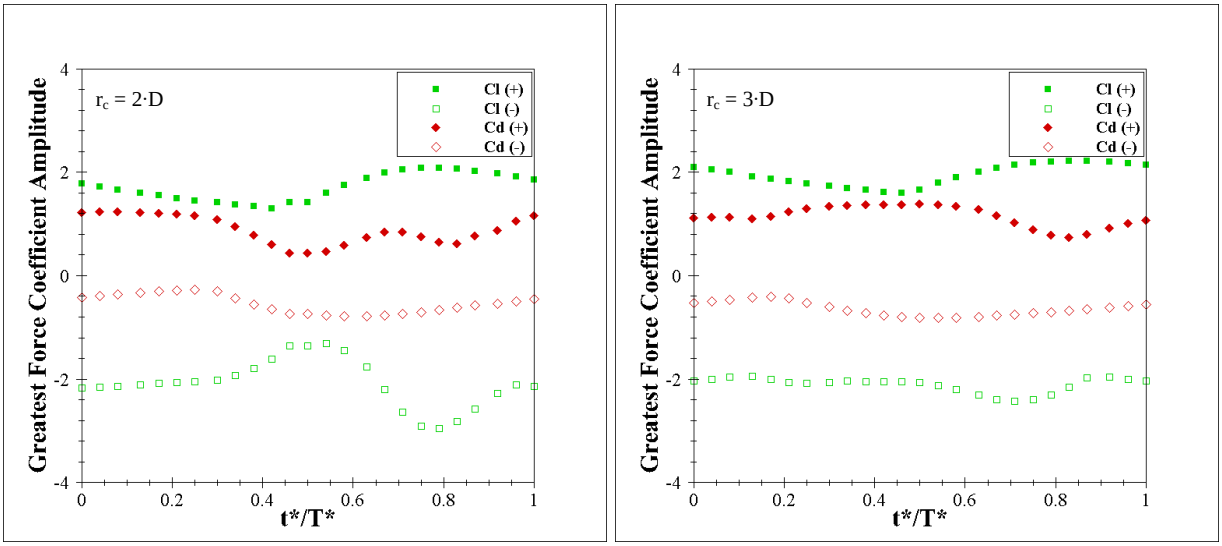
Table 5.1: Greatest and least maximum force coefficient amplitudes for impinging vortex of radius $r_c = 1 \cdot D$ impacting the cylinder at 25 TOI (Illustrated in Figure 5.5a).

	Maximum Force Coefficient Amplitudes From 25 Simulations			
	Cl' (+)	Cl' (-)	Cd' (+)	Cd' (-)
Greatest	1.851	-2.952	1.128	-0.735
Least	1.000	-0.994	0.275	-0.145
UP	84.99%	197.04%	310.42%	407.15%

*Underprediction: UP = (Greatest/Least – 1.0)·100%

UP quantifies the possible error that may be present if maximum force coefficient amplitudes from only a single simulation are considered. Gross under-prediction of the maximum force coefficients may occur if variation in cylinder loading amplitude with vortex impact time is neglected.

Now the preceding methodology, specifically using 25 TOI to define the curves of maximum force coefficient amplitudes for vortex impact at any time in the VSC, is repeated for impinging vortex critical radii of $r_c = 2 \cdot D$ and $3 \cdot D$. Recall that the maximum vortex tangential velocity $V_{\theta,max}$ remains fixed as the vortex size increases. Resulting curves of the maximum force coefficient amplitudes for critical radii of $r_c = 2 \cdot D$ and $3 \cdot D$ are respectively summarized in Figures 5.6a and 5.6b. Qualitative comparison of the maximum force coefficient amplitude curves for impinging vortex radii of $1 \cdot D$ to $3 \cdot D$ (Figure 5.5b and Figures 5.6a and 5.6b), shows that the variation in maximum force coefficient amplitude decreases rapidly as the size of the impinging vortex increases.



(a) (b)

Figure 5.6: Maximum force coefficient amplitudes for impinging vortex impact at 25 TOI for impinging vortex radii of (a) $2 \cdot D$ and (b) $3 \cdot D$ (Strasser and Selvam, 2015).

Table 5.2 quantifies the Variation in maximum force coefficient amplitude with vortex impact time by reporting the mean and mean-normalized standard deviation (NSD) for each maximum force coefficient amplitude curve. Mean maximum force coefficient amplitudes consistently increase with increasing vortex size. This is because increased cylinder surface area is exposed to high tangential velocity as the impinging vortex size increases; therefore, the amplitude of cylinder loading increases as well.

Table 5.2: Mean and mean-normalized standard deviation of maximum force coefficient amplitude curves for impinging vortex critical radii of 1·D to 3·D.

	Maximum Force Coefficient Amplitudes from 25 Simulations			
Vortex Radius	Cl (+)	Cl (-)	Cd (+)	Cd (-)
	Mean Values			
1·D	1.432	-2.030	0.707	-0.459
2·D	1.710	-2.083	0.886	-0.548
3·D	1.949	-2.109	1.150	-0.647
	Mean-Normalized St. Deviation			
	20.34%	33.44%	42.75%	45.90%
	15.62%	22.12%	31.30%	32.96%
	11.09%	6.91%	17.86%	20.91%

The NSD in maximum force coefficient amplitude curves progressively decreases as the impinging vortex size increases. Decreased variation in cylinder loading amplitude with vortex impact time implies that the interaction between the impinging and attached vortices has increasingly-less influence on the cylinder loading amplitude as the impinging vortex size increases. This is because the larger impinging vortex exerts greater influence on the flow over the cylinder prior to impacting it. The impinging vortex increasingly disrupts and then controls vortex shedding from the cylinder prior to impacting it. As the impinging vortex size is continually increased, it controls vortex shedding from the cylinder prior to impacting it, meaning the vortex impact time with respect to the original vortex shedding cycle no longer

influences the cylinder loading amplitude. Consequently, any starting position of the vortex will produce the same cylinder loading amplitude.

Table 5.3 summarizes the greatest and least values of the maximum force coefficient amplitudes for impinging vortex radii of 1·D to 3·D. The greatest underprediction of all maximum force coefficient amplitudes progressively decreases as the impinging vortex size increases, supporting the prior finding that the variation in maximum cylinder loading amplitude with vortex impact time rapidly decreases as impinging vortex size increases. However, underprediction, especially for the drag force coefficient's signed amplitudes, is still substantial when the vortex critical radius is 3·D.

Table 5.3: Summary of greatest and least maximum force coefficient amplitudes for impinging vortex radii of 1·D to 3·D.

	Maximum Force Coefficient Amplitudes from 25 Simulations			
Vortex Radius	Cl (+)	Cl (-)	Cd (+)	Cd (-)
	Greatest Value			
1·D	1.851	-2.952	1.128	-0.735
2·D	2.085	-2.954	1.243	-0.784
3·D	2.214	-2.431	1.380	-0.817
	Least Value			
	1.000	-0.994	0.275	-0.145
	1.303	-1.319	0.433	-0.267
	1.591	-1.947	0.740	-0.401
	Greatest Under-Prediction			
	84.99%	197.04%	310.42%	407.15%
	59.94%	123.94%	186.85%	193.74%
	39.15%	24.84%	86.54%	103.64%

*Underprediction: UP = (Greatest/Least – 1.0)·100%.

5.2.3 Visualization of the Interaction between Impinging and Attached Vortices

Impact of an r_c = 1·D vortex at TOI 1-4 is used to illustrate interaction between the impinging and attached vortices when the impinging vortex impacts the cylinder at different

times in the VSC. TOI 1-4 are selected for illustration of the interaction between vortices because the structure of the vortices attached to the cylinder due to the free stream are well

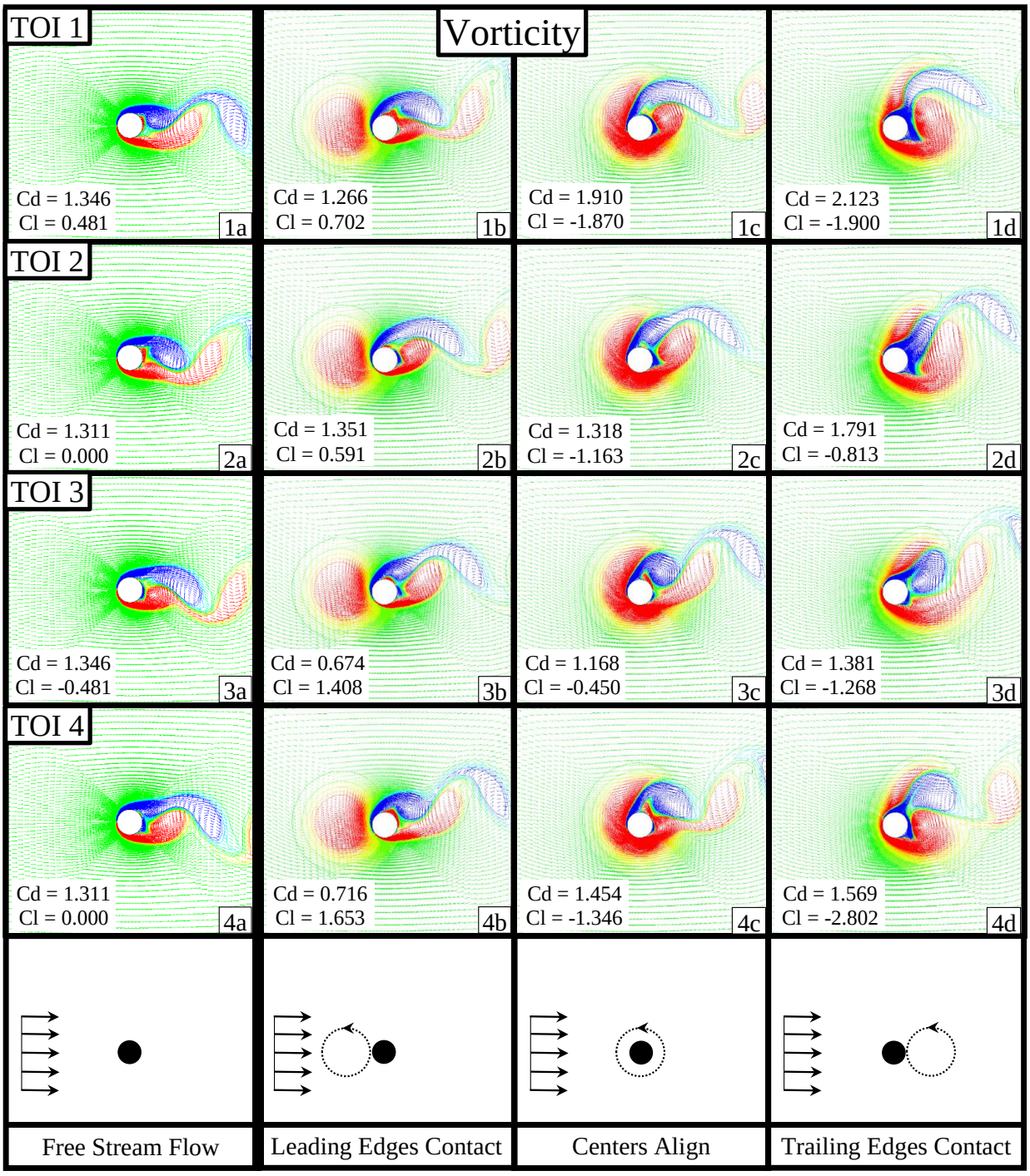


Figure 5.7: Vorticity contours and velocity vectors at TOI 1-4 (by row) for free stream flow over the cylinder (column a) and for the three relative positions of the vortex to the cylinder illustrated in row 5 (columns b-d) (Strasser and Selvam, 2015).

understood. Qualitative description of the attached vortex structure at TOI 1-4 is listed in bullet format below; rows 1-4 of column "a" in Figure 5.7 illustrate corresponding vorticity contours.

- TOI 1 – CW vortex is just shed. (CW – Largest, CCW – Small).
- TOI 2 – $T^*/4$ from the shedding of a CCW vortex. (CW – Smallest, CCW – Large).
- TOI 3 – CCW vortex is just shed. (CW – Small, CCW – Largest).
- TOI 4 - $T^*/4$ from the shedding of a CW vortex. (CW – Large, CCW – Smallest).

Figure 5.7 illustrates the vorticity field surrounding the cylinder for impinging vortex impact at TOI 1-4. Rows 1-4 represent TOI 1-4, and columns b-d correspond to the three "expected" relative positions of the vortex to the cylinder illustrated by the schematics in row 5. The contours are said to illustrate "expected" relative positions of the vortex with respect to the cylinder because it is assumed that the impinging vortex continues to translate at U_∞ throughout interaction with the cylinder. Instantaneous values of Cd and Cl are provided in the lower-left corner of each figure. The visualization in Figure 5.7 is used to discuss two significant forms of inter-vortex interaction, which is interaction between the impinging vortex and those attached to the cylinder. Specifically, the impinging vortex alters the positions of the vortices attached to the cylinder, and the impinging vortex delays the vortex shedding cycle.

5.2.3.1 Observed Interaction between Impinging and Attached Vortices

The free stream flowing over the cylinder develops CW and CCW vortices at the top and base of the cylinder, respectively, which are shed alternately as illustrated in column "a" of Figure 5.7. As the impinging CCW vortex approaches the cylinder, its tangential velocity alters the velocity of the stream over the cylinder. Consequently, the attached vortices are rotated CCW around the cylinder as shown in the column "b" of Figure 5.7. The attached CW and CCW vortices now partially occupy the upstream and downstream edges of the cylinder respectively.

The net strength of these attached vortices controls the amplitude of Cd, as shall be discussed shortly.

The impinging vortex delays the vortex shedding cycle by approximately $T^*/4$ in addition to shifting the positions of the vortices attached to the cylinder. This is seen when comparing the similarity of the vortices attached to the cylinder in Figures 5.7(1a) and 5.7(4b) and those in Figures 5.7(3a) and 5.7(2b). Therefore, the structure of the attached vortices when the impinging vortex impacts at TOI 1-4 is actually:

- TOI 1 – $T^*/4$ from the shedding of a CCW vortex. (CW – Smallest, CCW – Large).
- TOI 2 – CCW vortex is just shed. (CW – Small, CCW – Largest).
- TOI 3 - $T^*/4$ from the shedding of a CW vortex. (CW – Large, CCW – Smallest).
- TOI 4 – CW vortex is just shed. (CW – Largest, CCW – Small).

The attached vortices illustrated in column "b" of Figure 5.7 are noticeably larger than those in column "a". It is postulated that the delay of the vortex shedding cycle and the increased stream velocity over the cylinder (due to the impinging vortex's tangential velocity) cause the attached vortices to grow larger, thus they exert greater loading on the cylinder.

5.2.3.2 Influence of Impinging-Attached Vortex Interaction on Cylinder Loading

Discussion shall focus on inter-vortex interaction producing large force coefficient amplitudes. Interaction scenarios producing small amplitudes can be inferred but are omitted to avoid redundancy. It is convenient to begin discussion with Cd. A vortex is a low pressure region, hence, the attached vortices pull the cylinder towards themselves. The amplitude of the force on the cylinder is the net force produced by the two vortices, and the sign of the amplitude is in the direction of the larger attached vortex.

The attached CW and CCW vortices are rotated to partially occupy the upstream and downstream surfaces of the cylinder, respectively, as the impinging vortex approaches. One of the attached vortices is always larger than the other. A larger CW vortex produces high Cd'(-), while a larger CCW vortex results in high Cd'(+). Time histories in Figures 5.4a – 5.4d show that vortex impact at TOI 1 and 2 produce large Cd'(+) while impact at TOI 3 and 4 produce large Cd(-). It is now known that the VSC is delayed $T^*/4$ by the impinging vortex. Therefore, the structures of attached vortices (defined in the second set of bullet points) that produce large Cd'(+) and Cd'(-) are as expected.

The largest values of Cl'(+) and Cl'(-) occur when the impinging vortex impacts at TOI 4 (Figure 5.4d) as a CW vortex is being shed. The occurrence of the large value of Cl'(+) is expected, as the attached CW vortex is at its largest size, and therefore, exerts maximum pull along the top surface of the cylinder. In addition to exerting this pull, the large CW vortex shifts the path of the impinging vortex. In the absence of attached vortices, the impinging vortex will engulf the cylinder, simultaneously producing similar pull along the top and base of the cylinder. However, the large CW vortex that is now shifted towards the upstream edge of the cylinder interacts with and resists the impinging vortex. The path of the impinging vortex is shifted downward, and it merges with the attached CCW vortex attached to the base of the cylinder. The merged and now-large CCW vortex exerts a strong downward pull along the base of the cylinder, causing the large Cl'(-).

5.2.4 Summary of Interaction between Impinging and Attached Vortices

The interaction between impinging and attached vortices responsible for the variation in the maximum force coefficient amplitude with vortex TOI is attributed to two factors. For impinging vortex radius $r_c = 1 \cdot D$, the free stream VSC is delayed by $T^*/4$ as the impinging vortex

approaches the cylinder. The attached vortices enlarge during the delayed shedding. Cd'(+) and Cd'(-) are large if the attached CW and CCW vortices (respectively) are large when the impinging vortex impacts. Cl'(+) and Cl'(-) are both large if the attached CW vortex is large when the impinging vortex impacts.

The preceding discussion of interaction of shed and impinging vortices is only directly applicable to a system having the same parameters. Any number of parameters may influence the interaction: Reynolds number, impinging vortex size, maximum velocity of the impinging vortex relative to bulk velocity, etc. However, the phenomenon has been identified and explained, and the procedure and methodology developed herein can be applied to study any vortex-structure system.

5.3 Influence of Relative Vortex-to-Cylinder Size on Cylinder Loading

Section 5.3 utilizes Grid 2 to study the influence of the relative vortex-to-cylinder size on the resulting cylinder loading amplitude. The impinging vortex critical radius is incremented from 1·D to 100·D while the maximum vortex tangential velocity $V_{\theta,max}$ is fixed, and the trend in maximum cylinder loading amplitude is documented. Additionally, the influence of impinging vortex critical radius on the variation in cylinder loading with vortex impact time (Discussed in Section 5.2) is evaluated. The study performed herein specifically identifies the vortex core radii for which vortex impact time ceases to influence the maximum cylinder loading amplitude and the maximum cylinder loading amplitude becomes asymptotic, meaning subsequent increase of the critical radius does not influence the maximum cylinder loading amplitude. The phenomenon controlling the convergence of maximum force coefficient amplitudes to asymptotic values are then illustrated and explained.

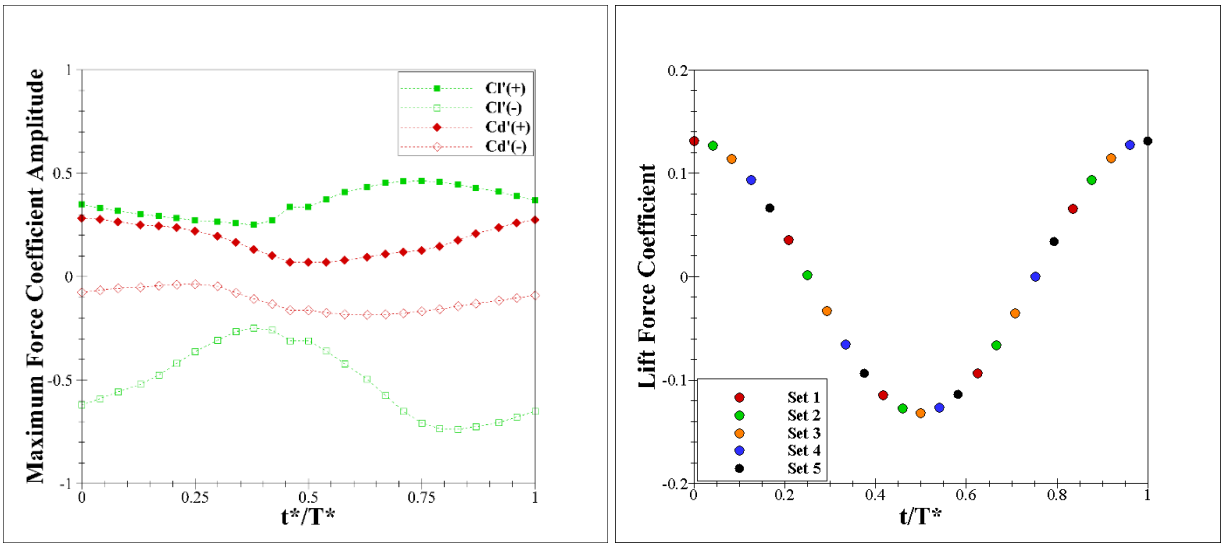
5.3.1 Methodology and Approach

Section 5.2 demonstrates that different impinging vortex impact times with respect to the free stream vortex shedding cycle produce variation in the resulting maximum cylinder loading amplitude. The forthcoming study accounts for this variation by presenting mean values of the maximum force coefficient amplitudes as well as maximum and minimum values of each maximum force coefficient amplitude for each impinging vortex size. The previous study in Section 5.2 utilizes twenty-five vortex impact times to define mean values for the maximum force coefficient amplitudes for impinging vortex critical radii of 1·D to 3·D. The forthcoming study spans critical radii of 1·D to 100·D, and it is not feasible to perform so twenty-five computer simulations for each impinging vortex size. Fortunately, an alternative procedure for computing the mean values of the maximum force coefficient amplitudes is developed as shall be discussed subsequently.

Through iterative investigation, which is basically a guess-and-check approach, it has been found that mean values for the maximum force coefficient amplitudes can be computed using five simulated vortex impacts spaced at $\Delta t^* = 1$ interval rather than twenty-five simulated vortex impacts spaced at $\Delta t^* = 0.23$ interval. Additionally, the first of the five impacts need not start at the beginning of the VSC, but rather may be an arbitrary time. Validation of the use of five versus twenty-five simulated vortex impacts to define the mean values of the maximum force coefficient amplitudes is demonstrated subsequently.

Maximum force coefficient amplitude curves for impinging vortex core radius $r_c = 1 \cdot D$ impacting the cylinder at twenty-five discrete times during one vortex shedding cycle, which are defined previously in Figure 5.5b, are re-dimensioned using reference velocity of two and illustrated in Figure 5.8a. The maximum force coefficient amplitudes are now separated into five

groups spaced at approximately $\Delta t^* = 1$ interval as indicated by colored circles in Figure 5.8b. Mean values for the maximum force coefficient amplitudes are computed using each of the five data sets and also using all twenty-five TOI as a single data set; summary and comparison of the six mean maximum force coefficient sets is provided in Table 5.4.



(a) (b)

Figure 5.8: (a) Maximum force coefficient amplitudes for impinging vortex ($r_c = 1 \cdot D$) impact at 25 TOI and (b) Separation of 25 TOI into 5 sets of 5.

Table 5.4: Comparison of mean maximum force coefficient amplitudes computed with 5 sets of 5 TOI with mean maximum force coefficient amplitudes computed using all 25 TOI as a set.

Mean Values				
Set	**Cl'**		**Cd'**	
	(+)	**(-)**	**(+)**	**(-)**
1	0.356	-0.506	0.178	-0.116
2	0.364	-0.513	0.177	-0.115
3	0.357	-0.506	0.178	-0.112
4	0.357	-0.506	0.175	-0.115
5	0.355	-0.506	0.176	-0.116
All (25)	0.358	-0.508	0.177	-0.115
Max Error	1.67%	1.05%	0.81%	1.15%

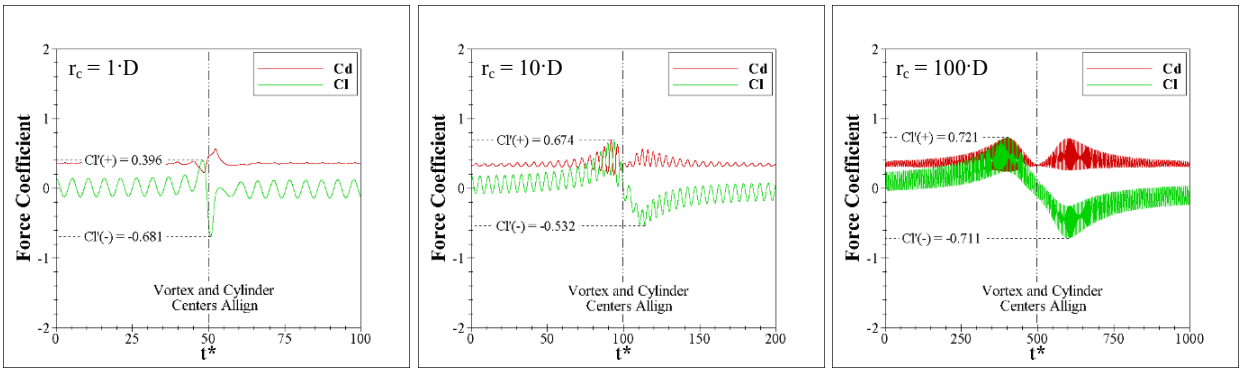
Mean maximum force coefficient amplitudes computed using the 5-TOI data sets are within 1.67% of means computed using all 25 TOI as a data set. This error is small, and the

accuracy of the 5-TOI approximation is sufficient for the present study. Note that all five of the 5-TOI groups yield practically the same mean maximum force coefficient amplitudes. This demonstrates that regardless of the time (t^*) that the first vortex impact occurs, four subsequent impacts spaced at $\Delta t^* \approx 1$ interval are sufficient to establish the mean values of the maximum force coefficient amplitudes.

A procedure has been established to document the trend in maximum cylinder loading amplitude with impinging vortex-to-cylinder size. Specifically, mean values of the maximum cylinder loading amplitude shall be computed from five simulated vortex impacts where the vortex impact time is progressively incremented by $\Delta t^* = 1$ between simulations. In addition to the mean values of the maximum force coefficient amplitudes, the greatest and least values of each amplitude from the five simulations shall be reported as envelopes to the mean values. This allows the influence of the impinging vortex size on the variation on cylinder loading with time of vortex impact to be documented as well.

5.3.2 Trend in Maximum Cylinder Loading with Impinging Vortex Size

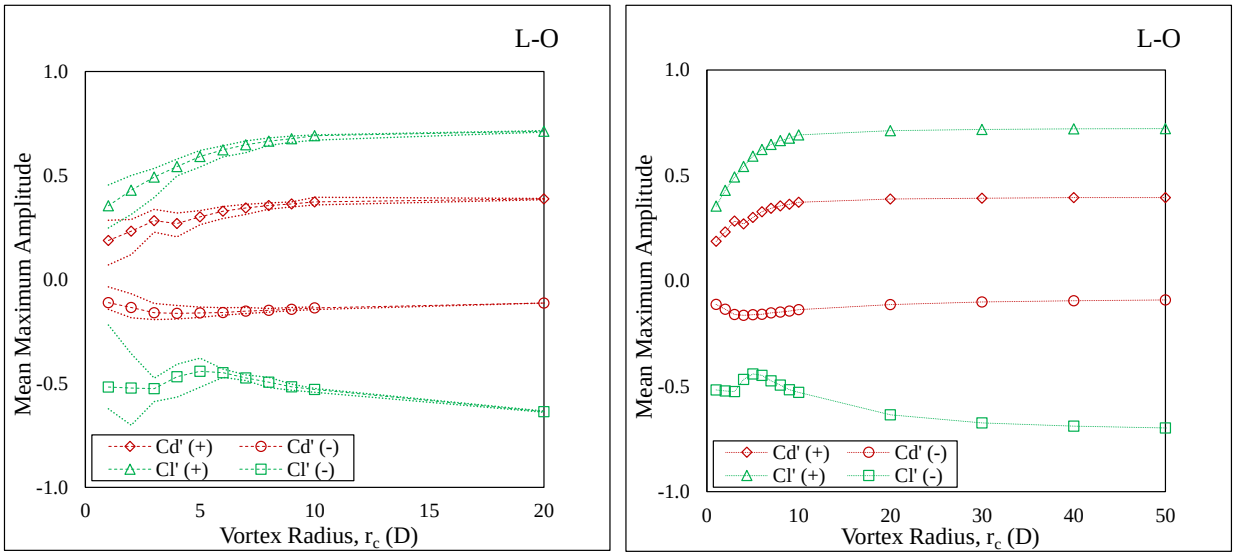
The critical radius of the impinging vortex is incremented from $r_c = 1 \cdot D$ to $100 \cdot D$, and five computer simulations are used to compute mean values for the maximum force coefficient amplitude for each impinging vortex size. Typical force coefficient time histories produced by impinging vortices having critical radii of $r_c = 1 \cdot D$, $10 \cdot D$, and $100 \cdot D$ are illustrated in Figures 5.9a – 5.9c. Generally speaking, the cylinder loading transitions from pulse-like to symmetric.



(a) (b) (c)

Figure 5.9: Typical time histories for impinging vortex radii (a) 1·D, (b) 10·D, and (c) 100·D.

Figures 5.10a and 5.10b summarize the mean maximum force coefficient amplitudes, as well as the variation therein due to vortex impact time, for impinging vortex critical radii of r_c = 1·D to 50·D. Simulations for critical radii of up to 100·D have been conducted but are not reported herein because maximum force coefficient amplitudes reach asymptotic values for impinging vortex critical radio of approximately 50·D. Envelopes in Figure 5.10a mark the greatest and least values of each maximum force coefficient amplitude from the five computer simulations and illustrate the variation therein with vortex impact time.



(a) (b)

Figure 5.10: Mean maximum force coefficient amplitudes from five simulations (envelopes mark the variation with vortex impact time) (a) for $1 \leq r_c/D \leq 20$ and (b) for $1 \leq r_c/D \leq 50$.

The envelopes bounding the mean values of the maximum force coefficient amplitudes in Figure 5.10a narrow rapidly as the impinging vortex size increases. This narrowing is quantified using Cl'(-), for which the difference in the greatest and least amplitudes falls from 183.60% to 36.99% to 3.47% for impinging vortex radii of 1·D, 5·D, and 10·D respectively. The difference in the greatest and least values for all maximum force coefficient amplitudes is less thant 1.5% for impinging vortices larger than $r_c = 20 \cdot D$. Diminishing variation in cylinder loading amplitude with vortex impact time implies that the impinging vortex controls vortex shedding from the cylinder prior to impacting it. Consequently the vortex impact time with respect to the free stream vortex shedding cycle is no longer influences the cylinder loading amplitude.

The preceding study, which was conducted using the L-O vortex profile, is now repeated using the RCVM and S-K vortex profiles; Figures 5.11a – 5.11d summarize the study findings. Once again, the variation in the maximum force coefficient amplitudes with vortex impact time decays rapidly as the size of the impinging vortex is increased as shown in Figures 5.11a and 5.11c. The maximum force coefficient amplitude mean values for the RCVM and S-K vortex profiles converge to asymptotic values more slowly (Figure 5.11a) and more quickly (Figure 5.11b), respectively, than do the mean maximum force coefficient amplitudes for the L-O vortex profile (Figure 5.10b). The amplitudes produced by the RCVM profile converge more slowly because the TVP is sharper, hence the vortex must be larger to effectively expose the cylinder surface to the maximum tangential velocity. Conversely, the S-K profile's amplitudes become asymptotic more rapidly than the amplitudes from the L-O profile because the S-K profile is flatter and effectively exposes the cylinder surface to the maximum tangential velocity at a smaller size.

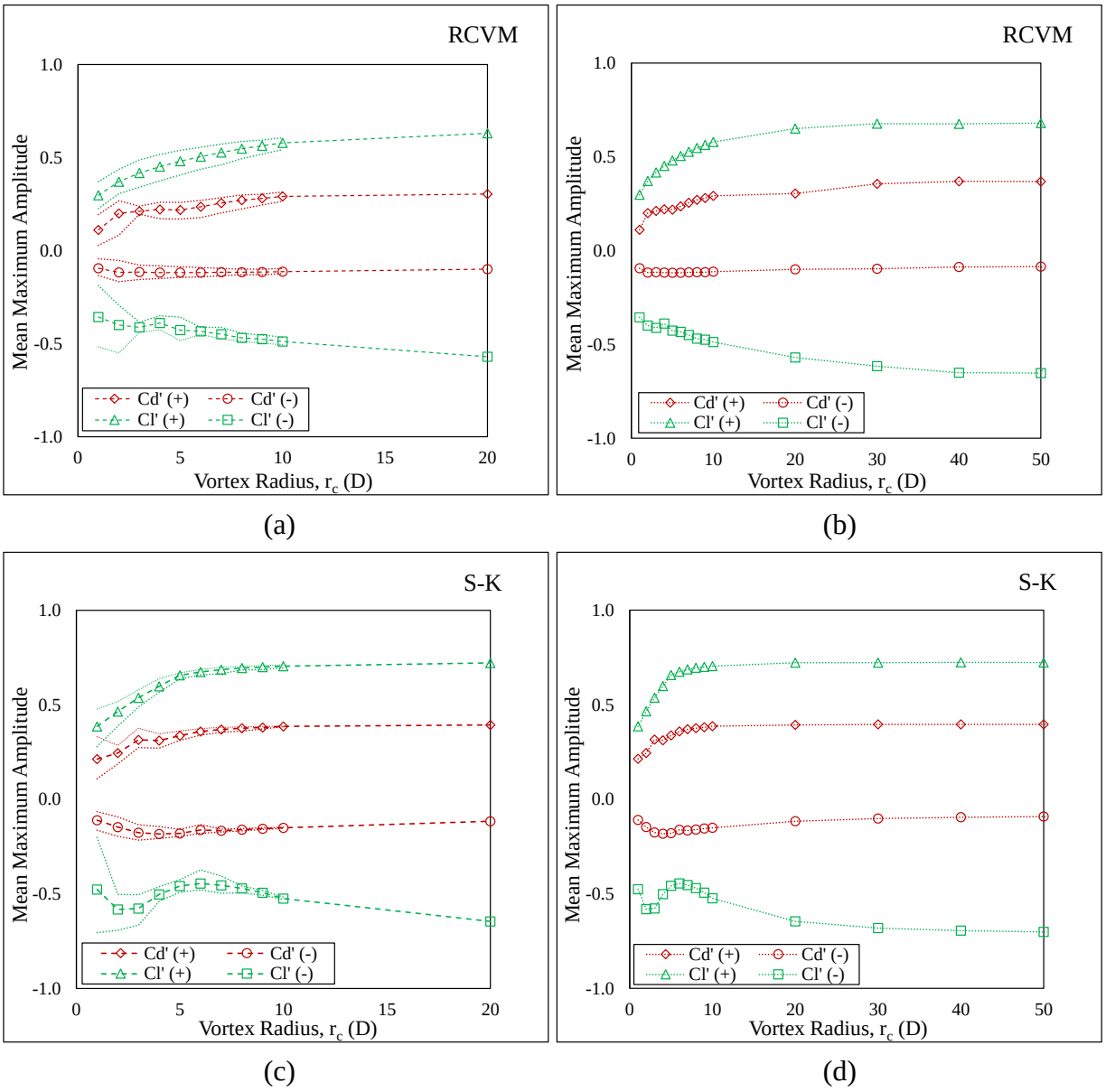


Figure 5.11: Mean maximum force coefficients and envelopes as function of impinging vortex size for (a-b) RCVM and (c-d) S-K vortex tangential velocity profiles.

Table 5.5 summarizes the asymptotic maximum force coefficient amplitudes for all three impinging vortex profiles. The maximum amplitudes are relatively similar, with the maximum difference in amplitudes computed using different profiles is less than 7.0%. Generally speaking, the maximum amplitude of all force coefficients progressively increases as the vortex TVP transitions from the sharper RCVM profile to the flatter S-K profile.

Table 5.5: Summary of asymptotic maximum force coefficient amplitudes for RCVM, L-O, and S-K vortex tangential velocity profiles.

TVP	Cd		Cl	
	(+)	(-)	(+)	(-)
RCVM	0.368	-0.085	0.679	-0.652
L-O	0.394	-0.091	0.721	-0.698
S-K	0.396	-0.091	0.723	-0.701

Prior to preceding, it is stressed that the proceeding conclusions regarding the influence of the impinging vortex size on variation in maximum force coefficient amplitude with vortex impact time and convergence of maximum force coefficient amplitudes to asymptotic values are only directly apply to the considered case where $V_{\theta,max} = \alpha \cdot r_c = 1$. Increasing α increases the sharpness of the vortex profile, and increasing the ratio $V_{\theta,max}/U_\infty$ results in the vortex having greater control over vortex shedding from the cylinder prior to impacting it at a smaller size. Consequently, it is likely that maximum force coefficient amplitudes produced by vortices having high $V_{\theta,max}/U_\infty$ will become independent of vortex impact time with respect to the free stream VSC at smaller sizes. This is simply a postulation, but the reader as well as subsequent investigators of these topics should at least be aware of how varying system parameters may influence the previously-stated conclusions.

Figures 5.10b, 5.11b, and 5.11d illustrate convergence of mean maximum force coefficient amplitudes to asymptotic values as the vortex's critical radius is increased. Cl'(+) and Cl'(-) are the first and last, respectively, to reach their asymptotic values. Figures 5.9a – 5.9c show that Cl'(+) and Cl'(-) occur prior to and after the vortex and cylinder centers align. More specifically, Cl'(+) and Cl'(-) occur when the cylinder falls within the leading and trailing edges of the vortex respectively. Figures 5.12a and 5.12c respectively illustrate the relative position of the vortex to the cylinder at these times. The vortex's tangential velocity produces maximum uppward and downward velocity to the cylinder surface, producing the maximum postive and

negative Cl amplitudes. The temporal order, Cl'(+) then Cl'(-), is set by the rotational direction of the impinging vortex which is counter-clockwise (CCW) in the present study.

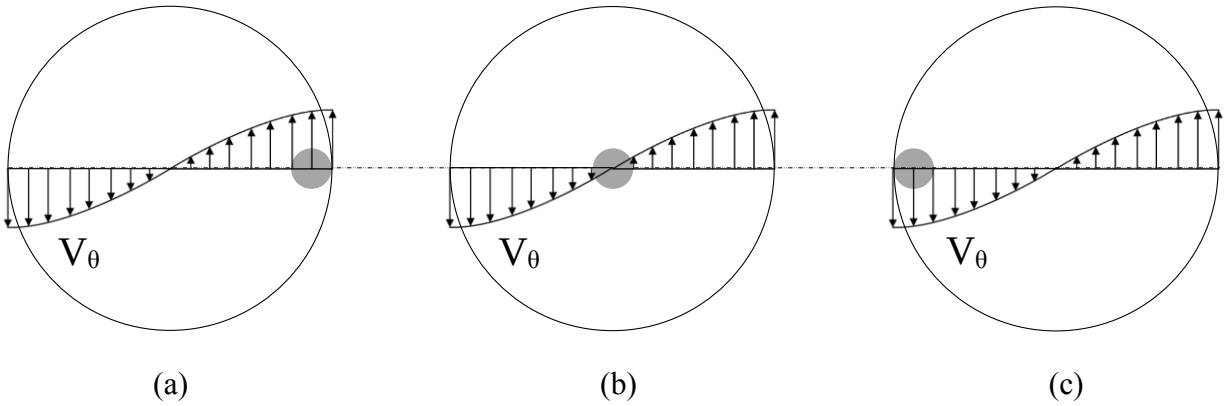


Figure 5.12: Schematic of the cylinder (a) within the leading edge of the vortex, (b) alligning with the vortex center, and (c) within the trailing edge of the vortex.

As the vortex size is increased, the tangential velocity gradient across the cylinder surface ($\Delta V_\theta/D$) decreases. The positive lift force coefficient maximum amplitude Cl'(+), Cd'(+), and Cd'(-) reach asymptotic values for $r_c \geq 20 \cdot D$; however, Cl'(-) does not reach its asymptotic value until $r_c \geq 50 \cdot D$. It is generally concluded that the convergence of Cl'(+), Cd'(+), and Cd'(-) occurs when $\Delta V_\theta/D$ becomes sufficiently small. Cl'(-) requires a larger impinging vortex to reach its asymptotic value because the impinging vortex must be sufficiently large to allow the cylinder's wake to rotate smoothly and without disruption, as shall be illustrated and discussed in the subsequent section.

5.3.3 Visualization of Cylinder Loading Trend with Increasing Vortex Size

Vorticity contour plots in Figure 5.13 correspond to the force coefficient time histories in Figures 5.10a – 5.10c. Rows (1-3) correspond to impinging vortex radii of 1·D, 10·D, and 100·D, and columns (a-c) correspond to the three "expected" relative positions of the vortex to the cylinder that are illustrated by the schematics in row 4.

When $r_c = 1 \cdot D$, the impinging vortex impacts the cylinder, merges with the CCW vortex attached to the base of the cylinder, and is then shed in the cylinder's wake (Figures 5.13.1a-5.13.1c). The position of the attached vortices is rotated CCW by the impinging vortex, but the cylinder's wake remains horizontal. Vortices shed in the cylinder's wake travel in the direction of the stream over the cylinder, hence, it is evident that the $r_c = 1 \cdot D$ vortex does not significantly alter vortex shedding from the cylinder prior to impact. The time with respect to the free stream vortex shedding cycle when the impinging vortex impacts the cylinder is significant because the impinging vortex does not control vortex shedding prior to impacting the cylinder hence the structure of the attached vortices will be different for impact at different times.

When r_c is increased to $10 \cdot D$, the cylinder's wake is shifted significantly CCW as the impinging vortex approaches the cylinder (Figure 5.13.2a). The time that the vortex impacts the cylinder with respect to the free stream vortex shedding cycle has little influence on the maximum force coefficient amplitudes because r_c is sufficiently large for the impinging vortex to control the vortex shedding cycle prior to impacting the cylinder. When the vortex engulfs the cylinder and the cylinder's wake, the velocity gradient within the vortex disrupts the wake (Figure 5.13.2b). The trailing edge of the vortex is distorted significantly due to interaction with the disrupted wake as shown in Figure 5.13.2c. Distortion of the trailing edge of the vortex is the reason Cl'(-) converges later than the other maximum force coefficient amplitudes.

Finally, when r_c is $100 \cdot D$, the velocity gradient within the vortex is sufficiently small so that the direction of the wake is gradually shifted without disruption (Figures 5.13.3a – 5.13.4c). The vortex is not disrupted by the wake, therefore, Cl'(-) reaches its asymptotic value. The cylinder's wake is shifted 45° CCW and clockwise (CW) when the cylinder is within the leading (Figure 5.13.3a) and trailing (Figure 5.13.3c) edges of the vortex respectively. This is because

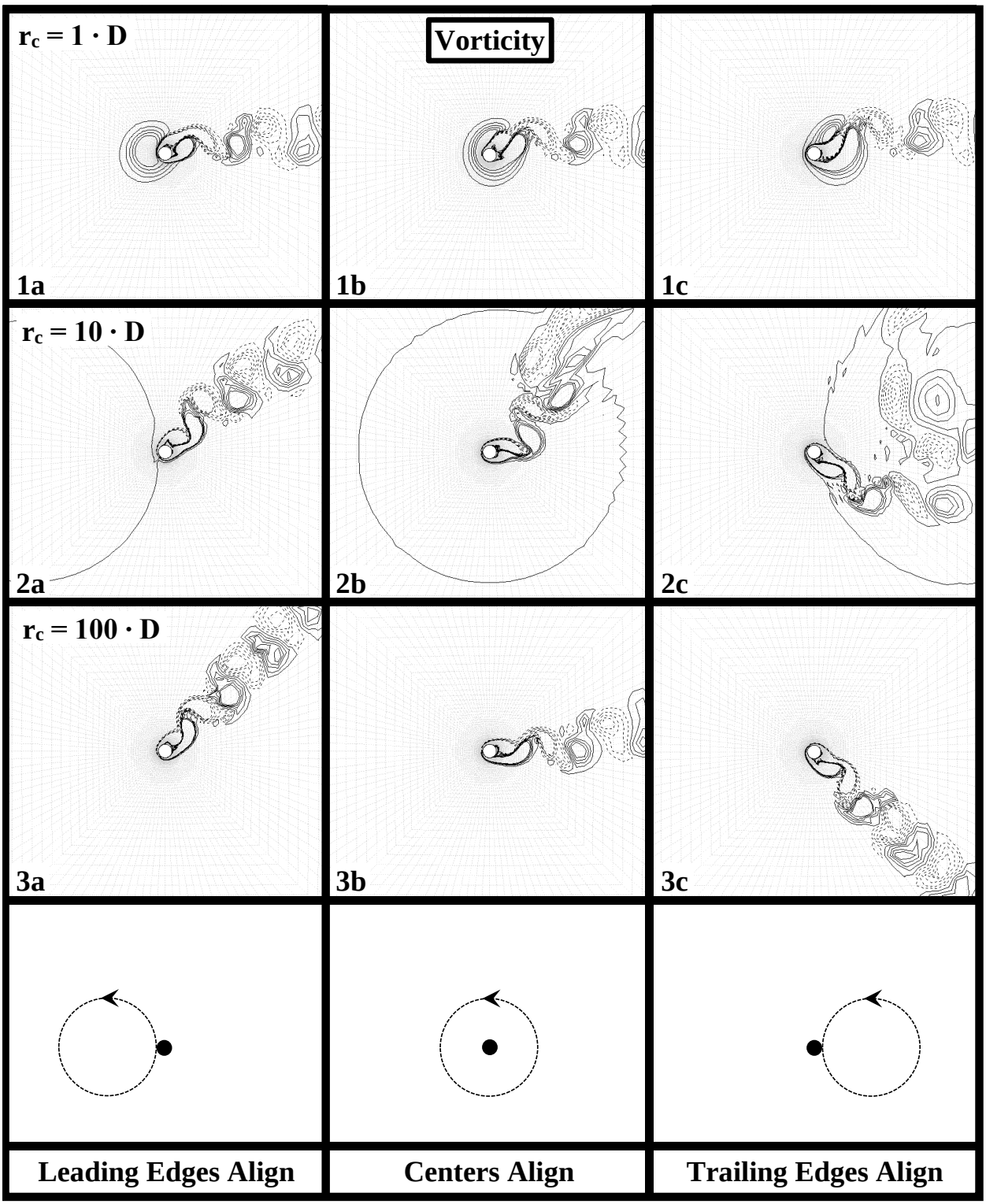


Figure 5.13: Vorticity contour plots of the vortex-cylinder interaction for impinging vortex of radius 1·D (Row 1), 10·D (Row 2), and 100·D (Row 3).

$V_\theta = U_\infty$ and contributes only vertical velocity to the stream over the cylinder at these times, hence the direction of the resultant velocity is 45° from the horizontal. When the vortex and cylinder centers align, the net tangential velocity on the cylinder is zero, meaning the flow over the cylinder is the free stream at Re = 150, which produces a horizontal wake (Figure 5.13.3b).

5.3.4 Summary of Cylinder Loading Trend with Increasing Vortex Size

The radius of the impinging vortex has been incremented from $1 \leq r_c/D \leq 100$, and the trend in cylinder loading with respect to impinging vortex size has been documented. For the present system ($V_{\theta,max} = U_\infty = 1$), vortex impact time with respect to the free stream vortex shedding cycle no longer influences maximum force coefficient amplitudes when $r_c/D \geq 20$. Maximum force coefficient amplitudes reach asymptotic values for $r_c/D \geq 50$, meaning subsequent increase in vortex size does not influence the maximum amplitude of cylinder loading.

It is emphasized that the vortex sizes identified in the previous paragraph only pertain to the specific vortex considered in the study. The broad conclusion of the study is that structure loading by a vortex becomes asymptotic when the three criterion are met:

1. The vortex becomes sufficiently large to control vortex shedding from the structure prior to impacting it.
2. The velocity gradient within the vortex becomes sufficiently small so that the cylinder wake can smoothly shift without being distorted.
3. The vortex becomes sufficiently large to expose the entire surface of the structure to $V_{\theta,max}$.

Numerous parameters such as the vortex translational velocity, the maximum tangential velocity of the vortex, the free stream Reynolds number, etc. may influence the vortex size beyond which vortex impact time ceases to influence the maximum structure loading amplitude and for which maximum force coefficient amplitudes become asymptotic. However, phenomenon which

control the convergence of the maximum force coefficient amplitudes have been identified, and methodology has been established to study the trend in maximum loading of a structure by a vortex as a function of the relative size of the impinging vortex to the loaded structure.

5.4 Influence of Vortex Path on Structural Loading

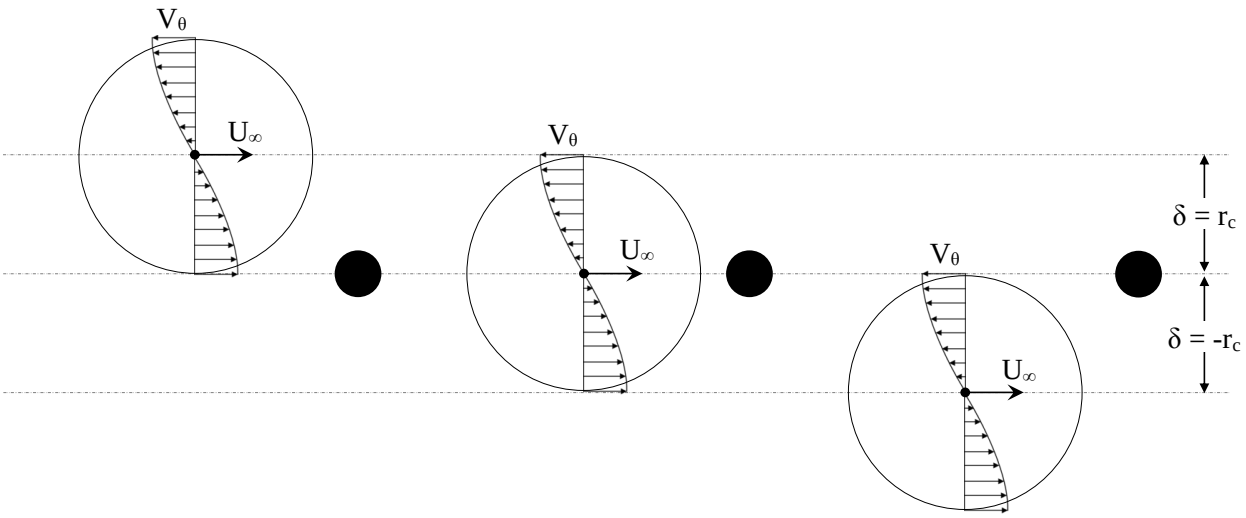
Section 5.3 establishes that an impinging vortex having critical radius $r_c = 50 \cdot D$ is large enough to produce asymptotic cylinder loading. To this point, all simulations have been of "direct" vortex impact where the vortex and cylinder centers fall on the same horizontal line. However, an impinging vortex may not always impact the loaded structure directly, so it is necessary to evaluate the influence of y-direction shift of the vortex path on the resulting structural loading. The outcome of this study answers the question of whether or not a rotational flow produces greater loading than an equivalent-velocity stream flow.

5.4.1 Methodology and Approach

A vortex having a critical radius $50 \cdot D$ is large enough to produce asymptotic cylinder loading, therefore, this fixed vortex size is used for the present study. Direct simulations conducted to this point have $\delta = 0$ y-direction shift of the impinging vortex path. Now the impinging vortex path is incremented through the interval $-4 \leq \delta / r_c \leq 4$ so that the impinging vortex travels below and above the cylinder. Maximum positive and negative force coefficient values are extracted following each simulation. These values are then compared with maximum force coefficients produced by a free stream having equivalent maximum velocity to the vortex within the free stream ($U_{eq} = V_{\theta,max} + U_{\infty}$).

5.4.2 Trend in Structural Loading with Vortex Path Shift

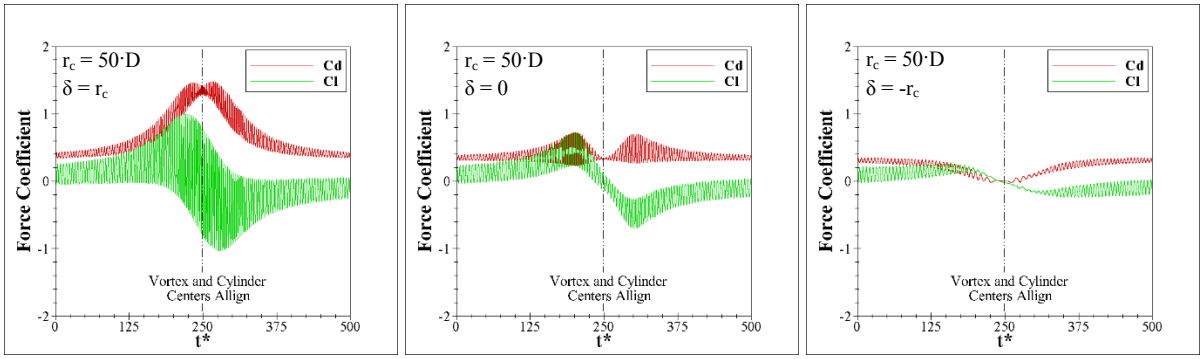
The schematics in Figures 5.14a – 5.14c illustrate the vortex travelling above the cylinder $\delta = r_c$, impacting the cylinder directly $\delta = 0$, and travelling below the cylinder $\delta = -r_c$.



(a) (b) (c)

Figure 5.14: Schematic of vertical shift of vortex's path by (a) $\delta = r_c$, (b) $\delta = 0$, and (c) $\delta = -r_c$.

When the vortex impacts the cylinder directly as illustrated in Figure 5.14b, it primarily applies a vertical velocity to the cylinder surface. As the vortex's path is shifted in the y-direction, it increasingly applies horizontal velocity to the cylinder surface. The present vortex rotates CCW, hence its tangential velocity augments the free stream when it travels above the cylinder (Figure 5.14a) and subtracts from the free stream when it travels below the cylinder (Figure 5.14c).



(a) (b) (c)

Figure 5.15: Force coefficient time histories for impinging vortex having r_c of 50·D and (a) $\delta = r_c$, (b) $\delta = 0$, and (c) $\delta = -r_c$.

Force coefficient time histories corresponding to the three vortex paths illustrated in Figures 5.14a – 5.14c are illustrated in Figures 5.15a – 5.15c. The cylinder loading is much

greater and much less when the vortex travels above (Figure 5.15a) and below (Figure 5.15c) the cylinder, respectively, than when it impacts the cylinder direction (Figure 5.15b). Now the path of the impinging vortex is shifted over the range $-4 \leq \delta/r_c \leq 4$, and maximum force coefficients are extracted from each simulation. These are summarized as function of vertical path shift in Figure 5.16 and compared with maximum force coefficients produced by a free stream of equivalent maximum velocity ($U_{eq} = V_{\theta,max} + U_\infty$). Note that Figure 5.16 reports maximum force coefficient values rather than maximum force coefficient amplitudes as reported in the preceding Section 5.3.

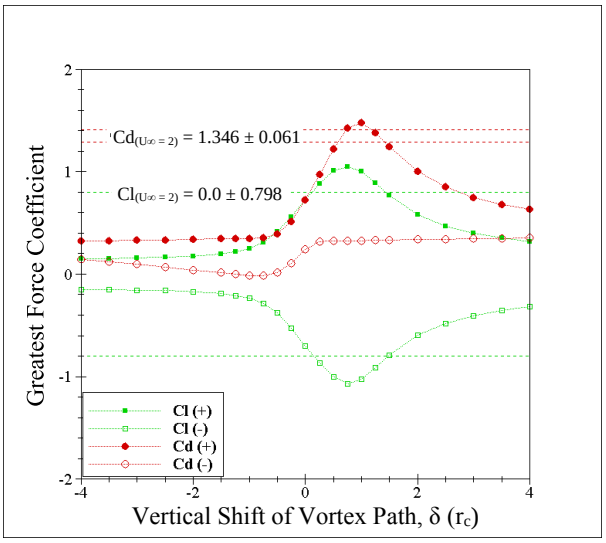


Figure 5.16: Maximum force coefficients for impinging vortex of $r_c = 50 \cdot D$ and vertical path shift of $-4 \leq \delta/r_c \leq 4$. Horizontal lines indicate maximum force coefficients for an Re = 300 equival-velocity ($U = U_\infty + V_{\theta,max}$).

The summary of maximum force coefficients in Figure 5.16 corroborates the previous statement that the impinging vortex produces greater cylinder loading when it travels above- and less cylinder loading when it travels below- than when it impacts the cylinder directly. The vortex within the free stream produces greater force coefficients than the force coefficients produced when the cylinder is immersed in an equivalent-velocity free stream (Free stream force coefficient are indicated by dashed, horizontal lines). Table 5.6 quantifies and compares the

maximum force coefficients produced by the vortex and the free stream. Maximum drag and lift force coefficients produced by the impinging vortex are under-predicted (UP) by the equivalent-velocity free stream force coefficients by up to 4.80% and 34.07% respectively.

Table 5.6: Comparison of maximum force coefficients produced by the vortex within the free stream with those produced by a Re = 300 equivalent-velocity free stream.

	Free Stream	Vortex	δ (r_c)	UP
Cd_{max}	1.407	1.475	1.00	4.80%
Cl_{max}	0.798	1.069	0.75	34.07%

5.4.3 Why the Vortex Produces Greater Loading than the Free Stream

Results from computer simulations reported in the previous subsection demonstrate that a vortex having maximum tangential velocity $V_{\theta,max}$ travelling within a free stream having velocity U_∞ can produce greater cylinder loading than an equivalent-velocity $U_{eq} = V_{\theta,max} + U_\infty$ free stream. This finding is not intuitive because the vortex and the equivalent-velocity free stream both produce the same maximum resultant velocity V_R on the cylinder; why does the rotational nature of the vortex result in greater cylinder loading? The answer to this question is that both

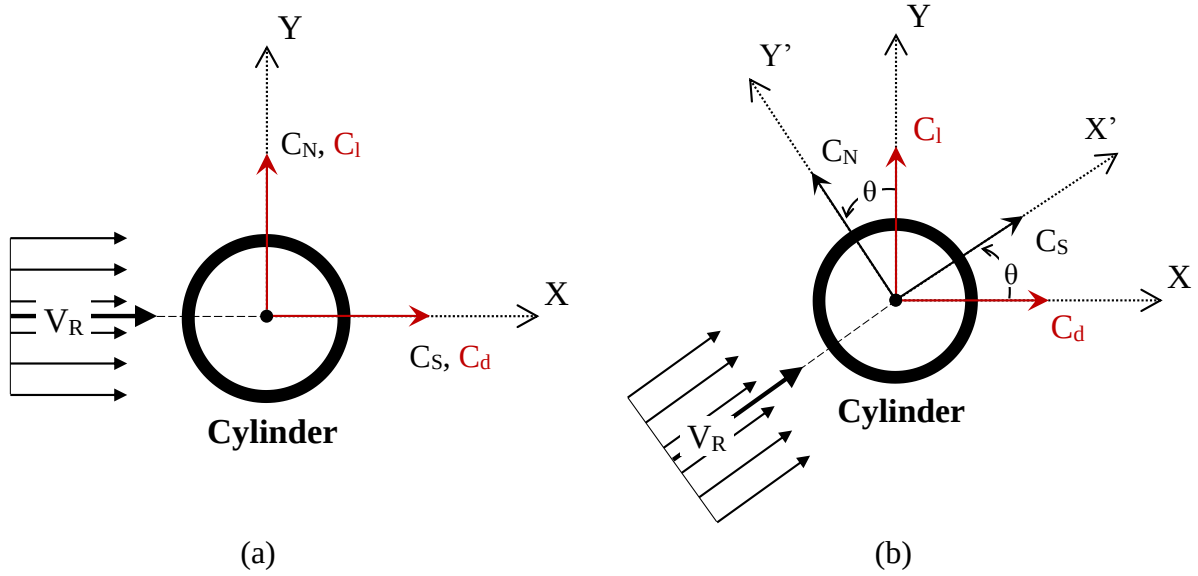
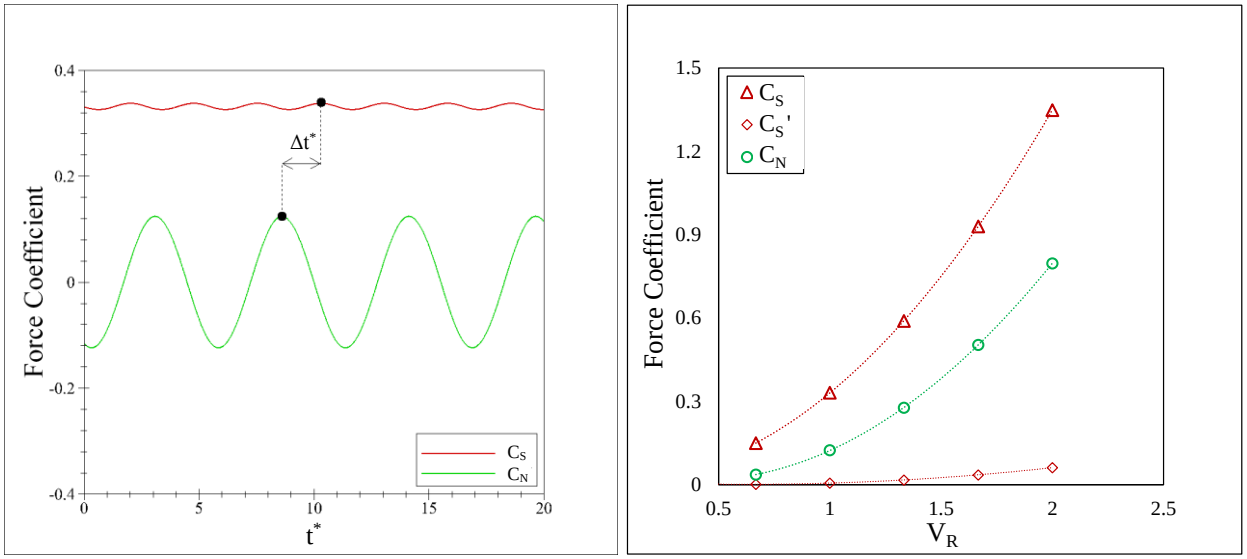


Figure 5.17: Forces produced on a cylinder (a) a free stream and (b) a stream incident from any direction.

the magnitude of V_R and its angle of incidence θ on the cylinder control the maximum cylinder loading amplitude. The forthcoming study expounds this fact to demonstrate that combinations of V_R and θ, rather than just the highest values of V_R, produce maximum cylinder loading.

Figure 5.17a illustrates a cylinder immersed in a free stream having resultant velocity V_R. The stream produces stream-wise (C_S) and cross-stream (C_N) cylinder loading components that respectively act in- and normal to the stream direction. Typical notation is to assign the X-axis along the stream direction and the Y-axis normal to the stream direction; the X-direction force is referred to as drag (C_d) and the Y-direction force is referred to as lift (C_l).



(a) (b)

Figure 5.18: (a) Typical free stream force coefficient time histories and (b) free stream force coefficient amplitudes as functions of V_R. Note that plot (b) is analogous to plotting Cd and Cl for Reynolds numbers of 100 to 300, but alternative notation is used here for consistency.

Figure 5.18a is a typical force coefficient time history of cylinder loading by a free stream. The stream-direction force C_S has a large mean component and small amplitude, while C_N has mean value of zero and large amplitude. The literature commonly reports C_S and C_N (They are referenced C_d and C_l) as function of the free stream Reynolds number. The present study fixes the cylinder diameter and the fluid kinematic viscosity, so the force coefficient

amplitudes are strictly functions of V_R. Figure 5.18b summarizes force coefficient amplitudes for $0.67 \leq V_R \leq 2.0$, which is the range ($Re \leq 300$) for which the present model is valid. Curve fits of the three cylinder loading components illustrated in Figure 5.18b are provided by Eqs. (5.1-3).

$$C_S' = 0.03 \cdot V_R^2 - 0.04 \cdot V_R + 0.01 \tag{5.1}$$

$$C_S = 0.36 \cdot V_R^2 - 0.05 \cdot V_R + 0.03 \tag{5.2}$$

$$C_N = 0.31 \cdot V_R^2 - 0.26 \cdot V_R + 0.07 \tag{5.3}$$

The harmonic component of the stream-wise cylinder loading C_S' is much smaller than C_S or C_N as shown in Figure 5.18b. Furthermore, C_S' and C_N are out of phase as illustrated by Δt^* in Figure 5.18a. Inclusion of C_S' in subsequent discussion is unnecessary and would introduce unnecessary complication. Moving forward, it is therefore assumed that the cylinder loading produced by the free stream consists only of C_S and C_N.

When a vortex is added to the free stream, V_R changes continuously due to the changing proximity of the vortex to the cylinder. Figure 5.17b illustrates the variation by defining the incidence angle (θ) of V_R as function of its horizontal (U) and vertical (V) components. As θ grows, the directions in which C_S and C_N act are shifted around the cylinder surface as indicated by X' and Y'. The incident angle θ is defined by Eq. (5.4), and Eqs. (5.5) and (5.6) are used to resolve C_S and C_N into the drag and lift force coefficients respectively.

$$\theta = \tan^{-1}(V/U) \tag{5.4}$$

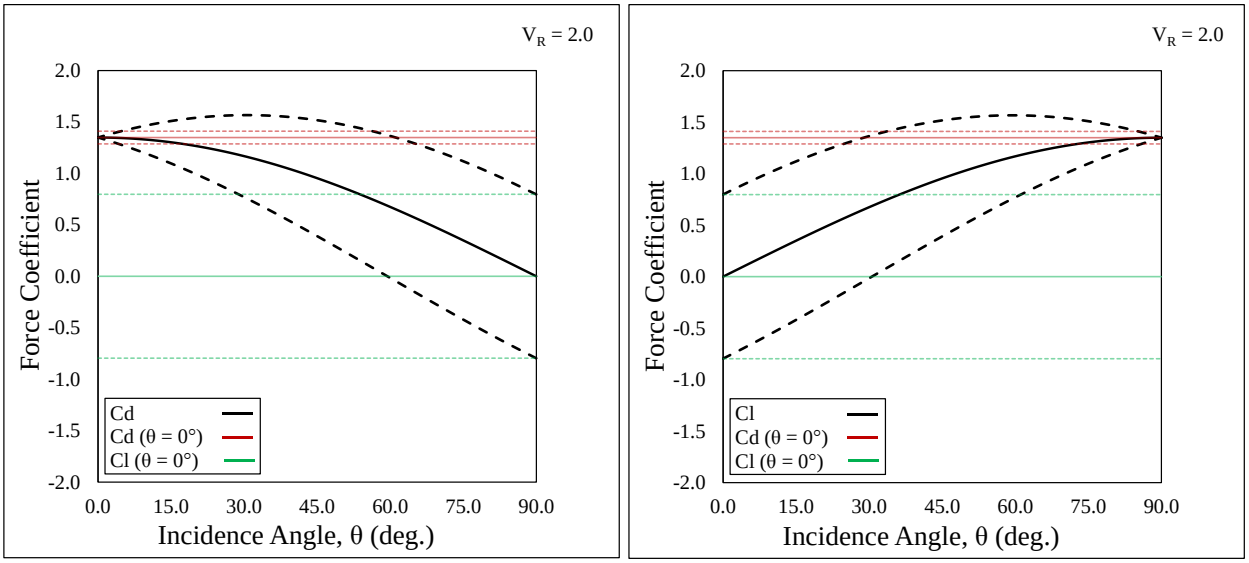
$$C_d = C_S \cdot \cos(\theta) - C_N \cdot \sin(\theta) \tag{5.5}$$

$$C_l = C_S \cdot \sin(\theta) + C_N \cdot \cos(\theta) \tag{5.6}$$

The maximum resultant velocity used in the present study $V_R = V_{\theta,max} + U_\infty = 2.0$ is now fixed and used to demonstrate the influence of θ on the cylinder loading amplitude. Figures 5.19a and 5.19b respectively illustrate the mean (solid lines) and harmonic (dashed lines) components

of the drag and lift force coefficients as function of θ; the maximum drag and lift force coefficients produced by a V_R = 2.0 and θ = 0º free stream are also provided for comparison. Note that Figure 5.19a and 5.19b replicate each other if the x-axis is reversed.

Figure 5.19a illustrates that the incidence angle range 4.5° ≤θ≤ 56° produce greater drag force coefficients than are produced by the free stream. The drag force coefficient reaches a maximum value of 1.567, which is 11.12% greater than the maximum free stream drag force coefficient 1.407, for θ = 30.5°. Figure 5.19b illustrates that any V_R incidence angle θ > 0° produces greater lift force coefficients than are produced by the free stream. The maximum lift force coefficient value of 1.567, which is 96.60% greater than the free stream value of 0.789, is reached for θ = 59.5°.



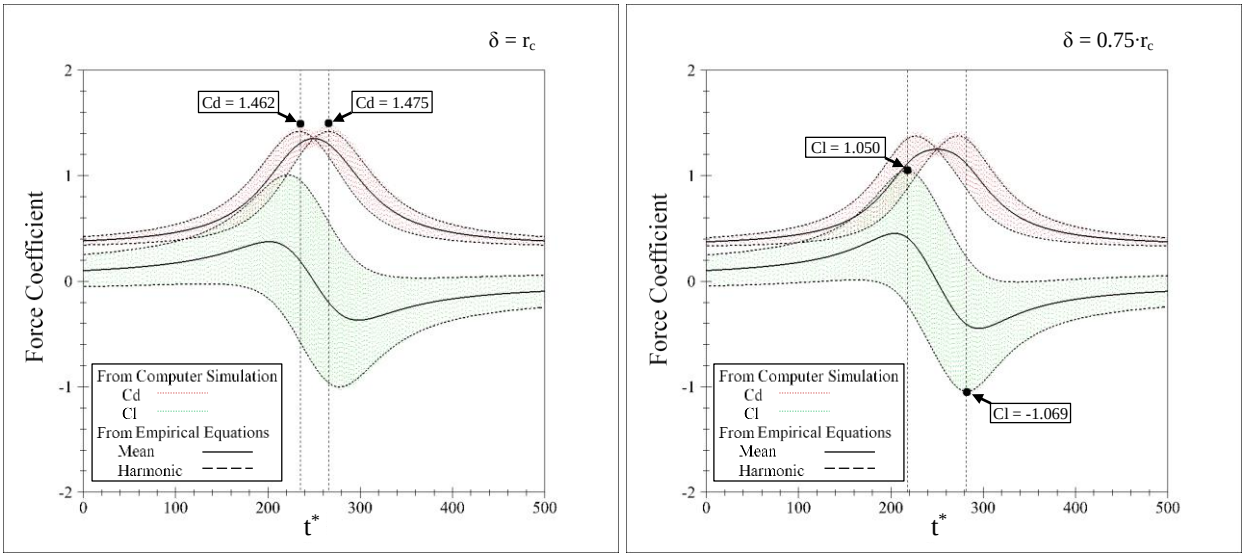
(a) (b)

Figure 5.19: Maximum (a) drag and (b) lift force coefficient amplitude as a function of resultant velocity incidence angle.

The preceding example demonstrates that, for a fixed V_R, a range of θ produce greater cylinder loading than an equivalent-velocity free stream. However, during vortex loading, V_R and θ change continuously. The stream over the cylinder may be incident at θ that produces maximum cylinder loading, such as 30.5° for Cd, but V_R may be too low to produce substantial

loading. The converse scenario may occur, where V_R is high, but θ is not within the range that produces high force coefficients. The present study validates the use of Eqs. (5.2-6) by comparing maximum cylinder loading defined using known V_R and θ with cylinder loading from the computer simulations which produces maximum force coefficient amplitudes.

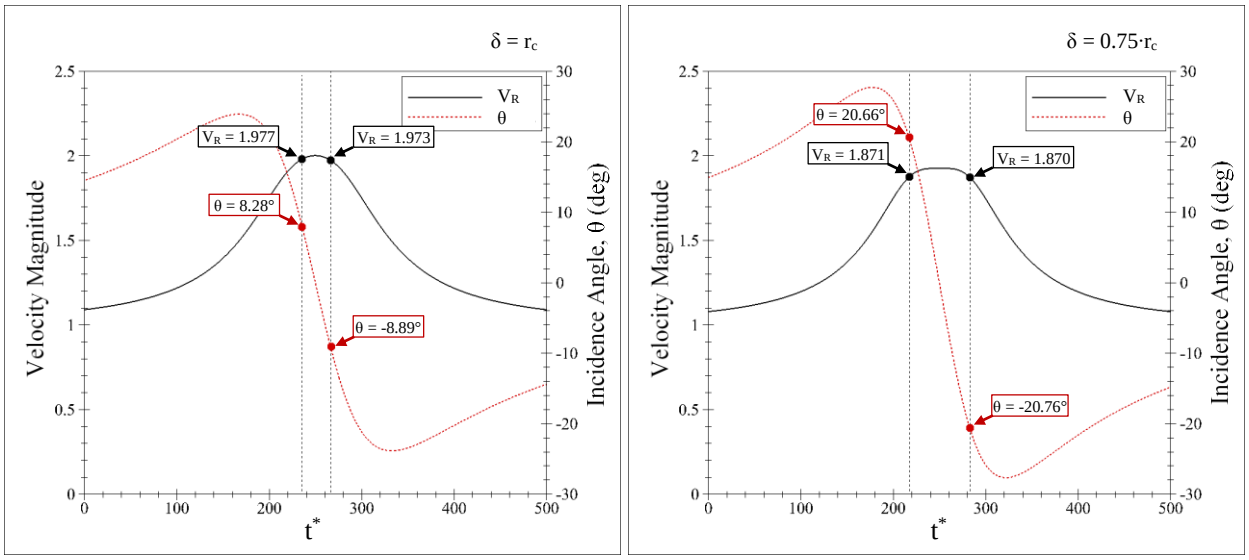
The vortex-loading scenarios which produce maximum drag and lift force coefficients are when the vortex path is shifted by $\delta = r_c$ and $0.75 \cdot r_c$ respectively. Figures 5.20a and 5.20b compare force coefficient time histories from computer simulation those defined using Eqs. (5.2-6) and demonstrate that the equations provide excellent replication of the cylinder loading from computer simulation. Boxed callouts in both figures indicate the maximum values of the drag and lift force coefficients that occur for the specified loading scenarios.



(a) (b)

Figure 5.20: Comparison of force coefficient time histories from computer simulation and defined using Eqs. (5.2-6) for impinging vortices travelling at (a) $\delta = r_c$ and (b) $0.75 \cdot r_c$.

Figures 5.21a and 5.21b provide the time histories of V_R magnitude and θ corresponding to the force coefficient time histories in Figures 5.20a and 5.20b. Callouts indicate V_R and θ combinations that produce the maximum force coefficient amplitudes. The maximum cylinder loading is not produced when V_R is greatest, but rather occurs for maximizing combination of V_R



(a) (b)

Figure 5.21: Time histories of resultant V_R magnitude and incidence angle for (a) $\delta = r_c$ and (b) $0.75 \cdot r_c$.

and θ. Table 5.7 summarizes the data from Figures 5.20 and 5.21 and compares maximum force coefficients computed using empirical equations Eqs. (5.2-6), based upon V_R and θ combinations indicated in Figure 5.21, with maximum force coefficients from computer simulation that are indicated in Figure 5.20. Empirical Eqs. (5.2-6) reproduce maximum drag and lit force coefficient values from computer simulation to within 4.07% and 2.06% respectively. It is worth noting that if the contribution of the harmonic component of the stream-wise forcing C_S' is added, the respective values of $C_{dm,eqs}$ and $C_{lm,eqs}$ are 1.474 and -1.065, which are within 0.10% and 0.37% of the maximum force coefficients from computer simulation.

The purpose of the preceding study is to explain why a vortex travelling within a free stream can produce greater cylinder loading than a free stream which has equivalent maximum velocity to the vortex within the free stream. It is shown that flow over a cylinder produces forces in the stream direction and normal to the stream direction. The amplitudes of these forces are dependent upon the magnitude of the incident stream velocity V_R, and the direction in which they act is set by the stream incidence angle θ. In summary, the vortex within the free stream

produces greater loading because it is able to produce combinations of V_R and θ that produce greater cylinder loading than a free stream, having the same maximum velocity, at 0° incidence angle.

Table 5.7: Comparison of maximum force coefficients computed using Eqs. (5.2-5.6) and maximum force coefficients from computer simulation.

$\delta = r_c$		$\delta = 0.75 \cdot r_c$
From Equations (5.2-6)		
V_R 1.977 θ 8.28		V_R 1.87 θ -20.76
$Cd_{m,eqs}$ 1.415		$Cl_{m,eqs}$ -1.047
From Computer Simulation		
$Cd_{m,sim}$ 1.475		$Cl_{m,sim}$ -1.069
Percentage Difference		
4.07%		2.06%

5.4.4 Visualization of Vortex-Cylinder Interaction Influenced by Vortex Path Shift

Figure 5.22 uses vorticity contour plots to illustrate the cylinder loading scenarios corresponding to the force coefficient time histories in Figures 5.15a – 5.15c. Rows 1 – 3 respectively illustrate the vortex traveling above the cylinder ($\delta = r_c$), impacting the cylinder directly ($\delta = 0$), and traveling below the cylinder ($\delta = -r_c$). Columns 1 – 3 correspond to the three relative positions of the vortex to the cylinder that are illustrated by the schematics in Row 4.

Cylinder loading is greatest when the impinging vortex travels above the cylinder (See Row 1 of Figure 22). The vortex's tangential velocity adds to and effectively doubles the velocity of the stream passing over the cylinder; this increased velocity produces a large mean drag force and large amplitude lift force. As the vortex approaches the cylinder, its tangential velocity adds a vertical velocity component to the stream over the cylinder as evidenced by the vertical shift of the cylinder's wake in Figures 5.22.1a and 5.22.1c. Consequently, both the

amplitude of the drag force coefficient and the mean value of the lift force coefficient are increased. This is the physical mechanism through which the vortex produces greater loading than the equivalent velocity free stream, as discussed in the previous subsection.

The impinging vortex's tangential velocity primarily adds a vertical velocity component to the stream over the cylinder when the vortex impacts the cylinder directly (See Row 2 of Figure 22). This is shown by 45° counter-clockwise and clockwise shifts in the cylinder wake that are illustrated in Figures 5.22.2a – 5.22.2c respectively. The force coefficient time history in Figure 5.15b shows that the amplitude of Cd and mean value of Cl are high for direct vortex impact. However, the maximum resultant velocity is relatively low because the vortex's tangential velocity primarily adds a vertical velocity component to the free stream; consequently, cylinder loading is less than that produced by the equivalent-velocity free stream.

Cylinder loading by the impinging vortex is least when the impinging vortex travels below the cylinder as illustrated in Row 3 of Figure 5.22. The vortex rotates counter-clockwise, hence its tangential velocity effectively counteracts the loading effects produced by the stream that it travels within. Vortex shedding from the cylinder slows and eventually stops as the Reynolds number characterizing the flow over the cylinder falls below $Re_{cr} \approx 47$. This is indicated by the non-periodic segment of the force coefficient time histories centered around $t^* = 250$ in Figure 5.15c. The reduced vortex shedding frequency can be seen when comparing the vorticity contours for $\delta = -r_c$ (Figures 5.17.3a – 5.17.3c) with those for $\delta = 0$ and $\delta = r_c$.

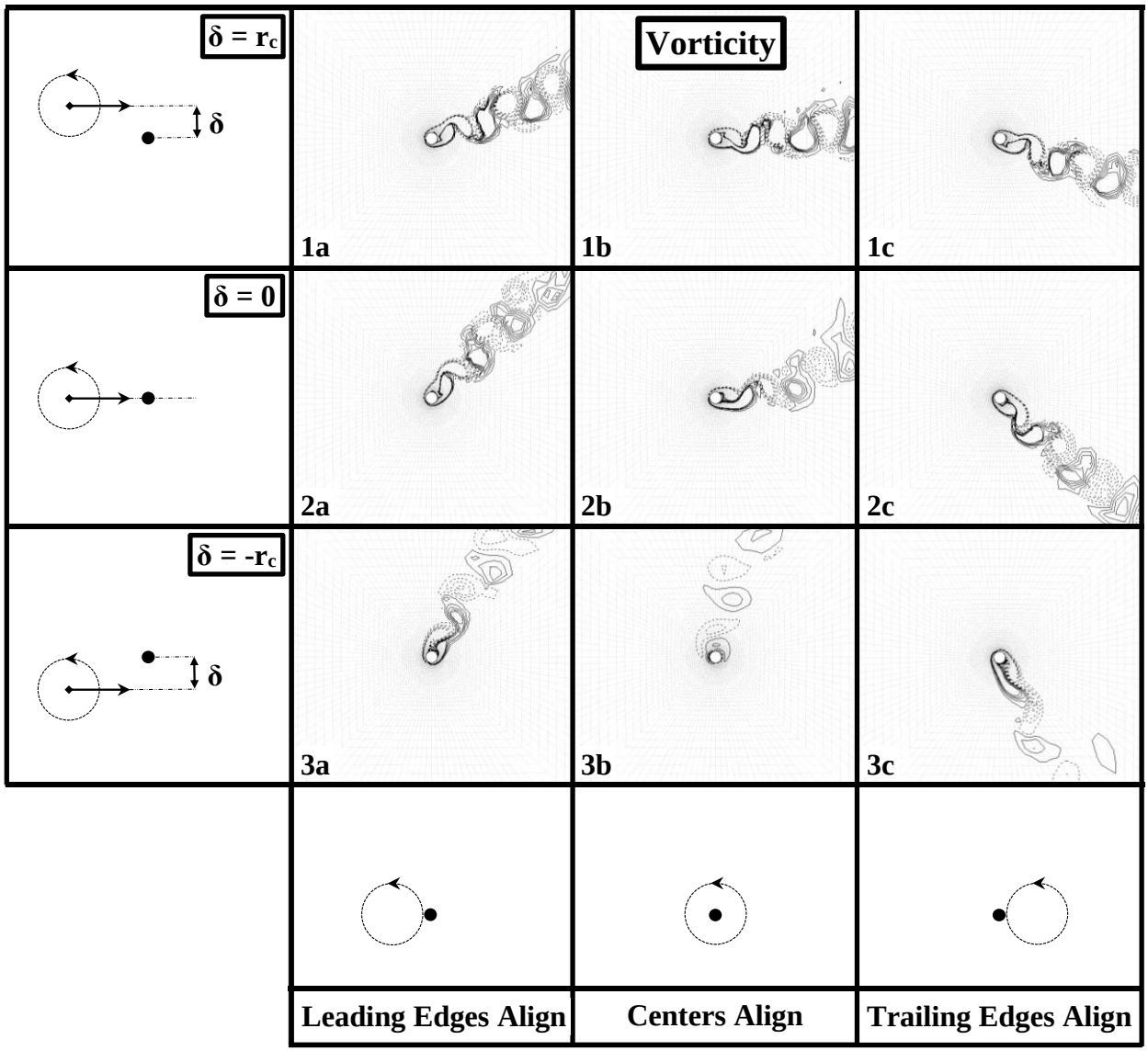


Figure 5.22: Vorticity contour plots of the vortex-cylinder interaction for impinging vortex of radius 50·D and vertical offset of $\delta = r_c$ (Row 1), $\delta = 0$ (Row 2), and $\delta = -r_c$ (Row 3).

5.5 Summary and Conclusions

Structural loading by vortices occurs at practically all relative vortex-to-structure size scales. Direct impact of a vortex with a slender, cylindrical structure is simulated to evaluate the influence of the relative vortex-to-structure size on the structural loading amplitude that is produced. The vortex's maximum tangential velocity and the velocity of the free stream that it travels within are fixed and equivalent ($V_{\theta,max} = U_\infty$). The vortex's critical radius is incremented

from one to one-hundred times the structure's diameter, and maximum force coefficient amplitudes used to illustrate the structural loading amplitude trend. Phenomenon which influence the structural loading trend are illustrated and explained using velocity and vorticity contour plots. Finally, the impinging vortex's path is shifted from the structure's centerline so that it travels along paths both above and below the structure. Maximum force coefficient values are utilized to document the influence of vortex path shift δ on the structural loading. Maximum force coefficients produced by the vortex are compared with maximum force coefficients produced by the equivalent velocity free stream to assess the influence of the rotational nature of the vortex on the maximum structural loading that it can produce. Based upon the content presented in Chapter 5, the subsequently-outlined conclusions have been reached.

1. A small vortex produces a wide spectrum of different structural loading amplitudes when it impacts a structure that is already sheading vortices at different times with respect to the vortex shedding cycle.
    a. The actual maximum force coefficient amplitudes that an $r_c = 1 \cdot D$ vortex produces may be under-predicted by 84.99%, 197.04%, 310.42%, and 407.15% [Cl' (+), Cl' (-), Cd' (+), and Cd' (-)] if only a single simulation is performed.
    b. The variation in structural loading with vortex impact time is caused by interaction between the impinging vortex and different attached vortices.
2. The variation in maximum force coefficients with vortex impact time is negligible for $r_c \geq 20 \cdot D$ because large vortices control vortex shedding from the structure pre-impact.
3. Maximum force coefficient amplitudes produced by a directly-impacting, fixed-maximum tangential velocity vortex are asymptotic for $r_c \geq 50 \cdot D$.
    a. The impinging vortex must be large enough to:

i. Control vortex shedding from the structure prior to impacting it.

ii. Have a sufficiently small tangential velocity gradient to allow the structure's wake to shift without distortion.

iii. Be large enough to effectively expose the entire structure to the maximum tangential velocity.

4. Maximum drag and lift force coefficients produced by impacting $r_c \geq 50 \cdot D$ vortices are respectively 94.77% and 10.66% less than force coefficients produced by the equivalent-velocity free stream.

    a. Forces produced on the structure are a function of the square of the incident resultant velocity. The maximum stream velocity over the structure for direct vortex impact is horizontal $U_\infty = 1$ and vertical $V_{\theta,max} = 1$, so the maximum resultant velocity on the structure is $(2)^{0.5}$ which is much less than the $U_\infty = 2$ free stream's resultant velocity $(4)^{0.5}$.

5. The impinging vortex's tangential velocity profile has little influence on maximum force coefficients produced by the impacting vortex.

    a. The Vatistas n = 1 vortex produces the greatest maximum force coefficient amplitudes, and maximum force coefficient amplitudes produced by the Vatistas n = 1 and Vatistas n = 100 respectively are within 1.0% and 7.0% less.

6. The CCW-rotating, impinging vortex respectively produces greater and less structural loading when it travels above and below the structure than when it impacts directly because its tangential velocity respectively augments and subtracts from the free stream velocity.

7. The CCW-rotating impinging vortex produces maximum drag and lift force coefficients that are respectively 3.80% and 34.07% greater than maximum force coefficients produced by the equivalent-velocity free stream.

CHAPTER 6: DYNAMIC AMPLIFICATION OF TORNADO WIND LOADS

6.1 Overview

Atmospheric vortices such as tornados and hurricanes are transient phenomenon, and the capability of their induced wind loads to dynamically excite structures is debated. Hurricane vortices translate slowly and are many kilometers in diameter, hence it can reasonably be inferred that they are incapable of dynamically exciting a practical structure. However, tornado vortices range greatly in size and may translate rapidly. Consequently, the capability of tornados to dynamically amplify structure response needs to be systematically assessed.

The literature contains several investigations of the capability of tornado wind loads to dynamically excite structures. The time history of the tornado wind speed on the structure is defined, and then empirical equations are used define the corresponding forcing time history. The forcing is then applied to various single- and multi-story structures, producing dynamic structure response amplification of 1.735 (Dutta et al., 2002) to 4.0 (Wen, 1975). However, their simulations are performed using forcing time histories developed for straight-line wind, so the aerodynamic effects of the structures' shape and the rotating vortex wind field are absent.

All preceding investigations report than tornado wind loads are capable of dynamically amplifying the loaded structure's response. However, their collective shortcoming is that they fail to develop a generalized assessment of the dynamic loading threat from tornados, but rather assess the response of a particular structure to loading by a particular tornado. Parameters of tornado vortices as well as real-world structure fundamental periods vary widely. The fundamental period of a structure can be computed with reasonable accuracy during design; computation of adequate design loadings necessitates the development of a methodology to assess the possible dynamic amplification of the structure's response to tornado wind loads.

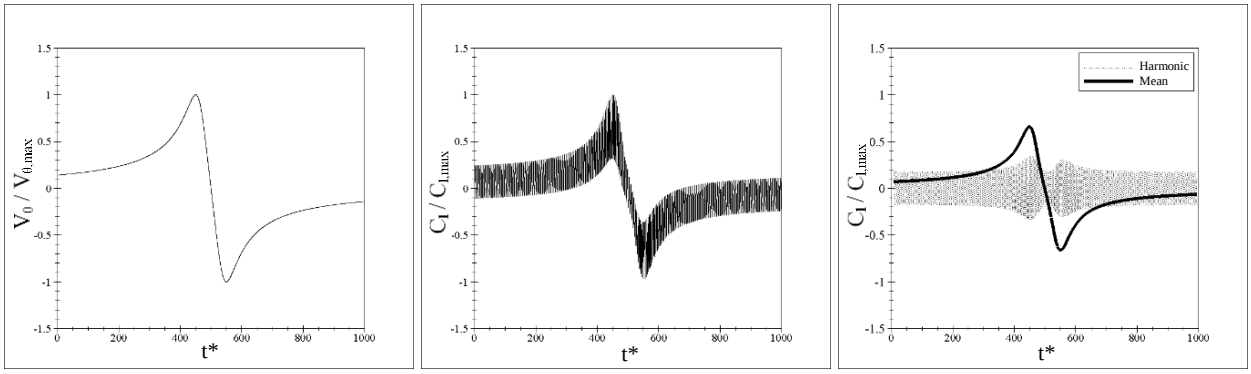
The overarching goal of this chapter is to define the possible dynamic amplification of a structure having specified fundamental period T_n to tornado wind loads. The dynamic load factor (DLF) concept is used to generalize computation of the dynamic structure response amplification because a Fourier transform of the forcing is unable to distinguish the vortex loading frequency f_v as illustrated in Figure 6.16 and discussed in Section 6.5.5. The subsequent sections provide general discussion of tornado wind loads prior to introducing and explaining the DLF concept. Construction of generalized DLF curves for an applied forcing profile is demonstrated. The DLF concept is then extended to define the vortex loading period T_v as a function of the vortex's parameters. Finally, documented tornado vortex parameters are used to define the possible dynamic response amplification for a structure having specified T_n.

6.2 The Vortex's Tangential Velocity

As a vortex crosses a structure, its tangential velocity rapidly changes the sign and magnitude of the component of the velocity incident on the structure normal to the vortex's path. Consequently, the cross-stream or lift force is the primary dynamic loading concern ((Tan, 1975) and (Seniwongse, 1977)). Numerous studies ((Wen, 1975), (Tan, 1975) and (Seniwongse, 1977)) also concur that the dynamic loading threat is greatest when the vortex impacts the cylinder directly because this case produces greatest variation in the cross-stream wind field. Therefore, the present study uses lift force coefficient time histories from direct impact of the cylinder by the vortex as the vortex wind loading.

Figure 6.1a illustrates the time history of the cross-stream velocity component incident on the cylinder surface as the impinging vortex passes over it. The corresponding lift force coefficient time history is illustrated in Figure 6.1b, and Figure 6.1c illustrates the lift force coefficient decomposed into its mean and harmonic components. The mean component of the lift

force coefficient is produced by surface shear and pressure due to the incident vortex wind field, and the harmonic component is produced by vortex shedding from the cylinder. Vortex shedding rarely occurs when wind speeds exceed 15 m/s due to excessive turbulence in the air; furthermore, gustiness and wind-field variation in tornados prevent vortex shedding (Giosan and, Eng, 2013). Therefore, the present study defines the vortex forcing profile as the mean component of Cl.



(a) (b) (c)

Figure 6.1: Time histories of (a) cross-stream velocity component, (b) lift force coefficient, and (c) decomposed lift force coefficient.

The decomposition of Cl illustrated in Figure 6.1c is performed by curve fitting the upper and lower bounds of Cl illustrated in Figure 6.1b and using them to define their mean, which is then subtracted to get the harmonic component. This procedure provides sufficient accuracy when the impinging vortex is large ($r_c = 50 \cdot D$ for Figure 6) so Cl does not change substantially between successive peaks of the harmonic component. However, this curve-fitting procedure becomes increasingly-erroneous as the impinging vortex size becomes smaller ($r_c \leq 10 \cdot D$), and it is not possible to simply extract the mean lift force component to analyze as forcing.

The vortex's proximity to the cylinder continuously changes the velocity of the stream over the cylinder, consequently, the frequency and amplitude of the harmonic component of Cl change as well. This means Fourier analysis cannot be used to identify and allow removal of the

harmonic component of Cl. Therefore, the forthcoming study applies the entirety of Cl as forcing to a single degree of freedom (SDOF) response model, and uses the dimensionless dynamic load factor (DLF) to identify the associated vortex loading period T_v. The duration T_v is defined as the fundamental structure period T_n for which the DLF reaches a peak value. The subsequent section introduces and develops the SDOF response model used throughout the following study and outlines the computation of the DLF.

6.3 Single Degree of Freedom Response Model

The SDOF system modeled herein is the spring-mass-damper system illustrated in Figure 6.2a, and the corresponding free-body diagram is illustrated in Figure 6.2b. The system's equation of motion Eq. (6.1) is attained by summing the x-direction forces acting on the system. Eq. (6.1) is written in Newtonian notation, where dots imply differentiation with respect to time. Variables M, K, and C are the mass, stiffness, and damping coefficient of the cylinder respectively. Displacement and forcing on the system are denoted x(t) and F(t) respectively.

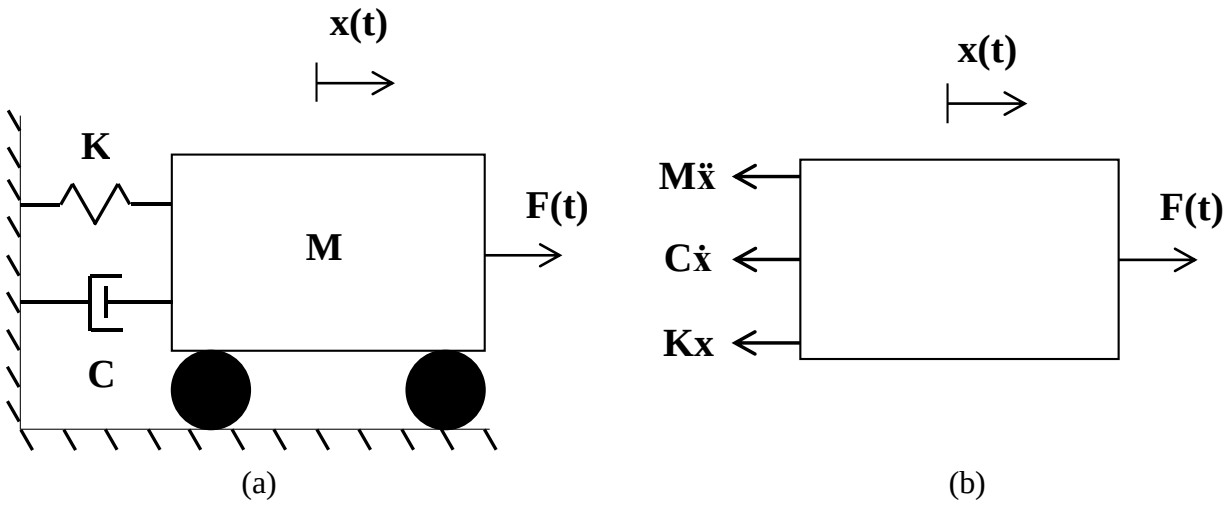


Figure 6.2: (a) Physical representation of the SDOF response model and (b) free body diagram of the SDOF system.

$$\sum F_x \rightarrow M\ddot{x} + c\dot{x} + Kx = F(t) \tag{6.1}$$

6.3.1 Reduction of System Order

The two subsequent subsections respectively outline the development of dimensional and dimensionless single degree of freedom response models. The dimensional model is utilized through Section 6.4 because the forcing is defined by the user and has units of force. The dimensionless model is utilized from Section 6.5 because dimensionless force coefficients from computer simulation are applied as focing.

6.3.1.1 Dimensional Response Model

The SDOF systems position, velocity, and acceleration are solved at each time step using Matlab's ® ODE 45 solver. ODE 45 solves systems of first order, ordinary differential equations (ODE's), hence Eq. (6.1) must be reduced from a second order ODE to two first order ODEs. However, it is convenient to first rewrite Eq. (6.1) in terms of the dimensionless damping ratio ζ and the system's angular frequency ω_n which are respectively defined in Eqs. (6.2) and (6.3). Substitution of ζ and ω_n into Eq. (6.1) produces Eq. (6.4) which is the convenient form of the SDOF system's EOM that will be used herein.

$$\zeta = C \cdot (2 \cdot M \cdot \omega_n)^{-1} \tag{6.2}$$

$$\omega_n = \sqrt{K \cdot M^{-1}} \tag{6.3}$$

$$\ddot{x} + 2\zeta\omega_n\dot{x} + \omega_n^2 x = F(t) \cdot M^{-1} \tag{6.4}$$

The second order EOM Eq. (6.4) is reduced to two first order ODE's by introducing state variables q_1 and q_2, which respectively represent the displacement and velocity of the SDOF system and are defined in Eqs. (6.5a) and (6.5b).

$$q_1 = x \quad \text{and} \quad q_2 = \dot{x} \tag{6.5a}$$

$$\dot{q}_1 = \dot{x} \quad \text{and} \quad \dot{q}_2 = \ddot{x} \tag{6.5b}$$

The definitions of the state variables are now introduced into the equation of motion Eq. (6.4), and the equation of motion is solved for the acceleration term $\ddot{x}$ as shown in Eq. (6.6a). Recognizing that q_2 is the time derivative of q_1 as defined in Eq. (6.6b), the system of Eqs. (6.6a) and (6.6b) can now be solved simultaneously at each time step to resolve the SDOF system's position, velocity, and displacement.

$$\dot{q}_2 = -2\zeta\omega_n q_2 - \omega_n^2 q_1 + F(t) \cdot M^{-1} \tag{6.6a}$$

$$\dot{q}_1 = q_2 \tag{6.6b}$$

Finally, Eqs. (6.6a) and (6.6b) are placed in the vector format that is taken by Matlab's ODE 45 solver as shown in Eq. (6.7).

$$\bar{f}(\bar{q}(t), t) = \begin{bmatrix} \dot{q}_1 \\ \dot{q}_2 \end{bmatrix} = \begin{bmatrix} 0 & 1 \\ -\omega_n^2 & -2\zeta\omega_n \end{bmatrix} \begin{bmatrix} q_1 \\ q_2 \end{bmatrix} + \begin{bmatrix} 0 \\ F(t)/M \end{bmatrix} \tag{6.7}$$

6.3.1.2 Dimensionless Response Model

The computer model utilized in this study is nondimensionalized, and the structural loading produced by vortex impact with the structure is computed as dimensionless force coefficients rather than dimensional forces. It is convenient to re-dimension the state variable vector given in Eq. (6.7) into a dimensionless format so that the force coefficients from the computer model can directly applied as forcing. The dimensionless groups proposed in Selvam and Govindaswamy (2001) are utilized herein.

The dimensional equation of motion for the SDOF system is defined previously in Eq. (6.4). Dimensionless position x^* and time t^* are defined in Eqs. (6.8) and (6.9) respectively.

$$x^* = x \cdot D^{-1} \tag{6.8}$$

$$t^* = t \cdot U_\infty \cdot D^{-1} \tag{6.9}$$

Dimensionless velocity $\dot{x}^*$ and acceleration $\ddot{x}^*$ are respectively defined in Eqs. (6.10) and (6.11) by taking the first and second derivatives of x^* with respect to t^*.

$$\dot{x} = \frac{dx}{dt} = \frac{d(D \cdot x^*)}{d(t^* \cdot D \cdot U_\infty^{-1})} = U_\infty \cdot \dot{x}^* \tag{6.10}$$

$$\ddot{x} = \frac{d^2x}{dt^2} = \frac{d}{dt}\left(\frac{dx}{dt}\right) = \frac{dt^*}{dt} \cdot \frac{d}{dt^*}\left(\frac{d(D \cdot x^*)}{dt^*} \cdot \frac{dt^*}{dt}\right) = \frac{U_\infty^2}{D} \cdot \ddot{x}^* \tag{6.11}$$

Now the definitions of x^*, $\dot{x}^*$, and $\ddot{x}^*$ are substituted into Eq. (6.4). After multiplying through by $D \cdot U_\infty{}^{-2}$ to simplify the expression, the equation of motion Eq. (6.4) is redefined as Eq. (6.12).

$$\ddot{x}^* + \frac{2\zeta\omega_n D}{U_\infty}\dot{x}^* + \frac{\omega_n^2 D^2}{U_\infty^2}x^* = \frac{F(t)D}{MU_\infty^2} \tag{6.12}$$

Dimensional force F(t) is replaced with the dimensionless force coefficient definition $C_F(t) = 2F(t) \cdot (\rho A U_\infty{}^2)^{-1}$. Mass and density are grouped into the dimensionless mass term R_m defined in Eq. (6.13). Substitution of the definitions of $C_F(t)$ and R_m into Eq. (6.12) produces the equation of motion defined in Eq. (6.14).

$$R_m = \rho \cdot D \cdot A \cdot M^{-1} \tag{6.13}$$

$$\ddot{x}^* + \frac{2\zeta\omega_n D}{U_\infty}\dot{x}^* + \frac{\omega_n^2 D^2}{U_\infty^2}x^* = \frac{C_F(t)R_m}{2} \tag{6.14}$$

Finally, the dimensional reference velocity U_∞ is eliminated by introducing the dimensionless reference velocity $U_\infty{}^*$ which is defined in Eq. (6.15). The dimensionless reference velocity $U_\infty{}^*$ is substituted into Eq. (6.14) yielding the fully dimensionless equation of motion for the SDOF system Eq. (6.16).

$$U_\infty^* = U_\infty \cdot (\omega_n \cdot D)^{-1} \tag{6.15}$$

$$\ddot{x}^* + \frac{2\zeta}{U_\infty^*}\dot{x}^* + \frac{1}{U_\infty^*}x^* = \frac{C_F(t)R_m}{2} \tag{6.16}$$

The second order, dimensionless equation of motion Eq. (6.16) is now reduced to two first order ODE's using the state variables that are respectively defined as q_1 and q_2 in Eqs. (6.17) and (6.18).

$$q_1 = x^* \quad \text{and} \quad q_2 = \dot{x}^* \tag{6.17}$$

$$\dot{q}_1 = \dot{x}^* \quad \text{and} \quad \dot{q}_2 = \ddot{x}^* \tag{6.18}$$

Equations (6.17) and (6.18) are now placed in the vector format required for Matlab's ODE 45 solver. The resulting expression Eq. (6.19) is the dimensionless state representation of the dimensioned equation of motion Eq. (6.7) and allows direct application of force coefficient time histories from computer simulation $C_F(t)$ as forcing.

$$\bar{f}\left(\bar{q}(t), t\right) = \begin{bmatrix} \dot{q}_1 \\ \dot{q}_2 \end{bmatrix} = \begin{bmatrix} 0 & 1 \\ -U_\infty^{*\,-2} & -2\zeta U_\infty^{*\,-1} \end{bmatrix} \begin{bmatrix} q_1 \\ q_2 \end{bmatrix} + \begin{bmatrix} 0 \\ 0.5 C_F(t) R_m \end{bmatrix} \tag{6.19}$$

6.3.2 RK4 Formulation and Validation

The SDOF system response is solved via fourth order Runge-Kutta (RK4) at each time step. Four weighted terms are used to approximate the state variables (Specifically displacement and velocity of the cylinder) at each time step. The "k" terms or "Kutta coefficients" are defined in Eqs. (6.20-23) and are intermediate solutions to $\bar{f}\left(\bar{q}(t), t\right)$ at each time step. The state variables are computed using the weighted summation of Kutta coefficients defined Eq. (6.24).

$$\bar{k}_1 = \bar{f}\left(\bar{q}^t, t\right) \tag{6.20}$$

$$\bar{k}_2 = \bar{f}\left(\bar{q}^t + \Delta t/2 \cdot \bar{k}_1, t + \Delta t/2\right) \tag{6.21}$$

$$\bar{k}_3 = \bar{f}\left(\bar{q}^t + \Delta t/2 \cdot \bar{k}_2, t + \Delta t/2\right) \tag{6.22}$$

$$\bar{k}_4 = \bar{f}\left(\bar{q}^t + \Delta t \cdot \bar{k}_3, t + \Delta t\right) \tag{6.23}$$

$$\bar{q}^{t+\Delta t} = \bar{q}^t + \Delta t/6 \cdot \left[\bar{k}_1 + 2\bar{k}_2 + 2\bar{k}_3 + \bar{k}_4\right] \tag{6.24}$$

The SDOF response model is integrated into a computer model that is now validated by computation of a response spectrum. The mass, stiffness, and damping ratio of the system are M = 200,000 kg, K = 200,000 N/m, and $\zeta = 0.1$ respectively. The applied forcing is a sine wave, which is selected because an analytical solution is available for a SDOF structure's response to sinusoidal loading, having amplitude and frequency of $A_F = 1.0$ N and $0 \leq \omega_F \leq 2$ rad/s

respectively. The analytical solution to the maximum structure response as function of the structure's fundamental frequency is given in Eq. (6.25).

$$A_s = \frac{A_F}{M} \cdot \left(\sqrt{(\omega_n^2 - \omega_F^2)^2 + (2\zeta\omega_n\omega_F)^2} \right)^{-1} \tag{6.25}$$

Figure 6.3 compares the response spectrum defined by Eq. (6.25) with the response spectrum computed by the computer model.

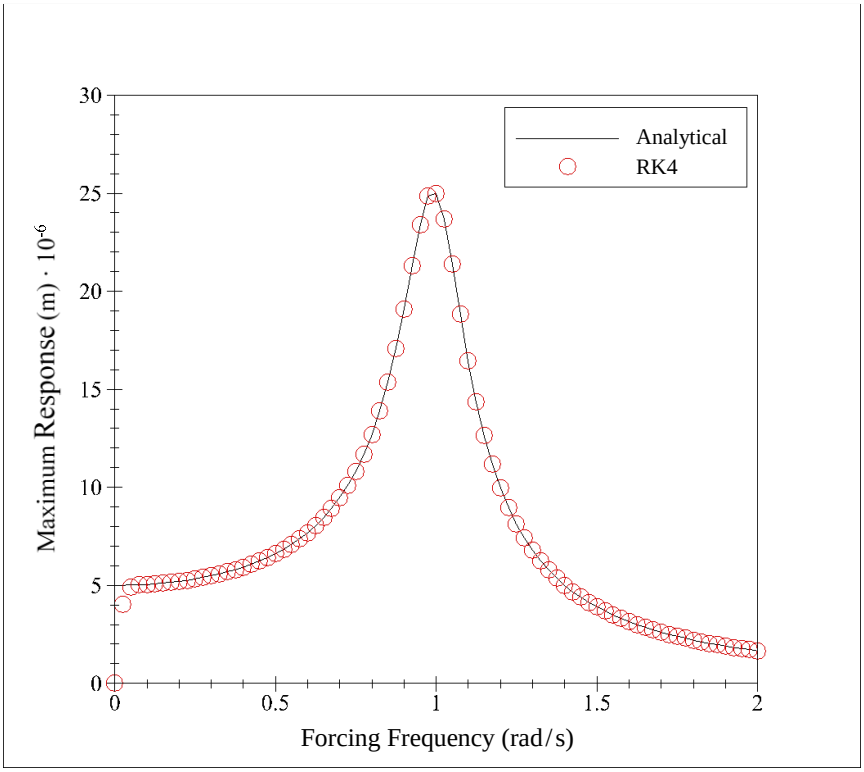


Figure 6.3: Comparison of the response spectra defined analytically by Eq. (6.25) and that defined numerically by the RK4 numerical solution.

The response spectra computed via RK4 solution of the computer model replicates that defined by the analytical solution defined by Eq. (6.25). The maximum response occurs at the damped natural frequency ω_d = 0.995 rad/s defined by Eq. (6.2) which for practical purposes is the same as the structure's undamped natural frequency.

$$\omega_d = \omega_n \cdot \sqrt{1 - \zeta^2} \tag{6.26}$$

Having now confirmed the accuracy of the SDOF response model, the model can be applied to assess dynamic amplification of structure response to vortex loading. The dimensionless DLF shall be used to perform this study, hence the following section explains the concept, computation, and application of the DLF.

6.4 The Dynamic Load Factor

Consider the application of arbitrary forcing F(t) to a structure having stiffness K, where the amplitude of the forcing is F_o. If each discrete value of F(t) is applied as static structure loading, the maximum static displacement of the structure is defined by Eq. (6.27).

$$x_{o,st} = F_o/K \tag{6.27}$$

Now when the complete forcing time history F(t) is applied to the structure, the time history of the structure's response is x(t). The dynamic amplification of the applied forcing at each time instant is defined by normalizing the instantaneous displacement using the maximum static displacement $x_{o,st}$ as shown in Eq. (6.28).

$$DLF(t) = x(t)/x_{o,st} \tag{6.28}$$

It is common practice to present the maximum dynamic response amplification produced by a specific forcing profile using dimensionless DLF curves (see structural dynamics texts such as Paz and Leigh (2004) and Chopra (2005)). An un-damped ($\zeta = 0$), SDOF system having fundamental period T_n is dynamically loaded over the period T_d. The response of the SDOF structure is computed, and the maximum value of DLF(t) is reported as the dynamic amplification of the applied forcing when the forcing is applied to a structure having the specified fundamental period T_n. This procedure is repeated as the fundamental period of the loaded structure is incrementally increased. Subsequently, the maximum values of DLF(t) for each value of T_n are reported in a single curve, which is rendered dimensionless by plotting the

DLF associated with each fundamental structure period as function of the ratio T_d/T_n. DLF curves for some common forcing profiles are shown in Figure 6.4.

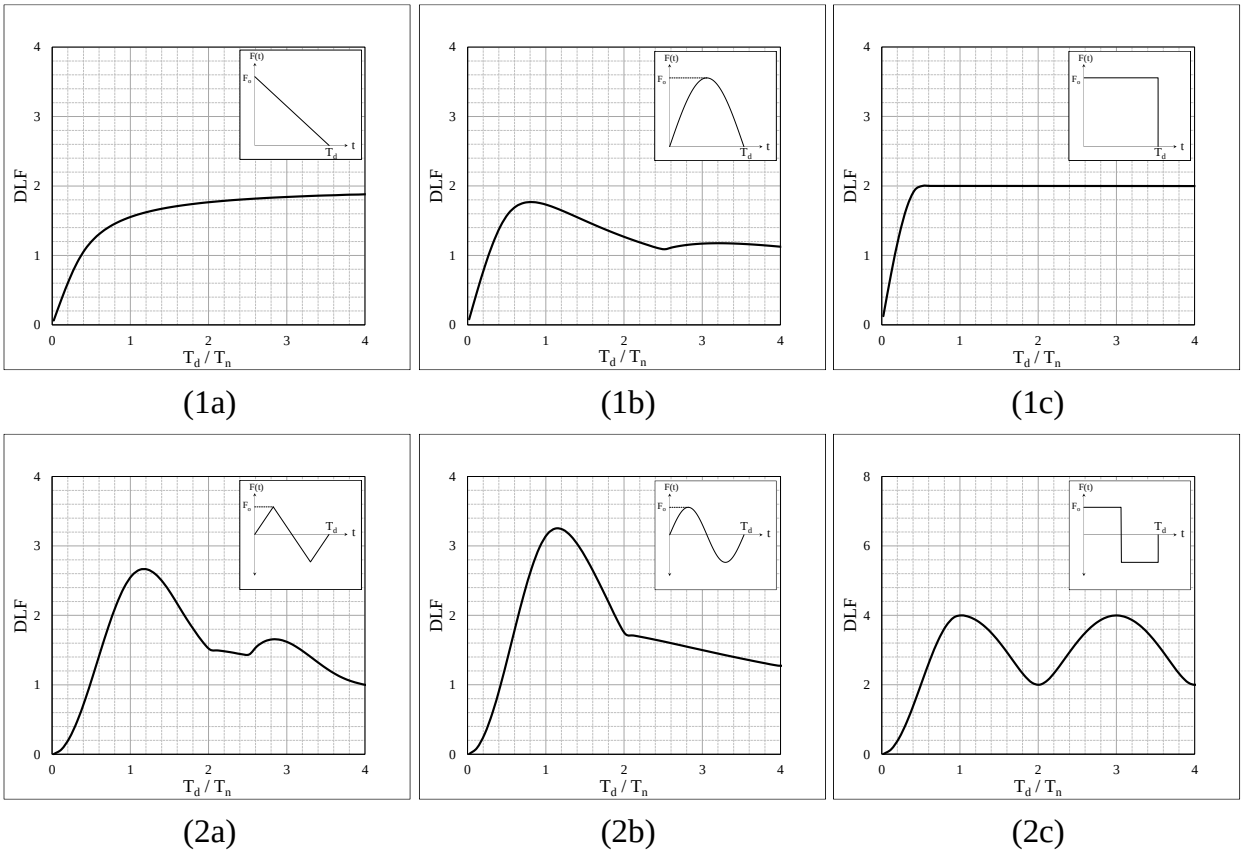


Figure 6.4: DLF curves for some common forcing profiles ($\zeta = 0$).

Defining DLF curves for forcing profiles is analogous to defining aerodynamic force coefficients (Such as Cd and Cl) as functions of Reynolds number for various body shapes. The Reynolds number combines parameters characterizing flow over the body, and the similarity principal explains that any combination of system parameters producing the same characterizing Reynolds number will produce the same type of flow around the body. This allows force coefficients to be defined as a function of the characterized system rather than for each of the individual system variables. Similarly, when a structure is dynamically loaded by a specified forcing profile, there are practically infinite possible combinations of forcing amplitude, forcing application period, and structure fundamental period. However, once the curve DLF(T_d/T_n) is

defined for the specified forcing profile, the dynamic amplification of the maximum static structure response defined previously in Eq. (6.28) can be easily read.

6.4.1 Construction of DLF Curves

This subsection demonstrates the procedure for constructing DLF curves for a specified forcing profile. Special focus is given on explaining and illustrating the benefit of using the dimensionless DLF to evaluate dynamic amplification of structure loading. Subsequently, the DLF concept is used to define the vortex load-application period T_v and to assess the dynamic amplification of vortex-induced loading.

The considered forcing profile is the single-period sinusoid illustrated in Figure 6.5. The forcing has amplitude $F_o = 1$ N and load application period $T_d = 1$ s. The forcing is applied to an undamped $\zeta = 0$ structure having fixed mass M = 200,000 kg. The responses of four separate structures, each of which having a different fundamental frequency $f_n = T_n^{-1}$, the stiffness and frequency of each structure are summarized in Table 6.1. For each structure, the fundamental frequency is specified and the corresponding structure stiffness is computed as $K = (f_n/2\cdot\pi)^2\cdot M$.

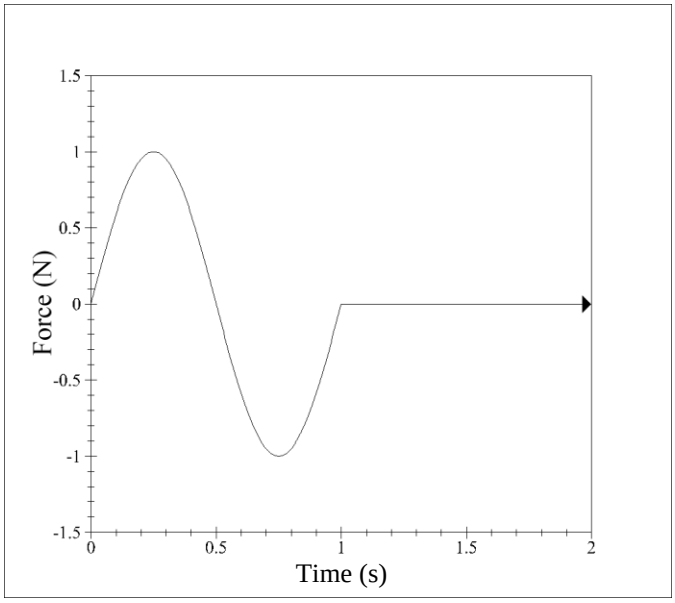


Figure 6.5: Sinusoid impulse applied as forcing.

Table 6.1: Parameters for the four considered SDOF structures.

Structure	f_n (Hz)	K (N/m)	T_d / T_n
1	0.25	493,480	0.25
2	0.50	1,973,900	0.50
3	1.00	7,895,700	1.00
4	2.00	31,583,000	2.00

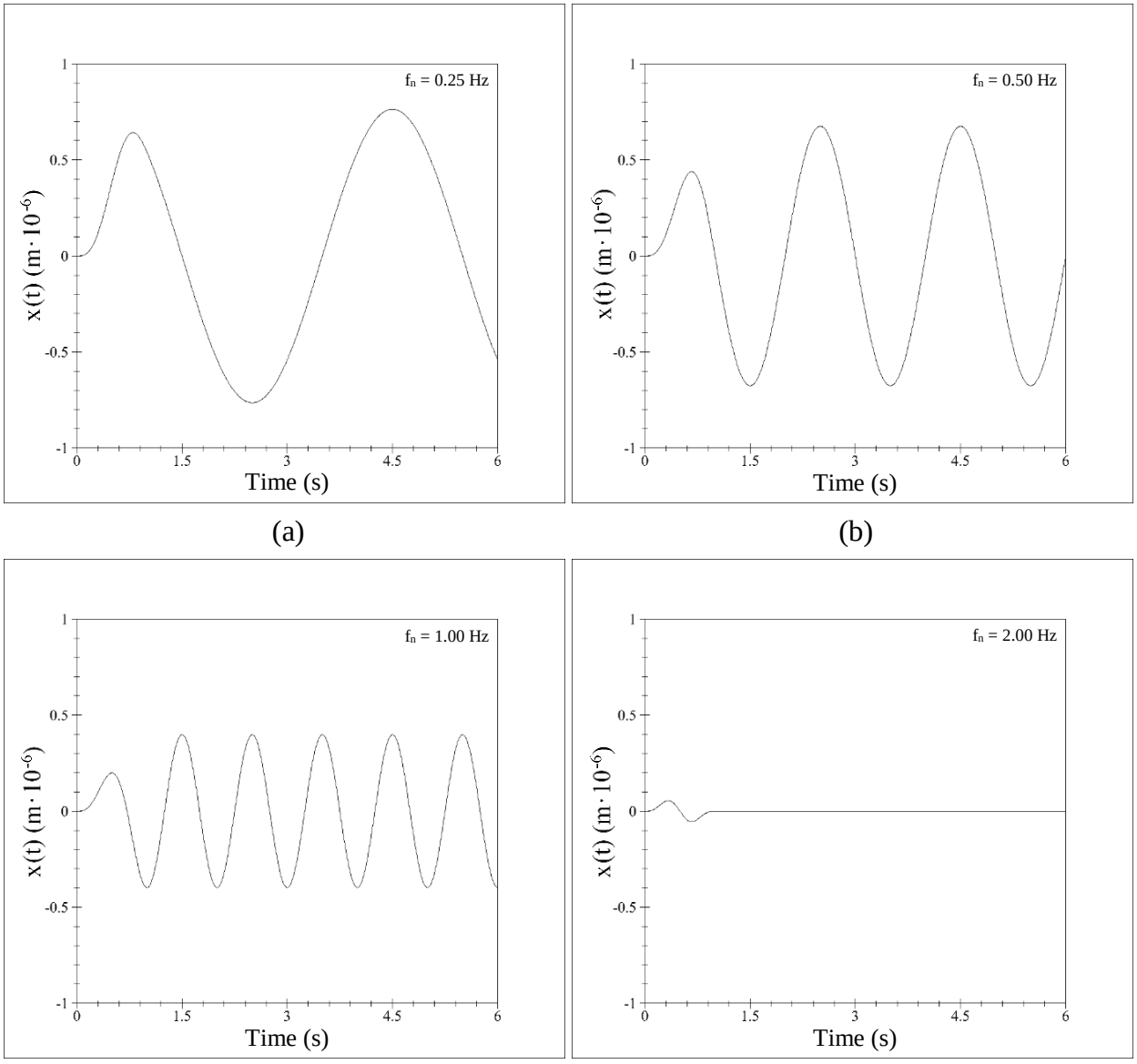


Figure 6.6: Responses of the four SDOF structures defined in ***Table 6.1*** to the sinusoidal forcing shown in ***Figure 6.5***.

The sinusoid of forcing is applied to each of the four structures defined in Table 6.1 producing the responses illustrated in Figure 6.6. The amplitude of the structure's response generally decreases progressing from Figure 6.6a to 6.6d due to the increasing stiffness of the structure. However, analyzing the structure responses in this manner provides no meaningful insight regarding structure response amplification due to the dynamic nature of the sinusoidal forcing.

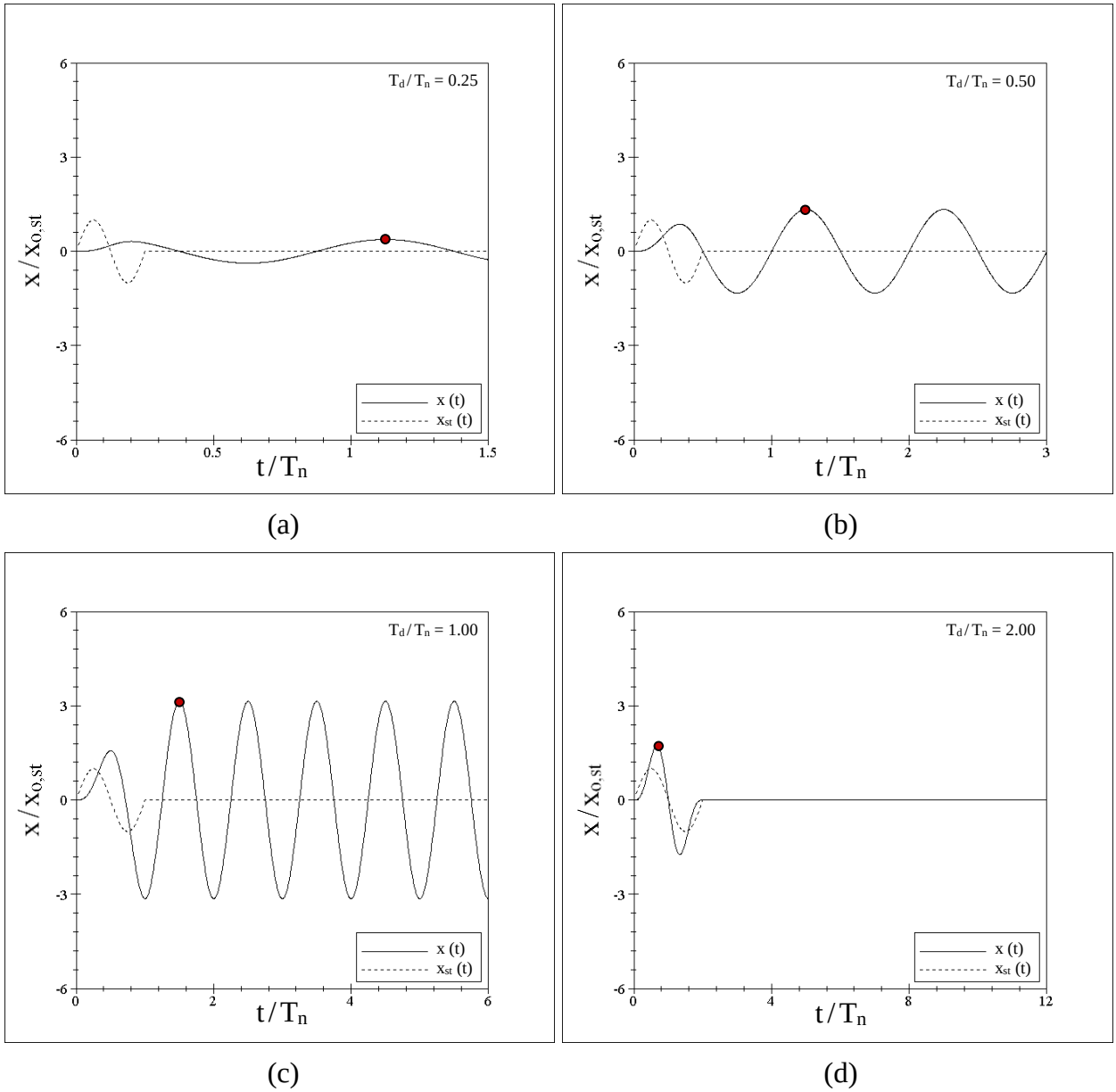


Figure 6.7: Dimensionless response of the four SDOF structures to the sinusoid forcing.

Dynamic amplification of the structure's response is illustrated in a more meaningful manner by plotting DLF(t) instead of x(t). This approach effectively eliminates the influence of the different structures' stiffness and conveys only the dynamic loading effect. The maximum static deflection $x_{o,st}$ previously defined in Eq. (6.27) is defined using each structures' stiffness and used to normalize the time history of the structure response (thereby defining DLF(t)). Time is also converted to dimensionless format, following Chopra's (1995) convention, by normalizing time with respect to the loaded structure's T_n. The four resulting response time histories are presented in Figure 6.7. Solid lines plot the DLF time history, and the dashed line illustrates the SDOF time history if the discrete values of the sinusoid of forcing were applied as static loads.

Figures 6.7a – 6.7d, provide far better illustration of the dynamic response amplification than Figures 6.6a – 6.6d. All four structures experience greater displacement than they would if a static force equivalent to the sinusoid's amplitude were applied. Generally speaking, the DLF increases as T_d/T_n approaches unity and decreases moving away from unity. The maximum DLF value for each structure is indicated by a red circle. Now a range of fundamental structure periods is selected, and structures having discrete T_n spanning that range are defined. The sinusoid forcing is applied to the SDOF system for each value of T_n, and the maximum DLF value is extracted. The DLF curve for a single sinusoid forcing profile is defined by plotting the DLF values for each value of T_n as a function of the ratio of the application period of the sinusoid to the fundamental period of the structure as shown in Figure 6.8. DLF values marked by red circles correspond to the values identified in Figure 6.7.

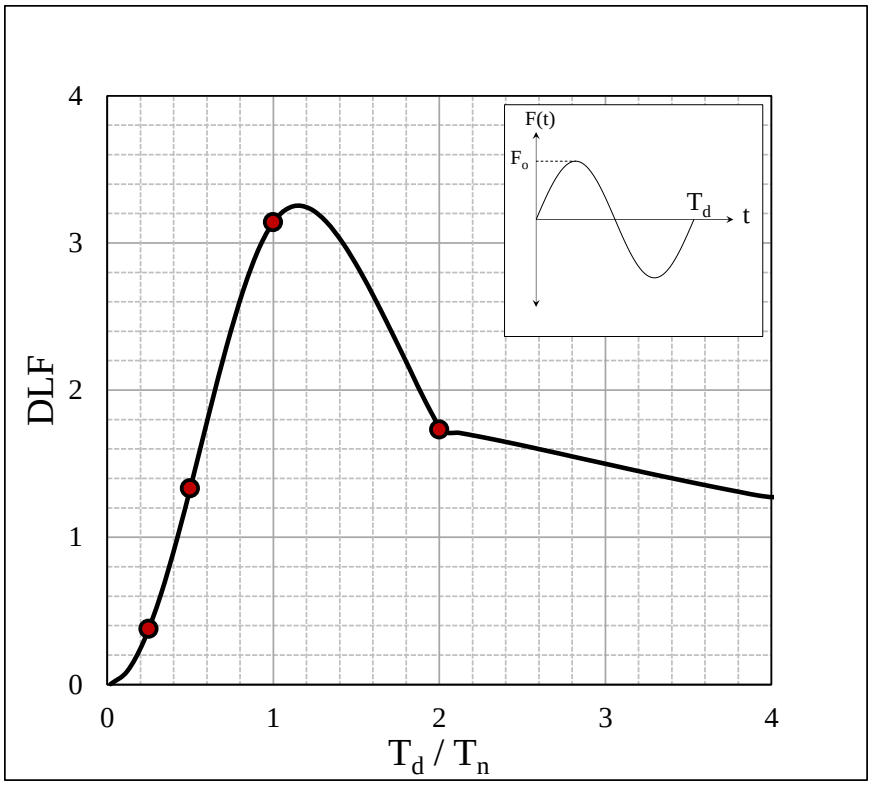
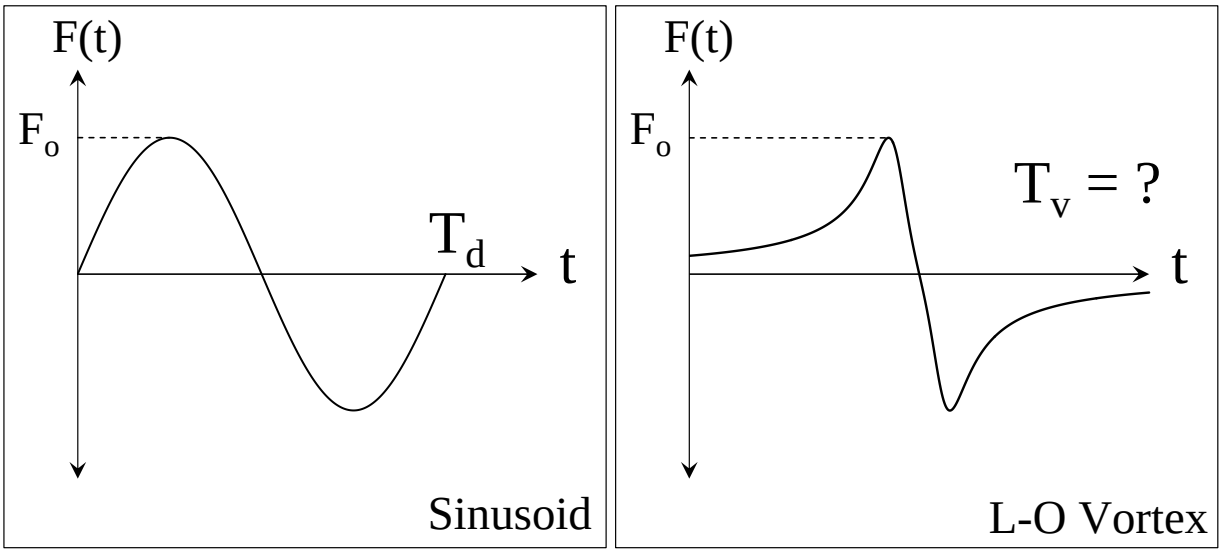


Figure 6.8: DLF curve for a single period of sinusoidal loading.

Figure 6.8 illustrates that when the period of the applied sinusoid and the fundamental period of the structure are similar, the sinusoidal profile of the applied loading results in a more than three-fold increase in the structure's deflection than if the load of equivalent magnitude F_o were applied statically. It is important to note that the dynamic nature of the forcing profile may substantially increase structure deflection even if T_d is less than or greater than T_n. This example illustrates the construction methodology and benefit of DLF curves. Specifically, if the profile of the impulsive forcing and the ratio of the load application period to the fundamental structure period are known, the associated dynamic amplification of the structure response can be deduced regardless of the individual values of T_d or T_n.

6.5 Definition of the Vortex Loading Period

The previous section discusses the DLF concept and illustrates the procedure for computing the DLF curve for a specified forcing profile. Generally stated, the DLF is a scalar value that increases or decreases the maximum structure response that the dynamically-applied forcing would produce if the maximum forcing amplitude were applied statically. Use of DLF curves requires knowledge of only the profile of the applied forcing and the ratio T_d/T_n to define the dynamic amplification of $x_{o,st}$. The fundamental structure period T_n can be computed during design or measured in existing structure; however, defining T_d for vortex forcing presents a challenge. Unlike the periodic sinusoid forcing profile shown in Figure 6.9a, the vortex's cross-stream forcing profile shown in Figure 6.9b does not become zero at a discrete time. Therefore, there is no intuitive definition of the vortex load application period T_v (T_d and T_v are analogous, but T_d defines generic forcing while T_v is specific to vortex forcing).



(a) (b)

Figure 6.9: (a) Sinusoid forcing profile having application period T_d and (b) vortex forcing profile having unknown application period T_v.

Generalization of the dynamic amplification of tornado wind loading necessitates definition of T_v. Previous studies of structure response to dynamic tornado wind loads study only

the response of a specific structure to a specific wind field rather than arriving at general conclusions. Parameters of vortices that load structures vary greatly, hence it is necessary to develop a methodology go compute T_v as function of the vortex's parameters. The subsequent sections utilize the DLF concept, applying forcing from two-dimensional computer simulation as forcing, to define T_v as function of the impinging vortex's parameters.

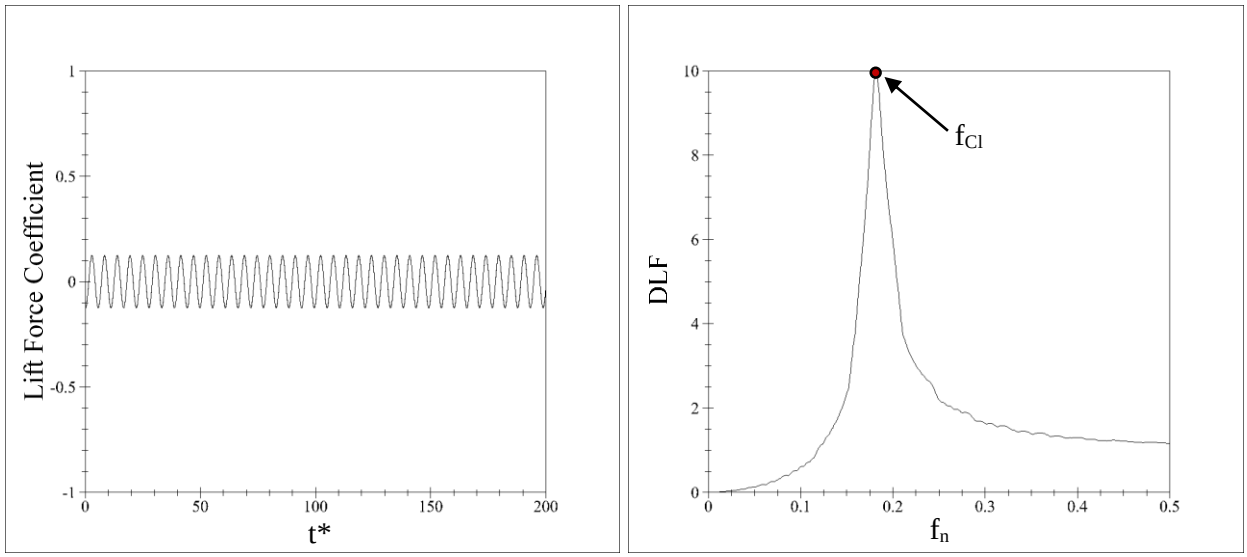
6.5.1 Methodology

Lift force coefficients from computer-simulated vortex loading of a rigid circular cylinder are applied as forcing to the SDOF response model. The DLF concept is applied to compute the fundamental structure period for which the structure's response experiences greatest dynamic amplification, and this is defined as the vortex load-application period T_v. The computer simulations are performed at $Re \leq 300$, hence the lift force coefficient is composed of mean and harmonic components. Giosan and Eng (2013) explain that vortex shedding does not occur when wind speeds exceed 15 m/s due to excessive turbulence in the air. This means the harmonic component of Cl is not a realistic component of tornado wind loading; therefore, the present study defines the vortex forcing profile as the mean component of Cl.

When the SDOF response model is forced with the Cl time history, it is expected that the mean component should produce dynamic response amplification at the vortex loading frequency $f_v = T_v^{-1}$. However, the presence of the harmonic component of Cl adds a complication, specifically that it should produce dynamically-amplified structure response at the vortex shedding frequency f_{Cl}. As the vortex approaches the cylinder, its tangential velocity augments the velocity of the stream over the cylinder and consequently increases the vortex shedding frequency. The impinging vortices studied herein are relatively large and slow-moving, hence it is speculated that the vortex loading frequency is notably less than the vortex shedding

frequency ($f_v < f_{Cl}$). Therefore, after noting the peak in the DLF curve at f_{Cl} produced by vortex shedding, the dynamic amplification produced by the mean component of Cl should appear as a distinct, lower-frequency peak at f_v.

Flow over the cylinder immersed in the free stream is simulated producing the force lift force coefficient time history illustrated in Figure 6.10a. This lift force coefficient time history is then applied as forcing to the SDOF response model; breaking from common convention, the damping ratio of the system is set to $\zeta = 5\%$ to avoid resonant response when the structure fundamental frequency $f_n \approx f_{Cl}$. Figure 6.10b plots the DLF curve for the lift force coefficient time history; the distinct peak at the vortex shedding frequency $f_n \approx f_{Cl}$ is marked by the callout. The maximum DLF value of 9.99 is practically equivalent to the theoretical maximum value $DLF = (2 \cdot \zeta)^{-1} = 10.0$ for a system damped at $\zeta = 5\%$.

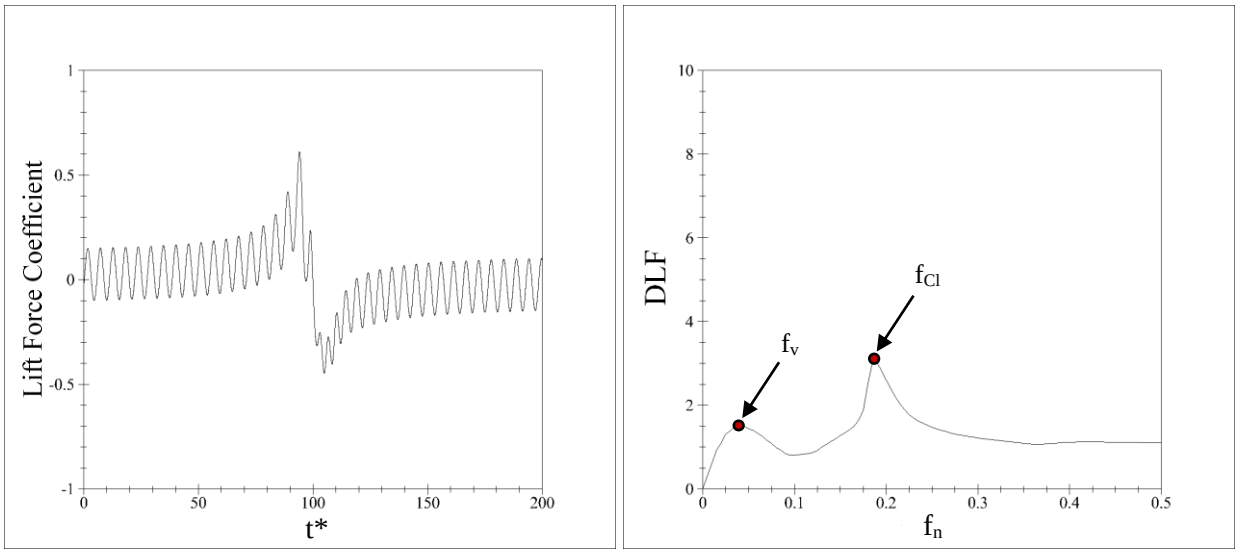


(a) (b)

Figure 6.10: Free stream lift force coefficient (a) time history and (b) DLF curve.

Vortex impact with the cylinder is now simulated, and the resulting lift force coefficient time history is illustrated in Figure 6.11a. The lift force coefficient time history as forcing to the SDOF response model, allowing construction of the DLF curve illustrated in Figure 6.11b. The

harmonic component of Cl still produces the distinct DLF curve peak at f_{Cl}. However, there is an additional distinct, lower frequency peak in the DLF curve indicated by the callout f_v. This is the vortex loading frequency and is the fundamental structure frequency which experiences the maximum dynamic response amplification due to the vortex loading.



(a) (b)

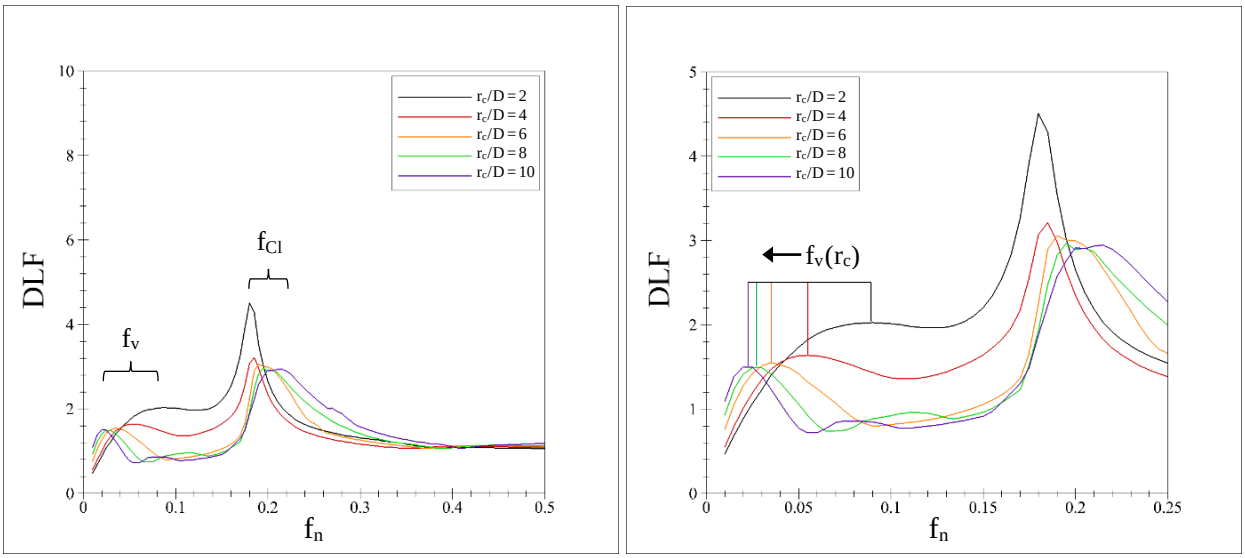
Figure 6.11: Vortex loading lift force coefficient (a) time history and (b) DLF curve.

The vortex loading frequency f_v is now defined as the fundamental structure frequency that exhibits the greatest dynamic response amplification to the mean component of Cl. The subsequent subsections use the L-O vortex profile and define $T_v = f_v^{-1}$ as function of the vortex's critical radius r_c and translational velocity U_∞. Finally, cylinder loading by RCVM and S-K vortices is simulated to establish the influence of the vortex's tangential velocity profile on T_v.

6.5.2 Influence of Vortex Size on Vortex Loading Period

The first parameter studied in defining the vortex loading period is the size, specifically the critical radius r_c, of the impinging vortex. The maximum vortex tangential velocity and vortex translational velocity are fixed and equivalent ($V_{\theta,max} = U_\infty = 1.0$), and the size of the impinging vortex is increased from $r_c = 2 \cdot D$ to $10 \cdot D$. Lift force coefficient time histories from

each simulation are applied as forcing to the SDOF response model, and the resulting DLF curves are plotted in Figure 6.12a. Figure 6.12b is a zoomed view of the peaks in the DLF curves.



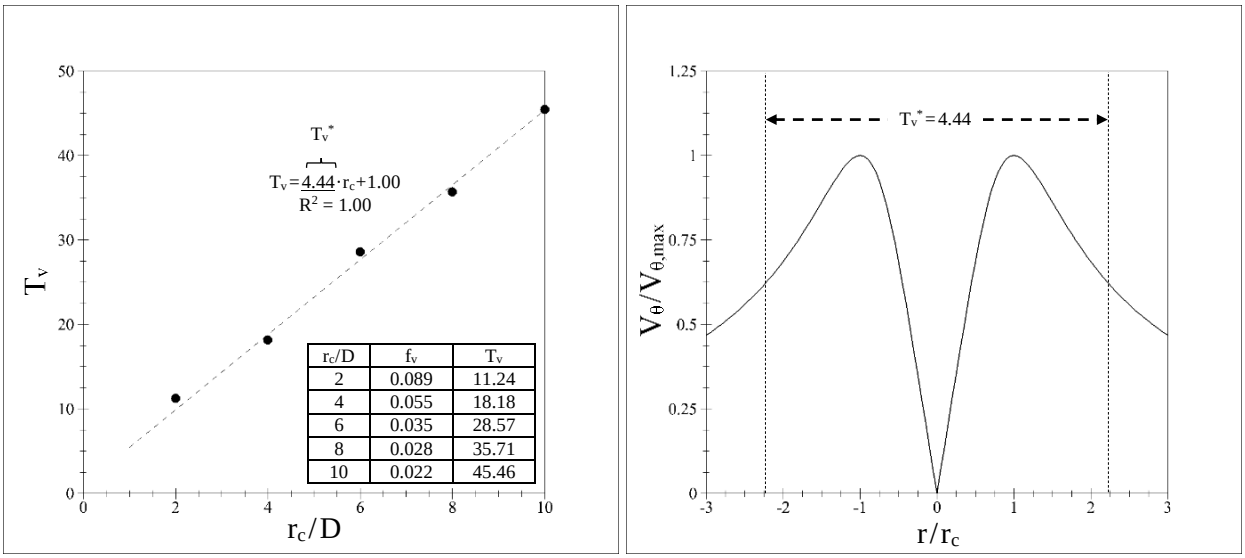
(a) (b)

Figure 6.12: (a) Lift force coefficient DLF curves and (b) zoomed view of f_v illustrating the progressive decrease in f_v with increasing r_c.

Two general observations are made from the DLF curves in Figures 6.12a and 6.12b. First, the DLF curve peaks associated with f_{Cl} progressively move right-ward and broaden as r_c increases. This is because the larger impinging vortex progressively augments the velocity of the stream over the cylinder pre-impact, hence f_{Cl} progressively increases. Second, $T_v = f_v^{-1}$ progressively increases with r_c as shown in Figure 6.12b. Intuitively, this is because a larger vortex interacts with the cylinder for longer time, hence the load application period is longer.

Vortex loading frequency values (marked by vertical lines in Figure 6.12b are extracted and inverted to give the vortex loading period for each considered r_c value. The vortex load application period T_v is then plotted as function of r_c in Figure 6.13a, revealing that $T_v(r_c)$ is a linear trend. The slope of $T_v(r_c)$, is now defined as the dimensionless vortex loading period T_v^*. The dimensionless vortex loading period T_v^* corresponds to the dimensionless region of the

vortex's tangential velocity profile that is illustrated in Figure 6.13b for the L-O vortex. It is postulated that T_v is the time required for the portion of the vortex's tangential velocity profile defined by T_v^* to cross the loaded structure.

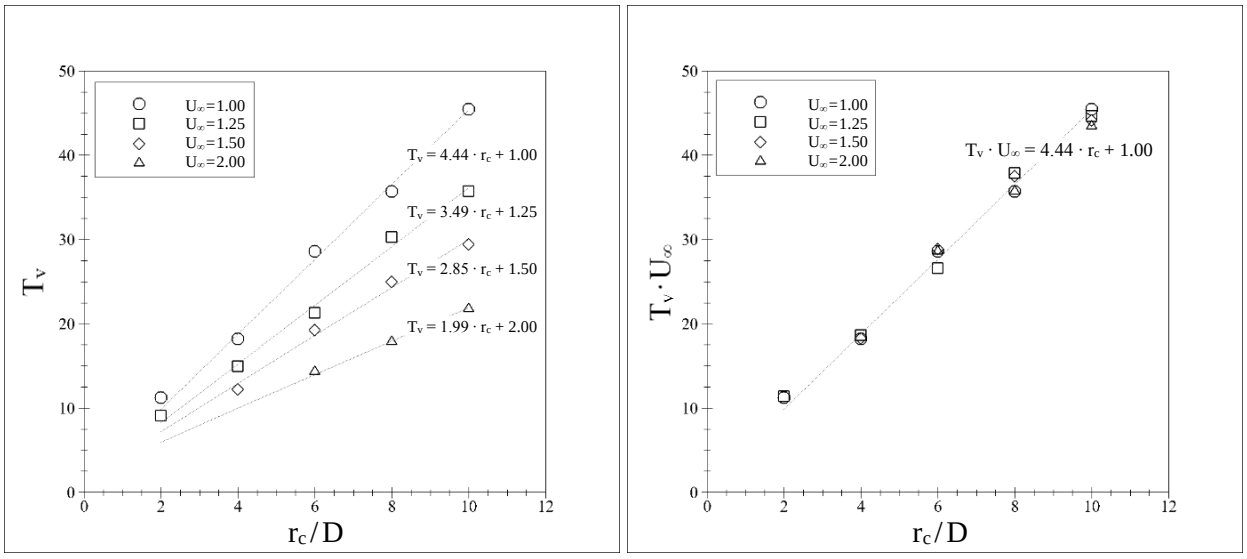


(a) (b)

Figure 6.13: (a) Vortex loading period as function of vortex critical radius for $r_c = 2 \cdot D$ to $10 \cdot D$ and (b) dimensionless region of the L-O vortex's tangential velocity profile corresponding to T_v.

6.5.3 Influence of Vortex Translational Velocity on Vortex Loading Period

Now the influence of the impinging vortex's translational velocity on the vortex loading period is evaluated. The vortex's maximum tangential velocity remains fixed at $V_{\theta,max} = 1.0$, and the vortex's translational velocity is incremented from $U_\infty = 1.0$ to 2.0. For each considered translational velocity, the vortex size is incremented from $r_c = 2 \cdot D$ to $10 \cdot D$. Lift force coefficient time histories from each simulation are applied as forcing to the SDOF response model, and T_v is extracted for each. The vortex loading period decreases when r_c decreases or U_∞ increases, hence f_v approaches f_{Cl} and there is no distinct peak in the DLF curve for some combinations of small r_c and large U_∞ (which is why the data set for $U_\infty = 2.0$ only has three data points). Figure 6.14a summarizes $T_v(r_c)$ for each considered translational velocity.



(a) (b)

Figure 6.14: (a) Vortex loading period as function of vortex translational velocity and (b) consolidation of vortex loading period curves using Eq. (6.29).

The trend $T_v(r_c)$ is linear for all considered U_∞, and, as one would expect, increasing the vortex's translational velocity decreases the associated value of T_v. The postulation raised in the previous subsection, specifically that T_v is the time required for the portion of the dimensionless vortex profile defined by T_v^* to cross the loaded structure is defined by Eq. (6.29).

$$T_v = T_v^* \cdot r_c \cdot U_\infty^{-1} \tag{6.29}$$

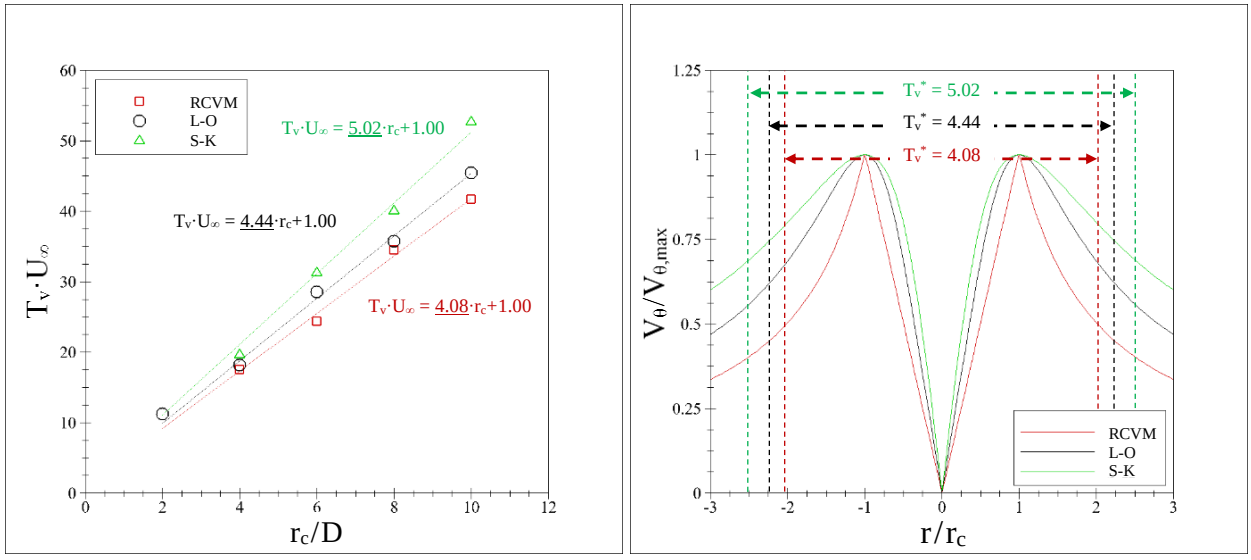
The data plotted in Figure 6.14a are now re-plotted in Figure 6.14b using the definition of T_v defined by Eq. (6.18). The $T_v(r_c)$ curves compress to the trend line previously defined in Figure 6.13a (Defined using $U_\infty = 1$). This confirms the postulation that T_v is the time required for the dimensionless region of the vortex profile defined by T_v^* to cross the loaded structure. Eq. (6.2) establishes the generalized relationship between T_v and the two vortex parameters r_c and U_∞.

6.5.4 Influence of Vortex Profile on Vortex Loading Period

Chapter 3 reports an extensive review of analytical and measured vortex tangential velocity profiles. Measured tornado vortex profiles range from smooth (S-K vortex) to sharp and discontinuous (RCVM vortex), meaning a tornado vortex's forcing profile may vary greatly.

Dynamic amplification of a structure's response depends upon the applied forcing profile, hence it is postulated that T_v is a function of the impinging vortex's tangential velocity profile in addition to its size and translational velocity.

The L-O vortex profile has been used up to this point because it is representative of the "typical vortex". Now the S-K and RCVM vortex profiles are used to evaluate the respective influences of flatter and sharper vortex profiles on T_v. Analysis in Chapter 3 concludes that that the Sullivan vortex profile is a better representation of most of the sharper measured vortex profiles than the RCVM profile is. However, the RCVM profile is used here for two reasons: it is a more extreme sharper profile, and some measured vortex profiles do fit it. Therefore, use of the RCVM profile in place of the Sullivan profile affords a better representation of the sharpest possible vortex profile. The methodology outlined in Section 6.5.2 is now repeated for the S-K and RCVM profiles, and the resulting trends $T_v \cdot U_\infty(r_c)$ are summarized in Figure 6.15a along with the trend for the L-O vortex previously-defined in Figure 6.13a.



(a) (b)

Figure 6.15: (a) Definition of $T_v(r_c)$ for the three vortex profiles and (b) dimensionless regions of the three vortex tangential velocity profiles corresponding to T_v^*.

Figure 6.15a shows that T_v progressively lengthens (RCVM to L-O to S-K) as the vortex's tangential velocity profile flattens. The definition to T_v^* is retained and illustrated for all three vortex profiles in Figure 6.15b. The vortex load-application period has now been defined as function of the three primary variables that characterize intense vortices, specifically, size (r_c), translational velocity (U_∞), and vortex tangential velocity profile (RCVM, L-O, or S-K). The definition of T_v in Eq. (6.29) defines the fundamental structure frequency that will experience maximum dynamic response amplification due to cross-stream loading from a vortex.

6.5.5 Why Use the DLF Instead of the Fourier transform to Identify T_v?

The present study utilizes DLF analysis, specifically comparing the response of structures having a spectrum of fundamental periods T_n, to identify the vortex loading period T_v. The DLF analysis may seem to be a roundabout approach, as one might think that the discrete Fourier transform (DFT) should directly decompose the forcing into constitute components, directly yielding T_v. However, the DFT is unable to isolate T_v from a given vortex forcing time history while the DLF is able to. One postulation for the superior performance of the DLF anlysis is that practically any T_n resolution may be utilized, while f_n resolution is constrained to integer multiples of $2/T_{signal}$, where T_{signal} is the duration of the forcing. If the exact vortex loading period is not considered in the DFT, specifically $T_v = 1/f_n$, the component of forcing at the vortex frequency $f_v = 1/T_v$ will be leaked to the neighboring adjacent frequencies, thereby reducing its resolution. Stull (1988) reports numerous other factors that influence accuracy and resolution of the DFT. Briefly summarized, DLF analysis is used to identify T_v because the DFT is unable to do so. Numerous parameters of the forcing can influence accuracy of the DFT, but identification of the specific parameters in the vortex forcing is beyond the scope of this study.

The subsequent examples illustrate the inability of the DFT to resolve T_v utilizing the forcing produced by a free stream and by vortex impact from Section 6.5.1.

Figure 6.16.1a illustrates the lift force coefficient time history from simulated free stream flow over a cylinder. The forcing is harmonic due to shedding of vortices from the cylinder at frequency f_{Cl}. The vortex shedding frequency f_{Cl} is accurately captured by both Fourier Transform and DLF analysis as respectively shown in Figures 6.16.1b and 6.16.1c.

Figure 6.16.2a illustrates the lift force coefficient time history from vortex impact with the cylinder. The vortex shedding frequency changes as the vortex approaches the cylinder as evidenced by the numerous constituting frequencies detected on either side of the original vortex shedding frequency identified in Figure 6.16.1b. The vortex loading frequency f_v that is

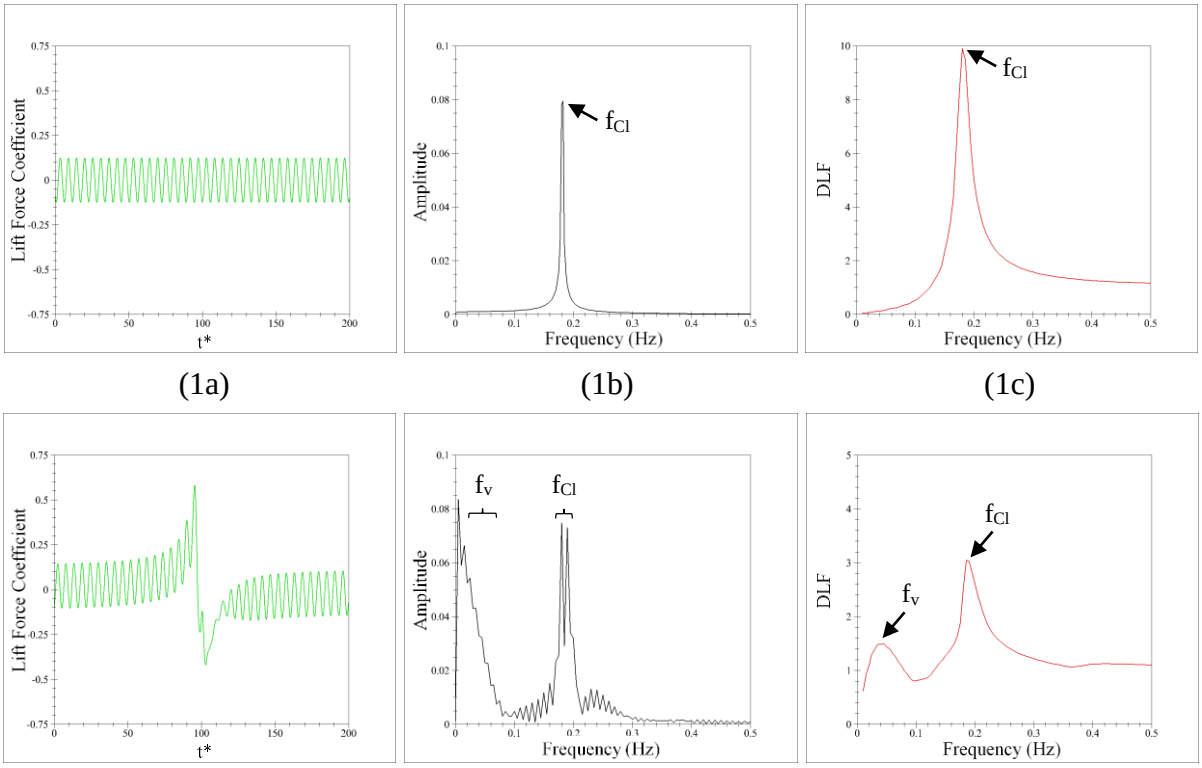


Figure 6.16: (a) Lift force coefficient time history, (b) corresponding Fourier Transform, and (c) corresponding dynamic load factor curve for (1) simulated free stream flow over a cylinder and (2) simulated vortex impact with a cylinder.

associated with the mean component of the lift force coefficient is an indistinguishable lower frequency $f_v < f_{Cl}$ as indicated in Figure 6.16.2b. However, when the vortex loading is applied to a response model in DLF analysis, f_v emerges as the distinct peak indicated in Figure 6.16.2c. It is therefore concluded that DLF analysis rather than Fourier analysis is necessary to identify the vortex loading frequency f_v.

6.6 Use of Empirical Equations to Define Vortex Loading

6.6.1 Overview

Up to this point, lift force coefficient time histories from computer-simulated loading of a circular cylinder by an impinging vortex have been applied as forcing to define T_v. These simulations are restricted to $Re \leq 300$ because the current computer model is two-dimensional. Consequently, vortex shedding from the cylinder produces a harmonic loading component that is not realistic of loading by tornado vortices. Additionally, the computer simulations are computationally expensive, requiring approximately 48 hours of CPU time to execute. Finally, the utilized grid and the model's numerical stability limit the range of usable vortex parameters.

Generalization of the methodology to assess the possible dynamic response amplification of structures to tornado wind loads requires definition of DLF curves for the identified vortex velocity profiles. Tornado wind loads do not produce vortex shedding, hence only the mean component of the lift force coefficient need be applied as forcing. A set of empirical equations Eqs. (5.1-6) are developed in Section 5.4.3 to define the cylinder loading as a function of the velocity incident on the cylinder. The present analysis applies the vortex velocity boundary condition's governing equations Eqs. (4.8a-4.10b) to define the time history of the stream velocity incident on the cylinder, and then uses the empirical equations to define the corresponding force coefficient time histories. The equation-defined forcing is validated by

comparison with force coefficient time histories from computer simulation. Subsequently, it is applied to assess the influence of the vortex velocity ratio on T_v, a study which could not be performed previously due to numerical instability of the computer model.

6.6.2 Validation of Empirical Equation-Defined Forcing

The primary assumptions that are made when using the empirical equations to define the cylinder loading are that the same velocity effectively acts over the entire cylinder surface and that the velocity is the velocity that would act at the location of the cylinder center if the cylinder were not present to disrupt the flow around it. These assumptions are reasonably met when the impinging vortex is much larger than the cylinder. Therefore, the first stage of model validation is to assess the accuracy with which they replicate the cylinder loading from computer simulation. This serves as additional validation to that previously reported in Figure 5.20.

Following the approach used in Section 5.4.3, the validation study is performed with impinging vortices having critical radius $r_c = 50 \cdot D$. The maximum resultant velocity V_R in the domain is restricted to 2.0, because this is the limit to which the empirical equations are defined. The first comparison is for the vortex velocity ratio $V_{\theta,max}/U_\infty = 1.0$, and the second comparison is performed for $V_{\theta,max}/U_\infty = 4.3$. Figures 6.17a and 6.17b respectively illustrate the comparison of force coefficient time histories defined by the empirical equations with those from computer simulation for vortex velocity ratios of 1.0 and 4.3. Colored lines illustrate force coefficient time histories from computer simulation, and black solid and dashed lines respectively illustrate mean and harmonic components of the force coefficient time histories defined using the empirical equations. The equation-defined forcing replicates the computer simulation forcing with excellent accuracy.

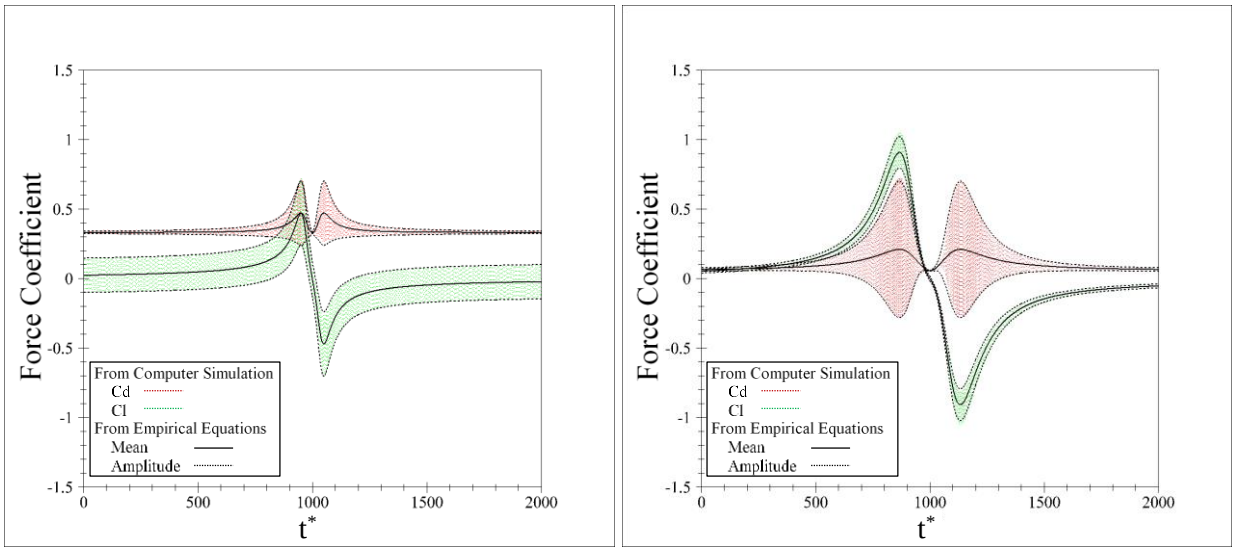


Figure 6.17: Comparison of force coefficient time histories from computer simulation and defined by the empirical equations: (a) $V_{\theta,max}/U_\infty = 1.0$ and (b) $V_{\theta,max}/U_\infty = 4.3$.

Empirical equations are able to replicate force coefficient time histories from computer simulation with excellent accuracy when the impinging vortex is much larger than the loaded cylinder. However, as the impinging vortex's size is reduced, the assumption that the entire cylinder surface is exposed to the same velocity becomes increasingly-erroneous. The purpose of this study is to attain the mean component of the lift force coefficient to assess its capability to produce dynamically-amplified structure response. The preceding studies have successfully identified the fundamental structure period that experiences maximum dynamic response amplification. Therefore, now mean lift force coefficient time histories are applied as forcing to the SDOF response model to determine whether or not they excite maximum structure response at the same fundamental periods as do force coefficient time histories from computer simulation.

The empirical equations are used to define the mean lift force coefficient time histories produced by vortices having RCVM, L-O, and S-K profiles, examples of which are illustrated in Figures 6.18.1a – 6.18.1c. Impinging vortex sizes of $r_c = 2 \cdot D$ to $10 \cdot D$ are considered for each of the three vortex profiles, while the vortex and stream velocity are fixed $V_{\theta,max} = U_\infty = 1.0$. The

equation-defined forcing is applied to the SDOF response model, and the resulting vortex loading periods are extracted and summarized in Figures 6.18.2a – 6.18.2c. Vortex loading periods defined using the equation-defined forcing are practically identical to those defined by applying vortex loading from computer simulation as forcing. It is therefore concluded that the mean lift force coefficient time histories defined using the empirical equations accurately represents the mean component of the lift force coefficient time history from computer simulation, meaning the empirical equations can now be used to define force coefficient time histories for subsequent analysis.

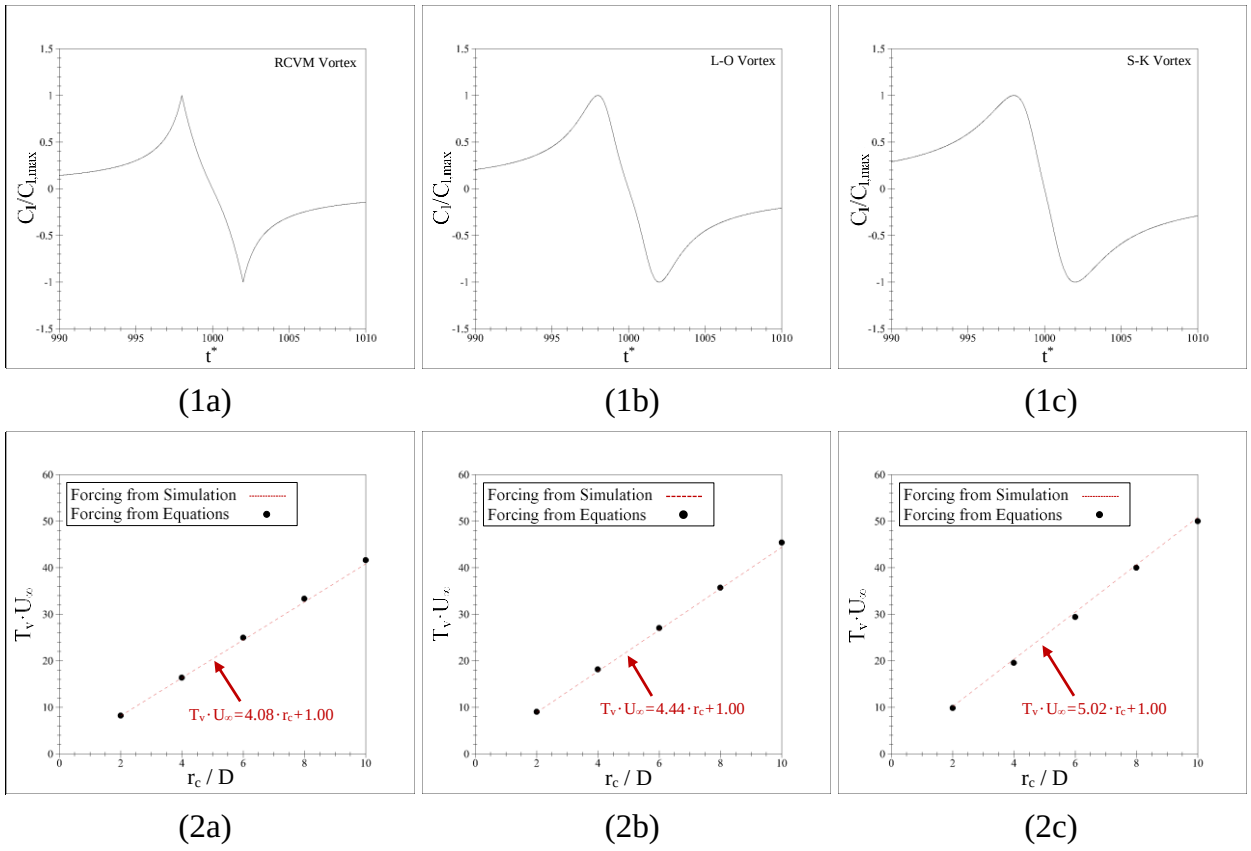
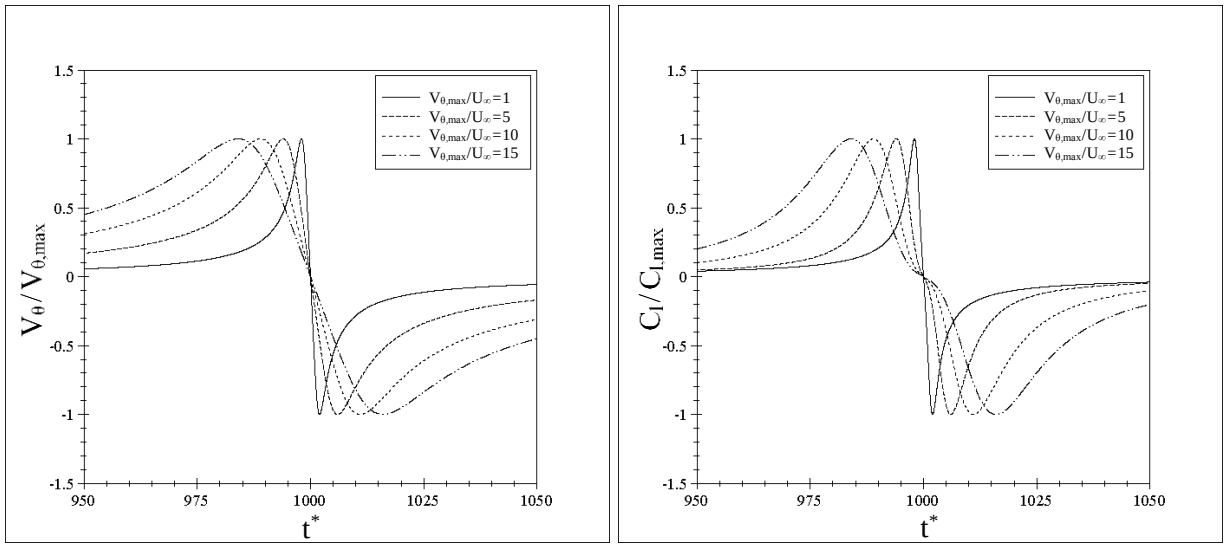


Figure 6.18: (1) Mean lift force coefficient time histories for (a-c) RCVM, L-O, and S-K vortex profiles and (2) comparison of T_v from DLF of equation-defined forcing (black dots) with Eq. (6.18) (dashed line).

6.6.3 Influence of Vortex Velocity Ration on Vortex Loading Period

Vortex loading of structures occurs in numerous scenarios, and the vortex velocity ratio $V_{\theta,max}/U_\infty$ varies greatly depending upon the loading scenario. Blade-vortex interaction is typically characterized by $V_{\theta,max}/U_\infty \leq 1.0$, while vortex velocity ratios of documented tornados and hurricanes span $3.0 \leq V_{\theta,max}/U_\infty \leq 15.0$. Figures 6.19a and 6.19b respectively illustrated time histories of the normalized tangential velocity incident on the cylinder from the vortex and the resulting lift force coefficient time histories for vortex velocity ratios ranging from $3.0 \leq V_{\theta,max}/U_\infty \leq 15.0$. For a velocity ratio of unity, the tangential velocity time history and lift force coefficient time history are similar. However, as $V_{\theta,max}/U_\infty \rightarrow 15$, the profile of the lift force coefficient becomes increasingly flatter near $t^* = 1000$ and deviates from the tangential velocity profile. The profile of the vortex loading controls T_v; because the profile visibly change, it is therefore necessary to confirm the validity of the definition of T_v given by Eq. (6.29).

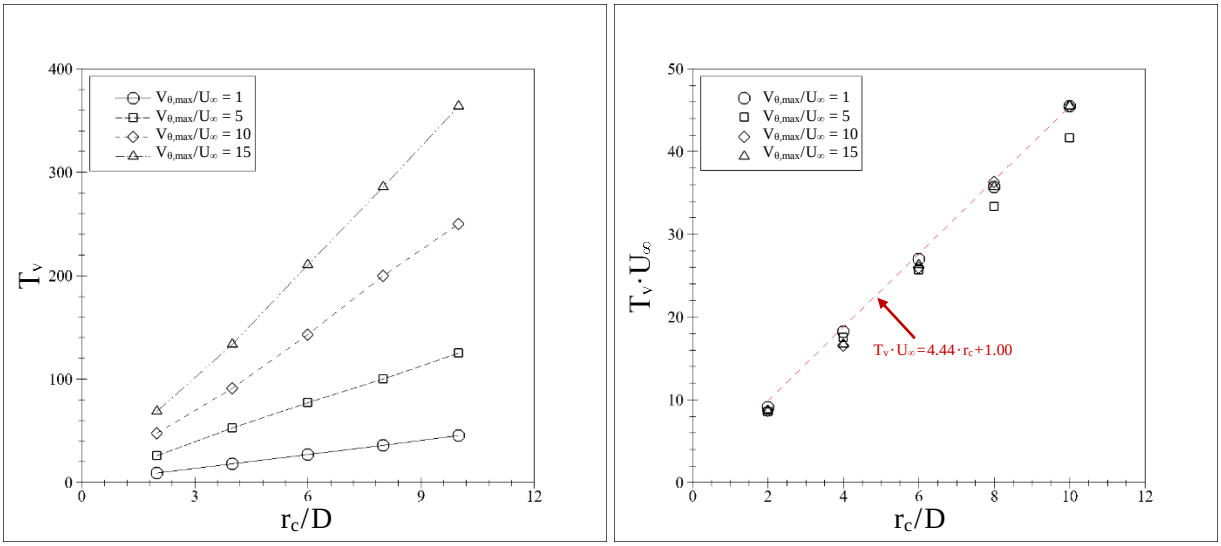


(a) (b)

Figure 6.19: Variation in (a) tangential velocity time history and (b) the mean lift force coefficient time history with variation in vortex velocity ratio.

Force coefficient time histories are defined for a L-O vortex having fixed maximum resultant velocity $V_R = 2.0$ for each of the vortex velocity ratios illustrated in Figure 6.19.

Impinging vortex sizes of $r_c = 2 \cdot D$ to $10 \cdot D$ are considered to maintain consistency with the methodology used up to this point. Each forcing profile is applied to the SDOF response model, and the resulting trends $T_v(r_c)$ are summarized for each vortex velocity ratio in Figure 6.20a. The maximum resultant velocity V_R is fixed, and the vortex velocity ratio is inversely proportional to U_∞; it follows that the vortex loading period increases with increasing vortex loading period as illustrated in Figure 6.20a. However, Figure 6.20b illustrates that the data in Figure 6.20a compress to the definition of Eq. (6.29).



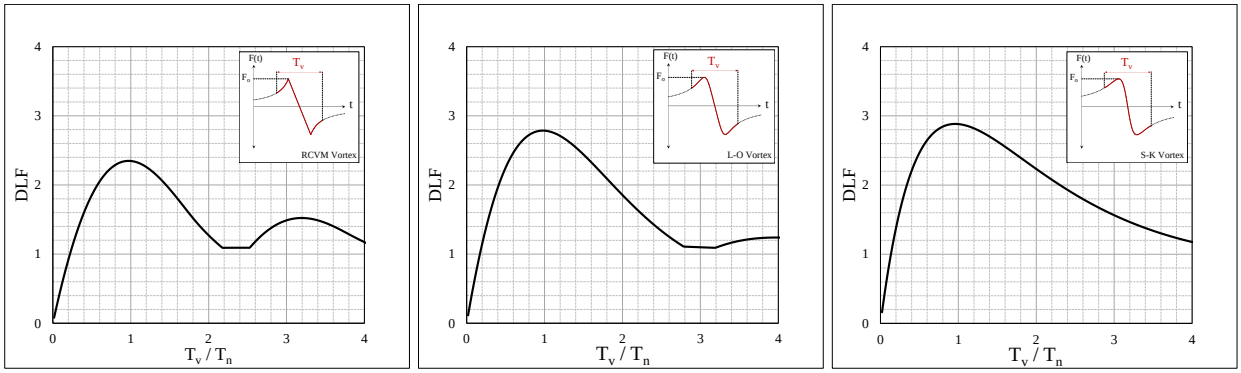
(a) (b)

Figure 6.20: (a) Vortex loading period curves for considered vortex velocity ratios and (b) comparison of vortex loading periods with the definition given by Eq. (6.29).

The preceding study has served the dual purpose of further validating the definition of the vortex loading period by Eq. (6.29) by further demonstrating the capability of the empirical equations to accurately reproduce cylinder loading from computer simulation. The mean lift force coefficient defined using the empirical equations can now be used with confidence to define DLF curves for vortex-induced loading.

6.7 Definition of DLF Curves for Vortex Loading

The previous section demonstrates that mean lift force coefficient profiles defined by empirical equations replicate those produced by computer simulation for RCVM, L-O, and S-K vortices. Now these force coefficient time histories are applied as forcing to the SDOF response model, and the procedure outlined in Section 6.4.1 is used to define DLF curves for each of the vortex profiles. For each of the vortex profiles, T_v is defined using Eq. (6.29). If comparing with Section 6.4.1, recall that T_v is analogous to T_d, but simply references to the vortex load application period rather than the load application period of a general dynamic load. Figures 6.21a – 6.21c respectively illustrate the DLF curves for the RCVM, L-O, and S-K vortex profiles.

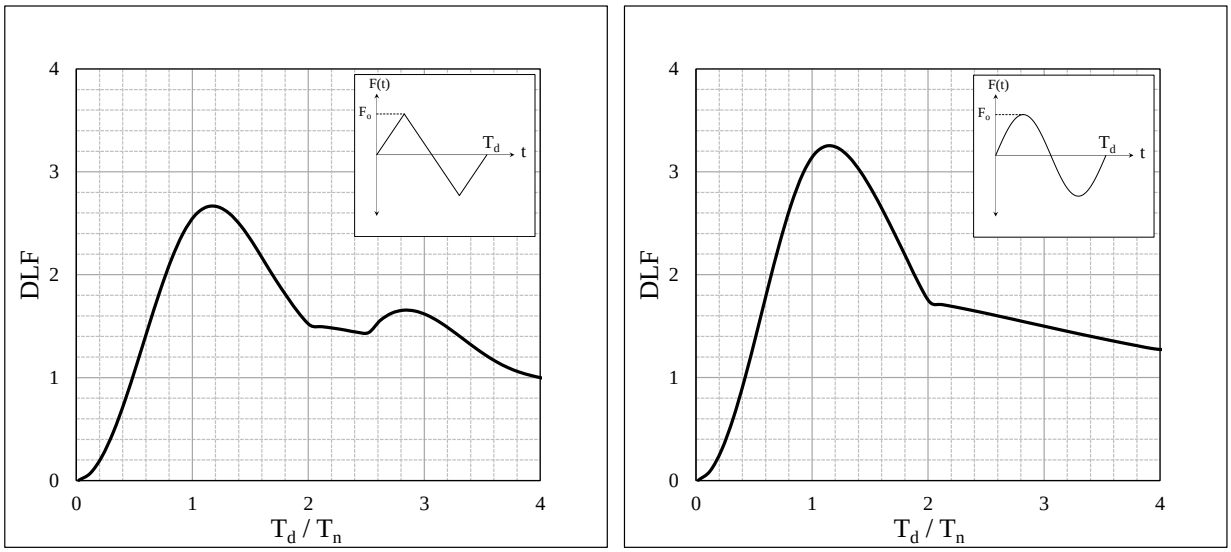


(a) (b) (c)

Figure 6.21: DLF curves for vortex loading by vortices having (a) RCVM, (b) L-O, and (c) S-K tangential velocity profiles.

The vortex loading DLF curves change in two primary ways as the vortex profile transitions from sharp (RCVM) to smooth (S-K). First, the maximum value of the DLF curve progressively increases: 2.35 (RCVM) → 2.78 (L-O) → 2.88 (S-K) as the vortex's profile flattens. Additionally, the pronounced, secondary peaks in the DLF curve (Figure 6.21a) flatten (Figure 6.21b) and disappear (Figure 6.21c) as the vortex profile flattens (RCVM to S-K profile). Both of these trends are observed when DLF curves for the sharp triangle wave and the smooth

sine wave (Figures 6.22a and 6.22b) are compared, providing qualitative validation of the methodology used to define the vortex loading DLF curves Figures 21a – 21c. Now the definition of T_v given by Eq. (6.29) and the vortex loading DLF curves can be used to define the dynamic amplification of a specified structure's response to loading by a specified vortex.



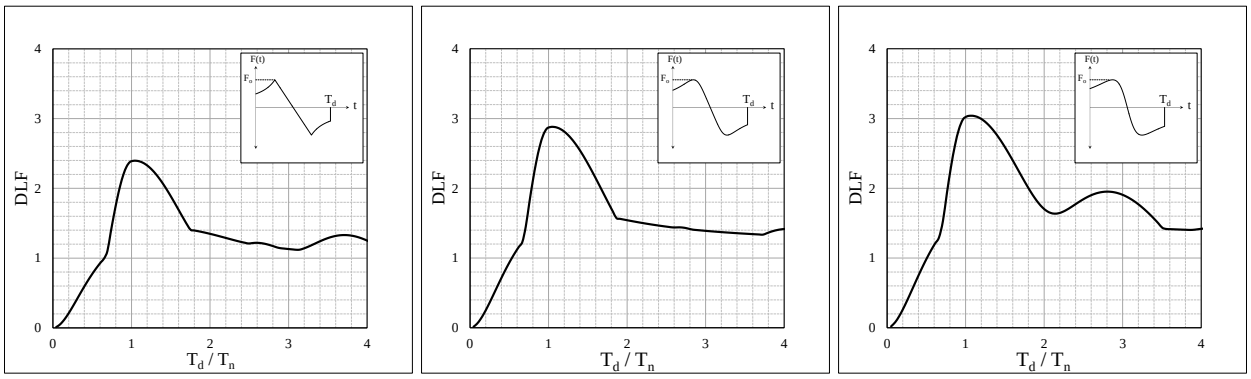
(a) (b)

Figure 6.22: DLF curves for (a) triangle wave and (b) sine wave forcing profiles.

6.7.1 Application of Only T_v as Forcing

An additional study is now conducted where only the region of the vortices' forcing profile defined by T_v^* as forcing and corresponding DLF curves are constructed. ***Figures 6.23a – 6.22c*** illustrate DLF curves produced by applying only the portion of the RCVM, L-O, and S-K profiles that constitute the vortex loading period to the SDOF response model. Generally speaking, the maximum amplitudes of these DLF curves are slightly greater than the maximum amplitudes produced when the entire vortex forcing profiles are applied. Additionally, the DLF curves in ***Figures 6.23a – 6.23c*** are much rougher and more irregular than the DLF curves in ***Figures 6.21a – 6.21c***. In reality, application of only the portion of the vortex loading profile defined by T_v is not realistic of loading by a vortex, where the wind field gradually builds as the

vortex approaches the loaded structure. Instead, it immolates a suddenly-applied load that varies in time before being suddenly removed. Therefore, the DLF curves defined in ***Figures 6.20a – 6.20c*** are the vortex loading DLF curves that shall be considered in subsequent analysis.



(a) (b) (c)

Figure 6.23: DLF curves produced by application of only the portion of the vortex forcing profile defined by T_v for (a) RCVM, (b) L-O, and (c) S-K vortex profiles.

6.8 Definition of the Generalized DLF Curve for Tornado Wind Loads

Section 6.5 develops Eq. (6.29) to compute the vortex load application period T_v based upon the vortex's size r_c, translational velocity U_∞, and tangential velocity profile. ***Sections 6.6 – 6.7*** develop DLF curves (***Figures 6.21a – 6.21c***) defining the maximum dynamic response amplification for a structure having specified fundamental period T_n. Now ***Section 6.8*** combines these findings along with the documented range of tornado vortex parameters to define the generalized DLF curve for structure response to tornado wind loadings.

6.8.1 Tornado Vortex Parameters and Fundamental Structure Periods

The vortex loading period defined in Eq. (6.29) is a function of two vortex parameters, r_c and U_∞, and the vortex's tangential velocity profile, the influence of which is integrated through T_v^*. It is not possible to define the range of tornado vortex parameters with complete confidence because vortex parameters change continuously throughout the tornado's duration and are notably different between storms. Furthermore, both technological limitations and the random

nature of tornado occurrence limit the documentation of tornado properties. However, the tornado-vortex parameters reported herein are compiled following extensive review of extreme tornado events, and the parameters summarized in Table 6.2 are believed to represent the documented severe-storm parameter range.

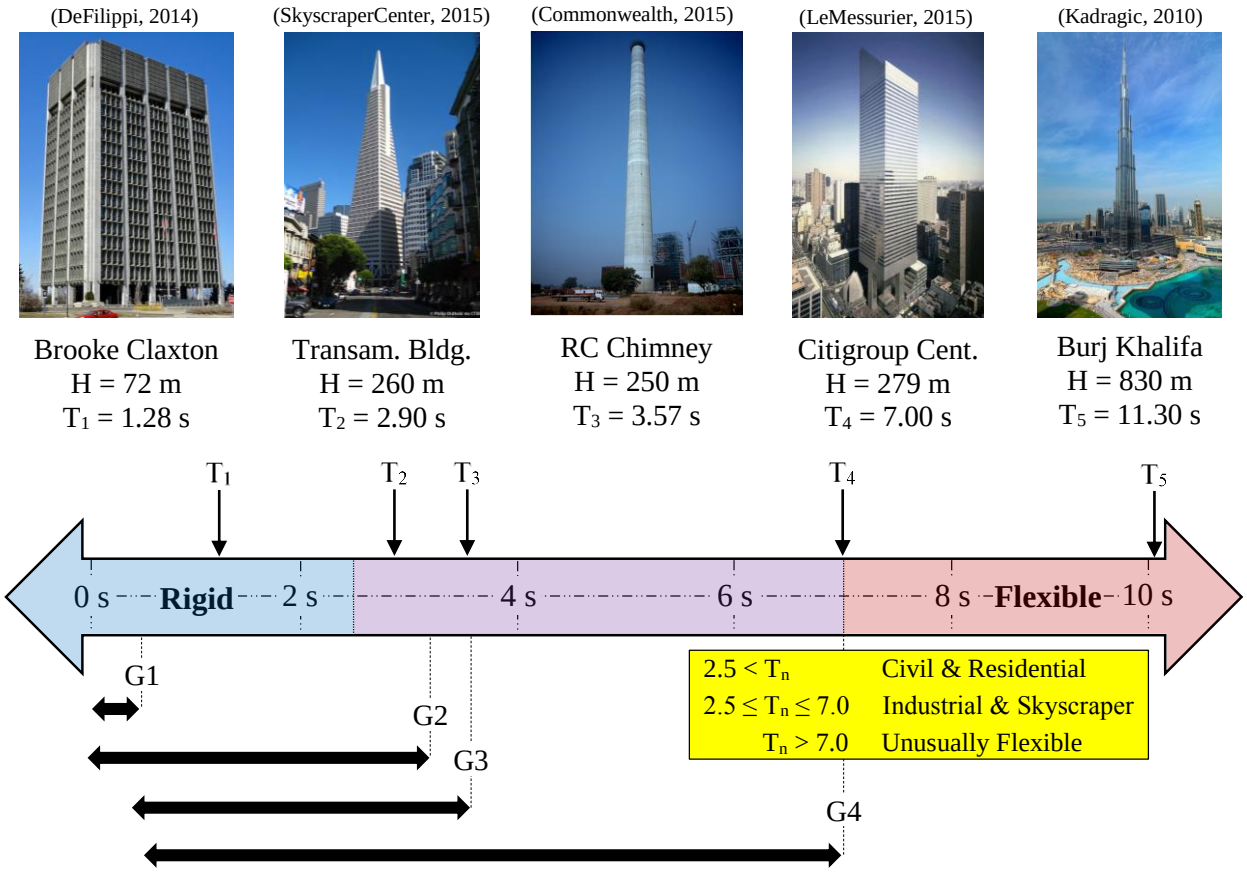
Table 6.2: Range of documented tornado vortex parameters for defining T_v using Eq. (6.18).

Parameter	Units	Minimum	Maximum
r_c	m	46.0 (Fujita, 1981)	2008.0 (NOAA, 2013a)
U_∞	$m \cdot s^{-1}$	11.6 (NOAA, 2013b)	32.6 (Fujita, 1973)
T_v^*	~~~	4.08	5.02

Table 6.3: Fundamental periods for real-world structures.

Structure	Description	T_n (s)	Source
Wood-Frame Structures			
"Typical" Single-Story Residence	Undamaged	0.15 to 0.20	Graf (2008)
···	Damaged	< 0.50	···
4-Story Structure on CC Slab	Undamaged	0.233 to 0.250	Hafeez et al. (2014)
···	Damaged	0.345 to 0.370	···
5-Story Structure on CC Slab	H = 15.24 m	0.40 to 0.55	Thompson (2015)
Civil Structures and Skyscrapers			
Shear Wall Structures	RC, (12 x 8 x 5.6m)	0.035	Balkaya and Kalkan (2003)
···	RC, (27 x 24 x 42m)	0.918	···
Buildings with Load Bearing Walls and	RC, (71 x 10.98 x 8.45m)	0.146 to 0.186	Hong and Hwang (2000)
Moment-Resisting Frames	RC, (51.64 x 17 x 77.1m)	0.877 to 1.449	···
Nuclear Reactor Housing	RC, Dome-Roofed	0.15 to 0.50	Chopra (2005)
13 Buildings with Load Bearing Walls	RC, H = 15 m	0.155 to 0.294	Kuz. and Was. (2006)
Morrow Point Dam	RC, H = 139 m	0.268 to 0.303	Chopra (2005)
37 Moment-Resisting Frame Structures	RC, 9 < H < 91 m	0.27 to 3.19	Goel and Chopra (1997)
PineFlat Dam	RC, H = 122 m	0.288 to 0.306	Chopra (2005)
21 Buildings in LA, CA	RC and Steel, 20 < H < 100 m	0.397 to 3.704	Todorovska et al. (2005)
53 Moment-Resisting Frame Structures	Steel, 12.5 < H < 257 m	0.60 to 6.50	Goel and Chopra (1997)
Medical Center, Richmond CA	Steel, H ≈ 10 m	0.63 to 0.74	Chopra (2005)
National Health/Welfare Building	RC and Steel, (43 x 27 x 72m)	0.99 to 1.28	Crawford and Ward (1964)
Alcoa Building	Steel, H = 120 m	1.67 to 2.21	Chopra (2005)
Transamerica Building	Steel, H = 260 m	2.9	···
Golden Gate Bridge Main Span	L = 1280 m	3.81 to 18.2	···
601 Lexington Ave. (Citigroup Cent.)	RC and Steel, H = 279 m	7.0	FEMA (2006)
Burj Khalifa	H = 830 m	11.3	Baker (2010)
Slender Structures			
Anemometer Pole	Steel Tube, H = 10 m	0.4902	Repetto and Solari (2010)
Industrial Chimneys	Steel Tube, H = 25 m	0.775	Repetto and Solari (2002)
···	Steel Tube, H = 30 m	0.787	···
···	Steel Tube, H = 100 m	2.058	···
···	RC, H = 250 m	3.57	Chopra (2005)
Antenna Pole	Steel Tube, H = 30 m	0.92 to 1.09	Repetto and Solari (2010)
Urban Light Pole	Steel, H = 14 m	1.85	Repetto and Solari (2004)

Table 6.3 compiles measured fundamental periods of real-world structures, which, vary greatly, ranging from rigid, single-story concrete structures (T_n = 0.035 s) to very flexible structures such as the main span of the Golden Gate Bridge (T_n = 18.2 s). It is convenient to define four groups of structures based upon their fundamental periods: "G1 – Wood Frame" ($0.15 \leq T_n \leq 0.55$), "G2 – Reinforced Concrete" ($0.04 \leq T_n \leq 3.19$), "G3 – Poles and Chimneys" ($0.49 \leq T_n \leq 3.57$), and "G4 – Steel Structures" ($0.60 \leq T_n \leq 7.00$). Figure 6.24 illustrates G1-G4 along with examples of structures having fundamental periods within the specified ranges.



Group	Description	Height (m)	T_n (s)
G1	Wood Frame	4.00 - 14.27	0.15 - 0.55
G2	Reinforced Concrete	5.60 - 91.00	0.04 - 3.19
G3	Poles & Chimneys	10.00 - 250.00	0.49 - 3.57
G4	Steel with MRF	12.50 - 257.00	0.60 - 7.00

Figure 6.24: Illustration of the four structure period groups G1-G4 and examples of structures within these ranges.

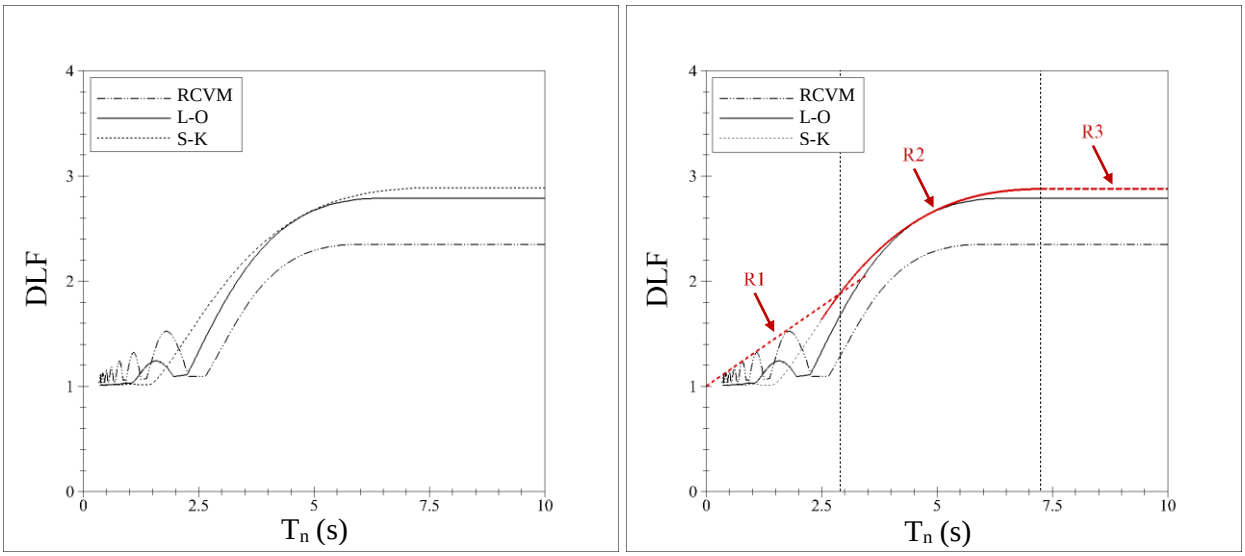
6.8.2 Generalized DLF Curve for Tornado Wind Loads

Eq. (6.29) defines that T_v is proportional to r_c and T_v^* while being inversely proportional to U_∞. The vortex load application period T_v is smallest when r_c / U_∞ is minimized ($r_{c,min}/U_{\infty,max}$ = 46 m/32.6 m·s^{-1} = 1.41 s^{-1}) and largest when r_c / U_∞ is maximized ($r_{c,max}/U_{\infty,min}$ = 2008 m/11.6 m·s^{-1} = 173.10 s^{-1}). Documented tornado-vortex parameters span a wide range, and any vortex load application period in the range $T_{v,min} < T_v < T_{v,max}$ is possible. Table 6.4 summarizes $T_{v,min}$ for each profile based upon the documented tornado vortex parameters in Table 6.2 and the definition of T_v provided by Eq. (6.29). The response of any structure for which $T_n \geq T_{v,min}$ can experience maximum dynamic amplification of tornado wind loads. Structures for which $T_n < T_{v,min}$ require that DLF(T_v / T_n) be defined using the DLF curves in Figures 6.21a – 6.21c, where the ratio T_v / T_n is computed using $T_v = T_{v,min}$.

Table 6.4: Minimum vortex loading period for each vortex profile.

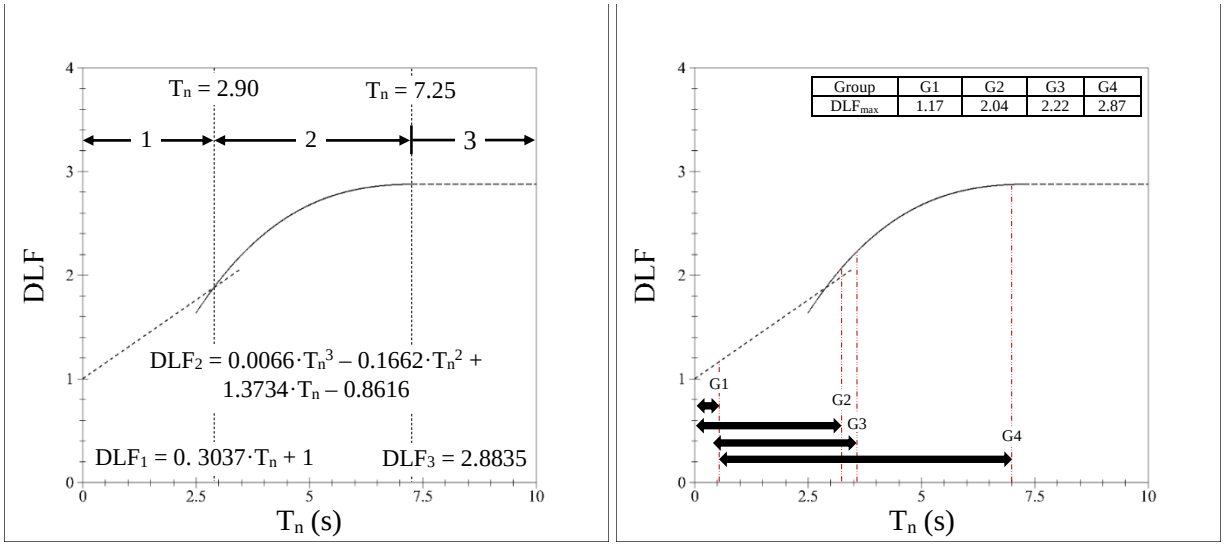
Profile	T_v^* (dim)	$r_{c,min}$ (m)	$U_{\infty,max}$ (m/s)	$T_{v,min}$ (s)
RCVM	4.08	46.00	32.60	5.76
L-O	4.44	···	···	6.27
S-K	5.02	···	···	7.17

Figure 6.25a plots DLF(T_n) curves for each of the three vortex profiles (Recall that these three profiles represent the range of measured tornado-vortex profiles). Now a general DLF curve for tornado wind loading is defined by curve fitting the upper bound of the three DLF curves using the three region (R1-R3) envelope, which is shown by the red line in Figure 6.25b. The three regions are: (R1) a linear region from $0 < T_n \leq 2.90$ s, (R2) an exponential region from 2.90 s $< T_n <$ 7.25 s, and (R3) a constant region for $T_n \geq 7.25$ s. The general tornado-vortex DLF curve is re-plotted in Figure 26a, and the equations for R1-R3 are provided.



(a) (b)

Figure 6.25: (a) DLF curves for three vortex tangential velocity profiles and (b) 3-region, piecewise curve fit defining the maximum DLF value for each fundamental structure period.



(a) (b)

Figure 6.26: (a) Generalized maximum DLF curve for tornado wind loads as function of T_n and (b) illustration of maximum DLF values for structure groups G1-G4.

Figure 26b illustrates where each of the four structure groups (G1-G4) fall allong the general tornado-vortex DLF curve. Typical wood frame structures (G1) will experience minimal dynamic amplification of tornado wind loads. However, tall concrete (G2) and steel (G4) structures as well as slender structures such as chimneys and poles (G3) may experience

significant dynamic response amplification to tornado wind loads. The potential for dynamic response amplification to tornado wind loads is relevant and should be weighed in the design and construction of such structures.

6.8.3 Practical Assessment of Tornado Dynamic Loading Threat

Figure 6.26a shows that the responses of structures having $T_n \geq 7.25$ s to tornado wind loads may be dynamically amplified by up to 2.88 times. There are very few practical structures with $T_n \geq 7.25$ s; however, DLF values of 2.0 are possible for structures with T_n as low as 3.10 s, which is well within the practical fundamental frequency range for multi-story steel and concrete structures. Furthermore, the fact that tornado-like vortices have been shown to produce up to 1.5 times greater lateral wind loading than straight line wind ((Selvam and Millet, 2005) and (Hann et al., 2010)) must also be considered. Computation of tornado wind loads for tall structures assuming the tornadic wind can be treated as straight-line wind could be quite erroneous as lateral tornado wind loadings may easily be in excess of $2.0 \cdot 1.5 = 3.0$ times greater than those produced by straight line winds.

However, prior to suggesting that structures need be designed for this extreme level of load amplification, the basis and methodology of this study must be taken into account. Specific assumptions that need to be considered are the tornado vortex parameters and the assumed manner in which the tornado loading is applied to the structure.

The tornado vortex parameters used to defined the minimum vortex loading period $T_{v,min}$ are those that minimize T_v as defined in Eq. (6.18) and are specifically $U_{\infty,max} = 32.6$ m·s^{-1} and $r_{c,min} = 46$ m. These parameters ($U_{\infty,max}$ and $r_{c,min}$) are not documented from the same tornado; in fact, the loading periods of the tornados from which they are documented are respectively $T_v > 100$ s and $T_v > 12$ s. This is not to say that dynamic loading by tornado winds is not possible, as

there are many documented small, rapidly translating vortices in the literature. Furthermore, tornado core radii dimensions reported in the literature are primarily approximated from field-observation or post-storm damage investigation and likely over-predict the actual core radii. Finally, small vortices orbiting within "multi-vortex" tornados have been documented (Lewellen et al., 2000) and may themselves have greater propensity to dynamically amplify structure response than the larger parent cyclone. In short, dynamic amplification or tornado wind loads requires a very small, rapidly-translating tornado and is not likely a significant concern.

The premise of the present analysis is that the same vortex loading is applied to the entire loaded structure and that the structure does not disrupt the vortex during their interaction. Restating the summary of the previous paragraph, small, rapidly-translating tornados produce a dynamic loading threat. The possible dynamic response amplification increases rapidly with T_n; generally speaking, structures that may experience dynamic response amplification are multistory steel and concrete buildings. Such structures have large footprints and cross sections, hence there is question as to whether or not a small tornado can produce uniform loading across the structure's cross section. Furthermore, three-dimensional simulation reported in Gorecki and Selvam (2015) shows that impact of a vortex with a prismatic structure substantially disrupts the vortex. If the vortex is disrupted, the forcing profile that it produces on the loaded structure will change as well. Once again, this speculation does not remove the concern of dynamic load amplification of tornado wind loads, rather it opens the door for subsequent investigation using three-dimensional computer simulation to account for the disruption of the impinging vortex by the loaded structure.

6.9 Summary and Conclusions

The dynamic load factor (DLF) concept has been applied to define the first generalized assessment of the dynamic loading threat of tornado-like wind loads to real-world structures. Two-dimensional loading of a rigid, circular cylinder by an impinging vortex is directly simulated. The resulting cylinder loading is applied as forcing to a single degree of freedom (SDOF) response model, and the vortex loading period T_v is defined as the fundamental structure frequency at which the dynamic amplification of the SDOF structure's response is greatest. Three impinging vortex tangential velocity profiles (RCVM, L-O, and S-K) are considered because they represent the range of documented tornado vortex tangential velocity profiles. The vortex loading period T_v is defined as a function of the vortex's critical radius r_c, translational velocity U_∞, and tangential velocity profile. Documented tornado-vortex parameters are surveyed leading to the definitions of the core radii range of $46\ m \leq r_c \leq 2008\ m$ and translational velocity range of $11.60\ m \cdot s^{-1} \leq U_\infty \leq 32.60\ m \cdot s^{-1}$. The possible dynamic amplification of a structure's response to cross-stream tornado wind loads is defined as function of T_n. Based upon the content presented in Chapter 6, the conclusions outlined below have been reached.

1. The load-application period of a vortex's tangential wind field is "$T_v = T_v^* \cdot r_c \cdot U_\infty^{-1}$".
    a. Documented tornado-vortex parameters:
        i. Critical radii: $46\ m \leq r_c \leq 2008\ m$
        ii. Translational velocity: $11.60\ m \cdot s^{-1} \leq U_\infty \leq 32.60\ m \cdot s^{-1}$
    b. Influence of vortex's tangential velocity profile incorporated through dimensionless vortex loading period:
        i. $T_v^* = 4.08$ – RCVM vortex profile
        ii. $T_v^* = 4.44$ – L-O vortex profile

iii. $T_v^* = 5.02$ – S-K vortex profile

2. The maximum dynamic response amplification of a structure having fundamental period T_n to tornado wind loads is:

   a. $2.90 \text{ s} \geq T_n \rightarrow \text{DLF} = 0.3037 \cdot T_n + 1$

   b. $2.90 \text{ s} < T_n < 7.25 \text{ s} \rightarrow \text{DLF} = 0.0066 \cdot T_n^3 - 0.1662 \cdot T_n^2 + 1.3734 \cdot T_n - 0.8616$

   c. $T_n \geq 7.25 \text{ s} \rightarrow \text{DLF} = 2.8835$

3. Dynamic amplification of tornado wind loads:

   a. Requires a small, rapidly-translating tornado

   b. Is not a concern for typical wood-frame structures and residences

   c. Is possible and a concern for tall, flexible structures

CHAPTER 7: SUMMARY AND CONCLUSIONS

7.1 Summary

Structure loading from impacting vortices is a hazardous phenomenon that is encountered in numerous engineering applications. The complex physics governing vortex-structure interaction necessitate study using either physical experiment or computer simulation. Investigation via either methodology is fraught with challenges, hence the amplitude and character (static or dynamic) of the induced loading is at best poorly understood.

Structure loading by vortices occurs across a wide spectrum of relative vortex-to-structure size scales. Rotor- and wing-tip vortices are typically smaller or similar-sized to the components of aerospace vehicles that they impact. Tornado and hurricane vortices range from similar-sized to many times larger than the structures that they load. The primary objective of this thesis is to grow the current knowledge of vortex loading of structures by evaluating the influence of the impinging vortex's size on the amplitude and character of the structure loading that it produces. This knowledge can be applied to better predict air loads on aerospace vehicles and to better design residential and civil structures to withstand wind loadings from tornados and hurricanes.

A two-dimensional computer model is used to directly simulate the impact of an impinging vortex with a slender, cylindrical structure. A rigorous review of analytical and measured vortex tangential velocity profiles (TVPs) is conducted, and analytical models which realistically represent the intense vortices encountered in engineering applications are integrated into the computer model. The vortex's maximum tangential velocity is fixed, and its critical radius is incrementally increased from one to one-hundred times the structure's diameter. The structure loading amplitude trend with respect to impinging vortex size is documented, and

phenomenon that control the trend are illustrated and explained. The vortex's path is then shifted so that it travels both above and below the structure. The trend in structure loading amplitude with respect to this path shift is then documented, and the path shift that produces maximum loading amplitude is identified. Finally, a generalized methodology is developed to assess the dynamic amplification of a structure's response to vortex loading. The dynamic load factor concept is applied to define the duration of the load application period as a function of the impacting vortex's parameters. Documented tornado-vortex parameter ranges are established and used to define the first generalized expression for possible dynamic amplification of tornado wind loads as function of the structure's fundamental period. Documented fundamental periods of existing structures are compiled, and the dynamic loading threat posed by tornados to typical civil and residential structures is assessed.

7.2 Conclusions

The subsequent subsections restate the five primary objectives of these thesis as Objectives 1-5. Each objective is restated, the methodology utilized to achieve each objective is briefly summarized, and the conclusions presented while pursuing each objective are summarized. The conclusions reached herein directly apply only to the considered physical system, which is two-dimensional impact of a vortex with a slender, cylindrical structure having the parameters specified in Section 4.1.1. However, the methodology utilized herein can be used to extend the findings presented subsequently to any physical vortex-structure system and parameter range.

7.2.1 Objective 1

❖ *To select physically-realistic analytical vortex tangential velocity profiles (TVPs) for use in computer simulation of structural loading by vortices.*

Physically-realistic analytical vortex TVPs are required to simulate physically-realistic vortex-structure interaction. Measured vortex TVPs are qualitatively similar but differ quantitatively, hence no single analytical vortex TVP replicates all measured vortex TVPs. Measured vortex TVPs were exhaustively surveyed from documented experimental and atmospheric vortices. Analytical vortex TVPs were compiled and normalized for comparison with the measured vortex TVPs. A group of analytical TVPs that adequately represent the spectrum of measured TVPs were identified for use in computer-simulated vortex-structure interaction. The conclusions reached while pursuing Objective 1 are outlined subsequently.

- ✓ The algebraic Vatistas or Wood-White TVPs are ideal for integration into computer models because they can replicate numerous analytical vortex TVPs.
- ✓ Three analytical vortex TVPs represent the spectrum of measured vortex TVPs
    - The normalized S-K (Vatistas n = 1) TVP is the upper bound to the measured TVPs.
    - The normalized L-O (Vatistas n = 2) TVP replicates the typical measured TVP.
    - The Wood-White $\lambda = 0.435$ TVP is the lower bound to the measured TVPs.
- ✓ The normalized L-O (Vatistas n = 2) TVP is the best representation of the typical measured vortex TVP and should be utilized as the default for computer simulation unless alternative justification is provided.

7.2.2 Objective 2

❖ *To identify the phenomenon that cause variation in structural loading when an impinging vortex impacts a structure, which is shedding vortices, at different times and to quantify the possible variation in the maximum force coefficient amplitude.*

An impinging vortex with critical radius r_c equal to the structure diameter D produces a spectrum of different structural loading when it impacts the structure at different times with respect to the beginning of the computer simulation. For all computer simulations, the free stream establishes vortex shedding from the cylinder prior to vortex impact with the structure. The relative size and strength of the vortices produced on the structure by the free stream change continuously during vortex shedding. It was postulated that interaction between the impinging vortex and different attached vortex structures causes the variation in structural loading when the impinging vortex impacts the structure at different times.

Impinging vortex impact was simulated at twenty-five discrete times within a single period of the vortex shedding cycle (VSC), and signed maximum drag Cd and lift Cl force coefficient amplitudes were extracted and utilized to assess the variation in structural loading amplitude with vortex impact time. Contour plots of vorticity and velocity were used to illustrate the interaction between impinging and attached vortices. A procedure was introduced to ascertain the variation in maximum force coefficient amplitudes with vortex impact time using five computer simulations instead of twenty-five. The influence of the impinging vortex's size on the variation in maximum force coefficient amplitude with vortex impact time was then assessed by incrementing the impinging vortex's critical radius from one to one-hundred times the structure's diameter. The conclusions reached while pursuing Objective 2 are outlined subsequently.

- ✓ Interaction between the impinging vortex and vortices produced on the structure by the free stream causes variation in structural loading amplitude when the impinging vortex impacts the structure at different times with respect to the free stream VSC.
    - Maximum force coefficient amplitudes produced by an $r_c = 1 \cdot D$ vortex may be under-predicted by 84.99%, 197.04%, 310.42%, and 407.15% [Cl' (+), Cl' (-), Cd' (+), and Cd' (-)] if only a single vortex impact is simulated.
- ✓ Variation in maximum force coefficients when the vortex impacts at different times is negligible for $r_c \geq 20 \cdot D$. Large vortices control vortex shedding from the structure prior to impacting, so the vortex impact time with respect to the free stream VSC is irrelevant.

7.2.3 Objective 3

❖ *To define the trend in maximum force coefficient amplitudes produced by a directly-impacting vortex when the vortex size is increased at fixed maximum tangential velocity and to explain the phenomenon controlling the trend in maximum force coefficient amplitudes.*

Structural loading by vortices occurs at practically all relative vortex-to-structure size scales, and adequate design of structures to resist vortex loading necessitates understanding how the relative vortex-to-structure size influences the resulting structural loading amplitude. The impinging vortex's maximum tangential velocity was fixed, direct impact of vortices ranging from $r_c = 1 \cdot D$ to $100 \cdot D$ with the structure was simulated, and maximum force coefficient amplitudes from the simulations were utilized to document the influence of relative vortex-to-structure size on the structural loading amplitude. The aforementioned study, first performed with the Vatistas n = 2 vortex, was repeated with the Vatistas n = 1 and n = 100 vortices to evaluate if the vortex's TVP independently influences trend. Finally, contour plots of vorticity and velocity were utilized to illustrate underlying phenomenon that control the trend in structural

loading amplitude with respect to the impinging vortex's size. The conclusions reached while pursuing Objective 3 are outlined subsequently.

- ✓ Maximum force coefficient amplitudes increase to asymptotic values for impinging vortex sizes $r_c \geq 50 \cdot D$. The impinging vortex must be large enough to satisfy three requirements:
    - Be large enough to control vortex shedding from the structure prior to impacting.
    - Have a small enough tangential velocity gradient to allow the structure's wake to shift without distortion.
    - Be large enough to expose the entire structure surface to maximum tangential velocity.
- ✓ Asymptotic ($r_c \geq 50 \cdot D$) maximum drag and lift force coefficients from direct vortex impact are respectively 94.77% and 10.66% less than maximum force coefficients produced by the equivalent-velocity free stream.
    - Forces on a structure immersed in a fluid stream increase with the square of the stream's resultant velocity. The maximum stream velocity incident on the structure for direct vortex impact is horizontal $U_\infty = 1$ and vertical $V_{\theta,max} = 1$, so the maximum resultant velocity on the structure is $(2)^{0.5}$. An equivalent-velocity free stream with $U_\infty = 2$ produces the much greater resultant velocity over the structure of $(4)^{0.5}$, hence produces greater structural loading.
- ✓ The impinging vortex's TVP does not significantly influence the trend in maximum force coefficient amplitudes with increasing vortex size or the asymptotic maximum force coefficient values.

- The Vatistas n = 1 TVP produces greatest maximum force coefficients, and maximum force coefficients produced by the Vatistas n = 2 and Vatistas n = 100 respectively agree within 1.0% and 7.0%.

7.2.4 Objective 4

❖ *To evaluate the influence of shifting an impacting vortex's path from the structure's centerline on the maximum structural loading produced by the vortex and to determine if the vortex produces greater structural loading than an equivalent-velocity free stream.*

An impinging vortex may approach and impact a structure travelling along a path other than the structure's centerline. The impinging vortex may rotate clockwise (CW) or counterclockwise (CCW), so its path shift with respect to the structures' centerline will cause the vortex's tangential velocity to either augment or subtract from the free stream velocity. The present study incremented the path of an $r_c = 50 \cdot D$, CCW-rotating vortex so that it travelled a range of paths both above and below the loaded structure's centerline. Maximum force coefficient values were extracted, used to document the influence of vortex path shift on structural loading amplitude, and compared with maximum force coefficients produced by an equivalent-velocity free stream. The conclusions reached while pursuing Objective 4 are outlined subsequently.

- ✓ The CCW-rotating vortex respectively produces greater and less structural loading when it travels above and below the structure because its tangential velocity respectively augments and subtracts the free stream velocity.
- ✓ The impacting vortex produces maximum drag and lift force coefficients that are respectively 4.80% and 34.07% greater than maximum force coefficients produced by the equivalent-velocity free stream.

7.2.5 Objective 5

❖ *To develop a generalized methodology to assess dynamic amplification of structures' response to loading produced by an impacting vortex and to apply the methodology to assess the dynamic loading threat that tornados pose to residential and civil structures.*

The impact of an impinging vortex with a structure is a transient loading event that may produce dynamically-amplified structure response. Previous studies have shown that structures' responses to tornado-like vortex loading may be dynamically amplified, but no generalized, applicable methodology is in place to assess the possible dynamic amplification of a structure's response to vortex loading. Failure to account for dynamic loading effects may result in dramatic under-prediction of loading produced by an impacting vortex, necessitating the development of generalized approach to compute dynamic load amplification from an impacting vortex.

The present study simulated direct vortex impact with a slender structure and analyzed the forcing time history produced on the structure to define the impinging vortex's loading period T_v. The vortex loading period T_v could not be clearly distinguished by taking the Fourier transform of the forcing time history. However, T_v was clearly distinguished by dynamic load factor (DLF) analysis, specifically by analyzing the responses of structures having a spectrum of fundamental frequencies to the forcing time history. The vortex loading period T_v was defined as a function of three parameters (r_c, U_∞, and T_v^*) which respectively incorporate the influences of the impinging vortex's critical radius, translational velocity, and tangential velocity profile (RCVM, L-O, or S-K). Documented tornado vortex parameters were compiled to establish the known range of tornado vortex core radius and translational velocity. The definition of T_v along with the documented tornado vortex parameter ranges were then used to define the possible dynamic amplification of a structure having fundamental period T_n to tornado vortex loading.

Fundamental periods of existing structures were then surveyed, and the dynamic loading threat that tornados pose to real-world residential and civil structures was assessed. The conclusions reached while pursuing Objective 5 are outlined subsequently.

- ✓ A Fourier transform of the forcing time history produced by the vortex is not able to distinguish T_v, while DLF analysis of the same forcing is able to distinguish T_v.
    - The current hypothesis is that only a single period of the vortex loading is present in the forcing time history, so Fourier analysis is not able to resolve T_v.
    - An avenue to future study has been opened to assess why analysis of structures' responses can be used to isolate T_v, while frequency decomposition via Fourier analysis cannot be used to isolate T_v.
- ✓ The loading period of a directly-impacting vortex's tangential wind is $T_v = T_v^* \cdot r_c \cdot U_\infty^{-1}$.
    - Documented tornado-vortex parameter ranges are:
        - Critical radii: $46\ \text{m} \leq r_c \leq 2008\ \text{m}$
        - Translational velocity: $11.60\ \text{m} \cdot \text{s}^{-1} \leq U_\infty \leq 32.60\ \text{m} \cdot \text{s}^{-1}$
    - The influence of the vortex's tangential velocity profile is incorporated through the dimensionless vortex loading period:
        - $T_v^* = 4.08$ – RCVM vortex TVP
        - $T_v^* = 4.44$ – L-O vortex TVP
        - $T_v^* = 5.02$ – S-K vortex TVP
- ✓ The maximum dynamic response amplification (DLF value) of a general structure having fundamental period T_n to a directly-impacting vortex's tangential wind field is:
    - $2.90\ \text{s} \geq T_n \quad \rightarrow \quad \text{DLF} = 0.3037 \cdot T_n + 1$
    - $2.90\ \text{s} < T_n < 7.25\ \text{s} \quad \rightarrow \quad \text{DLF} = 0.0066 \cdot T_n^3 - 0.1662 \cdot T_n^2 + 1.3734 \cdot T_n - 0.8616$

- $T_n \geq 7.25$ s $\rightarrow$ DLF = 2.8835

✓ Generally speaking, dynamic amplification of tornado wind loads:

- Requires a atypical small, rapidly-translating tornado.
- Is not likely a concern for typical wood-frame structures and residences.
- Is possible and a concern for tall, flexible structures.

7.3 Primary Contributions to the Scientific Community

The body of work presented in this thesis substantially advances the scientific community's knowledge of structural loading produced by impacting vortices. The four primary contributions from this body of work are listed subsequently.

1. The normalized Vatistas vortex TVP is introduced in Eq. (3.19) and is shown to be capable of replicating the spectrum of measured vortex TVPs in the literature.
2. The concept that interaction between an impinging vortex and vortices attached to a structure causes great variation in structural loading when the impinging vortex impacts the structure at different times with respect to the vortex shedding cycle is identified and explained.
3. The vortex loading period T_v of an impacting vortex's tangential wind field is defined by Eq. (6.29), as a part of the first generalized methodology to assess dynamic amplification of structures' response to vortex loading.
4. Documented tornado vortex parameters and the vortex loading period T_v are utilized to define the possible dynamic amplification of loading produced by a tornado's tangential wind field as function of the loaded structure's fundamental period (See Figure 6.26b).

Diligent effort has been made to rapidly disseminate the findings of this thesis. The content has been submitted as four peer-reviewed papers (two have been accepted and the two others are

currently under review) and presented as three technical posters. References for the papers are listed below, and a complete list of the author's publication history is provided in the vitae at the end of the thesis.

Strasser, M.N., Yousef, M.A., and Selvam, R.P., 2015. Defining the Vortex Loading Period and Application to Assess Dynamic Amplification of Tornado-Like Wind Loading, In Review with *J. Fluids and Structures*, Manuscript Number: YJFLS-D-15-00381.

Strasser, M.N. and Selvam, R.P., 2015. The Influence of Vortex Size on the Maximum Loading of a Slender, Cylindrical Structure Impacted by Aerospace to Tornado-Scale Vortices, In Review with *J. Fluids and Structures*, Manuscript Number: YJFLS-2015-126.

Strasser, M.N., & Selvam, R.P., 2015. Selection of a Realistic Vortex Tangential Velocity Profile for Computer Simulation of Vortex-Structure Interaction, *J. Arkansas Academy of Science **69***, Manuscript Number: JAAS MS69-12.

Strasser, M.N., & Selvam, R.P., 2015. The variation in the maximum loading of a circular cylinder impacted by a 2D vortex with time of impact, *J. Fluids and Structures **58**, 66-78*.

7.4 Limitations of the Present Study

As stated in the opening paragraphs of Section 7.2, the conclusions reached within the scope of the present study only pertain directly to physical system and parameter ranges considered in the present study. The computer model utilized herin simulates two-dimensional impact of a vortex with a slender, cylindrical structure. For the considered Reynlolds number range of less than 300 used throughout this study, vortex shedding from slender, cylindrical structures is known to be primarily two-dimensional in nature. However, it is not currently known whether or not impact by an impinging vortex may produce three-dimensinal phenomenon in the vortex-structure interaction.

The assessment of dynamic loading produced by tornado vortices is conducted by applying lift force coefficient time histories from simulated, two-dimensional impact of an impinging vortex with a slender structure to a single degree of freedom system. In reality, a tornado produces time-varying structural loading along all three of the structure's axis. The

structure's response to simultaneous application of forcing in all three directions needs to be considered for a more realistic assessment of the dynamic loading threat that tornados pose. Furthermore, a tornado's wind field varries moving upards from the ground until the edge of the boundary layer from the ground's surface is reached, meaning the loading produced by the tornado varries as well. The present analysis does not account for this variation, hence it is only physically realistic for impact of a tornado with a tall, slender structure where the variation in forces along the structure's height is minimal.

7.5 Suggested Future Work

At the conclusion of this body of work, several additional topics have been identified as potential avenues for future researchers. These topics are outlined and discussed subsequently in what the author believes to be their order of importance.

Forcing time histories from computer-simulated, direct vortex impact with a slender structure were analyzed to define the loading period of a vortex's tangential wind field Tv and the possible dynamic amplification of structural loading produced by tornados' tangential wind fields. Dynamic load factor (DLF) analysis was utilized to identify T_v because a Fourier transform of the forcing time history failed to isolate T_v. This raises question as to why T_v can be distinguished from structures' responses in DLF analysis but not from decomposition of the constitutive frequencies of the forcing time history via Fourier analysis. The present hypothesis is that only a single period of vortex loading is present in the force coefficient time history, so it cannot be adequately resolved. One factor that may diminish the clarity of the Fourier transform is that when the exact frequency vortex loading frequency $f_v = T_v^{-1}$ is not considered in the Fourier analysis, the amplitude associated with f_v is distributed to adjacent frequencies. Additionally, the vortex shedding frequency from the structure changes continuously as the

impinging vortex approaches the structure, so the non-stationary nature of the forcing time history may also reduce clarity of the Fourier transform. Regardless of the source of the discrepancy, analysis of structures' response has been shown to be a superior means to frequency decomposition to identify forcing frequencies within a forcing time history produced by an impacting vortex. Subsequent studies are needed to assess why DLF analysis provides superior resolution to Fourier analysis.

The present study analyzes a structure impacted by a vortex where the critical radius r_c of the impinging vortex is one to one-hundred times the structure's diameter D. However, rotor- and wing-tip vortices may be substantially smaller than the rotors and airframe components that they load. Subsequent study is needed to evaluate structural loading when the impinging vortex is smaller than that of the loaded structure. It is expected that the vortex impact time with respect to the vortex shedding cycle from the the structure will increasingly influence structural loading amplitude as the vortex size increases, and interaction between impacting vortices and rotor- and wing-tip vortices may become increasingly significant. However, studies using smaller impinging vortices will introduce computational time issues because extensive grid refinement will be required to accurately transport vortices. It is likely that a parallel computer program will be required to conduct the necessary number of simulations required to study the variation in structural loading with vortex impact time.

Force coefficient time histories from computer-simulated, two-dimensional vortex impact with slender structures are utilized as forcing to assess the possible dynamic amplification of tornado-vortex wind loads. This methodology is invaluable because it develops a conceptual framwork for the analysis procedure. However, the next step in the analysis is to utilize forcing produced by a three-dimensional computer model applied to a multi-degree of freedom structure.

The three dimensional simulation and multi degree of freedom structure can account for variation in tangential velocity along the height of the tornado vorrtex, thereby providing a more realistic reresentation of structural loading by a tornado-like vortex.

All simulations reported in the present study use a maximum vortex tangential velocity to translational velocity ratio $V_{\theta,max} / U_{\infty}$ of unity. This ratio is realistic for some aerospace applicatons, but the vortex velocity ratio varies widely, from 3.11 to 14.19, for documented tornados and hurricanes. The vortex velocity ratio greatly influences the forcing time history produced by the vortex. Therefore, the cylinder loading trend with vortex size needs to be re-evaluated to determine its influence on the phenomenon controlling the cylinder loading trend with increasing vortex size.

The final suggested study is to reexamine the trend in the maximum amplitude of Cl'(-) for $r_c / D \leq 5$. Figures 5.10b, 5.11b, and 5.11d show that the trend in the maximum amplitude of Cl'(-) exhibits a progressively-pronounced dip as the vortex tangential velocity profile progresses from sharp (RCVM) to flat (S-K). The reason for this dip has not been investigated, and the underlying phenomenon are not known.

CITED WORK

Aboelkassem, Y., and Vatists G.H., 2005. Viscous dissipation of Rankine vortex profile in zero meridional flow, *Acta Mechanica Sinica* ***21.6***, *550-556*.

Alexander, C.R., and Wurman, J., 2005. The 30 May 1998 Spencer, South Dakota, storm. Part I: The structural evolution and environment of the tornadoes, *Monthly weather review* ***133.1***, *72-97*.

Alrasheedi, N.H., 2012. Computer Modeling of the Influence of Structure Plan Areas on Tornado Forces, Ph.D. Dissertation, University of Arkansas Department of Civil Engineering, Fayetteville, AR.

Alrasheedi, N. H., and Selvam R. P., 2011. Computing Tornado Forces on Different Building Sizes, *Proc. 13th Int. Conf. on Wind Engineering (ICWE13)*, Amsterdam, Netherlands.

Baker, 2010. The Burj Khalifa Triumphs: Engineering an Idea: The Realization of the Burj Khalifa, *Civil Engineering-ASCE* ***80.3***, *44-47*.

Bagai, A., and Leishman, J.G., 1993. Flow visualization of compressible vortex structures using density gradient techniques, *Exp. Fluids* ***15***, *432-442*.

Balkaya, C., and Kalkan, E., 2003. Estimation of fundamental periods of shear-wall dominant building structures, *Earthquake Engineering and Structural Dynamics* ***32***, *985-998*.

Baranyi, L., and Lewis, R.I., 2006. Comparison of a grid-based CFD method and vortex dynamics predictions of low Reynolds number cylinder flows, *The Aeronautical Journal* ***110***, *63-71*.

Barba, L.A., 2013. Student guest blog post: the Wagner effect, (Photograph). Available Online: http://lorenabarba.com/blog/student-guest-blog-post-the-wagner-effect/. (Accessed: 2-24-2015).

Bhagwat, M.J., and Leishman, J.G., 2002. Generalized Viscous Vortex Model for Application to Free-Vortex Wake and Aeroacoustic Calculations, *Annual Forum Proceedings-American Helicopter Society* ***58.2***.

Bhagwat, M.J., and Leishman, J.G., 2000. Measurements of Bound and Wake Circulation on a Helicopter Rotor, *J. Aircraft* ***37.2***, *227-234*.

Blake, E.S., Rappaport, E.N., Jarrell, E.N., Landsea, C.W., 2005. The Deadliest, Costliest, and Most Intense United States Tropical Cyclones from 1851 to 2004 (And Other Frequently Requested Hurricane Facts), *NOAA Technical Memorandum NWS TPC-4*.

Bluestein, H.B., Lee, W-C., Bell, M., Weiss, C.C., and Pazmany, A.L., 2003. Mobile Doppler Radar Observations of a Tornado in a Supercell near Bassett, Nebraska, on 5 June 1999. Part II: Tornado-Vortex Structure, *Monthly Weather Review* ***131***, *2968-2984*.

Bodeen, C., 2012. Aerolastic Flutter, (Photograph). Available Online: http://forums.x-plane.org/?showtopic=57178. (Accessed: 2-19-2015).

BOM, 2015. Storm Spotters' Handbook. Available Online: http://www.bom.gov.au/storm_spotters/handbook/dont_be_deceived.shtml. (Accessed: 2-19-2015).

Brooks, H.E., and Doswell, C.A., 2001. Normalized Damage from Major Tornadoes in the United States: 1890-1999, *Weather and Forecasting* ***16***, *168-176*.

Burgers, J.M., 1948. A mathematical model illustrating the theory of turbulence, *Advances in applied mechanics* **1**, *171-199*.

Commonwealth, 2015. CDI's Largest Concrete Chimney Reaches Full Height (Photograph), comdynam.com, Available Online: http://www.comdynam.com/current-news-0. (Accessed: 4-29-2015).

Cao, S., Ozono, S., Tamura, Y., Ge, Y., and Kikugawa H., 2010. Numerical simulation of Reynolds number effects on velocity shear flow around a circular cylinder, *J. Fluids and Structures* ***26***, *685-702*.

Cao, Y., Fovell, R.G., and Corbosiero, K.L., 2011. Tropical Cyclone Track and Structure Sensitivity to Initialization in Idealized Simulations: A Preliminary Study, *Terrestrial, Atmospheric and Oceanic Sciences* ***22.6***.

Chandler, J., 2005. Gallery – NAVY.mil, (Photograph). Available Online: http://www.navy.mil/gallery/FA+18c+Vapor+trail. (Accessed: 4-13-2015).

Cheong, D., 2015. Dubai – danielcheongphotography.com, (Photograph). Available Online: http://www.danielcheongphotography.com/search#q=dubaiandi=0ands=popular. (Accessed: 4-13-2015).

Chopra, A.K., 2005. Dynamics of Structures: Theory and Application to Earthquake Engineering. Prentice Hall, Englewood Cliffs, NJ, USA.

Church, C.R., and Snow, J.T., 1993. Laboratory models of tornadoes, *The Tornado: its structure, dynamics, prediction, and hazards, pp. 277-295*.

Church, C.R., Snow, J.T., Baker, G.L., and Agee, E.M., 1979. Characteristics of Tornado-Like Vortices as a Function of Swirl Ratio: A Laboratory Investigation, *J. Atmospheric Sciences* ***36***, *1755-1776*.

Coronado, P., Velez, C., Ilie, M., Zha, G-C., 2011. High angle of attack helicopter blade-vortex interaction; numerical studies using LES, *Proc. 49th AIAA Aerospace Sciences Meeting*. January 4-7, Orlando, FL.

Crawford, R., and Ward, H.S., 1964. Determination of the Natural Periods of Buildings, *Bulletin of the Seismological Society of America* ***54.6****, 1743-1756*.

Davies-Jones, R., Trapp, R.J., and Bluestein, H.B., 2001. Tornadoes and tornadic storms (Chapter 5), *Severe convective storms* ***28****, 167-221*.

Diaz, J., 2010. A Cobra Helicopter Slicing the Air, (Photograph). Available Online: http://gizmodo.com/5655960/a-cobra-helicopter-slicing-the-air. (Accessed: 4-13-2015).

DeFilippi, S., 2014. Brooke Claxton Building (Photograph), Flickr.com, Available Online: https://www.flickr.com/photos/sheldef/13943827673/in/photolist-oFdnkU-oFdNA6-ooJ5gd-oGYFAD-ooJNJ6-nfaLaX. (Accessed: 4-29-2015).

Devenport, W.J., Rife, M.C., Liapis, S.I., and Follin, G.J., 1996. The structure and development of a wing-tip vortex, *J. Fluid Mechanics* ***312****, 67-106*.

Domengo, P.X.C., and Ilie, M., 2012. Numerical study of helicopter blade-vortex mechanism of interaction using the potential flow theory, *Applied Mathematical Modelling* ***36****, 2841-2857*.

Dosanjh, D.S., Gasparek, E.P., and Eskinazi, S., 1962. Decay of a viscous trailing vortex, *Aeronautical Quarterly* ***13.2****, 167-188*.

Dukowicz, J., and Ramshaw, J., 1979. Tensor viscosity method for convection in numerical fluid dynamics, *J. Computational Physics* ***32.1****, 71-79*.

Dutta, P.K., Ghosh, A.K., and Agarwal, B.L., 2002. Dynamic response of structures subjected to tornado loads by FEM, *J. Wind Engineering and Industrial Aerodynamics* ***90****, 55-69*.

Edwards, R., and Brooks, H.E., 2010. Possible Impacts of the Enhanced Fujita Scale on United States Tornado Data, *Proc. 25th Conf. on Severe Local Storms*, Denver, CO. Available Online: www.spc.ncep.noaa.gov/publications/edwards/eftrends.pdf. (Accessed: 2-26-2015).

Engel, P., 2014. A Rare Fire Tornado Sprung Up in Missouri, (Photograph). Available Online: http://www.businessinsider.com/a-rare-fire-tornado-sprung-up-in-missouri-2014-5. (Accessed: 2-19-2015).

EOL, 2015. Earth Observing Laboratory (Specs. on AVAPS dropsonde). Available Online: http://www.eol.ucar.edu/rtf/facilities/dropsonde/. (Accessed: 2-24-2015).

Faler, J.H., and Leibovich, S., 1977. Disrupted states of vortex flow and vortex breakdown, *Physics of Fluids **20.9**, 1385-1400*.

FEMA, 2006. Designing for Earthquakes (Chapter 4). Available Online: http://www.fema.gov/media-library-data/20130726-1556-20490-5679/fema454_complete.pdf. (Accessed: 6-1-2015).

Filippone, A. and Afgan, I., 2008. Orthogonal Blade-Vortex Interaction on a Helicopter Tail Rotor, *AIAA **46**, 1476-1488*.

Franke, R., Rodi, W., and Shönung, B., 1990. Numerical Calculation of Laminar Vortex Shedding Flow Past Cylinders, *J. Wind Engineering and Industrial Aerodynamics **35**, 237-257*.

Fujita, T.T., 1981. Tornado Wind Effects on the Grand Gulf Cooling Tower, *Proc. 2nd Specialty Conference on Dynamic Response of Structures—Experimentation, Observation, Prediction, and Control, 555-566*.

Fujita, T.T., 1973. Tornadoes Around the World, *Weatherwise **26.2**, 56-83*.

Fujita, T.T., 1971. Proposed Characterization of Tornadoes and Hurricanes by Area and Intensity. *Satellite and Mesometeorology Research Project Research Paper **91***. Department of Geophysical Sciences, University of Chicago.

Giosan, I., and Eng, P., 2013. Vortex shedding induced loads on free standing structures. *Structural Vortex Shedding Response Estimation Methodology and Finite Element Simulation*. Available Online: http://www.wceng-fea.com/vortex_shedding.pdf (Accessed: 7-8-2015).

Goel, R.K., and Chopra, A.K., 1997. Period Formulas for Moment-Resisting Frame Buildings, *J. Structural Engineering **123.11**, 1454-1461*.

Goerss, J.S., and Jeffries, R.A., 1994. Assimilation of Synthetic Tropical Cyclone Observations into the Naval Operational Global Atmospheric Prediction System, *Weather and Forecasting **9**, 557-576*.

Golden, J.H., 1974. The Life Cycle of Florida Keys' Waterspouts. I, *J. Applied Meteorology **13**, 676-692*.

Gorecki, P., and Selvam, R.P., 2015. Rankine combined vortex interaction with a rectangular prism, *I.J. Computational Fluid Dynamics, 1-13*.

Gorecki, P., and Selvam, R.P., 2014. Visualization of tornado-like vortex interacting with wide tornado-break wall, *J. Visualization, 1-14*.

Graf, W, 2008. The ShakeOut Scenario: Supplemental Study: Woodframe Buildings (USGS/CGS Report), colorado.edu. Available Online: http://www.colorado.edu/hazards/shakeout/woodframe.pdf. (Accessed 6-1-2015).

Gutro, R., and Braun, S., 2012. Two Hurricane Global Hawks, Two Sets of Instruments, NASA.gov (Photograph). Available Online: http://www.nasa.gov/centers/wallops/two-hawks.html. (Accessed: 2-24-2015).

Haan, F.L., Sarkar, P.P., Prevatt, D., Rouche, D., Graettinger, A., Dao, T.N., Crawford, P.S., 2014. Using tornado damage surveys to improve laboratory tornado simulations, *Structures Congress **2014**, 1472-1483*.

Haan, F.L., Balaramudu, V. K., and Sarkar, P.P., 2010. Tornado-Induced Wind Loads on a Low-Rise Building, *J. Structural Engineering **136**, 106-116*.

Haan, F.L., Sarkar, P.P., and Gallus, W.A., 2008. Design, construction and performance of a large tornado simulator for wind engineering applications, *Engineering Structures **30**, 1146-1159*.

Hafeez, G., Doudak, G., and McClure, G., 2014. Effect of Non-Structural Components on the Natural Period of Wood Light-Frame Buildings, Proc. World Conference on Timber Engineering. Available Online: http://newbuildscanada.ca/wp-content/uploads/2010/11/wcte-2014_PAP084_Hafeez.pdf. (Accessed: 6-22-2015).

Henderson, R.D., 1995. Details of the drag curve near the onset of vortex shedding, *Physics of Fluids **7(9)**, 2102-2104*.

Hock, T.F., and Franklin, J.L., 1999. The NCAR GPS Dropwindsonde, *BAMS **80.3**, 407-420*.

Hoecker, W.H., 1960. Wind Speed and Air Flow Patterns in the Dallas Tornado of April 2, 1957, *Monthly Weather Reviw **88.5**, 167-180*.

Holland, G.J., Belanger, J.I., and Fritz, A., 2010. A Revised Model for Radial Profiles of Hurricane Winds, *Monthly Weather Review **138**, 4393-4401*

Holland, G.J., 1980. An Analytical Model of the Wind and Pressure Profiles in Hurricanes, *Monthly Weather Review **108**, 1212-1218*.

Holmes, J.D., 2004. *Wind Loading of Structures (pg. 11)*. Taylor and Francis Group, New York, NY.

Hong, L-L., and Hwang, W-L., 2000. Empirical formula for fundamental vibration periods of reinforced concrete buildings in Taiwan, *Earthquake Engineering and Structural Dynamics **29**, 327-337*.

Horner, M.B., Galbraith, R.A., Coton, F.N., Stewart, J.N., and Grant, I., 1996. Examination of Vortex Deformation During Blade-Vortex Interaction, *AIAA **34(6)**, 1188-1194*.

Hughes, L.A., 1952. On the Low-Level Wind Structure of Tropical Storms, *J. Meteorology **9**, 422-428*.

Ilie, M., 2009. Numerical Study of helicopter blade-vortex mechanism of interaction using large-eddy simulation, *Computers and Structures **87**, 758-768*.

Kadragic, A., 2010. First Residents to Move into Burj Dubai in February (Photograph), *World Property Journal*. Available Online: http://www.worldpropertyjournal.com/international-markets/residential-real-estate/real-estate-news-burj-dubai-armani-residences-armani-hotel-emaar-properties-sheikh-mohammed-bin-rashid-al-maktoum-burj-dubai-station-1837.php. (Accessed 4-29-2015).

Kaufmann, W., 1962. Über die Ausbreitung kreiszylindrischer Wirbel in zähen (viskosen) Flüssigkeiten, *Archive of Applied Mechanics* **31**, *1-9*.

Kepert, J.D., 2010. Tropical cyclone structure and dynamics (Chapter 1), *Global perspectives on tropical cyclones: From science to mitigation **4***.

Kepert, J.D., 2006a. Observed Boundary Layer Wind Structure and Balance in the Hurricane Core. Part I: Hurricane Georges, *J. Atmospheric Sciences **63**, 2169-2193*.

Kepert, J.D., 2006b. Observed Boundary Layer Wind Structure and Balance in the Hurricane Core. Part II: Hurricane Mitch, *J. Atmospheric Sciences **63**, 2194-2211*.

Kessler, E., 1970. Tornadoes, *BAMS **51.10**, 926-936*.

Kosiba, K., and Wurman, J., 2010. The Three-Dimensional Axisymmetric Wind Field Structure of the Spencer, South Dakota, 1998 Tornado, *J. Atmospheric Sciences **67**, 3074-3083*.

Kuai, L., Haan, F.L., Gallus, W.A., and Sarkar, P.P., 2008. CFD simulations of the flow field of a laboratory-simulated tornado for parameter sensitivity studies and comparison with field measurements, *Wind and Structures **11.2**, 1-22*.

Kuo, J.L., 1971. Asisymmetric Flows in the Boundary Layer of a Maintained Vortex, *J. Atmospheric Sciences **28.1**, 20-41*.

Kuźniar, K., and Waszczyszyn, Z., 2006. Neural Networks and Principal Component Analysis for Identification of Building Natural Periods, *J. Computing in Civil Engineering **20**, 431-436*.

Labbe, D.F.L., and Wilson, P.A., 2007. A numerical investigation of the effects of the spanwise length on the 3-D wake of a circular cylinder, *J. Fluids and Structures **23**, 1168-1188*.

Lam, H.C., 1993. An Experimental Investigation and Dimensional Analysis of Confined Vortex Flows, Ph.D. Dissertation, Concordia University, Montréal, Québec, Canada.

Lamb, H., 1932. Hydrodynamics 6th ed., Cambridge University Press, Cambridge, UK.

Lee, S., and Bershader, D., 1994. Head-on Parallel Blade-vortex interaction, *J.AIAA **32.1**, 16-22*.

LeMessurier, 2015. Image of 601 Lexington Avenue (Formerly: Citigroup Center), LeMessurier.com. Available Online: http://www.lemessurier.com/citigroup_center (Accessed 6-1-2015).

Leslie, F.W., Snow, J.T., 1980. Sullivan's Two-Celled Vortex, *J. AIAA **18.10**, 1272-1274*.

Leslie, L.M., and Holland, G.J., 1995. On the Bogussing of Tropical Cyclones in Numerical Models: A Comparison of Vortex Profiles, *Meteorology and Atmospheric Physics **56**, 101-110*.

Lewellen, D.C., Lewellen, W.S., and Xia, J., 2000. The Influence of a Local Swirl Ratio on Tornado Intensification near the Surface, *J. Atmospheric Sciences **57**, 527-544*.

Li, Y., Zhang, R., Shock, R., and Chen, H., 2009. Prediction of vortex shedding from a circular cylinder using a volumetric Lattice-Boltzmann boundary approach, *European Physical Journal **171**, 91-97*.

Liu, Y., Cao, N., Wang, Q., and Li, B., 2012. Numerical Simulation of Two-Dimensional Parallel Blade-Vortex Interactions Using Large Eddy Simulation, *Proc. International Conference on Advances in Computational Modeling and Simulation **31**, 703-707*.

Magill, R., 2012. Volunteers and local workers make a difference as drought threatens Joplin's newly planted trees – Arbor Day Foundation Blog (Photograph). Available Online: http://blog.arborday.org/2012/08/. (Accessed: 4-13-2015).

Mallen, K.J., Montgomery, M.T., and Wang, B., 2005. Reexamining the Near-Core Radial Structure of the Tropical Cyclone Primary Circulation: Implications for Vortex Resiliency, *J. Atmospheric Sciences **62**, 408-425*.

Martin, P.B., Pugliese, G.J., and Leishman, J.G., 2003. High Resolution Trailing Vortex Measurements in the Wake of a Hovering Rotor, *J. American Helicopter Society **48.1**, 39-52*.

McDonald, J.R., Mehta, K.C., Smith, D.A., Womble, J.A., 2009. The Enhanced Fujita Scale: Development and Implementation, *Forensic Engineering Congress, 719-728*.

Mehta, K.C. and McDonald, J.R., 1986. Structural Dynamics in Hurricanes and Tornadoes, *Dynamic response of structures: Proc. 3rd conference organized by the Engineering Mechanics Division of the ASCE, 28-43*.

Millet, P., Riordan, J., and Selvam, R.P., 2005. Computation of Moment Coefficients on a Cubic Building During a Tornado, *Proc. Of the Americas Conference on Wind Engineering*, May 30-June 4, Baton Rouge, LA.

Mittal, S., 2005. Excitation of shear layer instability in flow past a cylinder at low Reynolds number, *I.J. Numerical Methods in Fluids **49**, 1147-1167*.

MemphisWeather, 2011. 2011 Atlantic Hurricane Season Outlook. Available Online: http://blog.memphisweather.net/2011/05/2011-atlantic-hurricane-season-outlook.html. (Accessed: 2-19-2015).

NASA, 2013. Von Karman Vortices Off Chile, EarthObservatory.nasa.gov. Available Online: http://earthobservatory.nasa.gov/IOTD/view.php?id=80197. (Accessed 4-13-2015).

Newman, P., 2013. What the Heck is a Dropsonde? Available Online: http://www.nasa.gov/content/goddard/what-the-heck-is-a-dropsonde. (Accessed: 2-24-2015).

NOAA, 2015a. U.S. Tornado Climatology: Historical Records and Trends. Available Online: http://www.ncdc.noaa.gov/climate-information/extreme-events/us-tornado-climatology/trends. (Accessed: 3-18-2015).

NOAA, 2015b. Aircraft (Dropsonde delivery plane used by NOAA). Available Online: http://www.aoc.noaa.gov/aircraft_lockheed.htm. (Accessed: 2-24-2015).

NOAA, 2014a. State of the Climate: Tornadoes for Annual 2014, NOAA.gov. Available Online: http://www.ncdc.noaa.gov/sotc/tornadoes/2014/13. (Accessed: 3-18-2015).

NOAA, 2014b. Tornadoes/Flooding on April 27-28, 2014, NOAA.gov. Available Online: http://www.srh.noaa.gov/lzk/?n=svr0414c.htm. (Accessed: 10-2-2014).

NOAA, 2013a. The May 31-June 1, 2013 Tornado and Flash Flooding Event, NOAA.gov. Available Online: http://www.srh.noaa.gov/oun/?n=events-20130531. (Accessed: 10-2-2014).

NOAA, 2013b. The May 20, 2013 Newcastle-South OKC-Moore EF-5 Tornado, NOAA.gov. Available Online: http://www.srh.noaa.gov/oun/?n=events-20130520-ef5tornado. (Accessed: 10-2-2014).

NOAA, 2012. Minor Modification to Saffir-Simpson Hurricane Wind Scale for the 2012 Hurricane Season, NOAA.gov. Available Online: http://www.nhc.noaa.gov/pdf/sshws_2012rev.pdf. (Accessed: 2-26-2015).

NOAA, 2005. Wow! A Site to Behold (Photograph). Available Online: http://www.srh.noaa.gov/images/tbw/2005/Wow.pdf. (Accessed: 2-19-2015).

NOAA, 1999. The Great Plains Tornado Outbreak of May 3-4, 1999, NOAA.gov. Available Online: http://www.srh.noaa.gov/oun/?n=events-19990503-storma. (Accessed: 10-2-2014).

NOAA, 1980. Pertinent Meteorological Data for Hurricane Allen of 1980, NOAA.gov. Available Online: www.nws.noaa.gov/oh/hdsc/Technical_reports/TR35.pdf. (Accessed: 10-2-2014).

Nolan, D.S., and Farrell, B.F., 1999. The Structure and Dynamics of Tornado-Like Vortices, *J. Atmospheric Sciences **56**, 2908-2936*.

NSF, 2005. Rapid-Scanning Doppler on Wheels Keeps Pace with Twisters. Available Online: http://www.nsf.gov/news/news_summ.jsp?org=NSFandcntn_id=104209. (Accessed 2-24-2015).

NWS, 2014. Natural Hazard Statistics – NOAA.gov. Available Online: http://www.nws.noaa.gov/om/hazstats.shtml. (Accessed: 4-13-2015).

NWS, 2012. Tornados and Hurricanes –NOAA.gov. Available Online: http://www.prh.noaa.gov/cphc/pages/FAQ/Hurricanes_vs_tornadoes.php. (Accessed: 4-13-2015).

Oppenheim, A.V., and Schafer, R.W., 2013. Discrete-Time Signal Processing 3rd Ed. Dorling Kindersley, licensees of Pearson Education in South Asia.

Oseen, C.W., 1912. Uber Wirbelbewegung in Einer Reibenden Flussigkeit, *Ark. J. Mat. Astrom. Fys. **7**, 14-21*.

Park, J., Kwon, K., and Choi, H., 1998. Numerical Solutions of Flow Pas a Circular Cylinder at Reynolds Numbers up to 160, *KSME International Journal **12(6)**, 1200-1205*.

Patankar, S.V., 1980. Numerical Heat Transfer and Fluid Flow, Hemisphere Publishing Corporation, McGraw Hill.

Paz, M., and Leigh, W., 2004. Structural Dynamics: Theory and Computation 5th Ed. Kluward Academic Publishers Norwel, MA.

Porter, C., Rennie, M., and Jumper, E., 2010. Aero-Optic Effects of a Wing Tip Vortex, *Proc. 48th AIAA Aerospace Sciences Meeting, AIAA 2010-435*. January 4-7, Orlando, FL.

Posdziech, O., and Grundmann, R., 2007. A systematic approach to the numerical calculation of fundamental quantities of the two-dimensional flow over a circular cylinder, *J. Fluids and Structures **23**, 479-499*.

Posdziech, O., and Grundmann, R., 2001. Numerical Simulation of the Flow around an Infinitely Long Circular Cylinder in the Transition Regime, *Theoretical and Computational Fluid Dynamics* ***15***, *121-141*.

Pritchard, W.G., 1970. Solitary waves in rotating fluids, *J. Fluid Mechanics* ***42.1***, *61-83*.

Qu, L., Norberg, C., Davidson, L., Peng, S-H., and Wang, F., 2013. Quantitative numerical analysis of flow past a circular cylinder at Reynolds number between 50 and 200, *J. Fluids and Structures* ***39***, *347-370*.

Ramasamy, M., and Leishmann, J.G., 2006. A Generalized Model for Transitional Blade Tip Vortices, *J. American Helicopter Society* ***51.1***, *92-103*.

Ramasamy, M., and Leishman, J.G., 2004. Interdependence of Diffusion and Straining of Helicopter Blade Tip Vortices, *J. Aircraft* ***41.5***, *1014-1024*.

Rankine, W. J. M. "A Manual of Applied Physics." (1882).

Repetto, M.P., and Solari, G., 2010. Wind-induced fatigue collapse of real slender structures, *Engineering Structures* ***32***, *3888-3898*.

Repetto, M.P., and Solari, G., 2004. Directional Wind-Induced Fatigue of Slender Vertical Structures, *J. Structural Engineering* ***130***, *1032-1040*.

Repetto, M.P., and Solari, G., 2002. Dynamic crosswind fatigue of slender vertical structures, *J. Wind and Structures* ***5.6***, *527-542*.

Rockwell, D., 1998. Vortex-Body Interactions, Annual Rev. Fluid Mech. 30, 199-229.

Rott, N., 1958. On the Viscous Core of a Line Vortex, *Zeitschrift für angewandte Mathematik und Physik* ***9***, *543-553*.

Scully, M.P., 1975. Computation of Helicopter Rotor Wake Geometry and Its Influence on Rotor Harmonic Airloads, PhD Thesis, Massachusetts Institute of Technology.

Seath, D., Kim, J-M., and Wilson, D.R., 1989. Investigation of the parallel blade-vortex interaction at low speed, *J. Aircraft* ***26.4***, *328-333*.

Selvam, R.P., Ahmed, N., Strasser, M.N., Yousef, M., Ragan, Q.S., and Costa, A., 2015a. RAPID: Documentation of Tornado Track of Mayflower Tornado in Hilly Terrain. *US National Science Foundation*. Available online: http://compmech.cveg.uark.edu.

Selvam, R.P., Strasser, M.N., Ahmed, N., Yousef, M., & Ragan, Q.S., 2015. Observations of the Influence of Hilly Terrain on Tornado path and Intensity from Damage Investigation of the 2014 Tornado in Mayflower, Arkansas. *Proc. ASCE Structures Congress*, Portland, OR, pp. 2711-2721.

Selvam, R.P., and Gorecki, P., 2012. Effect of tornado size on forces on thin 2D cylinder, *Proc. 3rd American Association for Wind Engineering Workshop*, August 12-14, Hyannis, MA, USA.

Selvam, R.P., and Millet, P.C., 2005. Large eddy simulation of the tornado-structure interaction to determine structural loadings, *Wind and Structures* ***8.1****, 49-60*.

Selvam, R.P., and Millet, P.C., 2003a. Computer Modeling of Tornado Forces on a Cubic Building Using Large Eddy Simulation, *J. Arkansas Academy of Sciences* ***57****, 140-146*.

Selvam, R.P., and Millet, P.C., 2003b. Computer modeling of tornado forces on buildings, *Wind and Structures* ***6.3****, 209-220*.

Selvam, R.P., Roy, U.K., Jung, Y., and Mehta, K.C., 2002. Investigation of Tornado Forces on a 2D Cylinder Using Computer Modeling, *Wind Engineering, Proc. NCWE (2002), 342-353*.

Selvam, R.P. and Govindaswamy, S., 2001. Aeroelastic analysis of bridge girder section using computer modeling, *Mack-Blackwell Rural Transportation Study Center Report No. MBTC FR-1095*. Available Online: http://ntl.bts.gov/lib/11000/11100/11186/1095.pdf. (Accessed: 10-14-2015).

Selvam, R.P., 1998. Computational procedures in grid based computational bridge aerodynamics, in *Bridge Aerodynamics, 327-336*.

Selvam, R.P., 1997a. Computation of pressures on Texas Tech University building using large eddy simulation, *J. Wind Engineering and Industrial Aerodynamics* ***67*** *and* ***68****, 647-657*.

Selvam, R.P., 1997b. Finite element modelling of flow around a circular cylinder using LES, *J. Wind Engineering and Industrial Aerodynamics* ***67*** *and* ***68****, 129-139*.

Selvam, R. P. and Paterson, D.A., 1993. Computation of conductor drag coefficients, *J. Wind Engineering and Industrial Aerodynamics* ***50****, 1-8*.

Selvam, R.P., 1985. Application of Boundary Element Method for Tornado Forces on Building, Ph.D. Dissertation, Texas Tech University, Lubbock, TX.

Sengupta, A., Haan, F.L., Sarkar, P.P., Balaramudu, V., 2008. Transient loads on buildings in microburst and tornado winds, *J. Wind Engineering and Industrial Aerodynamics* ***96****, 2173-2187*.

Sengupta, A., Haan, F.L., Sarkar, P.P., and Balaramudu, V., 2006. Transient Loads on Buildings in Microburst and Tornado Winds, *Proc. 4th International Symposium on Computational Wind Engineering (CWE2006),* Japan, July.

Seniwongse, M-S-N., 1977. Inelastic Response of Multistory Buildings to Tornadoes, PhD Dissertation, Texas Tech University Department of Civil Engineering, Lubbock, TX.

Simpson, R.H., and Saffir, H., 1974. The hurricane disaster potential scale, *Weatherwise **27.8**, 169*.

SkyscraperCenter, 2015. Transamerica Pyramid (Photograph), Available Online: http://www.skyscrapercenter.com/building/transamerica-pyramid/772. (Accessed 4-29-2015).

Stålberg, E., Brüger, A., Lötstedt, P., Johansson, A.V., and Henningson, D.S., 2006. High Order Accurate Solution of Flow Past a Circular Cylinder, *J. Scientific Computing **27(1-3)**, 431-441*.

Strasser, M.N., & Selvam, R.P., 2015. The variation in the maximum loading of a circular cylinder impacted by a 2D vortex with time of impact, *J. Fluids and Structures **58**, 66-78*.

Stull, R.B., 1988. An Introduction to Boundary Layer Meteorology (Chapter 8). Klewar Academic Publishers, The Netherlands. Available Online: http://nature.berkeley.edu/~sewolf/FLUXNET/Books/Stull.1988_Boundary-Layer-Meteorology.pdf. (Accessed: 10-16-2015).

Sullivan, R.D., 1959. A Two-Cell Vortex Solution of the Navier-Stokes Equations, *J. Aero/Space Sciences **26**, **767-768***.

Tamura, A., Tsutahara, M., Kataoka, T., Aoyama, T., and Yang, C., 2008. Numerical Simulation of Two-Dimensional Blade-Vortex Interactions Using Finite Difference Lattice Boltzmann Method, *AIAA Journal **46.9**, 2235-2247*.

Tan, C-T., 1975. Inelastic Response of High-Rise Buildings to Tornadoes, Master's Thesis, Texas Tech University Department of Civil Engineering, Lubbock, TX.

Tanamachi, R.L., Bluestein, H.B., Lee, W-C., Bell, M., and Pazmany, A., 2007. Ground-Based Velocity Track Display (GBVTD) Analysis of W-Band Doppler Radar Data in a Tornado near Stockton, Kansas, on 15 May 1999, *Monthly Weather Review **135**, 783-800*.

Thom, A., and Duraisamy, K., 2010. High-Resolution Simulations of Parallel Blade-Vortex Interactions, *J. AIAA **48.10**, 2313-2324*.

Thompson, D.S., 2015. WoodWorks Design Example: Five-Story Wood-Frame Structure over Podium Slab (pgs. 21-26) Available Online: woodworks.org. http://www.woodworks.org/wp-content/uploads/5-over-1-Design-Example.pdf (Accessed 6-1-2015).

Todorovska, M.I., Trifunac, M.D., Hao, T-Y., and Rjoub, Y.Al., 2007. Building Periods for Use in Earthquake Resistant Design Codes – Earthquake Response Data Compilation and Analysis of Time and Amplitude Variations, Final Report, US Geological Survey External Response Program. Project No. 05HQGR027.

Tornado Facts, 2009. Tornado Photograph. Available Online: http://tornado-facts.com/wp-content/uploads/2009/07/0.jpg. (Accessed: 2-19-2015).

UCAR, 2012. Getting the Drop on Storms, UCAR.edu. Available Online: http://www2.ucar.edu/atmosnews/in-brief/7188/getting-drop-storms. (Accessed 2-24-2015).

uiowa, 1999. Image Gallery – Vortices, uiowa.edu (Photograph). Available Online: http://user.engineering.uiowa.edu/~cfd/gallery/vortex.html. (Accessed: 4-13-2015).

Vatistas, G.H., 2006. Simple Model for Turbulent Tip Vortices, *J. Aircraft **43.5**, 1577-1578*.

Vatistas, G.H., 1998. New Model for Intense Self-Similar Vortices, *J. Propulsion and Power **14.4**, 462-469*.

Vatistas, G.H., Kozel, V., and Mih, W.C., 1991. A simpler model for concentrated vortices, *J. Experiments in Fluids **11.1**, 73-76*.

Vatistas, G.H., and Lin, S., 1988. A similar profile for the tangential velocity in vortex chambers, *Experiments in Fluids **6**, 135-137*.

Vatistas, G.H., Lin, S., and Kwok, C.K., 1986. Theoretical and Experimental Studies on Vortex Chamber Flows, *J. AIAA **24.4**, 635-642*.

Vickery, P.J., Wadhera, D., Powell, M.D., and Chen, Y., 2009. A Hurricane Boundary Layer and Wind Field Model for Use in Engineering Applications, *J. Applied Meteorology and Climatology* **48**, *381-405*.

Wan, C.A., and Chang, C.C., 1972. Measurement of the Velocity Field in a Simulated Tornado-Like Vortex Using a Three-Dimensional Velocity Probe, *J. Atmospheric Sciences **29**, 116-127*.

Weiland, C. and Vlachos, P.P., 2009. A mechanism for mitigation of blade-vortex interaction using leading edge blowing flow control, Exp. Fluids ***47***, *411-426*.

Wen, Y-K., 1975. Dynamic Tornadic Wind Loads on Tall Buildings, *J. Structural Division **101**, 169-185*.

Wilkins, E.M., 1964. The Role of Electrical Phenomena Associated with Tornadoes, *J. Geophysical Research **69.12**, 2435-2447*.

Williamson, C.H.K., 1996. Vortex Dynamics in the Cylinder Wake, *Annual Reviews in Fluid Mechanics* ***28****, 477-539.*

Willoughby, H.E., 1990. Temporal Changes of the Primary Circulation in Tropical Cyclones, *J. Atmospheric Sciences* ***47.2****, 242-262*.

Womble, J.A., Smith, D.A., Mehta, K.C., and McDonald, J.R., 2009. The Enhanced Fujita Scale: For Use Beyond Tornadoes?, *Forensic Engineering Congress, 699-708*.

Wood, V.T., and White, L.W., 2011. A New Parametric Model of Vortex Tangential-Wind Profiles: Development, Testing, and Verification. *J. Atmospheric Sciences,* ***68****, 990-1006*.

Wurman, J., Alexander, C., Robinson, P., and Richardson, Y., 2007. Low-Level Winds in Tornadoes and Potential Catastrophic Tornado Impacts in Urban Areas, *Bull. American Meteorological Society* ***88.1****, 31-46*.

Yang, Z., Sarkar, P., and Hu, H., 2011. An experimental study of a high-rise building model in tornado-like winds, *J. Fluids and Structures* ***27****, 471-486*.

Yang, Z., Sarkar, P., and Hu, H., 2009. Flow around a High-Rise Building Model in Tornado-like Wind, *Proc. 46th AIAA Aerospace Sciences Meeting and Exhibit,* Orlando, FL, USA.

Zimmerman, K.A., 2012. Tornado Alley: Where Twisters Form, livesicence.com. Available Online: http://www.livescience.com/25675-tornado-alley.html. (Accessed 2-19-2015).

APPENDIX A: USE OF CFD CODE "FCIR24.EXE"

A.1 Introduction and Overview

The present study utilizes the 2D, finite element code developed by Dr. R. Panneer Selvam to directly simulate impact of a vortex with a slender, cylindrical structure. The author modified the original program fcir23.exe by replacing the Rankine Combined vortex model with Vatistas' vortex model. Vatistas' model is selected because it replicates numerous vortex profiles as reviews in Chapter 3. This modified program is now referred to as fcir24.exe.

Figure A.1 is a flow chart that illustrates the three step process used to simulate vortex loading of a structure. The user first prepares f2dinp.txt which is the input data file for F2DINP2.exe and contains the simulation parameters and necessary information for constructing the grid. F2DINP2.exe reads in simulation and grid parameters from f2dinp.txt and assigns the grid points and elements for the finite element mesh. The output data file f2dinp-p.txt is formatted to plot the grid in Tecplot® if the user desires to view the grid prior to executing the CFD simulation. The other output data file cir.txt is then used as the input data file for the CFD simulation program fcir24.exe; cir.txt contains the simulation parameters as well as the grid information in the required finite element format.

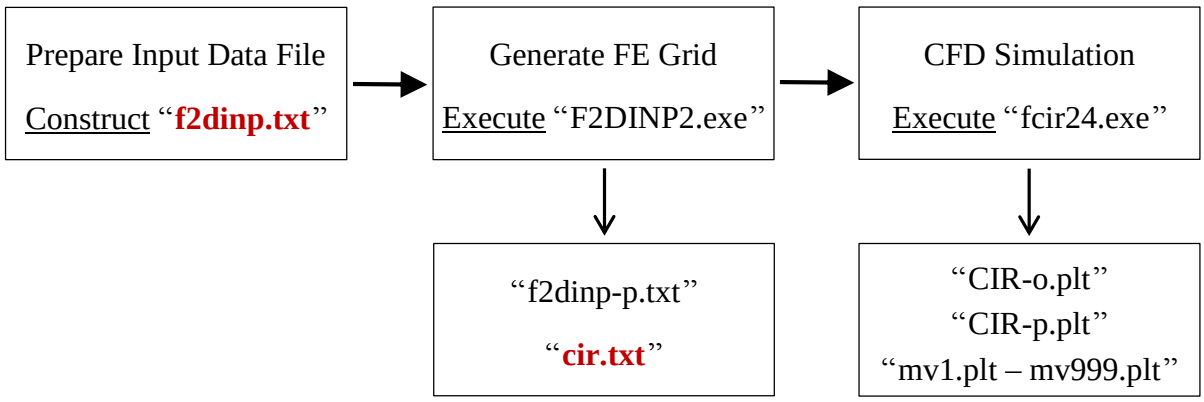


Figure A.1: Flow chart illustrating the simulation process using fcir24.

After running the CFD simulation a variable number of output data files are produced as indicated in the second box in the second row of Figure A.1. CIR-p.plt is used to plot contours of the values of the field variables (velocity, pressure, and vorticity) at the last time step of the CFD simulation using Tecplot®. Movie data files mv1.plt - mv999.plt contain the same information as CIR-p.plt but are plotted at the interval specified by the program's user. The text file char.txt contains the list of movie file names and must be kept in the same folder as fcir24.exe. Individual movie files can be combined in Tecplot® to create a running movie of the simulation. Procedure for creating a running movie in Tecplot® (360 EX 2014) is given below. Note that "+" implies a mouse click.

1. Select the movie files, and use drag-drop to upload them into Tecplot® (Figure A.2a).
2. Select the Data menu + Edit Time Strand (Figure A.2b) + Constant Delta + Apply (Figure A.2c).
3. Select Animate + Time… (Figure A.2d) + Destination → To File + Animate to File + Export Format → AVI + OK (Figure A.2e).

CIR-o.plt contains three tab-delineated columns of data which are dimensionless time, drag force coefficient, and lift force coefficient. Force coefficients are defined by integrating surface pressure and shear forces around the cylinder; drag and lift force coefficients are respectively defined by resolving the x- and y-direction forces and using the definition $C = 2 \cdot F/A \cdot \rho \cdot U_{ref}{}^2$. The program is written with the assumption that the reference area A, fluid density ρ, and reference velocity U_{ref} are all unity. Therefore, the actual output data in CIR-o.plt is dimensionless time, twice the horizontal force, and twice the vertical force. It is left to the user's discretion to adequately adjust the output data in CIR-o.plt to accommodate the traditional force

coefficient definitions. It is left to the user's discretion to adequately adjust the output data in CIR-o.plt to accommodate the traditional force coefficient definitions.

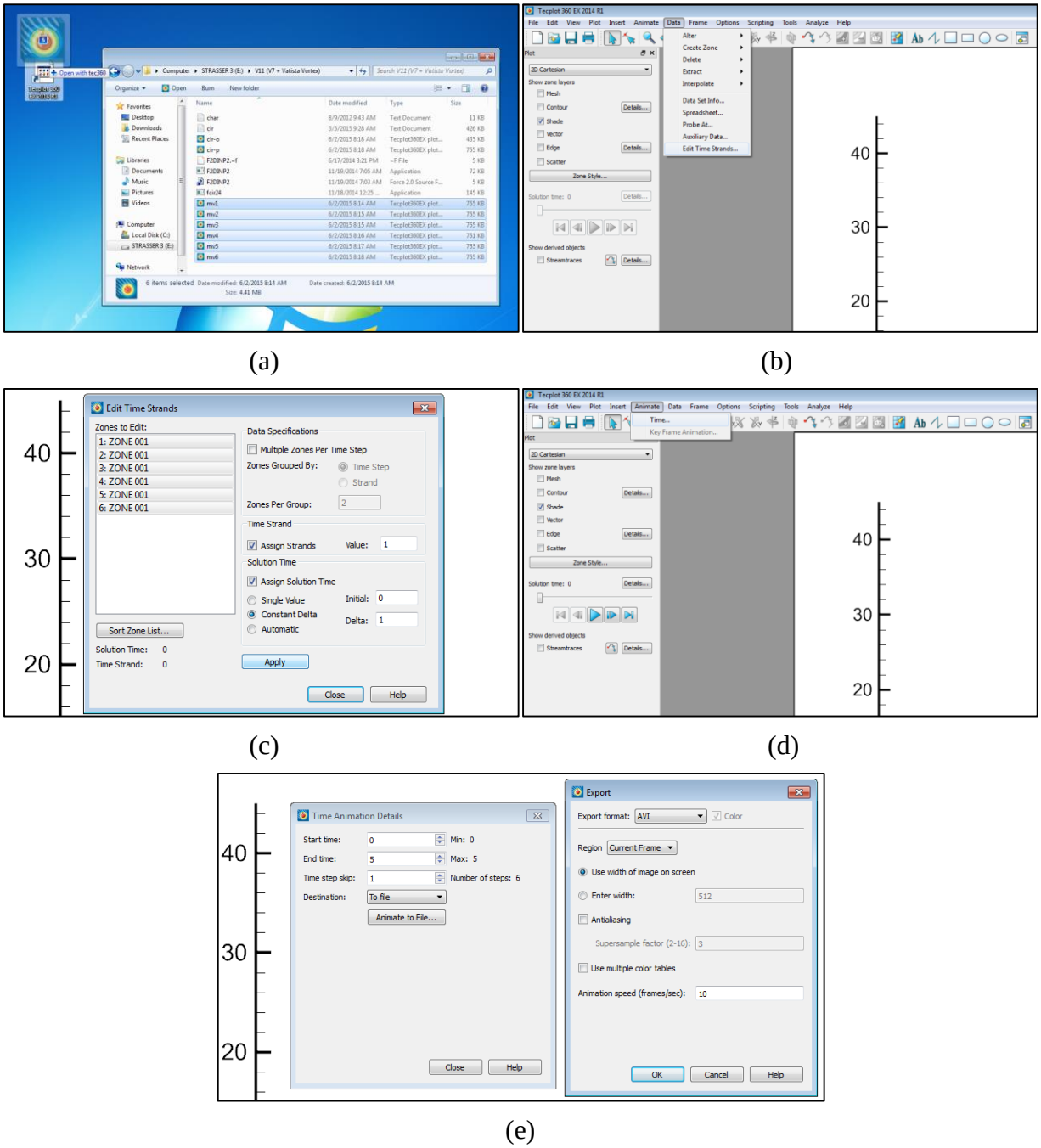


Figure A.2: Illustration of process for compressing individual movie (.mov) files into a running movie using Tecplot®.

It is prudent to always structure the grid around the grid so that the diameter of the cylinder is unity; consequently, the projected area per unit length is also unity and does not complicate computation of the force coefficient. As explained in Chapter 4, the fluid density is also assumed to be unity when introducing the dimensionless terms in the Navier Stokes equations. The present work utilizes different reference velocities depending upon the parameters of the system being simulated. It is left to the user to post-process CIR-o.plt if they wish to use a different reference velocity than the default value of unity.

A.2 Preparation of Input Data File f2dinp.txt

F2DINP2.f reads data from f2dinp.txt using the command lines listed below. Descriptions of each of the variables are provided subsequently on a line-by-line basis. Note that Line 4 requires the user to input JM1 radial node points. These are defined along the shortest line from the cylinder surface to the edge of the square; it is convenient to define the first grid point, which is the cylinder radius, because this corresponds to a cylinder diameter of unity and simplifies force coefficient calculations. Subsequently, Line 5 requires that the user input IM2 horizontal grid point locations for the rectangular downstream region of the grid. The radial point provided in Line 4 and the first horizontal point provided in Line 5 must be the same.

```
READ(5,*)IM1,JM1,IM2,JM2,ANGLE
READ(5,*)TLAG,TTIME,DT,IFB,IFE,IFL2
READ(5,*)VISC,RAMAX,ROTC,VTRAN,PN,YSHIFT
READ(5,*)(R(I),I=1,JM1)
READ(5,*)(RX2(I),I=1,IM2)
```

Line 1: READ(5,*)IM1,JM1,IM2,JM2,ANGLE

IM1 number of tangential nodes (around the circumference) in Region I.
JM1 number of radial nodes in Region I.
IM2 number of nodes along the I-axis (horizontal axis) in region II.
JM2 number of nodes along the J-axis (vertical axis) in region II (**JM2** = **IM1**/4 + 1).
ANGLE angle between nodes in Region I (**ANGLE** = 360/**IM1**).

Line 2: READ(5,*)TLAG,TTIME,DT,IFB,IFE,IFL2

TLAG number of time units before vortex and cylinder centers coincide.
TTIME total number of time units in simulation.
DT time step length.
TW1 is the time at which the first movie file is written.
TW2 is the time at which the last movie file is written.
IFL2 number of time steps between movie files being written.
*Note that a maximum of 999 movie files may be written.

Line 3: READ(5,*)VISC,RAMAX,ROTC,VTRAN,YSHIFT

VISC kinematic viscosity o the fluid.
RAMAX radius of forced vortex.
ROTC rotational constant.
VTRAN rate at which center of vortex translates (left to right).
PN exponent for Vatistas vortex model
YSHIFT is the vertical distance between horizontal axes of vortex and cylinder.
*"-**YSHIFT**" moves the vortex up and "+**YSHIFT**" moves the vortex down.

Line 4: READ(5,*)(R(I),I=1,JM1)

R(I) radial node points for Region I.
*Maximum of 120 radial node points may be used.

Line 5: READ(5,*)(RX2(I),I=1,IM2)

RX2(I) node points along I-axis (x-axis) of Region II.
*Maximum of 60 horizontal node points may be used.
*Note that **RX2(1)** = **R(JM1)** – The last radial node and first horizontal node coincide.

A.2.1 Sample Input Data File

An example of the input data file f2dinp.txt is provided in three columns below. ***Figure A.3*** illustrates the grid produced, which is f2dinp-p.txt, when F2DINP2.f is executed. Note that JM1 is marked in red text along with the corresponding radial grid points, and IM2 is marked in blue text along with the corresponding horizontal grid points in the downstream region of the rectangular region of the grid. Finally, note that the last radial node and first horizontal node, designated by bold text and yellow highlight, both have values of 10.

120 55 22 31 3.	0.51575	0.571153782
250. 300. 0.01 1 300 10	0.524825	0.585769161
0.006667 5. 0.2 1. 0.	0.5348075	0.601846077
0.5	0.54578825	0.619530685
0.5075	0.557867075	0.638983753

0.660382128	2.34107524	10.5
0.683920341	2.53268276	11.05
0.709812375	2.74345104	11.65
0.738293613	2.97529614	12.3
0.769622974	3.23032576	13.
0.804085271	3.51085833	13.75
0.841993799	3.81944417	14.55
0.883693178	4.15888858	15.4
0.929562496	4.53227744	16.3
0.980018746	4.94300519	17.25
1.03552062	5.39480571	18.25
1.09657268	5.89178628	19.3
1.16372995	6.34825447	20.4000001
1.23760295	6.80472266	21.5500001
1.31886324	7.26119085	22.7500001
1.40824956	7.71765904	24.0000001
1.50657452	8.17412723	25.3000001
1.61473197	8.63059543	26.6500001
1.73370517	9.08706362	28.0500001
1.86457569	9.54353181	29.5000001
2.00853326	**10.**	31.00000
2.16688658	**10.**	

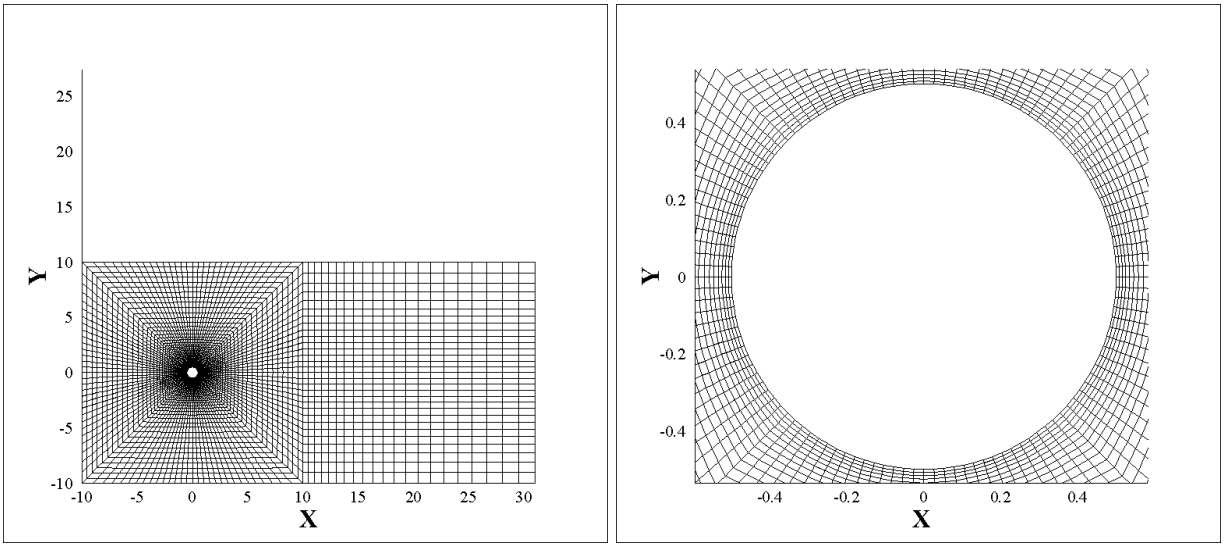


Figure A.3: Grid produced using the sample f2dinp.txt data file.

A.2.2 Use of GW.f to Produce f2dinp.txt

Manual construction of f2dinp.txt is time consuming as the user must define the positions of all radial nodes in Region I of the grid and the horizontal positions of all columns of nodes in

Region II of the grid; furthermore, manual construction and entry of the grid points is another potential source of error. Therefore, a program titled GW.f has been developed to construct f2dinp.txt from user-specified grid dimensions and spacing. The required input data file input.txt is structured as listed below. The only new terms that have not been previously explained are listed in Row 3, hence these are the only new variables that shall be explained. GC.f is currently configured to use constant horizontal node spacing in Region II. However, it can easily be modified to stretch horizontal node spacing, as is used in the Grid illustrated in Figure A.3, by employing a growth coefficient as is done for the radial node spacing.

```
READ(2,*)VISC,PN,VTRAN,RAMAX,ROTC,YSHIFT
READ(2,*)TLAG,TTIME,DT,IFB,IFE,IFL2
READ(2,*)RO,RF,DRO,DRM,GC,ANGLE,X
```

Row 3: READ(2,*)RO,RF,DRO,DRM,GC,ANGLE,X

RO is the location of the first radial node (should be taken as 0.5 for simplicity).
RF is the location of the last radial node (side length of Region I).
DRO is the first radial node spacing.
DRF is the maximum radial node spacing.
GC is the growth coefficient used to stretch radial node spacing (1.10 is used herein).
ANGLE has the same definition as given above.
X is the length of Region II.

A.2.3 Source Code for GW.f

```
C     %%%%
```

```
C     %%% interworking of this program prior to use.                 %%%
C     %%%%%%%%%%%%%%%%%%%%%%%%%%%%%%%%%%%%%%%%%%%%%%%%%%%%%%%%%%%%%%%%%
      PARAMETER (NR=1000)
      IMPLICIT REAL *8 (a-h,o-z)
      DIMENSION R(NR),X2(NR)
      OPEN(2,FILE='input.txt')
      OPEN(3,FILE='f2dinp.txt')

      READ(2,*)VISC,PN,VTRAN,RAMAX,ROTC,YSHIFT
      READ(2,*)TLAG,TTIME,DT,IFB,IFE,IFL2
      READ(2,*)RO,RF,DRO,DRM,GC,ANGLE,X

      DO I=1,NR
         R(I)=0.
         X2(I)=0.
      END DO
C.....................................................................C
C.....................Generate Radial Nodes in RI.....................C
C.....................................................................C
C     Radial nodes are defined as Ri = [(Ri-1)-(Ri-2)]*GC until spacing
C     exceeds the maximum given in the input. Then, the remaining radial
C     distance to be spanned is computed, and nodes are equally spaced
C     to cover it. The actual maximum radial node spacing is slightly
C     less than that given.
C.....................................................................C
      R(1)=RO
      R(2)=R(1)+DRO
      DO I=3,NR
         R(I)=R(I-1)+(R(I-1)-R(I-2))*GC
         IF(R(I).GT.RF)THEN
            R(I)=RAMAX
            JM1=I
            GOTO 1000
         END IF
         CHECK=(R(I-1)-R(I-2))*GC
         IF(CHECK.GT.DRM)THEN
            DRR=RF-R(I-1)
            NMAX=DRR/DRM
            DREQ=DRR/(NMAX+1)
            DO J=I,I+NMAX
               R(J)=R(J-1)+DREQ
            END DO
            JM1=J-1
            GOTO 1000
         END IF
      END DO
C.....................................................................C
C.............Compute Horizontal Node Spacing in RII .................C
C.....................................................................C
C     Horizontal node spacing in Region II is taken as the average of
C     the vertical node spacing.
C.....................................................................C
1000  IM1=360./ANGLE       ! Nodes Around the Cylinder (Region I)
      JM2=IM1/4+1          ! Vertical Nodes (Region II)
      NYO=(JM2-1)/2        ! Number of Vertical Spaces
      DYAVG=RF/NYO         ! Average Vertical Spacing
      NDX=X/DYAVG
```

```
      DX=X/(NDX+1)
      X2(1)=R(JM1)
      DO I=2,NDX+2
         X2(I)=X2(I-1)+DX
      END DO
      IM2=NDX+2
C.....................................................................C
      WRITE(3,*)IM1,JM1,IM2,JM2,ANGLE
      WRITE(3,*)TLAG,TTIME,DT,IFB,IFE,IFL2
      WRITE(3,*)VISC,RAMAX,ROTC,VTRAN,PN,YSHIFT
      DO I=1,JM1
         WRITE(3,*)R(I)
      END DO
      DO I=1,IM2
         WRITE(3,*)X2(I)
      END DO
      STOP
      END
```

APPENDIX B: DATA EXTRACTION PROGRAM "GET_DAT.M"

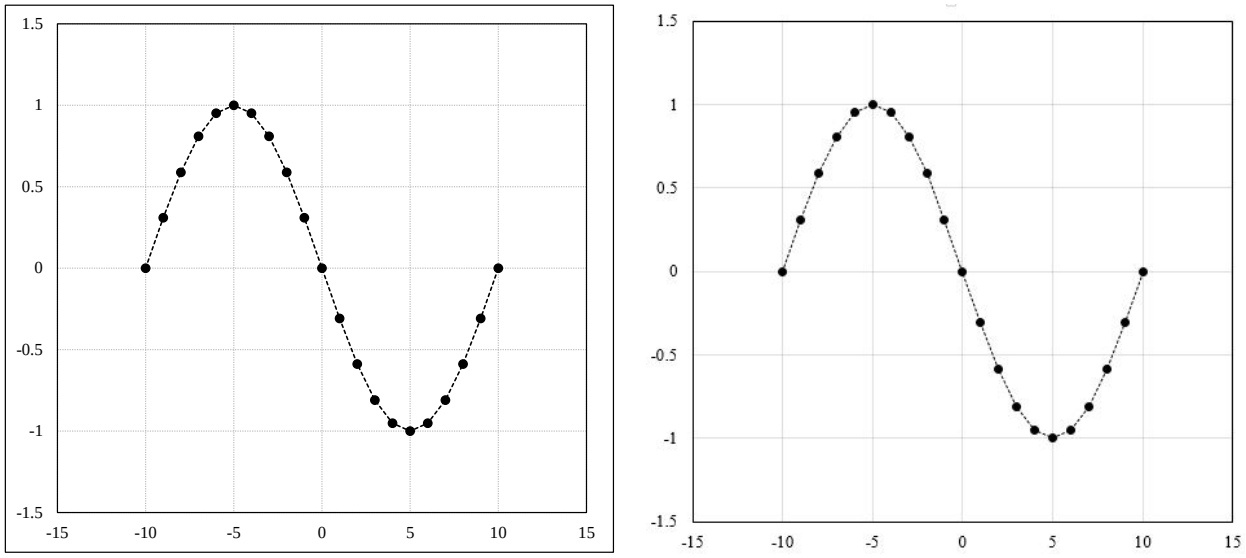
B.1 Overview and Description

Technical documents typically report experimental findings graphically rather than in tabular form so significant trends can be easily identified. The primary problem with graphical data presentation is that the numerical values of the plotted data typically are not reported in the literature. Consequently, it is difficult to locate numerical data values for validation and comparison of data values attained in subsequent studies. The authors of the technical documents can, in some cases, be contacted with requests for the numerical values of the plotted data. However, this is a tedious, time-consuming process, and original data are frequently lost in the years following publication of the technical documents. In short, methodology is needed to read discrete data points from images of plot files.

"Get_Dat.m" is a program developed using the Matlab® programming environment. The program allows the user to extract discrete data points from a .jpg image file of a plot having linear axis. The user is prompted to click-select the plot's origin, right x-axis bound, and top y-axis bound as well as to specify the x- and y-values at each location. The user then is prompted to click-select any number of discrete data points which are then converted to the user-assigned coordinate system and output as a .txt file. The accuracy with which the user-defined data points represent the original data points in the .jpg image of the plot depends upon the user's accuracy in click-selecting the values. However, discrete points are selected with sufficient accuracy for applications such as the present study. It is the user's responsibility to establish if the extracted points have sufficient resolution for their particular study. The subsequent subsection illustrates the use of "Get_Dat.m" and effectively serves as a user's manual.

B.2 Demonstration of Use

After compiling “Get_Dat.m” in a folder, the user should then save the selected plot image as a “Capture.jpg” in the same folder (The author suggests using the “Snip” tool to select the desired region of the plot for data extraction). Figures B.1a and B.1b illustrate the original data plot from which points are to be extracted and the .jpg file produced using the snip tool respectively.



(a) (b)

Figure B.1: (a) Original data plot and (b) .jpg impage of the original data plot.

When “Get_Dat.m” is executed, the program reads in “Capture.jpg” and assigns axis in the top-left corner of the image (This is a default setting because the command “imread(image name)” command is used). The user is prompted to (1) click-select and (2) define values at the locations of the origin, top of the y-axis, and end of the x-axis, the locations of which are illustrated in Figure B.2. The click-selected axis locations are important because they establish the origin locations with respect to the matlab-defined axis system (which is defined with respect to the top-left corner of the image). The user-defined axis values are important because they,

along with the click-selected axis values, provide a means to transform the data points from the matlab-defined axis to the user-defined axis.

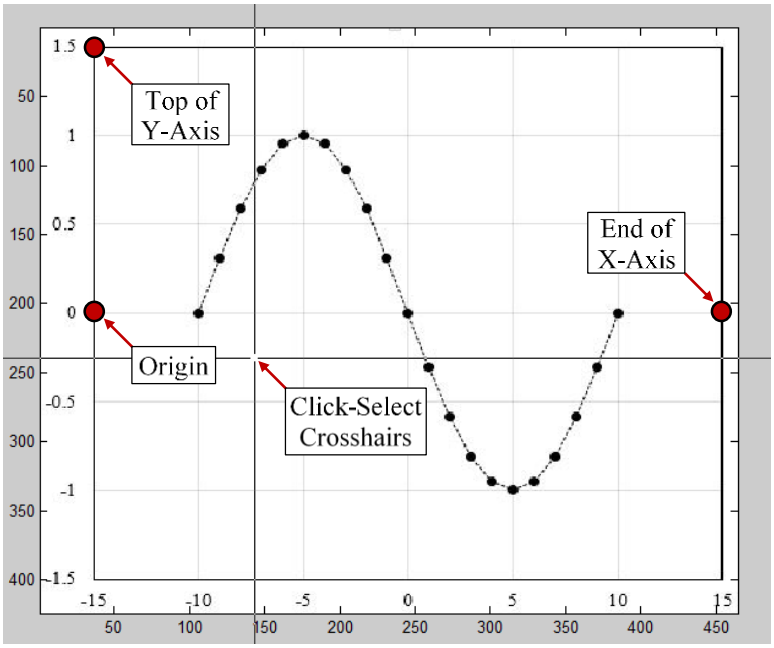


Figure B.2: Illustration of "Capture.jpg" in the Matlab® environment and the three axis that the user must click-select and assign values of.

After establishing and defining the locations of the origin, top of y-axis, and end of x-axis, the user is then prompted to select any number of discrete data points from the curve. Discrete points are click-selected and recorded until the user terminates the data-selection phase by striking the "Enter" key. The extracted data points are output in a tab-dilineated .txt file titled "DataPoints.txt" and displayed via a pop-up Matlab® plot.

Figure B.3 compares the extracted data points with the original data points. The extracted data points are excellent representation of the the original data points. There are small variations between the original and extracted values in some cases, as there is user-error in manually click-selecting the locations of the data points within the .jpg image. However, for applications such as extracting measurements of vortex tangential velocity profiles or curves of

force coefficient and Strouhal number trends for qualitative comparison (Which are the specific uses in the present study), “Get_Dat.m” provides sufficient accuracy.

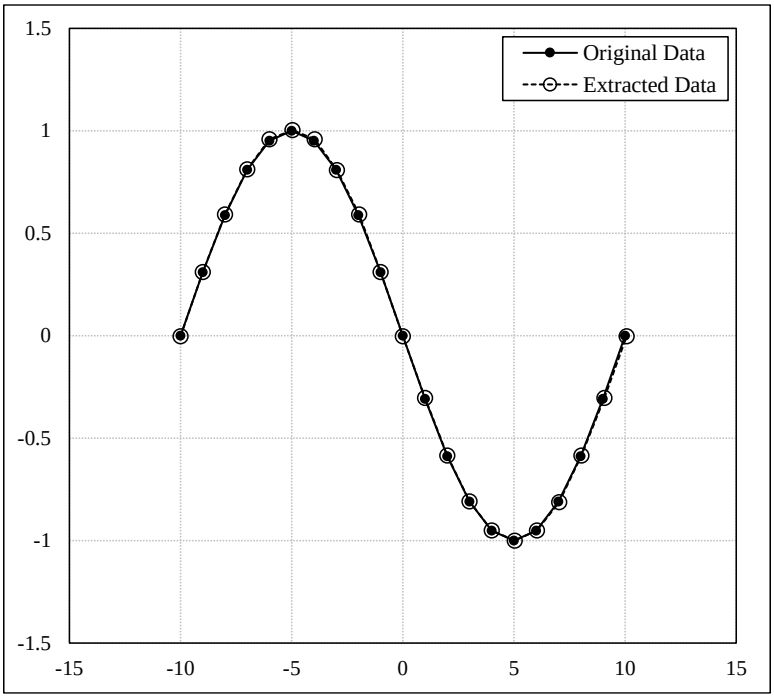


Figure B.3: Comparison of original data points with extracted data points.

B.3 Source Code

“Get_Dat.m” has been an invaluable resource that has allowed the author to rapidly compile large quantities of data from physical and computer simulations reported in the literature that would otherwise have been unatainable or at least would have required extensive time to compile. This program can be utilized for the same purpose in other studies, hence the author wishes to dissiminate it for use by other authors as they pursue their studies. However, the author requests that subsequent users give credit where due and retain the header file (Green text).

```
%%%%%%%%%%%%%%%%%%%%%%%%%%%%%%%%%%%%%%%%%%%%%%%%%%%%%%%%%%%%%%%%%%%%%%%%%%%%
%%%*****************************--- Get_Dat.m ---*****************************%%%
%%%%%%%%%%%%%%%%%%%%%%%%%%%%%%%%%%%%%%%%%%%%%%%%%%%%%%%%%%%%%%%%%%%%%%%%%%%%
%%% Developed by: Matthew N. Strasser & Cyrus Garner                        %%%
%%% June 30, 2015                                                           %%%
%%%%%%%%%%%%%%%%%%%%%%%%%%%%%%%%%%%%%%%%%%%%%%%%%%%%%%%%%%%%%%%%%%%%%%%%%%%%
%%%*****************************--- Description ---*****************************%%%
%%%%%%%%%%%%%%%%%%%%%%%%%%%%%%%%%%%%%%%%%%%%%%%%%%%%%%%%%%%%%%%%%%%%%%%%%%%%
%%% This program allows the reading of discrete data points from a .jpg %%%
%%% image file of a data plot having LINEAR axis. The user click-assigns%%%
%%% the locations of the axis and origin and provides values for each.  %%%
%%% The user then click-selects points on the plot image, which are     %%%
%%% then converted to discrete points based upon the user-defined axis. %%%
%%%%%%%%%%%%%%%%%%%%%%%%%%%%%%%%%%%%%%%%%%%%%%%%%%%%%%%%%%%%%%%%%%%%%%%%%%%%
%%%*****************************--- Disclaimer ---*****************************%%%
%%%%%%%%%%%%%%%%%%%%%%%%%%%%%%%%%%%%%%%%%%%%%%%%%%%%%%%%%%%%%%%%%%%%%%%%%%%%
%%% To the best of the author's knowledge, this program is usable for   %%%
%%% any plot image having linear axis. The user should be cautious      %%%
%%% and verify that GET_DAT.m provides sufficient accuracy for their    %%%
%%% application. The outputted discrete values are approximate, with    %%%
%%% their resolution being determined by the accuracy of the user's     %%%
%%% click-selection of data points.                                     %%%
%%%%%%%%%%%%%%%%%%%%%%%%%%%%%%%%%%%%%%%%%%%%%%%%%%%%%%%%%%%%%%%%%%%%%%%%%%%%
close all;
clear all;
im_mat = imread('Capture.JPG');    % Read input .jpg file
fName = 'DataPoints.txt';          % Write output .txt file
imagesc(im_mat)                    % Scale and assign .jpg file
% Define plot area from which data will be extracted and assign axis and
% dimensions for extracted data.
check_flag = 0;
while check_flag == 0
    disp('Select Origin')
    Oc = ginput(1);
    Ox = input('Input Origin "X-Value"');
    Oy = input('Input Origin "Y-Value"');
    check_flag = input('Is Origin Correct? (1 yes, 0 no)');
end
check_flag = 0;
while check_flag == 0
    disp('Select Top End of Y-Axis')
    Yc = ginput(1);
    Yy = input('Input "Y-Value"');
    check_flag = input('Is End Y-Axis Value Correct? (1 yes, 0 no)');
end
check_flag = 0;
while check_flag == 0
    disp('Select End of X-Axis')
    Xc = ginput(1);
    Xx = input('Input "End of X-Axis Value"');
    check_flag = input('Is End X-Axis Value Correct? (1 yes, 0 no)');
end
% Length Scales for Matlab-Assigned Axis
XLc = abs(abs(Oc(1,1))-abs(Xc(1,1)));
YLc = abs(abs(Oc(1,2))-abs(Yc(1,2)));
% Length Scales for User-Defined Axis
XLu = abs(Xx-Ox);
```

```
YLu = abs(Yy-Oy);
% Scalers for Conversion from Matlab-to-User Axis
XS = XLu/XLc;
YS = YLu/YLc;
% Read Click-Selected Data Points
disp('HIT RETURN TO EXIT');
[Px,Py] = ginput;
% Flip Y-Axis (Matlab Assigns at Top-Left Image Corner)
Pyf = - Py + Oc(1,2);
% Convert Matlab-Axis Data Points to User-Defined Axis
for i=1:length(Px)
    DXc = Px(i)-Oc(1,1);
    DYc = Pyf(i);
    TEMP(i,1) = Ox + DXc*XS;
    TEMP(i,2) = Oy + DYc*YS;
end

dlmwrite(fName,TEMP,'\t');

figure(1)
plot(TEMP(:,1),TEMP(:,2),'k--o','linewidth',2)
title('Extracted Points','fontsize',20,'fontweight',...
    'b','fontname','Times New Roman')
grid on
```

APPENDIX C: DLF ANALYSIS PROGRAM "DLF.M"

C.1 Overview and Description

One aspect of this body of work is the assessment of the capability of latteral vortex loading to be dynamically amplified. Chapter 6 explains extensively how DLF analysis is an effective way to determine whether or not the manner in which a transient load is applied will producee dynamic amplification of the loading. The present program "DLF.m" is developed in the Matlab® environment. Both dimensional (Section C.3) and dimensionless (Section C.4) versions have been developed following the discussion in Section 6.3.1. The model's response is resolved at each time step via fourth order Runge Kutta. For each structure frequency, the maximum DLF value is defined; DLF(fn) values are then compiled, thereby defining the DLF curve for loading by both force coefficients.

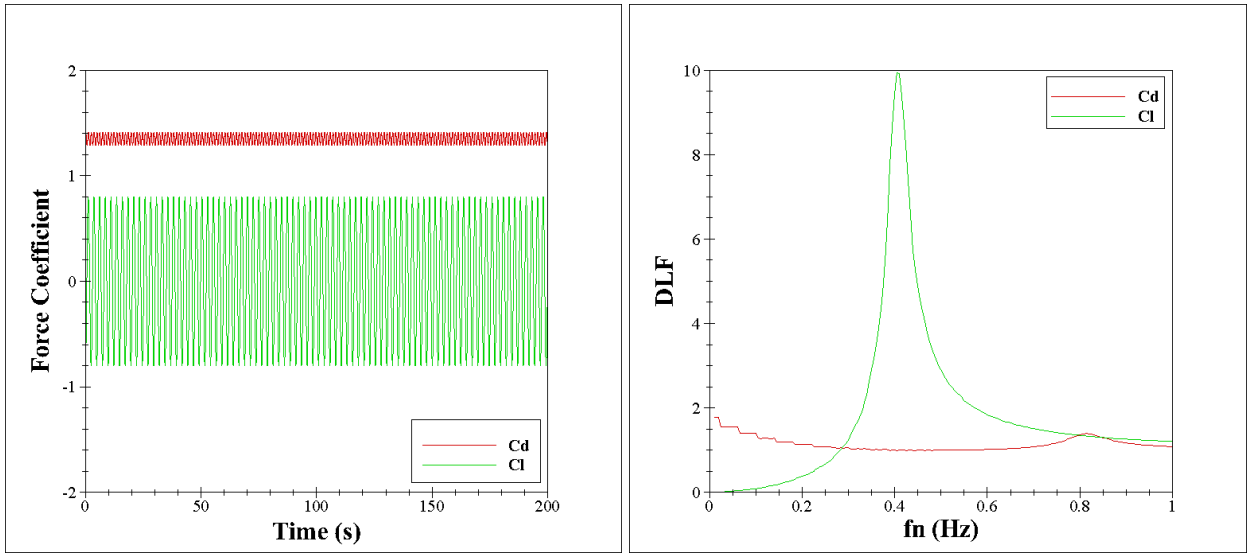
The user defines the SDOF system's "mass" and "damping ratio" inside the program, as well as the range and increment of the "fundamental structure frequency" inside the program. The nondimensional model requires extra parameters such as fluid density, refference area, etc. The program then computes the structure "stiffness" for each fundamental frequency prior to analyzing the SDOF system's response to the applied forcing. The program outputs the DLF(fn) curves for application of the drag and lift force coefficients in the .txt file "DLF_out.txt". The author validates "DLF.m" by comparison of a computed DLF curve from a sine wave forcing profile with the analytical definition for the same forcing profile. However, it is the responsibility of the user to verify the accuracy and usability of "DLF.m" in their individual application. The subsequent subsection illustrates the use of "DLF.m" and effectively serves as a user's manual.

"DLF.m" is a valuable program that may aid other authors in their studies and serve as a starting point for response models developed in their individul studies. The author wishes to

dissiminate it for use by other authors but requests that subsequent users give credit where due and retain the header if the program is not significantly modified (Green text).

C.2 Demonstration of Use

After typing and saving "DLF.m" in a folder, the user should also save the x- and y-direction forcing time histories as a .plt file titled "FC.plt" in the same folder. The forcing considered for this example is dimensionless drag and lift force coefficient time histories which are illustrated in Figure 6.1, hence the dimensionless version of the program is used. The fundamental structure frequency range is declared in Line 3l as "fn = (0.01:0.005:1.0)". This reads that the lowest frequency is 0.01 s^{-1}, the frequency increment is 0.005 s^{-1}, and the highest frequency is 1.0 s^{-1}. The structure's mass "m" and damping ratio "z" are respectively defined in Line 32 and 39. The reference velocity "Ur", reference dimension "D", and reference length "L" which are required to introduce the dimensionless force coefficient are respectively defined in Lines 34-36. Upon execution of DLF.m, the DLF curve produced for both force coefficients is shown in Figure C.1.



(a) (b)

Figure C.1: (a) Force coefficient time histories and (b) corresponding DLF curves.

C.3 Source Code (Dimensional)

```
%%%%%%%%%%%%%%%%%%%%%%%%%%%%%%%%%%%%%%%%%%%%%%%%%%%%%%%%%%%%%%%%%%%%%%%%%%%%%%%%
%%%*****************************--- DLF.m ---*****************************%%%
%%%%%%%%%%%%%%%%%%%%%%%%%%%%%%%%%%%%%%%%%%%%%%%%%%%%%%%%%%%%%%%%%%%%%%%%%%%%%%%%
%%% Developed by: Matthew N. Strasser                                       %%%
%%% March 10, 2015                                                          %%%
%%%%%%%%%%%%%%%%%%%%%%%%%%%%%%%%%%%%%%%%%%%%%%%%%%%%%%%%%%%%%%%%%%%%%%%%%%%%%%%%
%%%*************************--- Description ---*************************%%%
%%%%%%%%%%%%%%%%%%%%%%%%%%%%%%%%%%%%%%%%%%%%%%%%%%%%%%%%%%%%%%%%%%%%%%%%%%%%%%%%
%%% This program analyzes the response of a single degree of freedom    %%%
%%% (SDOF) structure to decoupled drag and lift forces and defines the  %%%
%%% dynamic load factor (DLF) curve for the applied forcing as function %%%
%%% of the fundamental structure frequency (fn).                        %%%
%%%%%%%%%%%%%%%%%%%%%%%%%%%%%%%%%%%%%%%%%%%%%%%%%%%%%%%%%%%%%%%%%%%%%%%%%%%%%%%%
%%%*************************--- Disclaimer ---*************************%%%
%%%%%%%%%%%%%%%%%%%%%%%%%%%%%%%%%%%%%%%%%%%%%%%%%%%%%%%%%%%%%%%%%%%%%%%%%%%%%%%%
%%% It is the responsibility of the user to verify the applicability of %%%
%%% this program for their study.                                       %%%
%%%%%%%%%%%%%%%%%%%%%%%%%%%%%%%%%%%%%%%%%%%%%%%%%%%%%%%%%%%%%%%%%%%%%%%%%%%%%%%%
clear all;
close all;
load FC.plt;            % Forcing Time Histories.
fName='DLF_out.txt';    % Output data file.
TIMEi  = FC(:,1);       % Time Vector.
Fdi = FC(:,2);          % Drag Force Vector.
Fli = FC(:,3);          % Lift Force Vector.
%%%%%%%%%%%%%%%%%%%%%%%%%%%%%%%%%%%%%%%%%%%%%%%%%%%%%%%%%%%%%%%%%%%%%%%%%%%%%%%%
%%%%%%%%%%%%%%%%%%%%%%%%%% Response Spectrum %%%%%%%%%%%%%%%%%%%%%%%%%%%%%%%%%%
%%%%%%%%%%%%%%%%%%%%%%%%%%%%%%%%%%%%%%%%%%%%%%%%%%%%%%%%%%%%%%%%%%%%%%%%%%%%%%%%
fn = (0.01:0.005:1.0);                          % Structure frequency (Hz)
m = 200000;                                     % Structure mass (kg)
z = 0.05;                                       % Damping ratio (dim)
tic;
for j=1:length(fn)
    wn = 2*pi*fn(j);                            % Structure frequency (rad/s)
    k = wn^2*m;                                 % Structure stiffness (N/m)
    Kt(j) = k;
    A = [0,1;-wn^2,-2*z*wn];                    % State matrix
    B = @(tt, qq, FF)(A*qq + [0; FF/m]);        % System of Eqs
    q0 = [0; 0];                                % Initial conditions
% Initialize dummy solution vectors.
    S1 = zeros(length(q0), length(TIMEi));
    S1(:,1) = q0;
    S2 = zeros(length(q0), length(TIMEi));
    S2(:,1) = q0;
% Analyze Fl
    for i = 1:length(TIMEi)-1
        if(i==1)
            dt = TIMEi(2)-TIMEi(1);
        else
            dt = TIMEi(i)-TIMEi(i-1);
        end
        k1 = B(TIMEi(i), S1(:,i), Fli(i));
        qmid = S1(:,i) + dt/2*k1;
        k2 = B(TIMEi(i) + 1/2*dt, qmid, (Fli(i) + Fli(i+1))/2);
```

```
        qmid = S1(:,i) + dt/2*k2;
        k3 = B(TIMEi(i) + 1/2*dt, qmid, (Fli(i) + Fli(i+1))/2);
        qend = S1(:,i) + dt*k3;
        k4 = B(TIMEi(i) + dt, qend, Fli(i));
        S1(:,i+1) = S1(:,i) + dt/6*(k1 + 2*k2 + 2*k3 + k4);
    end
% Analyze Fd
    for i = 1:length(TIMEi)-1
        if(i==1)
            dt = TIMEi(2)-TIMEi(1);
        else
            dt = TIMEi(i)-TIMEi(i-1);
        end
        k1 = B(TIMEi(i), S2(:,i), Fdi(i));
        qmid = S2(:,i) + dt/2*k1;
        k2 = B(TIMEi(i) + 1/2*dt, qmid, (Fdi(i) + Fdi(i+1))/2);
        qmid = S2(:,i) + dt/2*k2;
        k3 = B(TIMEi(i) + 1/2*dt, qmid, (Fdi(i) + Fdi(i+1))/2);
        qend = S2(:,i) + dt*k3;
        k4 = B(TIMEi(i) + dt, qend, Fdi(i));
        S2(:,i+1) = S2(:,i) + dt/6*(k1 + 2*k2 + 2*k3 + k4);
    end
% Take Steady Response (Avoid unsteadiness in initial RK4 solution)
    XFl = S1(1,round(length(TIMEi)/8):length(TIMEi));
    XFd = S2(1,round(length(TIMEi)/8):length(TIMEi));
% Compute Maximum Response Amplitude
    X1(1) = max(XFl);
    X1(2) = abs(min(XFl));
    X2(1) = max(XFd);
    X2(2) = abs(min(XFd));
    AFl(j) = max(X1);
    AFd(j) = max(X2);
    clear XFl XFd RMS X1 X2;
% Re-Set dummy solution vector
    S1 = zeros(length(q0), length(TIMEi));
    S1(:,1) = q0;
    S2 = zeros(length(q0), length(TIMEi));
    S2(:,1) = q0;
toc;
J=j
W=length(fn)
end
%%%%%%%%%%%%%%%%%%%%%%%%%%%%%%%%%%%%%%%%%%%%%%%%%%%%%%%%%%%%%%%%%%%%%%%%%%%%%%%
%%%%%%%%%%%%%%%%%%%% Convert maximum response to DLF %%%%%%%%%%%%%%%%%%%%%%%%%%
%%%%%%%%%%%%%%%%%%%%%%%%%%%%%%%%%%%%%%%%%%%%%%%%%%%%%%%%%%%%%%%%%%%%%%%%%%%%%%%
% Compute maximum static displacements.
Fdt(1) = abs(max(Fdi));
Fdt(2) = abs(min(Fdi));
Fdm = max(Fdt);                                 % Absolute maximum drag force
Flt(1) = abs(max(Fli));
Flt(2) = abs(min(Fli));
Flm = max(Flt);                                 % Absolute maximum lift force
for j=1:length(fn)
    DLFFd(j) = AFd(j)/(Fdm/(Kt(j)));
    DLFFl(j) = AFl(j)/(Flm/(Kt(j)));
end
% Write response data.
```

```
for i=1:length(fn)
    TEMP(i,1)=fn(i);         % Structure frequencies (Hz)
    TEMP(i,2)=DLFFd(i);      % Drag Force DLF
    TEMP(i,3)=DLFFl(i);      % Lift Force DLF
end
dlmwrite(fName,TEMP,'\t');

yl = 1.10*max(max(DLFFd),max(DLFFl));
figure (1)
plot(fn,DLFFl,':og',fn,DLFFd,':or','linewidth',2)
xlabel('Structure Frequency (Hz)','fontsize',14,'fontweight','b',...
    'fontname','Times New Roman')
ylabel('DLF','fontsize',14,'fontweight','b','fontname',...
    'Times New Roman')
set(gca,'xlim',[0 max(fn)],'ylim',[0 yl],'fontsize',12,'fontname',...
    'Times New Roman')
legend('Fl','Fd',2)
grid on
```

C.4 Source Code (Dimensionless)

```
%%%%%%%%%%%%%%%%%%%%%%%%%%%%%%%%%%%%%%%%%%%%%%%%%%%%%%%%%%%%%%%%%%%%%%%%%%%%%%%%
%%%*****************************--- DLF.m ---*****************************%%%
%%%%%%%%%%%%%%%%%%%%%%%%%%%%%%%%%%%%%%%%%%%%%%%%%%%%%%%%%%%%%%%%%%%%%%%%%%%%%%%%
%%% Developed by: Matthew N. Strasser                                       %%%
%%% October 15, 2015                                                        %%%
%%%%%%%%%%%%%%%%%%%%%%%%%%%%%%%%%%%%%%%%%%%%%%%%%%%%%%%%%%%%%%%%%%%%%%%%%%%%%%%%
%%%***************************--- Description ---***************************%%%
%%%%%%%%%%%%%%%%%%%%%%%%%%%%%%%%%%%%%%%%%%%%%%%%%%%%%%%%%%%%%%%%%%%%%%%%%%%%%%%%
%%% This program analyzes the response of a single degree of freedom       %%%
%%% (SDOF) structure to decoupled drag and lift force coefficients and      %%%
%%% defines the dynamic load factor (DLF) curve for the forcing as a        %%%
%%% function of the fundamental structure frequency (fn).                   %%%
%%%%%%%%%%%%%%%%%%%%%%%%%%%%%%%%%%%%%%%%%%%%%%%%%%%%%%%%%%%%%%%%%%%%%%%%%%%%%%%%
%%%***************************--- Disclaimer ---***************************%%%
%%%%%%%%%%%%%%%%%%%%%%%%%%%%%%%%%%%%%%%%%%%%%%%%%%%%%%%%%%%%%%%%%%%%%%%%%%%%%%%%
%%% It is the responsibility of the user to verify the applicability of    %%%
%%% this program for their study.                                           %%%
%%%%%%%%%%%%%%%%%%%%%%%%%%%%%%%%%%%%%%%%%%%%%%%%%%%%%%%%%%%%%%%%%%%%%%%%%%%%%%%%
clear all;
load FC.plt;              % Force Coefficient Time Histories.
fName1 = 'RSP_out.txt';   % Response Spectrum.
fName2 = 'DLF_out.txt';   % DLF Spectrum.
tFC  = FC(:,1);           % Time Vector.
CdFC = FC(:,2);           % Drag Coefficient Vector.
ClFC = FC(:,3);           % Lift Coefficient Vector.
%%%%%%%%%%%%%%%%%%%%%%%%%%%%%%%%%%%%%%%%%%%%%%%%%%%%%%%%%%%%%%%%%%%%%%%%%%%%%%%%
%%%%%%%%%%%%%%%%%%% Interpolate to Constant-Time-Step %%%%%%%%%%%%%%%%%%%%%%%%
%%%%%%%%%%%%%%%%%%%%%%%%%%%%%%%%%%%%%%%%%%%%%%%%%%%%%%%%%%%%%%%%%%%%%%%%%%%%%%%%
TIMEi = linspace(min(tFC),max(tFC),length(tFC));      % Time Vector.
dt  = TIMEi(2)-TIMEi(1);                              % Constant Time Step.
Cli = interp1(tFC,ClFC,TIMEi);                        % Interpolated Cl.
Cdi = interp1(tFC,CdFC,TIMEi);                        % Interpolated Cd.
%%%%%%%%%%%%%%%%%%%%%%%%%%%%%%%%%%%%%%%%%%%%%%%%%%%%%%%%%%%%%%%%%%%%%%%%%%%%%%%%
%%%%%%%%%%%%%%%%%%%%%%%%% Response Spectrum %%%%%%%%%%%%%%%%%%%%%%%%%%%%%%%%%%
%%%%%%%%%%%%%%%%%%%%%%%%%%%%%%%%%%%%%%%%%%%%%%%%%%%%%%%%%%%%%%%%%%%%%%%%%%%%%%%%
fn = (0.001:0.001:0.5);                          % Structure frequency (Hz)
m = 200000;                                      % Structure mass (kg)
RHO = 1.0;                                       % Fluid density (kg/m3)
Ur = 1.0;                                        % Reference velocity (m/s)
D = 1.0;                                         % Structure diameter (m)
L = 1.0;                                         % Structure unit length (m)
Ar = D*L;                                        % Refference area (m2)
Rm = RHO*Ar*D/m;                                 % Nondiminsionalize mass (dim)
z = 0.05;                                        % Damping ratio (dim)
tic;
for j=1:length(fn)
    wn = 2*pi*fn(j);                             % Structure frequency (rad/s)
    Us = Ur/(wn*D);                              % Nondim. reference vel. (dim)
    % Stiffness associated with structured wn(j) is still needed to compute
    % maximum static deflection.
    k = wn^2*m;                                  % Structure stiffness (N/m)
    Kt(j) = k;
    A = [0, 1; -(1/Us)^2, -2*z/Us];                  % State matrix
    B = @(tt, qq, FF)(A*qq + [0; FF*Rm/2]);          % System of Eqs
```

```
    q0 = [0; 0];                                    % Initial conditions
% Initialize dummy solution vectors.
    S1 = zeros(length(q0), length(TIMEi));
    S1(:,1) = q0;
    S2 = zeros(length(q0), length(TIMEi));
    S2(:,1) = q0;
% Analyze Cl
    for i = 1:length(TIMEi)-1
        k1 = B(TIMEi(i), S1(:,i), Cli(i));
        qmid = S1(:,i) + dt/2*k1;
        k2 = B(TIMEi(i) + 1/2*dt, qmid, (Cli(i) + Cli(i+1))/2);
        qmid = S1(:,i) + dt/2*k2;
        k3 = B(TIMEi(i) + 1/2*dt, qmid, (Cli(i) + Cli(i+1))/2);
        qend = S1(:,i) + dt*k3;
        k4 = B(TIMEi(i) + dt, qend, Cli(i));
        S1(:,i+1) = S1(:,i) + dt/6*(k1 + 2*k2 + 2*k3 + k4);
    end
% Analyze Cd
    for i = 1:length(TIMEi)-1
        k1 = B(TIMEi(i), S2(:,i), Cdi(i));
        qmid = S2(:,i) + dt/2*k1;
        k2 = B(TIMEi(i) + 1/2*dt, qmid, (Cdi(i) + Cdi(i+1))/2);
        qmid = S2(:,i) + dt/2*k2;
        k3 = B(TIMEi(i) + 1/2*dt, qmid, (Cdi(i) + Cdi(i+1))/2);
        qend = S2(:,i) + dt*k3;
        k4 = B(TIMEi(i) + dt, qend, Cdi(i));
        S2(:,i+1) = S2(:,i) + dt/6*(k1 + 2*k2 + 2*k3 + k4);
    end
% Take Steady Response (Avoid unsteadiness in initial RK4 solution)
    XCl = S1(1,round(length(TIMEi)/8):length(TIMEi));
    XCd = S2(1,round(length(TIMEi)/8):length(TIMEi));
% Compute Maximum Response Amplitude
    X1(1) = max(XCl);
    X1(2) = abs(min(XCl));
    X2(1) = max(XCd);
    X2(2) = abs(min(XCd));
    ACl(j) = max(X1);
    ACd(j) = max(X2);
    clear XCl XCd RMS X1 X2;
% Re-Set dummy solution vector
    S1 = zeros(length(q0), length(TIMEi));
    S1(:,1) = q0;
    S2 = zeros(length(q0), length(TIMEi));
    S2(:,1) = q0;
toc;
J=j
W=length(fn)
end
%%%%%%%%%%%%%%%%%%%%%%%%%%%%%%%%%%%%%%%%%%%%%%%%%%%%%%%%%%%%%%%%%%%%%%%%%%%%%%%
%%%%%%%%%%%%%%%%%%%%% Convert maximum response to DLF %%%%%%%%%%%%%%%%%%%%%%%%
%%%%%%%%%%%%%%%%%%%%%%%%%%%%%%%%%%%%%%%%%%%%%%%%%%%%%%%%%%%%%%%%%%%%%%%%%%%%%%%
% Compute maximum static displacements.
Cdt(1) = abs(max(Cdi));
Cdt(2) = abs(min(Cdi));
Cdm = max(Cdt);
Cs = RHO*Ar*Ur^2/2;                % Absolute maximum drag coefficient value
Fdm = Cdm*Cs;
```

```
Clt(1) = abs(max(Cli));
Clt(2) = abs(min(Cli));
Clm = max(Clt);                    % Absoluve maximum lift coefficient value
Flm = Clm*Cs;
for j=1:length(fn)
    % Convert diminsionless amplitudes (ACd & ACl) to dimensioned
    % amplitudes so they can be directly compared with static
    % displacements.
    DLFCd(j) = ACd(j)*D/(Fdm/(Kt(j)));
    DLFCl(j) = ACl(j)*D/(Flm/(Kt(j)));
end
% Write response data.
for i=1:length(fn)
    TEMP1(i,1)=fn(i);
    TEMP1(i,2)=ACd(i);
    TEMP1(i,3)=ACl(i);
    TEMP2(i,1)=fn(i);         % Corresponding structure frequencies (Hz)
    TEMP2(i,2)=DLFCd(i);      % Drag coefficient DLF
    TEMP2(i,3)=DLFCl(i);      % Lift coefficient DLF
end
dlmwrite(fName1,TEMP1,'\t');
dlmwrite(fName2,TEMP2,'\t');

yl = 10;
figure (1)
plot(fn,DLFCd,':og',fn,DLFCl,':or','linewidth',2)
xlabel('Structure Frequency (Hz)','fontsize',14,'fontweight','b',...
    'fontname','Times New Roman')
ylabel('Xmax/Xstatic','fontsize',14,'fontweight','b','fontname',...
    'Times New Roman')
title('DLF','fontsize',20,'fontweight','b','fontname','Times New Roman')
set(gca,'xlim',[0 max(fn)],'ylim',[0 yl],'fontsize',12,'fontname',...
    'Times New Roman')
legend('Signal 1','Signal 2',2)
```

APPENDIX D: EMPERICAL CYLINDER LOADING BY VORTEX "EFC.F"

D.1 Overview and Description

"EFC.f" is a program developed in the Fortran programming language to duplicate the loading of a rigid, circular cylinder by an impinging vortex at low Reynolds numbers ($Re \leq 300$). The program uses the equations and logic defined in Chapter 4 (for the transient velocity boundary condition) to compute the time history of the resultant velocity (V_R) at the prescribed location of the cylinder center. Additional studies reported in Chapter 6 simulate loading of a rigid, circular cylinder immersed in a free stream at $100 \leq Re \leq 300$ (while holding cylinder diameter "D" and fluid viscosity "ν" constant) allowing the mean (C_M) and harmonic (C_H) components of the cylinder loading to be defined as functions of V_R (See lines 60 and 61).

EFC.f reads the tornado parameters from the input data file "input.txt", which must be located in the same folder. The outputs are the mean drag and lift force coefficient time histories "FC(Mean).plt" and the envelopes that bound the amplitude of both force coefficient time histories "FC(Envelopes).plt". All force coefficients are computed using the reference velocity of $U_{ref} = 2$. Underlying assumptions of the application of EFC.f are that (1) V_R incident on the cylinder is VR that would be at the location of the cylinder center if the cylinder were not present to disrupt the flow and (2) the vortex is sufficiently large so that V_R is incident across the entire cylinder.

The user should be cautious when using EFC.f and understand what the limitations of the program are. Validation studies in Chapter 6 show that (1) EFC.f accurately reproduces force coefficient time histories from cylinder loading by a large vortex ($r_c/D = 50$) and (2) mean force coefficient time histories defined by EFC.f dynamically excite the same fundamental structure frequencies as force coefficient time histories from simulated structure loading by small vortices

($2 \leq r_c/D \leq 10$). That being said, EFC.f is not able to replicate the aerodynamic phenomenon (vortex shedding, interaction between attached and impinging vortices, etc.) which may also influence the cylinder loading. This means that the same force coefficient time history will always be produced for a given set of vortex parameters, and the variation in cylinder due to interaction between attached and impinging vortices (See Chapter 5) will not be captured. EFC.f provides a methodology to assess the character of low-Re vortex loading of a rigid circular cylinder; mean- and force coefficient envelopes are defined in a matter of minutes for simulations that require several days to execute via 2D direct simulation. This program can be used to assess have vortex parametes influence the cylinder loading, and then 2D CFD modelling can be used to simulate the loading cases deemed critical. The user must remain cautious, however, in that the emperical equations currently used to define the mean and harmonic components of the cylinder loading are only valid for $Re \leq 300$. The subsequent subsection illustrates the use of EFC.f and effectively serves as a user's manual.

D.2 Demonstration of Use

EFC.f must be typed, saved, and compiled in a folder. Subsequently, the input data file input.txt must be constructed and saved in the same folder. The input data consists of ten parameters listed in three rows. The sample data file is listed below, followed by the variable names, and finally by descriptions of each of the variables. The same equations used to define the transient velocity boundary condition are used to define the resultant velocity at the location of the cylinder center (See ***Figure 4.4***), consequently, Xp and Yp should remain fixed at zero.

```
1.,50.,0.02,2
0,0,0
500,1000,0.01

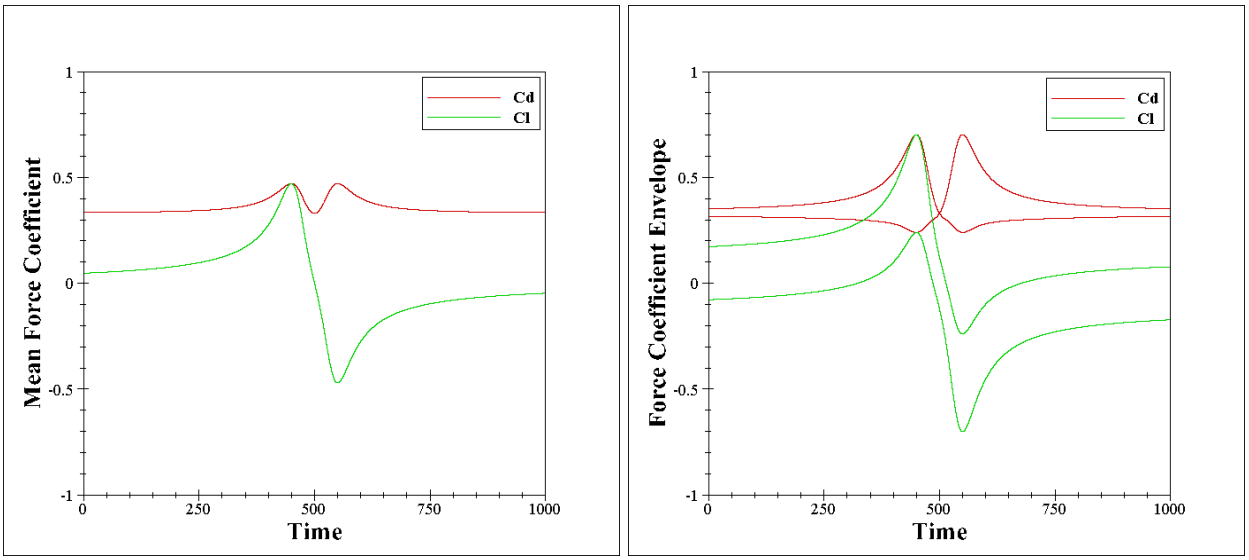
UFS,Rc,Alpha,Sn
Del,Xp,Yp
Tlag,TTIME,DT
```

```
UFS - Free stream velocity
Rc - Vortex critical radius
Alpha - Vortex rotational constant
Sn - Vatistas vortex coefficient
   (1) -> Normalized Sculley
   (2) -> Normalized Lamb-Oseen/Burgers-Rott
   (100) -> Rankine Combined

Del - Vertical shift in vortex path
Xp - Horizontal location of point W/R cylinder center
Yp - Vertical ...

Tlag - Time when vortex/cylider centers allign
TTIME - Total considered interaction time
DT - Time Step
```

The output data files containing the mean force coefficient time histories and the envelopes bounding the force coefficient time histories are plotted in Figures C.1a and C.1b respectively. Chapter 6 illustrates the combination of these two data sets and shows them to be excellent replication of the force coefficient time history produced by 2D computer simulation.



(a) (b)

Figure D.1: (a) Mean force coefficient time histories from "FC(Mean).plt" and (b) force coefficient envelop time histories from "FC(Envelopes).plt".

D.3 Source Code

"EFC.m" is a valuable program that may aid others in their studies of low-Re vortex loading of structures, hence the author would like to dissiminate the code. However, the author implores any that use the program to make sure that they first understand the applicabilty of the progam. Also, any duplication of the program without significant alteration should retain the header (Grey text).

```
C     %%%%
```

```
      Rpp = (Xpp**2.+Ypp**2.)**0.5
      Vtheta = Alpha*Rpp*(2./((Rpp/Rc)**(2.*Sn)+1))**(1./Sn)
      ! The denominator of Vtheta becomes too large for the RCVM
      ! approximation when Rpp << 0 or Rpp >> 0, so the RCVM vortex
      ! definition is used instead.
         IF(Sn.EQ.100)THEN
         IF(Rpp.LE.Rc)THEN
            Vtheta = Alpha*Rpp
         Else
            Vtheta = Alpha*Rc**2./Rpp
         END IF
      END IF
      U = UFS - Vtheta * (Ypp/Rpp)
      V = Vtheta * (Xpp/Rpp)
      Vres = (U**2.+V**2.)**0.5
      CH = 0.3111*Vres**2.-0.2594*Vres+0.0712
      CM = 0.3569*Vres**2.-0.0525*Vres+0.0261
      Ang = atan(V/U)
      CdH = CH*sin(Ang)
      CdM = CM*cos(Ang)
      ClH = CH*cos(Ang)
      ClM = CM*sin(Ang)
      Cdplus = CdM + CdH
      Cdminus = CdM - CdH
      Clplus = ClM + ClH
      Clminus = ClM - ClH
      WRITE(3,*)TIME,CdM,ClM
      WRITE(5,*)TIME,Cdplus,Cdminus,Clplus,Clminus
      PRINT*,TIME
      TSTAR = TSTAR + DT
      TIME = TIME + DT
   END DO
   STOP
   END
```

CURRICULUM VITAE

EDUCATION

Doctor of Philosophy, Civil Engineering (Structural) December 2015
University of Arkansas
GPA: 3.88/4.00
Dissertation: The Aerodynamic and Dynamic Loading of a Slender Structure by an Impacting Tornado-Like Vortex: The Influence of Relative Vortex-to-Structure Size on Structural Loading
Committee: R. Panneer Selvam, Micah Hale, Ernest Heymsfield, and Rick Couvillion

Master of Science, Civil Engineering (Structural) December 2012
University of Arkansas
GPA: 3.88/4.00
Thesis: Performance and Cost Analysis of a Structured Concrete Thermocline Thermal Energy Storage System
Committee: R. Panneer Selvam, Micah Hale, and Ernest Heymsfield

Bachelor of Science, Mechanical Engineering May 2011
Harding University
GPA: 3.20/4.00

LICENSURE AND CERTIFICATION

Concrete Field Technician Grade I (ACI-01242091) April 2012 - 2017
Engineer in Training (Arkansas EIT-7797) June 2011

QUALIFICATIONS

- A multi-disciplinary engineer who pursues leadership roles.
- Delivers work on time in high-pressure settings in individual and team environments.
- An experienced writer and presenter of technical documents and reports.
- An experienced programmer in Fortran and Matlab languages with experience in C++.
- An experienced user of Microsoft Office software: Word, Excel, and PowerPoint.

HONORS AND AWARDS

1st Place Poster Presentation – Arkansas Academy of Science 2014
1st Place Poster Presentation – U of A Abstract to Contract 2013
University of Arkansas Doctoral Academy Fellowship 2012 - 2015

RESEARCH EXPERIENCE

Location: University of Arkansas, Computational Mechanics Laboratory
Research Director: Dr. R. Panneer Selvam

Doctoral Research November 2013 – Present

- Applied a previously-developed, two-dimensional, fluid dynamics model to study phenomenon influencing structural loading by intense vortices.
- Identified new phenomenon: Interaction between an impinging vortex and vortices produced on the loaded body produces large variation in the structure loading.
- Developed a generalized methodology to assess dynamic amplification of structures' responses to a vortex's tangential wind field using the dynamic load factor concept.

Subsequent Research January – October 2013

- Applied numerical heat transfer models and cost analysis to assess cost savings by integrating thermal energy storage for residential climate control and industrial water heating.
- Rigorously surveyed parameters controlling pressure drop for flow through packed beds and demonstrated that utility-scale packed-bed thermocline thermal energy storage systems are not viable when gas is used as heat transfer fluid.
- Supervised five undergraduate students' research projects developing a wood gasifier.

Masters Research August 2011 – December 2012

- Evaluated performance and viability of a structured-concrete thermocline thermal energy storage system.
- Developed and applied one- and two-dimensional numerical heat transfer models to optimize solid media configuration for thermal performance.
- Conducted complete cost analysis of utility-scale 50 MW central receiver solar thermal power plant with packed-bed and structured-concrete thermal energy storage systems.
- Conducted thermal cycling tests to evaluate the chemical compatibility of propriety concrete mix designs in a 565°C molten salt environment.

PUBLICATIONS

Journal Papers

Strasser, M.N., Yousef, M.A., and Selvam, R.P., 2015. Defining the Vortex Loading Period and Application to Assess Dynamic Amplification of Tornado-Like Wind Loading, **In Review with** *J. Fluids and Structures*, Manuscript Number: YJFLS-D-15-00381.

Strasser, M.N. and Selvam, R.P., 2015. The Influence of Vortex Size on the Maximum Loading of a Slender, Cylindrical Structure Impacted by Aerospace to Tornado-Scale Vortices, **In Review with** *J. Fluids and Structures*, Manuscript Number: YJFLS_2015_126.

Strasser, M.N. and Selvam, R.P., 2015. Selection of a Realistic Viscous Vortex Tangential Velocity Profile for Computer Simulation of Vortex-Structure Interaction, *J. Arkansas Academy of Science* ***69***, Manuscript Number: JAAS MS69-12.

Strasser, M.N. and Selvam, R.P., 2015. The variation in the maximum loading of a circular cylinder impacted by a 2D vortex with time of impact, *J. Fluids and Structures* ***58****, 66-78*.

Strasser, M.N. and Selvam, R.P., 2014. A cost and performance comparison of packed bed and structured thermocline thermal energy storage systems, *J. Solar Energy* ***108****, 390-402*.

Skinner, J.E., Strasser, M.N., Brown, B.M., and Selvam, R.P., 2014. Testing of high-performance concrete as thermal energy storage medium at high temperatures, *J. Solar Energy Engineering* ***136(2)****, 021004*.

Conference Proceedings

Strasser, M.N. and Selvam, R.P., 2015. Evaluation of Pressure Drop in Air- and Salt-Based Thermocline Thermal Energy Storage Systems. Proc. XIX CONGRESO NACIONAL DE INGENIERIA CIVIL, Ancash-Huarez, Peru, November 11-14.

Selvam, R.P., Strasser, M.N., Ahmed, N., Yousef, M., & Ragan, Q.S., 2015. Observations of the Influence of Hilly Terrain on Tornado path and Intensity from Damage Investigation of the 2014 Tornado in Mayflower, Arkansas. Proc. ASCE Structures Congress, Portland, OR, pp. 2711-2721.

Strasser, M.N. and Selvam, R.P., 2014. Influence of Phase of Vortex Shedding at Vortex Impact on Peak Loading. Proc. ICAFD, India.

Strasser, M.N. and Selvam, R.P., 2013. A Comparative Cost and Performance Analysis of Structured and Packed-Bed Thermocline Thermal Energy Storage Systems. Proc. 7th Int. Conference on Energy Sustainability, Minneapolis, MN, DOI:10.1115/HT2013-17169.

Brown, B.M., Strasser, M.N., & Selvam, R.P., 2012. Development of a Structured Thermocline Thermal Energy Storage System. Proc. ASES, Denver, CO, Paper Number 0074.

Technical Reports

Selvam, R.P., Ahmed, N., Strasser, M.N., Yousef, M., Ragan, Q.S., and Costa, A., 2015. RAPID: Documentation of Tornado Track of Mayflower Tornado in Hilly Terrain. US National Science Foundation. Available online: http://compmech.cveg.uark.edu.

Selvam, R.P., Hale, W.M., and Strasser, M.N., 2013. Development and Performance Evaluation of High Temperature Concrete for Thermal Energy Storage for Solar Power Generation. US Department of Energy. DOI:10.2172/1072014.

POSTER PRESENTATIONS

Strasser, M.N. and Selvam, R.P., 2015. Selection of a Viscous Vortex Tangential Velocity Profile for CFD Application, Presented at: Meeting of the Arkansas Academy of Science, Henderson St. University, Arkadelphia, AR.

Strasser, M.N. and Selvam, R.P., 2014. The Influence of Vortex Size and Path on Structural Loading, Presented at: Abstract to Contract Research Contest, University of Arkansas, Fayetteville, AR.

Strasser, M.N. and Selvam, R.P., 2014. Influence of the Phasing of Vortex Shedding and Vortex Impact on Structural Loading, Presented at: Meeting of the Arkansas Academy of Science, Harding University, Searcy, AR.

Strasser, M.N. and Selvam, R.P., 2013. Cost and Performance Analysis of Thermal Energy Storage Systems for Concentrating Solar Power Plants, Presented at: Abstract to Contract Research Contest, University of Arkansas, Fayetteville, AR.

Strasser, M.N. and Selvam, R.P., 2012. Performance and Cost Analysis of Packed Bed and Structured Thermocline Thermal Energy Storage Systems, Presented at: High Performance Computing Center Seminar, University of Arkansas, Fayetteville, AR.

Selvam, R.P., Hale, W.M., John, E., & Strasser, M.N., 2012. Development and Performance Evaluation of High Temperature Concrete for Thermal Energy Storage for Solar Power Generation, Presented at: Sunshot Grand Technology Forum, Denver, CO.

PATENT FILINGS AND INTELECTUAL PROPERTY DISCLOSURES

R.P. Selvam, R. Foster, and M. Strasser, 2013. Thermal energy storage for electricity production using "Center-fed" packed bed and air or optional liquids as heat transfer fluid, IP disclosed to University of Arkansas, May 8, 2013.

R.P. Selvam, M. Strasser, and M. Hale, 2013. Thermal energy storage using packed bed using air for Heating and electricity production, IP disclosed to University of Arkansas, February 11, 2013.

MEMBERSHIPS

Arkansas Academy of Science	2014 – 2015
American Society of Mechanical Engineers	2009 – 2011, 2013 – 2014
American Solar Energy Society	2012 – 2013
Society of Tribologists and Lubrication Engineers	2011 – 2012

UNDERGRADUATE STUDENTS MENTORED

University of Arkansas Freshman Engineering Research Program

Nicholas Chavis & Christopher Maestri — August 2013 – April 2014
Project: Construction of combustion unit for a wood gasifier

William Chu & Alexander Raney — August 2013 – April 2014
Project: Construction of filtration unit for a wood gasifier
* Received 1st place award on poster presentation

George Washington Carver Summer Research Program

Kory Pough — Summer 2012
Project: Design of a wood gasifier

REVIEWER

J. Heat Transfer	Since 2013
J. Renewable and Sustainable Energy	Since 2013
Physics of Fluids	Since 2014
J. Solar Energy Engineering	Since 2014